ABSTRACT

PROCTOR, WILLIAM CYRUS. Reactor Loose Part Damage Assessments on Steam Generator Tube Sheets. (Under the direction of Joseph Michael Doster).

Damage from loose parts inside reactor systems can potentially cause integrity issues that jeopardize the operations of these facilities. Parts such as nuts, bolts, pins, sections of tubing and even hand tools are found inside the primary circuits of PWRs [Michel]. These parts carried by the coolant flow impact structures including the steam generator tube sheets and can cause significant damage leading to the unscheduled shut down of a facility. In this work we assess the behaviors of typical loose parts that may reside in the primary coolant system. Validations of scaled simulations are linked to previous experiments conducted by Shi [Shi]. Monte Carlo simulations of typical impact and energy distributions on a representative steam generator are analyzed and discussed.

To obtain a more complete understanding of loose part damage caused to the tube sheet of PWR steam generators, CFD using the ANSYS CFX software package is used to compute detailed three dimensional flow fields within the steam generator inlet plenum. The flow field information is then input into a Monte Carlo program developed as part of this work to predict the trajectory of the loose part. Existing software packages lack the ability to track finite volume, finite mass particles. Additionally, there were no packages available that allowed for detailed manipulation of the collision physics necessary to accurately model impacts. The particle tracking program developed here then allows for the calculation of loose part impact locations and the energy imparted from loose part impacts with the tube sheet surface. Ultimately given this information along with the previous models developed

by Shi, damage rates can be estimated aiding in the development of guidelines to improve the decision making process when loose parts are detected in the primary coolant system.

As part of previous research, a 1:8 scaled model of the McGuire steam generator inlet plenum and tube sheet was constructed by Shi. This scaled steam generator tube sheet impact pattern experiment was run with two different types of hexagonal nuts and varied fluid inlet velocities. These experiments serve as a benchmark reference for development of the computational models in this work.

Simulations of a full scale system similar to that of a Westinghouse Model D steam generator have also been performed. Detailed impact analysis is conducted as a function of coolant temperature, coolant inlet velocity, loose part type, shape, mass, density, initial starting location and initial kinetic energy. No a priori knowledge is assumed for the initial starting location and initial kinetic energy of the parts. Full scale results are compared to the scaled experiment to assess the validity of making predictions using only a scaled simulation.

Reactor Loose Part Damage Assessments on Steam Generator Tube Sheets

by
William Cyrus Proctor

A thesis submitted to the Graduate Faculty of
North Carolina State University
in partial fulfillment of the
requirements for the degree of
Master of Science

Nuclear Engineering

Raleigh, North Carolina

2010

APPROVED BY:

J. Michael Doster Committee Chair	Mohamed A. Bourham

Moody T. Chu

DEDICATION

To find yourself,

think for yourself.

- Fortune Cookie

BIOGRAPHY

William Cyrus Proctor was born July 9, 1985 in Asheville, North Carolina to Bill Proctor and Debby Smith. He attended A. C. Reynolds Middle and High School until 2003 where he moved to North Carolina State University to pursue an undergraduate career in Nuclear Engineering and Physics. Upon graduation in 2007 he continued on to pursue a Master of Science in Nuclear Engineering. In 2009, he continued towards his Ph.D.

ACKNOWLEDGEMENTS

It is to you, the reader, which I give my first acknowledgements to. For, it is because of the few who continue to read on that truly makes this composition worthwhile. May you find some small measure of meaning from the collection of words and numbers written below.

To my advisor, Dr. Mike Doster I give my appreciation. Truly, it is men *like* him that have made a difference in the course of many lives. Five classes and a thesis later I owe him a great deal of my fascination with Nuclear Engineering and my love of thermal-hydraulics, Monte Carlo techniques and a better appreciation on deterministic transport methods. Without his cultivating efforts my evolution from pond scum to amoeba to small gelatinous multi-cellular creature would not have been possible. It is to him that I owe a fighting chance at becoming worthy of the title of Nuclear Engineer.

To Dr. Bourham and Dr. Chu; who both have graciously taken time out of their schedules to read, review and solidify this work. Your thoughts and inputs are appreciated.

To my friends and colleagues, I give collective thanks. Without sounding boards for thoughts and ideas or without those times to distract me, this work would not be what it is. I appreciate times come and gone and hope for more times to be as memorable as these.

To my parents; thank you. It is because of both you that I am here today. You give me strength and wisdom in ways you cannot know. These pieces of paper are but a beginning.

TABLE OF CONTENTS

LIST OF TABLES

LIST OF FIGURES

Chapter 1 Introduction

1.1 Background

Damage from loose parts inside reactor coolant systems can potentially cause integrity issues that jeopardize the operations of these facilities. Parts such as nuts, bolts, pins, sections of tubing and even hand tools are found inside the primary circuits of PWRs [Michel]. Usually these parts tend to collect either in the lower internals of the reactor vessel or in the inlet plenum of the steam generators. These parts carried by the coolant flow impact structures including the steam generator tube sheets and can cause significant damage leading to the unscheduled shut down of a facility. These unexpected outages can cost utilities on the order of millions of dollars [Michel].

Most modern PWRs are equipped with loose parts monitoring systems. These systems have the capability to provide a reasonable estimate of loose part impact energy, location and mass. These systems usually rely on acoustic detectors, accelerometers and applications of Hertzian theory to make these assessments [Shi].

Although these systems are widely used, there is still a lack of understanding of the potential impact damage rates that these loose parts can cause. This leads to a high degree of uncertainty when determining what preventative measures to enact when a loose part is detected. If an action is delayed it could potentially damage critical reactor components forcing an unscheduled outage. If action is taken too aggressively, it could potentially cause the system to be unnecessarily offline.

This work expands upon previous research by Liang Shi [Shi]. At the time of his dissertation, computational resources for predicting the detailed flow distributions in steam generator inlet plena were unavailable, forcing the reliance on simplistic models. Since that time, commercially available Computational Fluid Dynamics (CFD) packages have become common, allowing for predictions of part trajectories and impact distributions in more realistic flow fields.

This work takes an in depth approach to assess the behaviors of typical loose parts that may reside in the primary coolant system. Verification of scaled and full scale simulations are linked to previous experiments conducted by Shi. Monte Carlo simulations of typical impact and energy distributions on a representative steam generator are analyzed and discussed.

1.2 Previous Work

Little relevant literature could be found by the author on the simulation of impact damage by loose parts in steam generator inlet plenums. More specifically the computational resources available at present day are just beginning to reach the level necessary to efficiently compute detailed three dimensional fluid flow fields inside these geometries. As a result, earlier research has relied on simplified flow distributions with assumed flow characteristics for the simulations.

Shi's relevant previous work was only able to construct a loose part impact model using estimated flow fields ascertained from scaled experiments. These experiments allowed Shi to develop models for quantifying impact damage, including effects from work hardening

due to multiple impacts, tube end radius reduction and generation of secondary pieces of debris also due to significant multiple impacts.

1.3 Scope of Present Work

To obtain a more complete understanding of loose part damage caused to the tube sheet of PWR steam generators, CFD is used to compute detailed three dimensional flow fields within the steam generator inlet plenum. The flow field information is then input into a Monte Carlo program to predict the trajectory of the loose part. This Monte Carlo program was developed because existing software packages that included particle tracking lacked the ability to track finite volume, finite mass particles. Additionally, there were no packages available that allowed for detailed manipulation of the collision physics necessary to accurately model impacts. This program then allows for the calculation of loose part impact locations and the energy imparted from impact with the tube sheet surface. Ultimately given this information along with the previous models developed by Shi, damage rates can be estimated and a detailed set of guidelines may be developed. These guidelines could serve in the decision making process when loose parts are detected in the primary coolant system.

As part of his research, a 1:8 scaled model of the McGuire steam generator inlet plenum and tube sheet was constructed by Shi. This scaled steam generator tube sheet impact pattern experiment was run with two different types of hexagonal nuts and varied fluid inlet velocities. These experiments serve as a benchmark reference for development of the computational models in this work.

Simulations of a full scale system similar to that of a Westinghouse Model D steam generator are also performed. Detailed impact analysis is conducted as a function of coolant

temperature, coolant inlet velocity, loose part type, shape, mass, density, initial starting location and initial kinetic energy. Based on these input parameters, this work attempts to assess which loose parts are correlated with significant steam generator tube sheet damage.

Chapter 2 presents the computational models and process used to predict impact frequency distributions. **Figure 1.1** summarizes the overall process discussed in **Chapter 2**. **Chapter 3** presents and discusses the results generated for the benchmark experiment and simulation as well as for the full scale simulation.

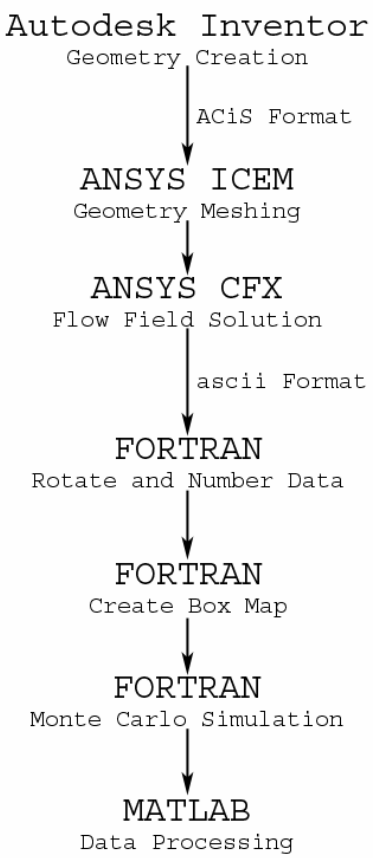

Figure 1.1 Generation of overall results flowchart

Chapter 2 Simulation Setup

2.1 Initial Benchmark Experiment Description

To investigate loose part impacts on representative steam generator tube sheets, Shi constructed a 1:8 scale model of the McGuire steam generator inlet plenum [McGuire]. The tube sheet was created from a semi-circular sheet of Inconel 600 [ESPI], 15.5 inches in diameter. Four hundred fifty two holes of diameter 0.19035 inches were drilled uniformly across the sheet with a triangular pitch of 0.450 inches to give a total open area ratio equal to that of the full scale tube sheet. The tube sheet was fitted inside a hemispherical collision chamber which simulated the inlet plenum. A 3.7 inch diameter inlet pipe attached at a 45 degree angle to the collision chamber to simulate the inlet seen in the hot leg of Westinghouse steam generators. The setup is represented in **Figure 2.1** below.

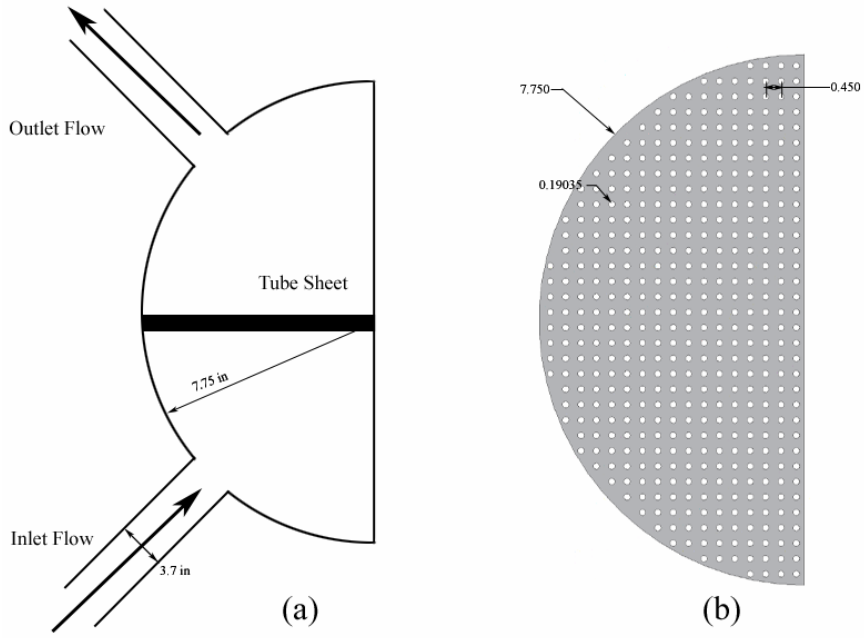

Figure 2.1 (a) Profile view of collision chamber, (b) Top down view of tube sheet

With the system operating at a constant mass flow rate, hexagonal nuts (see **Figure 2.2** and **Table 2.2**) were released through a valve system into the base of the inlet pipe. Once an impact occurred on the tube sheet or the part became inactive, the system was shut down and the part was retrieved. This process was repeated hundreds of times to create an impact distribution on the tube sheet. Three cases were conducted with two different size hexagonal nuts and two different fluid velocities. Results were fit to a 2-D Gaussian distribution defined as

$$f(x,y) = \frac{1}{\pi\sigma_x\sigma_y} e^{-\left(\frac{x^2}{2\sigma_x^2}+\frac{y^2}{2\sigma_y^2}\right)} \tag{2.1.1}$$

with the y-axis serving as the axis of symmetry on the tube sheet. **Table 2.1** summarizes the initial parameters and fitting results of the three cases. Note that the maximum impact probability was tallied using mesh boxes 1/20 the length and width of the tube sheet radius.

Table 2.1 Conditions and results of the scaled steam generator tube sheet impact test

Test case	Loose part mass (g)	Inlet flow velocity (m/s)	σ_x (% tube sheet radius)	σ_y (% tube sheet radius)	Experimental maximum impact probability
Case 1	16	5.3	7.6	20	0.048
Case 2	16	3.6	7.6	20	0.048
Case 3	30	5.3	7.6	20	0.048

2.2 Additional Previous Data and Results

In addition to the impact distribution experiments, in-flow experiments were performed with several hypothetical loose part types to characterize preferred orientation and average drag coefficients. These included hexagonal bolts and nuts as well as a rectangular

bar, cylinder and sphere. **Figure 2.2** and corresponding **Table 2.2** represent key dimensions and masses of the parts.

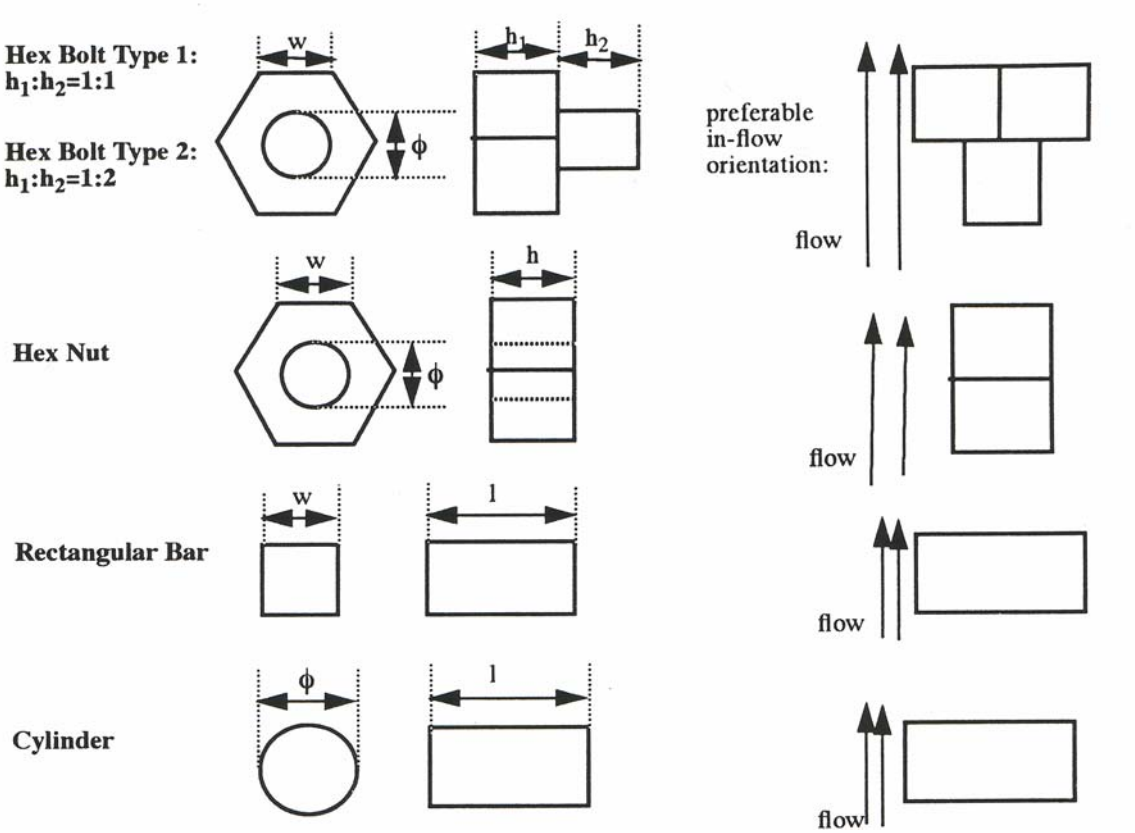

Figure 2.2 Loose part dimensions and their preferred in-flow orientations [Shi]

Table 2.2 Loose part dimensions and mass

Loose Part Type	Size	Dimensions (in)				Mass (g)
		ϕ	w	h (h_1, l)	h_2	
Hex Bolt Type 1	1/2''	0.5	0.43	0.31	0.29	26
Hex Bolt Type 1	5/8''	0.625	0.54	0.39	0.35	50
Hex Bolt Type 1	3/4''	0.75	0.64	0.47	0.45	88
Hex Bolt Type 1	7/8''	0.875	0.745	0.55	0.52	136
Hex Bolt Type 1	1''	1	0.845	0.62	0.62	206
Hex Bolt Type 2	1/2''	0.5	0.43	0.31	0.63	34
Hex Bolt Type 2	5/8''	0.625	0.54	0.39	0.78	66
Hex Bolt Type 2	3/4''	0.75	0.64	0.47	0.98	116
Hex Bolt Type 2	7/8''	0.875	0.745	0.55	1.06	178
Hex Bolt Type 2	1''	1	0.845	0.62	1.23	268
Hex Nut	1/2''	0.44	0.44	0.44	-	16
Hex Nut	5/8''	0.54	0.54	0.54	-	30
Hex Nut	3/4''	0.67	0.64	0.65	-	52
Hex Nut	7/8''	0.78	0.75	0.74	-	80
Hex Nut	1''	0.89	0.85	0.85	-	124
Rectangular Bar	1/2''	-	0.75	2w	-	32
Rectangular Bar	3/4''	-	0.5	2w	-	108
Rectangular Bar	7/8''	-	0.875	2w	-	172
Rectangular Bar	1''	-	1	2w	-	256
Cylinder	1/2''	0.5	-	2ϕ	-	26
Cylinder	3/4''	0.75	-	2ϕ	-	84
Cylinder	7/8''	0.875	-	2ϕ	-	134
Cylinder	1''	1	-	2ϕ	-	202
Sphere	1/2''	0.5	-	-	-	8
Sphere	3/4''	0.75	-	-	-	28
Sphere	9/10''	0.9	-	-	-	56
Sphere	1''	1	-	-	-	66
Sphere	3/2''	1.5	-	-	-	226

The typical velocity range of most measurements included the wake transition region due to the high degree of variance typically encountered here. Overall, results from this previous work show that especially in the low Reynolds number region ($< 10^3$) drag coefficients were very similar to that of a standard sphere [Shi, Donley]. A posteriori, the region beyond the wake transition region ($> 10^6$) also plays a significant role in producing

drag forces on the debris, particularly for high velocity cases before the debris has entered into the inlet plenum. For this region, little literature exists because this turbulent region is characterized as unstable. Averaged drag coefficient information regarding a sphere in this region was obtained. Analyzing the behavior of the part as it passed towards the end of the transition region, each part tends to converge around 0.5E+06 to a drag coefficient around 0.1. The literature suggests that the drag coefficients should then begin to recover to a value approaching 0.2 by the time a Reynolds Number of 1.0E+07 is reached [Donley]. **Figure 2.3** depicts the behavior of the drag coefficient found for the different types of parts over the Reynolds number range of 1.0E+04 to 1.0E+06. The tabulated data may be found in **Table 2.3**. The green shaded data is from Donley while the rest is tabulated from Shi's experiments.

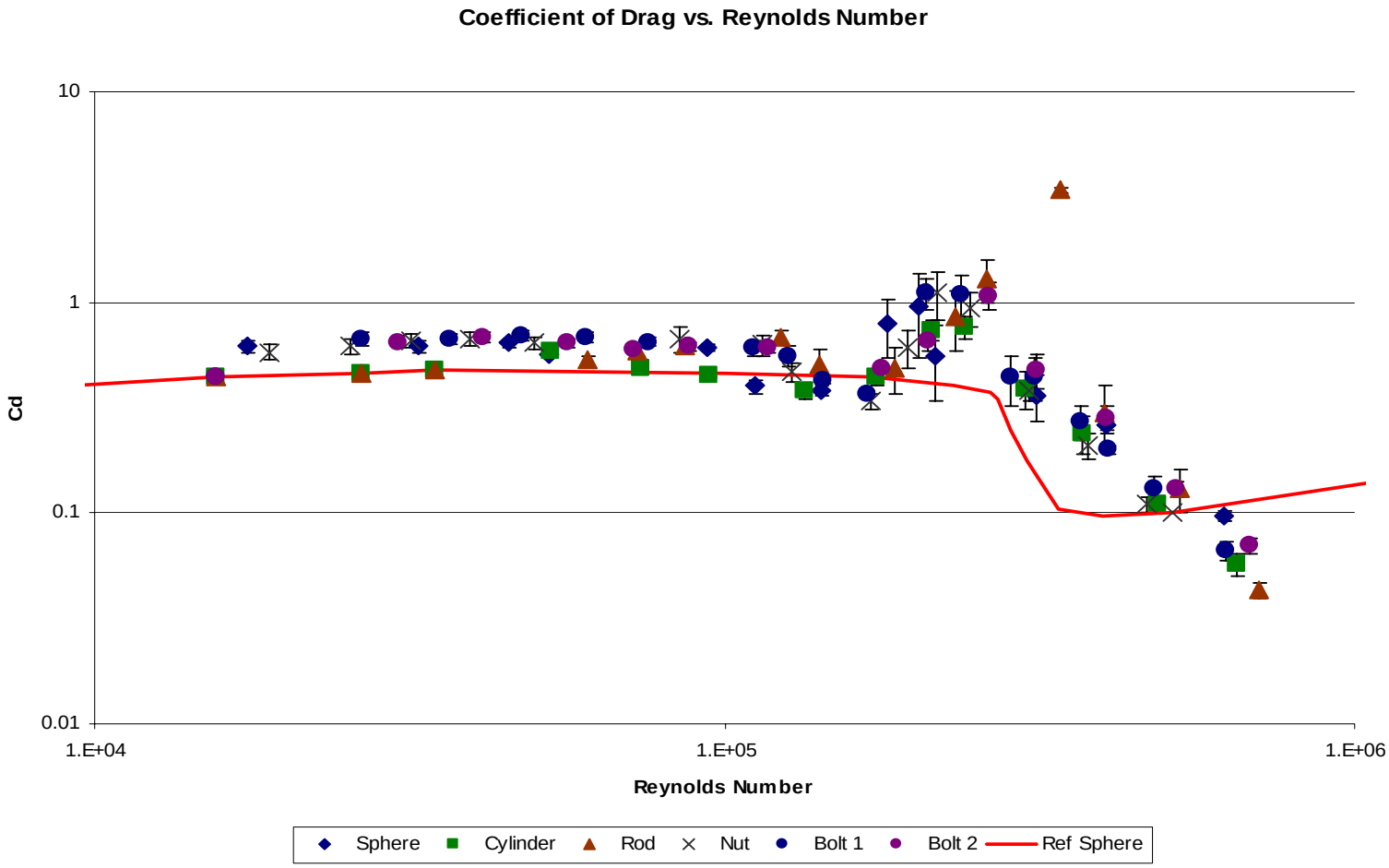

Figure 2.3 Drag Coefficients vs. Reynolds Number [Shi, Donley]

Table 2.3 Drag Coefficients vs. Reynolds Number [Shi, Donley]

Sphere		Cylinder		Rectangular Bar		Hexagonal Nut		Hexagonal Bolt Type 1		Hexagonal Bolt Type 2		Common Data	
Re	Cd	Re	Cd	Re	Cd	Re	Cd	Re	Cd	Re	Cd	Re	Cd
17500	0.62	15560	0.4395	15560	0.4395	19000	0.58	15560	0.4395	15560	0.4395	0.05875	492
32700	0.62	26480	0.4571	26480	0.4571	25400	0.62	26500	0.67	30300	0.65	0.1585	169.8
45400	0.64	34670	0.4775	34670	0.4775	31800	0.66	36700	0.67	41200	0.68	0.4786	58.88
52500	0.57	53100	0.59	60700	0.53	39500	0.67	47500	0.7	56400	0.64	3.02	10.86
93500	0.61	73500	0.49	72500	0.59	49700	0.64	60000	0.68	71800	0.6	7.015	5.623
112000	0.4	94500	0.45	86400	0.62	84600	0.67	75600	0.65	87500	0.62	15.49	3.388
142000	0.38	134000	0.38	123000	0.68	115000	0.63	111000	0.61	117000	0.61	57.54	1.479
181000	0.79	174000	0.44	141000	0.51	128000	0.47	126000	0.56	178000	0.49	144.5	0.9204
203000	0.96	213000	0.74	186000	0.49	171000	0.34	143000	0.43	210000	0.66	264.9	0.7194
216000	0.56	240000	0.76	233000	0.86	195000	0.61	168000	0.37	263000	1.08	512.9	0.5623
312000	0.36	301000	0.39	260000	1.3	217000	1.11	209000	1.11	313000	0.48	1000	0.4786
404000	0.26	370000	0.24	342000	3.4	246000	0.94	238000	1.09	404000	0.28	1862	0.4365
622000	0.097	486000	0.11	401000	0.3	305000	0.38	284000	0.44	522000	0.13	3162	0.4074
		649000	0.057	527000	0.13	378000	0.21	311000	0.44	682000	0.07	4764	0.389
						469000	0.11	367000	0.27			8375	0.3981
						512900	0.1	406000	0.2			1778000	0.1778
								479000	0.13			2291000	0.1862
								626000	0.066			5012000	0.1862

2.3 Simulation Setup and Process

To simulate the behavior of the scaled steam generator impact test, several software programs were utilized to first generate the flow field. The flow field data was then read into a Monte Carlo FORTRAN code developed specifically for the purpose of characterizing loose part impact behavior.

2.3.1 Flow Field Generation

A model of the fluid volume inside the inlet plenum was created using AutoDesk Inventor Professional 2008. The fluid volume was extended several inches into the tube themselves due to the eddy currents that formed at the transition point between the inlet plenum and the tube inlets. To properly solve for the flow field in this region the outlet boundary needed fluid only flowing out of the boundary. Eddy currents forced the fluid to come back into the model after having exited and the solver warned of inaccurate solutions in this case. This fact increased the length of the tubes which significantly increases memory requirements needed to compute an accurate solution. **Figure 2.4a** depicts the flow volume of the scaled simulation created with AutoDesk Inventor. **Figure 2.4c** depicts the flow volume of the full scale simulation. The final length of the tubes protruding from the plenum was 6 inches. The length of the inlet pipe was 22.25 inches to provide ample distance for the fluid to stabilize before entering the plenum. The flow volume is also cut along a plane of symmetry to reduce computational costs.

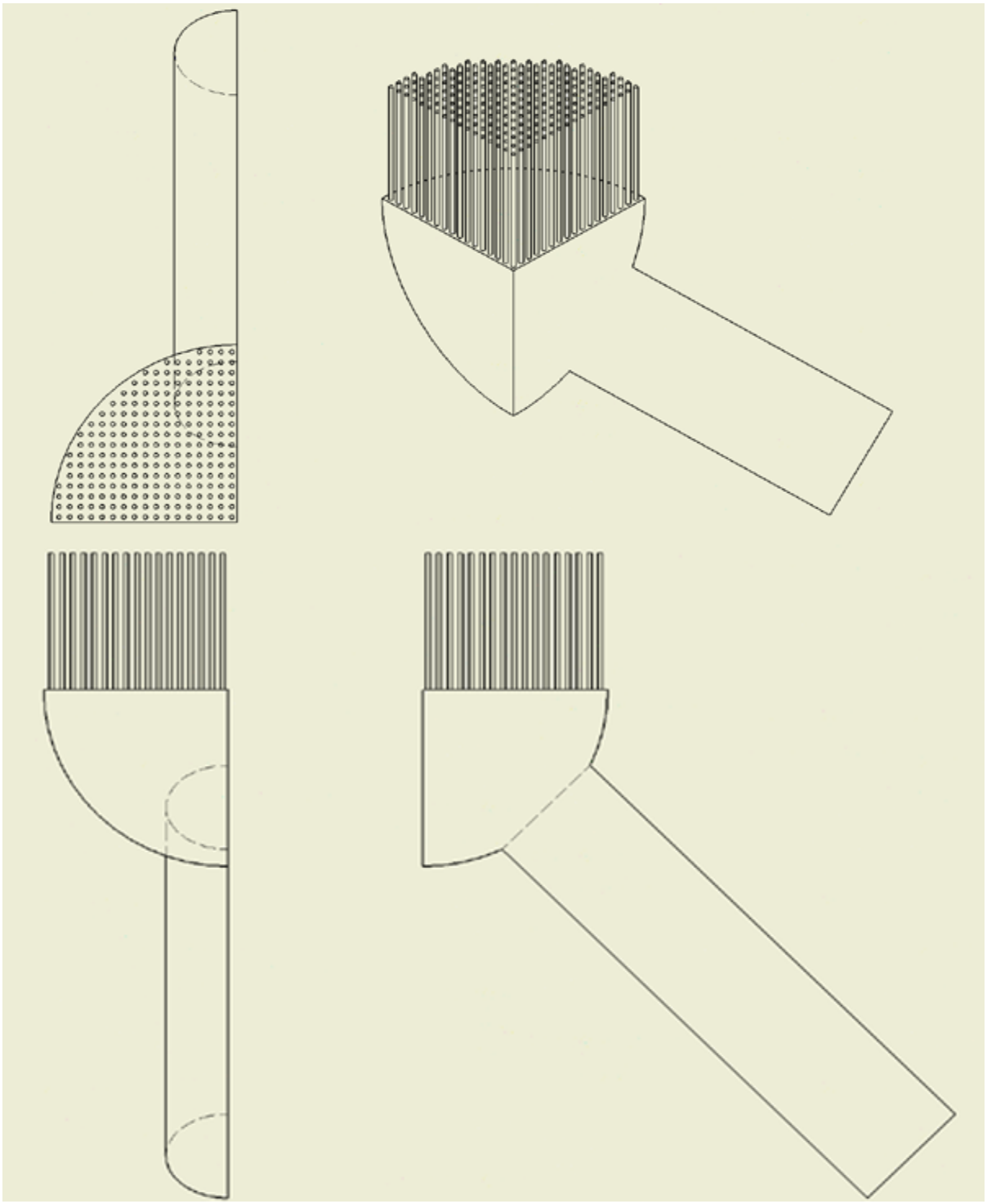

Figure 2.4a Scaled simulation flow volume

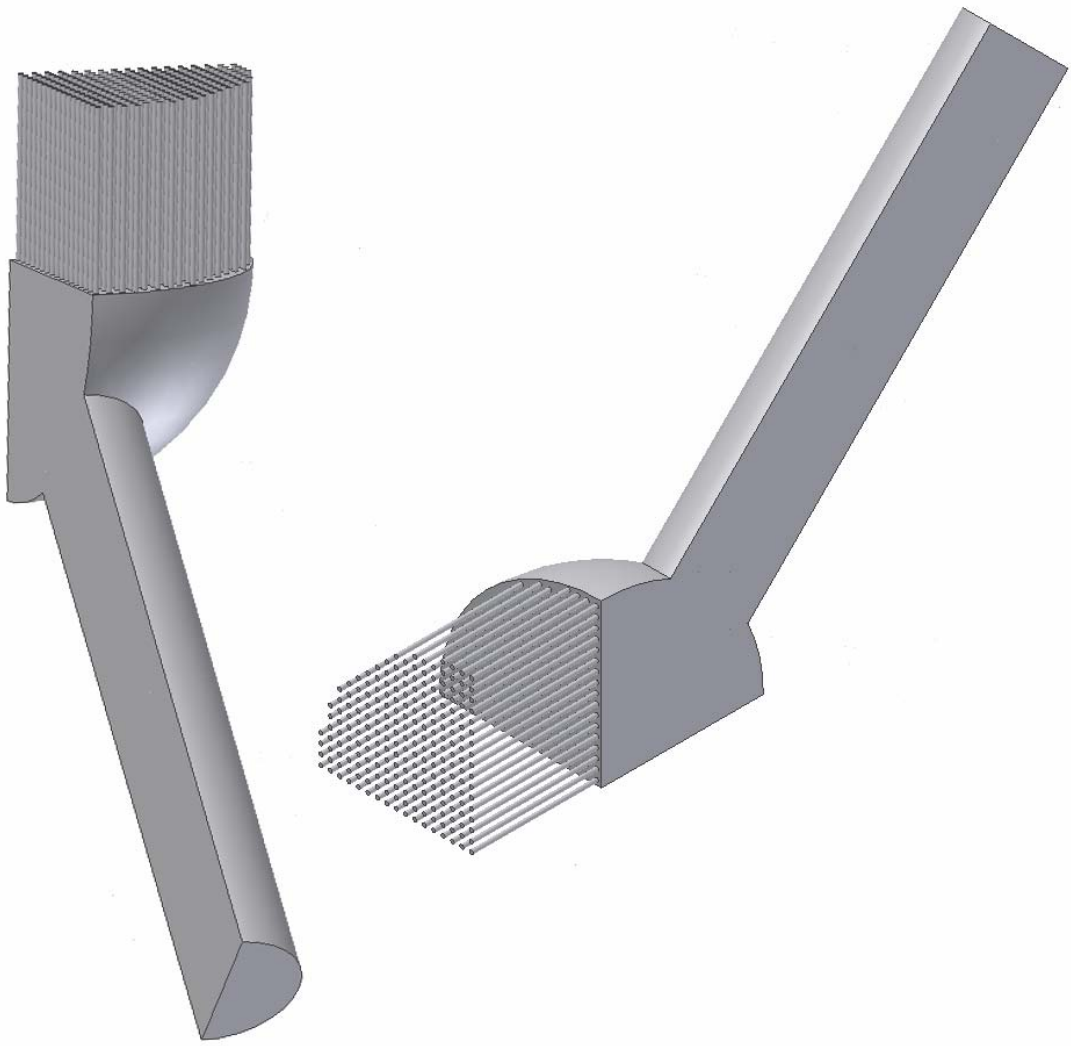

Figure 2.4b Scaled simulation flow volume

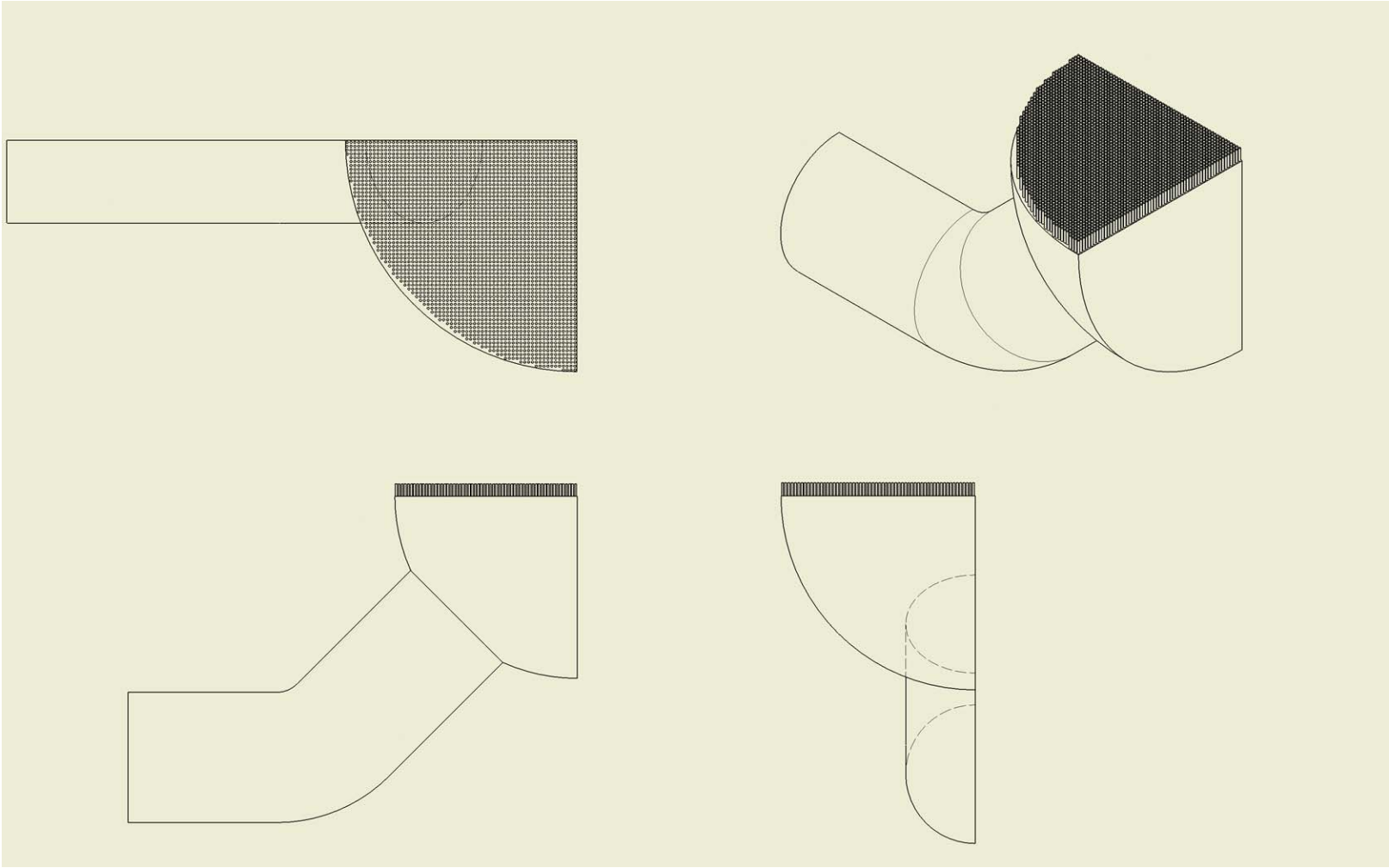

Figure 2.4c Full scale simulation flow volume

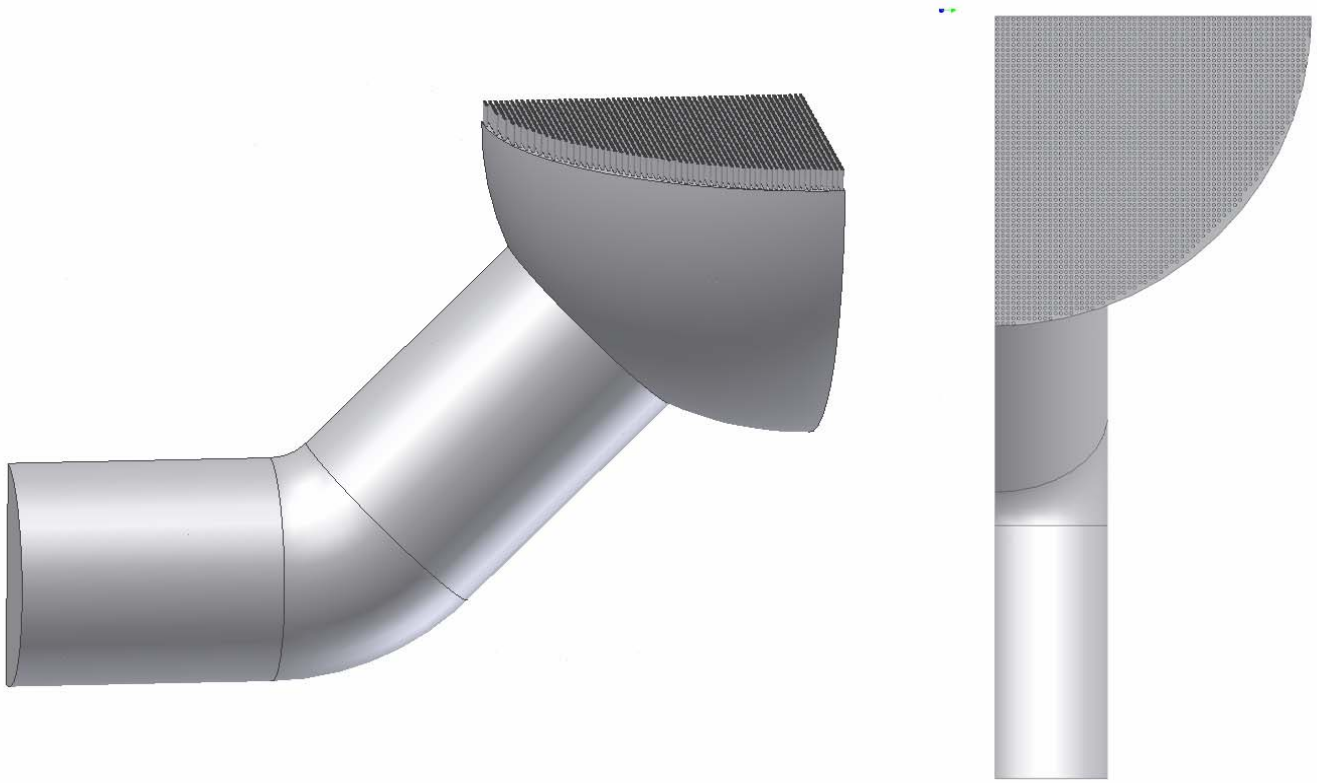

Figure 2.4d Full scale simulation flow volume

For the full scale model, the length of the tubes was increased to 10 inches. Each tube had a diameter of 0.608 inches with a square pitch of 0.98 inches [Lee, Young]. There are a total of 5646 tubes (1/2 that with symmetry) laid out on a tube sheet with a diameter of 117.5 inches. The inlet pipe, 48 inches in length and 42 inches in diameter, connected at a 45^0 angle with the inlet plenum. The 45^0 elbow bend has a toroidal radius of 30 inches. The horizontal section of the hot leg was also 48 inches in length and 42 inches in diameter.

Once the model had been created and transferred using the standard ACIS format, ANSYS ICEM CFD 11.0 was used for mesh generation. ICEM's mesh generation capabilities include multi-block structured, unstructured hexahedral, unstructured tetrahedral, hybrid meshes comprising hexahedral, tetrahedral, pyramidal and/or prismatic elements, quadrilateral and triangular surface meshes. For the purposes of this project, ICEM was used to produce a non-uniform three dimensional mesh within the imported geometry using a combination of elements focusing mainly on tetragonal elements and prism layers around the boundaries, with triangular elements along the surfaces. Non-uniform mesh generation is typically more straight forward and less work for the user up-front but structured meshes give the benefit of easier editing once the mesh has been created. To obtain an accurate solution, several iterations of mesh generation usually must be completed. The final parameter results of the mesh used for the scaled steam generator experiment are listed in **Table 2.4a**. The final parameters for the full scale mesh are given in **Table 2.4b.**

Table 2.4a Scaled simulation final mesh parameters

Total Number of Elements:	2864888	Number of Surface Elements:	
Element Type	Number	Surface	Number
Line	43381	Inlet	480
Tetragonal	1493679	Outlet	5204
Triangular	434308	Plenum	12309
Pentagonal	887896	Tubes	437616
Quadrilateral	4862		
Pyramidal	762		

Table 2.4b Full scale simulation final mesh parameters

Total Number of Elements:	18584664	Number of Surface Elements:	
Element Type	Number	Surface	Number
Line	239510	Inlet	521
Tetragonal	15246806	Outlet	84150
Triangular	2970056	Inlet Pipe	4596
Pentagonal	117408	Plenum	11017
Quadrilateral	5712	Tube Sheet	210723
Pyramidal	5172	Tubes	2897128

The mesh was imported into ANSYS CFX 11.0 for the solution of the steady state flow field. The inlet boundary condition consisted of a uniform velocity profile with 5% turbulence. Outlet conditions were set as the average static pressure across all of the tubes. The fluid temperature was taken as 68 ^{0}F (room temperature) to mimic the previous experiment. Corresponding state information for water at this temperature and 1 atm of pressure were used. Later, for the full scale simulation, these values would be expanded to include a typical PWR hot full power temperature and pressure of 614^{0}F and 2250 psia. The converged solution met the requirements of having RMS residuals of the momentum and

mass equations as well as the residuals of the $K-\varepsilon$ turbulence and turbulence eddy dissipation models under 1.0E-04.

In Shi's work, a central fluid plume was assumed directed up towards the tube sheet shown in **Figure 2.5**. While the fluid remains away from the walls this assumption is valid. Once an object begins to approach the plenum divide, or the tube sheet, the flow deviates from Shi's assumed flow model. An area of high pressure forms along the line of symmetry as the crux of the tube sheet and plenum divide are approached as shown in **Figure 2.6**. **Figures 2.7** and **2.8** clearly show the eddy regions in the corners between the tube sheet, plenum divide and inlet plenum.

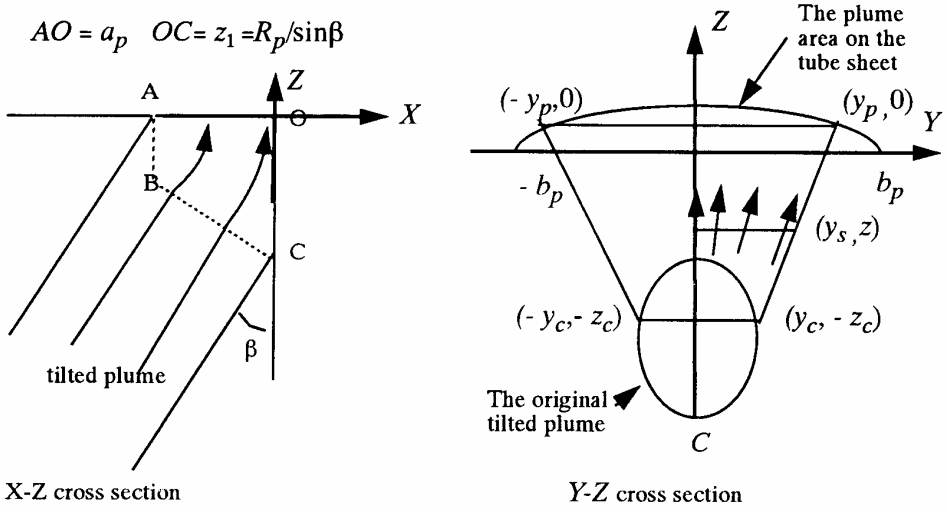

Figure 2.5 Original assumed flow plume [Shi]

Note that the assumed flow plume is represented on the tube sheet as an ellipse. The axes lengths of this plume are given by

$$a_p = R_p \csc\beta \tag{2.3.1}$$

$$b_p = 2R_p \cos\beta \qquad (2.3.2)$$

In the case of the inlet pipe tilted at 45^0 the ellipse reduces to a circle of radius

$R_p = 3.7\frac{\sqrt{2}}{2} = 2.616$ inches.

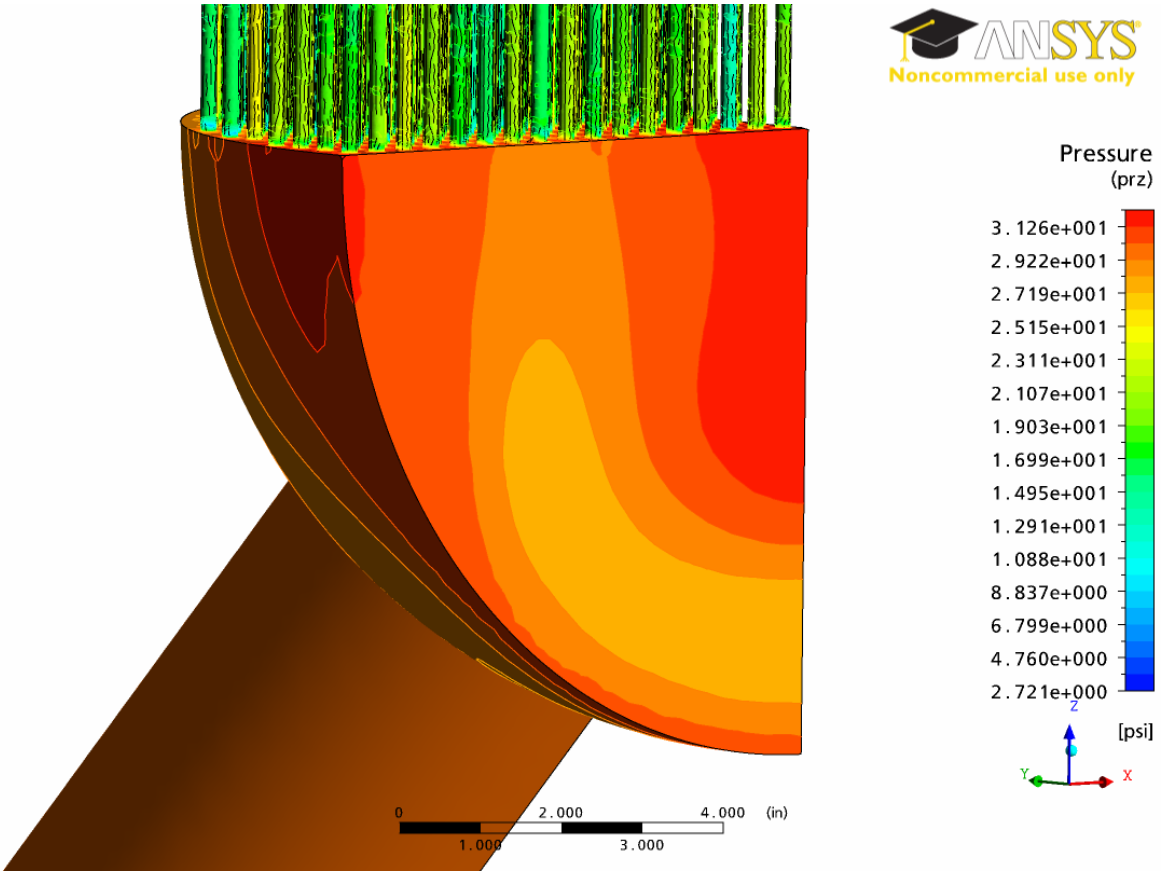

Figure 2.6a Contour plot of surface pressures for the scaled simulation

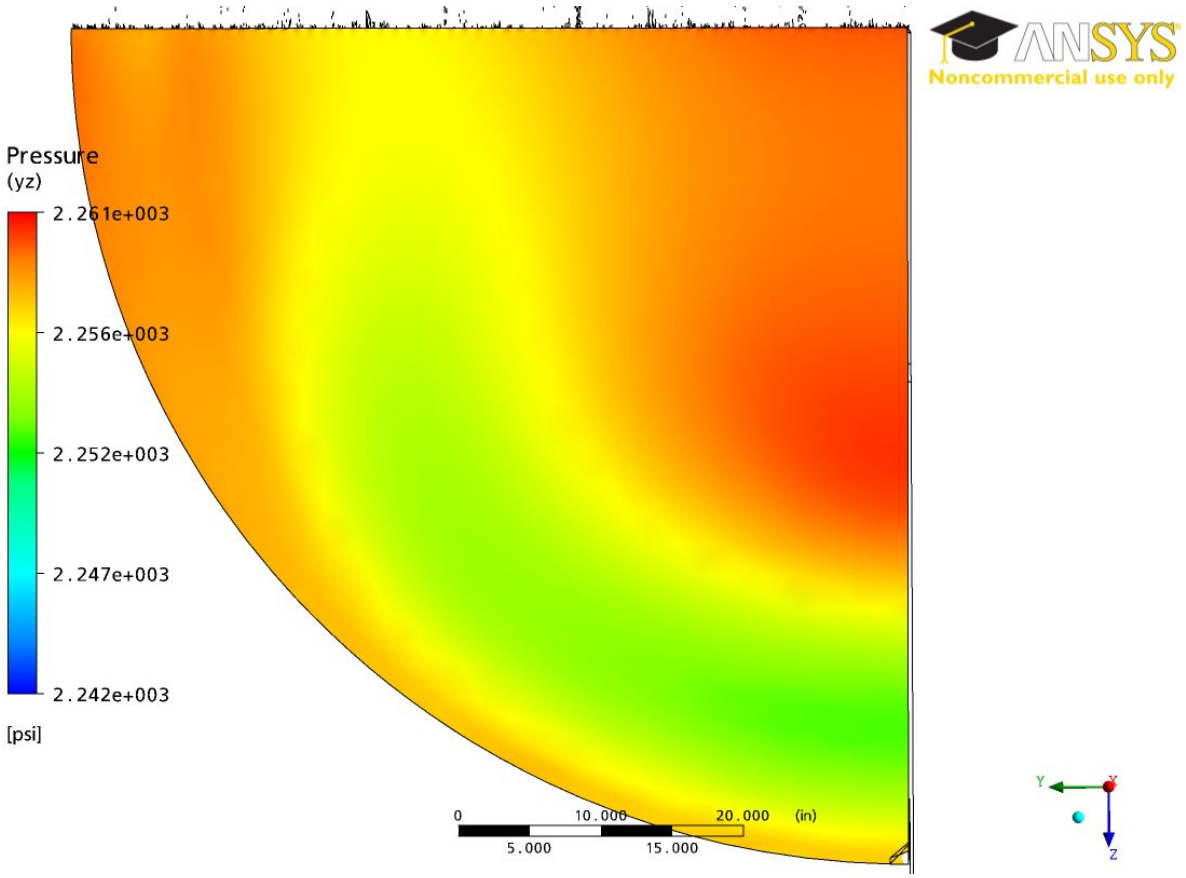

Figure 2.6b Contour plot of surface pressures for the full scale simulation

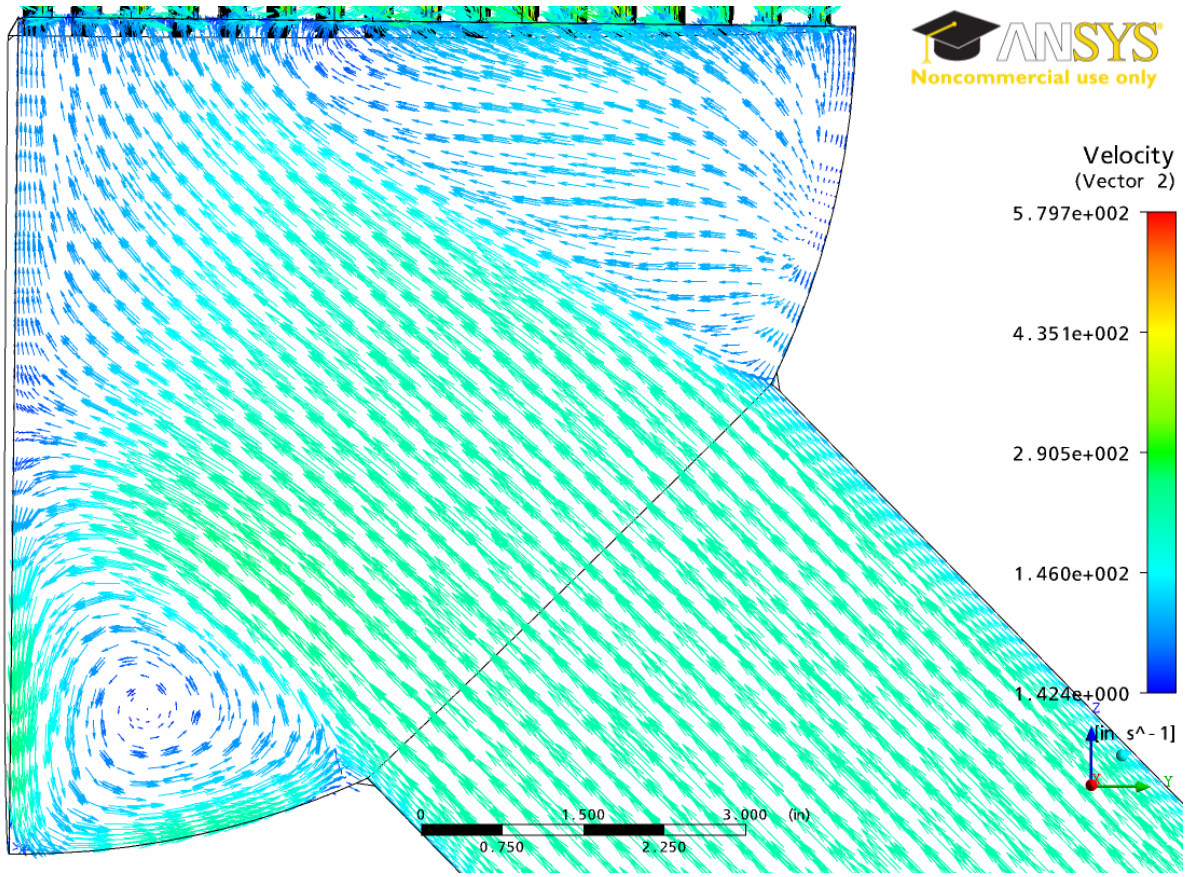

Figure 2.7a Cross sectional view of scaled simulation velocity field

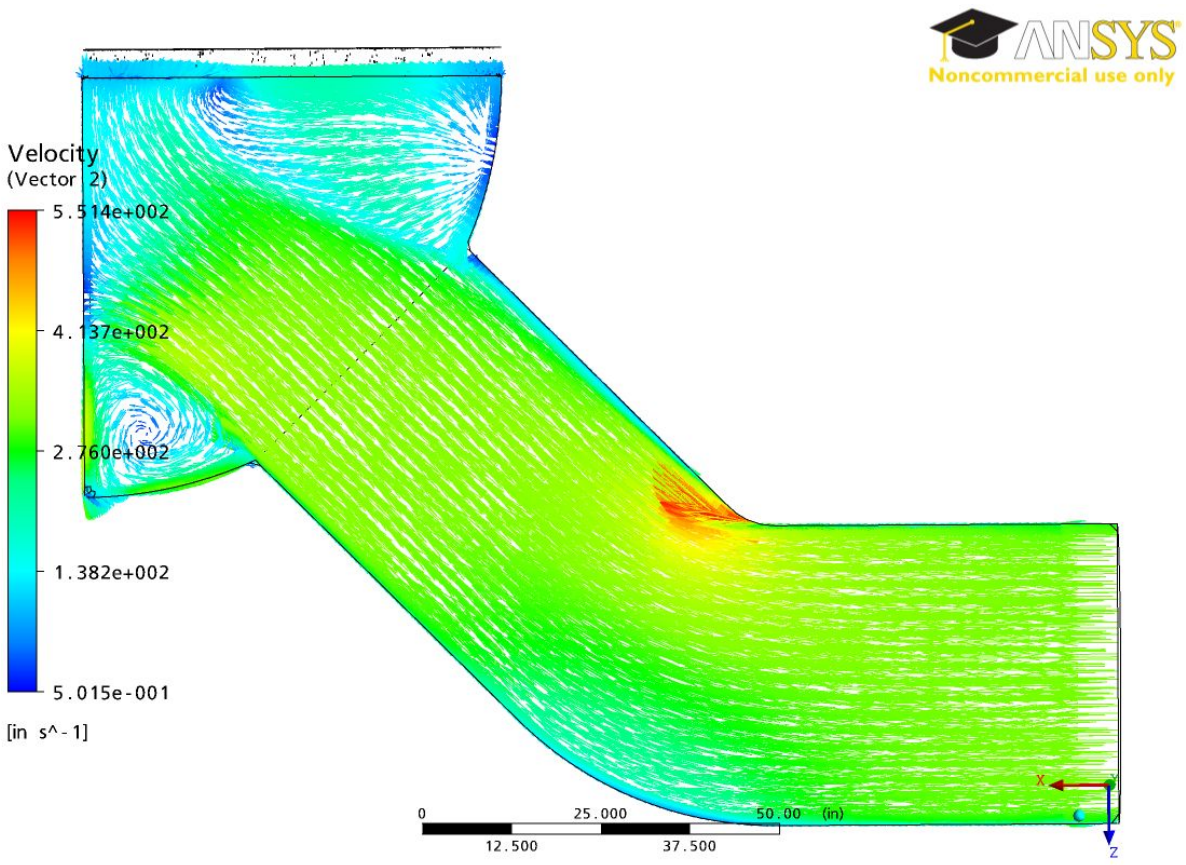

Figure 2.7b Cross sectional view of full scale simulation velocity field

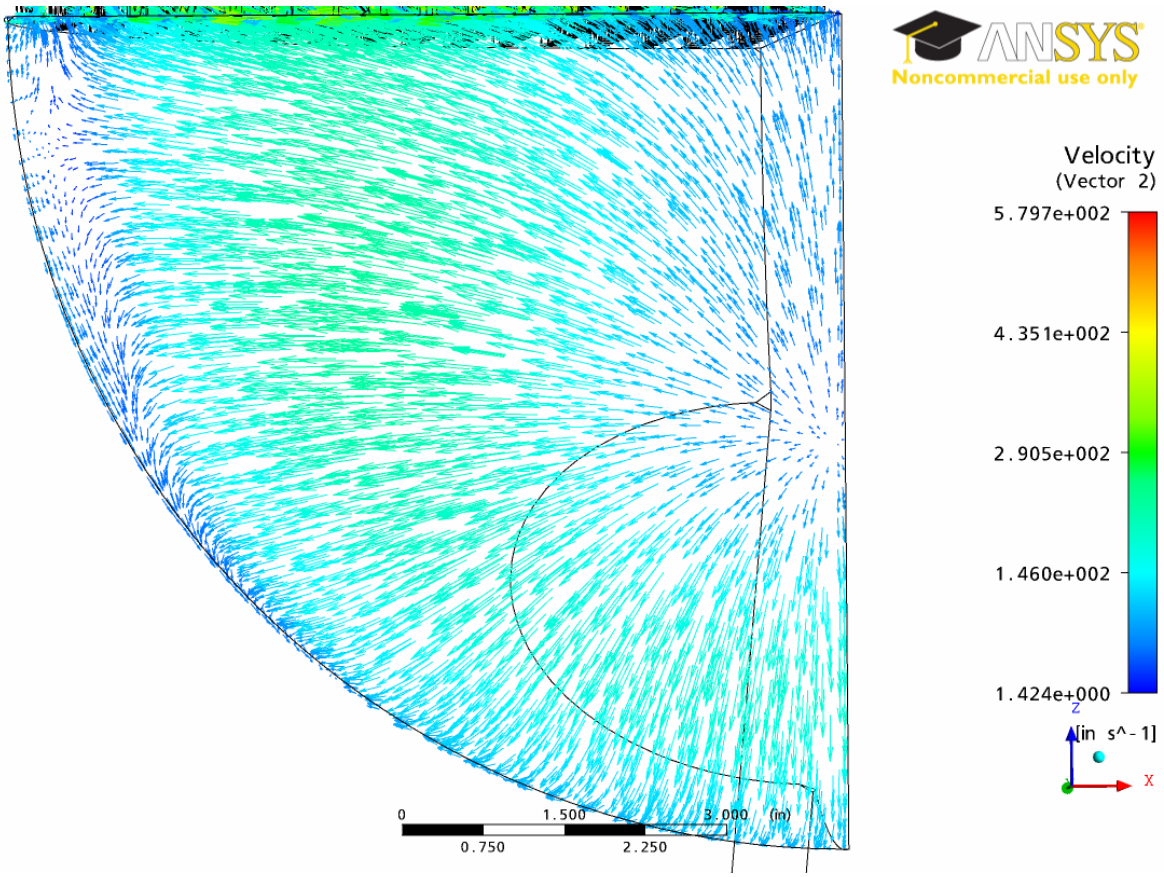

Figure 2.8a Cross sectional view of scaled simulation velocity field orthogonal to **2.7**

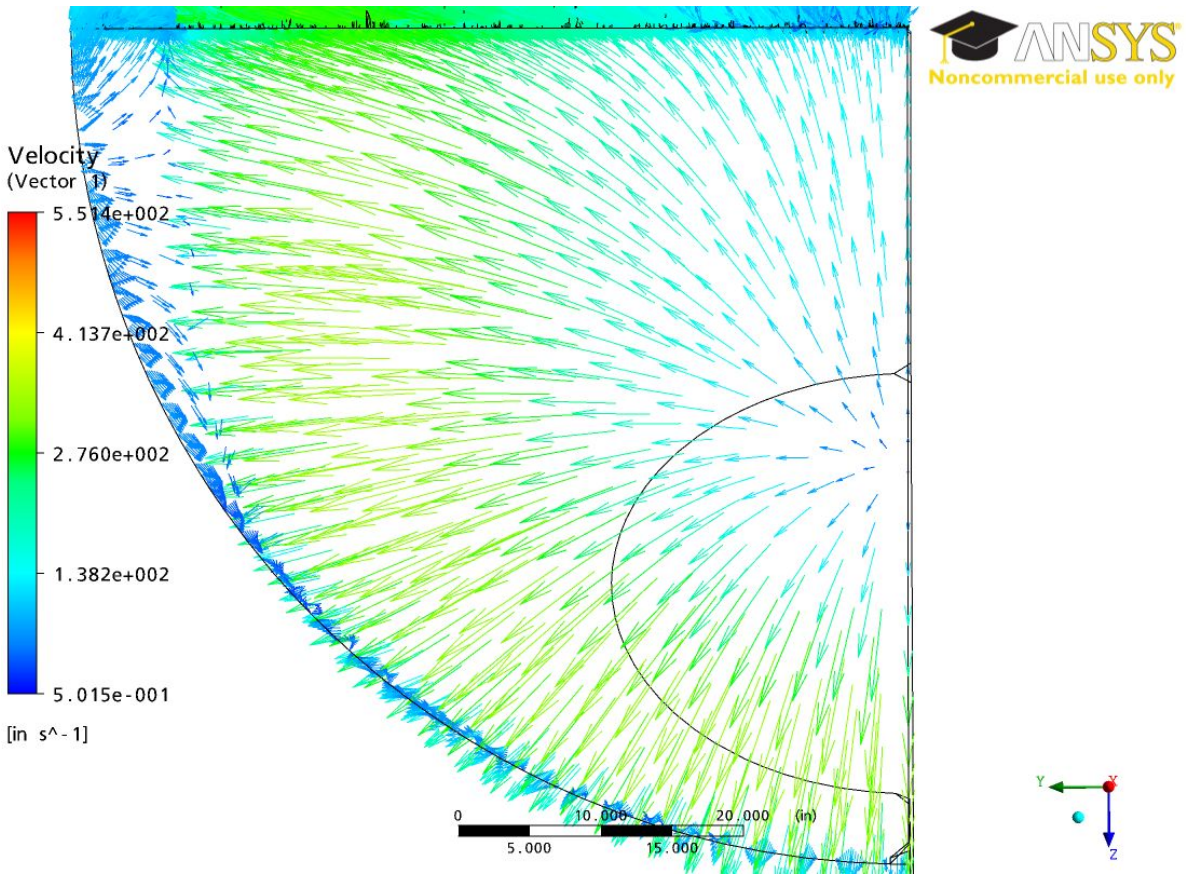

Figure 2.8b Cross sectional view of full scale simulation velocity field orthogonal to **2.7**

Notice in **Figure 2.7** the counter clock-wise eddy in the bottom left of the figure. Also notice the eddy in **Figure 2.8** at the left most edge of the figure. Both of these are areas of significant gradients in velocity and will be of particular interest when comparing results in **Chapter 3**.

2.4 Data Mining

Once the fluid field was successfully created using CFX, the pertinent data to be collected include the x, y and z components of the fluid velocity interpolated at each centroid of the finite elements inside the flow volume. With the assumption that the part is too large to enter into the tubes all data from this region may be discarded. Depending on the refinement of the mesh there were usually on the order of hundreds of thousands of relevant element centroid positions.

CFX exported this information using the form shown in **Figure 2.9**. The file header was deleted so the zero node information became the first line of the file. Next, a small FORTRAN file was created with the specific task of rotating the CFX output so that the coordinates were aligned with the main Monte Carlo program.

CFX Output.txt

```
[Name]
Default Domain

[Data]
Node Number,X[ in ],Y[ in ],Z[ in ],Velocity u[ in s^-1 ],Velocity v[ in s^-1 ],Velocity w[ in s^-1 ]
0 -1.29836157e-001 5.17559767e+000 0.00000000e+000 -2.05343903e+002 -1.37916855e+002 1.48229004e+002
1 -1.47986865e+000 2.47294474e+000 0.00000000e+000 -2.60910522e+002 3.54983592e+000 1.70908371e+002
2 -1.29822835e-001 7.42499971e+000 0.00000000e+000 -2.01026077e+002 2.98547363e+001 1.43850174e+002
3 -1.29822835e-001 2.24999994e-001 -7.41538102e-008 -2.45823853e+002 1.27322826e+001 1.58338593e+002
⋮
```

Figure 2.9 CFX flow field output information

Careful preparation made sure that the origin always occurred at the corner where the symmetry and tube sheet planes met. Refer to **Figure 2.10** to identify the origin and orientation of the coordinates based in the FORTRAN file.

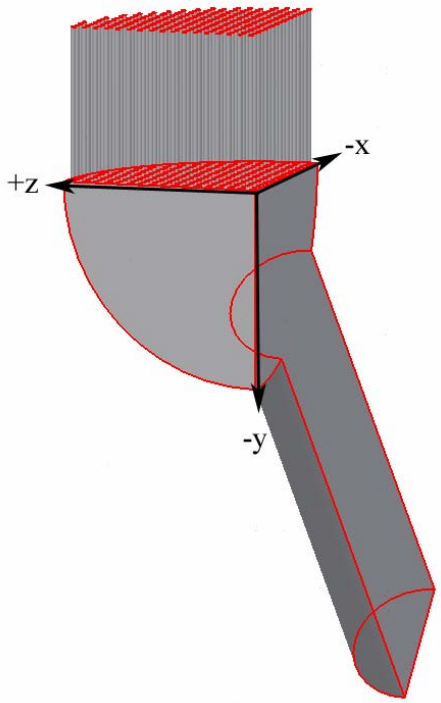

Figure 2.10 Coordinate set up in main code

With the coordinates rotated so that gravity is acting in the –y direction, all data points that were located above the x-z plane could be deleted because they were information about the flow field inside the tubes.

Lastly, the node ID numbers were renumbered in sequential order starting from the number one. These numbers serve the purpose of helping to map fluid points in the next data mining step.

2.4.1 The Box Scheme

To accurately model the drag forces imposed on the part from the fluid at any given location within the model a search was conducted each time step. Originally this search would open up the mined fluid data file and find the closest data point to the current location of the part. These velocities would then serve as the acting fluid velocities for the drag force on the part. With literally hundreds of thousands of data points to search, this quickly became impractical. Searches on the order of a second for a time step that was 1.0E-03 seconds was prohibitive. A method deemed the box scheme was created to more efficiently perform the search.

First, depending on the memory available for the computer running the Monte Carlo FORTRAN code the entire fluid file was loaded into arrays at the beginning of each run as opposed to opening and searching a file. If the mesh was refined too much the fluid data would become impossible to load into memory. This would become more of a concern when dealing with the full scale model.

Next, a FORTRAN program was created to crudely map the locations of each of the data points given by CFX. When exported, the output is arranged by node ID number, as opposed to any kind of geometrical information. More detailed output could be generated from CFX, but unless the individual is an expert at parsing finite element node and line connectivity information then this becomes more of a problem. The maximum and minimum x, y, z positions were found for the model. These six coordinates give a bounding rectangular prism for the model. From there, this prism can be divided into many more equally sided prisms. Each of these prisms would then have a triple index, i, j, k to indicate which ‘box’ it

is. The first box (1, 1, 1) begins at the minimum x, y, z location then iterates through z then y then x in that order. The number of boxes one should use depends on the total number of data points and the overall dimensions of the model. In the scaled model a 50 x 50 x 50 set of boxes for a total of 125,000 were used. The full scale model used 85 x 85 x 85 set of boxes for a total of 614,125.

With the boxes created, each data point was categorized into one of the boxes. Depending on the number of boxes created and the amount of the prism volume that the model takes up, many boxes will not contain any data points at all. Roughly 10% of the boxes for the scaled model contained data points. The total number of boxes was chosen to keep the number of data points in any one box below 300. The fewer points in one box corresponds to a possibly faster search time if the number of boxes to search is significantly less than the number of data points to begin with. Also, these boxes are created with the assumption that the part could only move as much as one box for any given time step. If this was not the case, then the algorithm would potentially search erroneous data points. Therefore the time step control and box size must be decided on together.

The idea is that when another x, y, z position at the next time step is calculated a search can be done on significantly fewer data points than the previous method. If at time step t_0 the part is closest to fluid data point Q in box(i, j, k), then it is only necessary to perform a search in the eight boxes that surround box(i, j, k), i.e. $(i \pm 1, j \pm 1, k \pm 1)$ and the original box(i, j, k). The time step should be chosen such that the same data point does not remain the closest to the part for more than just a couple of time steps. Otherwise the

calculations become unnecessarily refined. Even still, in the extreme case of say 300 data points per box, that is still only 2700 data points to search versus 200,000 plus for the previous method.

The box boundaries as described above were printed to an input file. Then, in another file, the box i, j, k index was printed out along with the total number of data points in the box and the data point ID numbers for that particular box. Coupled with the three dimensional array of fluid velocities this method significantly reduced search time such that the simulation, depending on the set time step and computer running the program, could run slightly faster than wall clock time.

2.5 Fluid Forces

The drag force on a particle in turbulent flow can be written as

$$F_D = \frac{1}{2} C_d A_x \rho_f u^2 \tag{2.4.1}$$

where C_d is the drag coefficient, A_x is the cross sectional area in the flow direction, ρ_f is the fluid density and $u = v_f - v$ is the relative fluid flow to particle velocity.

The drag coefficient of an object depends on its shape and Reynolds number. The object Reynolds number is defined as $v_f D / \nu$ where v_f is the absolute flow velocity. D is the typical dimension of the object and ν is the kinematic viscosity of the fluid. This type of correlation is originally for drag coefficients of a moving body in stagnant liquid or a fixed body in a flowing liquid [Shi]. D, the hydraulic diameter is given by the correlation $D = \sqrt[3]{6V/\pi}$, where V is the volume of the debris. The drag coefficient is constant

for a given absolute flow velocity and is equivalent to an average drag coefficient for loose parts moving in a steady flow.

The equations of motion that describe the part's movement in an open flow stream vary depending on flow direction and initial velocity. The equations may be solved analytically if the forces acting on the part are gravity and the surrounding fluid. The general force balance equation for a loose part with gravity acting downwards is given as:

$$m\frac{d\vec{v}}{dt} = \pm\vec{F}_D - m\vec{g}\left(1-\frac{\rho_f}{\rho}\right) = \pm\frac{1}{2}\rho_f C_d A_x\left(\vec{v}_f - \vec{v}\right)^2 - m\vec{g}\left(1-\frac{\rho_f}{\rho}\right) \tag{2.4.2}$$

$\vec{v}$ is the part velocity
$\vec{v}_f$ is the fluid flow velocity
ρ_f is the fluid density
ρ is the part density
m is the part mass

Taking advantage of the fact that the fluid flow is considered steady state

$$\frac{d\vec{v}_f}{dt} - \frac{d\vec{v}}{dt} = \frac{d\vec{v}_f}{dt} \mp \frac{1}{2m}\rho_f C_d A_x\left(\vec{v}_f - \vec{v}\right)^2 + \vec{g}\left(1-\frac{\rho_f}{\rho}\right)$$

$$\frac{d\left(\vec{v}_f - \vec{v}\right)}{dt} = 0 \mp \frac{1}{2m}\rho_f C_d A_x\left(\vec{v}_f - \vec{v}\right)^2 + \vec{g}\left(1-\frac{\rho_f}{\rho}\right)$$

$$\frac{d\vec{u}}{dt} = \pm\frac{1}{2m}\rho_f C_d A_x \vec{u}^2 - \vec{g}\left(1-\frac{\rho_f}{\rho}\right) \tag{2.4.3}$$

Equation (2.4.3) may be modified to handle the case when the part has come into contact with a static object such as a pipe wall with the addition of a normal force. This normal force depends on the part's initial trajectory and velocity. **Section 2.6** covers in more

detail this normal force. For now, given this normal force, Equation (2.4.3) can be rewritten as

$$\frac{d\vec{u}}{dt} = \pm\frac{1}{2m}\rho_f C_d A_x \vec{u}^2 - \vec{g}\left(1-\frac{\rho_f}{\rho}\right)+\frac{\vec{F}_N}{m} \tag{2.4.4}$$

In free flow conditions, the normal force may be set to zero to yield the required equations of motion. Let $a = \frac{\rho_f C_D A_x}{2m}$ and $\vec{b} = \vec{g}\left(1-\frac{\rho_f}{\rho}\right)+\frac{\vec{F}_N}{m}$. Then the above equation can be rewritten as

$$\frac{d\vec{u}}{dt} = \pm a\vec{u}^2 \pm \vec{b} \tag{2.4.5}$$

To fully describe all possible free flow conditions as well as conditions involved when a collision occurs with a single fixed surface up to twelve independent cases must be accounted for depending on which flow direction is being solved. The dependent parameters are the initial fluid velocity $\vec{u}_0$, the direction of the normal force (if any) $\vec{F}_N$ and the magnitude of the normal force term compared with the gravity and buoyancy terms $\frac{\vec{F}_N}{m}$ and $\vec{g}\left(1-\frac{\rho_f}{\rho}\right)$. Two cases of particular interest yield significantly different results for the velocity and displacement of the debris. These two cases will be derived below. The results of all cases are given in **Table 2.5**.

2.5.1 Case 1

For this case, assume that the equations of motion have been split into their component directions and gravity acts in the negative y-direction. Case 1 will focus on a

positive initial relative velocity $u_{0y} > 0$, a positive normal force in the y-direction $F_{Ny} > 0$, and the normal force is greater than the force with which gravity is pulling downward $F_{Ny} > g_y\left(1-\frac{\rho_f}{\rho}\right)$. **Figure 2.11** illustrates a possible scenario where this may occur. The part, on a collision course for a surface oriented perpendicular to the y-direction makes contact with the surface. As the particle begins to rebound off the surface the summation of the forces dictates the sign of the y-component of the $\vec{b}$ term be positive. This, along with the y-component of the drag force being positive, sets up case 1.

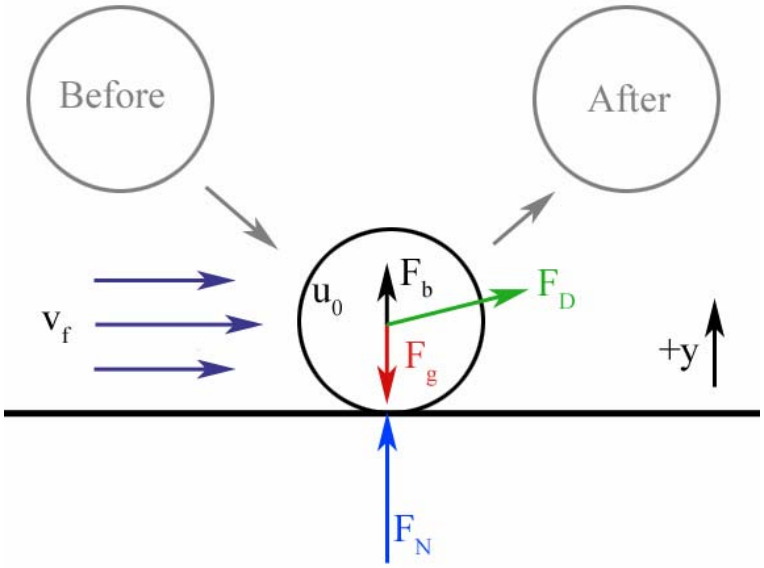

Figure 2.11 Collision force diagram

Dropping the vector notation and the y-subscripts yields from Equation (2.4.5)

$$\frac{du}{dt} = au^2 + b \tag{2.4.6}$$

Integrate from time zero to some time t, from initial relative velocity u_0 to velocity u

$$\int_{u_0}^{u} \frac{du'}{au'^2 + b} = \int_0^t dt'$$

$$\frac{1}{\sqrt{ab}}\left[\tan^{-1}\left(\sqrt{\frac{a}{b}}u\right) - \tan^{-1}\left(\sqrt{\frac{a}{b}}u_0\right)\right] = t$$

substituting $u_t = \sqrt{\frac{b}{a}}$ and solving for u

$$u = u_t \tan\left(\tan^{-1}\left(\frac{u_0}{u_t}\right) + au_t t\right)$$

solving for the velocity of the part at time t

$$v = v_f - u_t \tan\left(\tan^{-1}\left(\frac{u_0}{u_t}\right) + au_t t\right) \tag{2.4.7}$$

To solve for the displacement H at time t integrate the velocity.

$$\int_0^H dH' = \int_0^t v dt'$$

$$H = v_f t - u_t \int_0^t \tan\left(\tan^{-1}\left(\frac{u_0}{u_t}\right) + au_t t'\right) dt'$$

$$H = v_f t + \frac{1}{a}\left(\ln\left[\cos\left\{\tan^{-1}\left(\frac{u_0}{u_t}\right) + au_t t\right\}\right] - \ln\left[\cos\left\{\tan^{-1}\left(\frac{u_0}{u_t}\right)\right\}\right]\right)$$

$$H = v_f t + \frac{1}{a}\left(\ln\left[\sqrt{1+\left(\frac{u_0}{u_t}\right)^2}\cos\left\{\tan^{-1}\left(\frac{u_0}{u_t}\right) + au_t t\right\}\right]\right) \tag{2.4.8}$$

2.5.2 Case 2

Case 2 will focus on a positive initial relative velocity $u_{0y} > 0$, a positive normal force in the y-direction $F_{Ny} > 0$, and the normal force is less than the force with which gravity is

pulling downward $F_{Ny} < g_y\left(1-\frac{\rho_f}{\rho}\right)$. This change in magnitude of the normal force compared with gravity changes the sign on the $\vec{b}$ term. This in turn gives a different form for the solution.

$$-\frac{du}{dt} = au^2 - b \tag{2.4.9}$$

$$\int_{u_0}^{u} \frac{du'}{au'^2 - b} = -\int_0^t dt$$

$$\frac{1}{2au_t}\ln\left(\frac{u'-u_t}{u'+u_t}\right)\Bigg|_{u_0}^{u} = -t \qquad \begin{matrix} a>0 \\ b>0 \end{matrix}$$

By definition a and b must be positive as long as the density of the part is greater than that of the surrounding fluid.

$$\ln\left(\frac{(u-u_t)(u_0+u_t)}{(u+u_t)(u_0-u_t)}\right) = -2au_t t$$

solving for u

$$u = u_t\frac{(u_0+u_t)+(u_0-u_t)e^{-2au_t t}}{(u_0+u_t)-(u_0-u_t)e^{-2au_t t}}$$

and for v

$$v = v_f - u_t\frac{(u_0+u_t)+(u_0-u_t)e^{-2au_t t}}{(u_0+u_t)-(u_0-u_t)e^{-2au_t t}} \tag{2.4.10}$$

Again, integrate to obtain the displacement.

$$H = \int_0^t v_f\,dt' - \int_0^t u_t\frac{(u_0+u_t)+(u_0-u_t)e^{-2au_t t'}}{(u_0+u_t)-(u_0-u_t)e^{-2au_t t'}}dt'$$

Using a u-substitution

$$H = v_f t - \left(u_t t' + \frac{1}{a} \ln \left\{ \left(u_0 + u_t \right) - \left(u_0 - u_t \right) e^{-2au_t t'} \right\} \right) \Bigg|_0^t$$

$$H = v_f t - u_t t - \frac{1}{a} \ln \left\{ \frac{\left(u_0 + u_t \right) - \left(u_0 - u_t \right) e^{-2au_t t}}{2u_t} \right\} \tag{2.4.11}$$

This particular form was also addressed in Shi's previous work. A typographical error concerning the exponential term has been corrected here.

Table 2.5a Y-direction equations of motion summary (Gravity)

Case	$u_{0y} <> 0$	$F_{Ny} <> 0$	$\lvert F_{Ny}\rvert <> \left\lvert g\left(1-\frac{\rho_f}{\rho}\right)\right\rvert$	v_y	H_y
1	>	>	>	$v_f - u_t \tan\left(\tan^{-1}\left(\frac{u_0}{u_t}\right) - au_t t\right)$	$v_f t - \frac{1}{a}\ln\left(\sqrt{1+\left(\frac{u_0}{u_t}\right)^2}\cos\left(\tan^{-1}\left(\frac{u_0}{u_t}\right) - au_t t\right)\right)$
2	>	all	<	$v_f - u_t \frac{(u_0+u_t)+(u_0-u_t)e^{-2au_t t}}{(u_0+u_t)-(u_0-u_t)e^{-2au_t t}}$	$v_f t - u_t t - \frac{1}{a}\ln\left(\frac{(u_0+u_t)-(u_0-u_t)e^{-2au_t t}}{2u_t}\right)$
3	>	>	=	$v_f - \frac{u_0}{(1+au_t t)}$	$v_f t - \frac{1}{a}\ln(1+au_0 t)$
4	<	>	>	$v_f - u_t \frac{(u_0+u_t)+(u_0-u_t)e^{2au_t t}}{(u_0+u_t)-(u_0-u_t)e^{2au_t t}}$	$v_f t - u_t t + \frac{1}{a}\ln\left(\frac{(u_0+u_t)-(u_0-u_t)e^{2au_t t}}{2u_t}\right)$
5	<	all	<	$v_f - u_t \tan\left(\tan^{-1}\left(\frac{u_0}{u_t}\right) + au_t t\right)$	$v_f t + \frac{1}{a}\ln\left(\sqrt{1+\left(\frac{u_0}{u_t}\right)^2}\cos\left(\tan^{-1}\left(\frac{u_0}{u_t}\right) + au_t t\right)\right)$
6	<	>	=	$v_f - \frac{u_0}{(1-au_t t)}$	$v_f t + \frac{1}{a}\ln(1-au_0 t)$
7	=	>	>	$v_f - u_0 + bt$	$v_f t - u_0 t + \frac{1}{2}bt^2$
8	=	all	<	$v_f - u_0 - bt$	$v_f t - u_0 t - \frac{1}{2}bt^2$
9	=	>	=	$v_f - u_0$	$v_f t - u_0 t$

Table 2.5b X,Z-directions equations of motion summary (No Gravity)

Case	$u_{0x,z} <> 0$	$F_{Nx,z} <> 0$	$v_{x,z}$	$H_{x,z}$
1	>	>	$v_f - u_t \tan\left(\tan^{-1}\left(\frac{u_0}{u_t}\right) - au_t t\right)$	$v_f t - \frac{1}{a}\ln\left(\sqrt{1+\left(\frac{u_0}{u_t}\right)^2}\cos\left(\tan^{-1}\left(\frac{u_0}{u_t}\right) - au_t t\right)\right)$
2	>	<	$v_f - u_t \frac{(u_0+u_t)+(u_0-u_t)e^{-2au_t t}}{(u_0+u_t)-(u_0-u_t)e^{-2au_t t}}$	$v_f t - u_t t - \frac{1}{a}\ln\left(\frac{(u_0+u_t)-(u_0-u_t)e^{-2au_t t}}{2u_t}\right)$
3	<	>	$v_f - u_t \frac{(u_0+u_t)+(u_0-u_t)e^{2au_t t}}{(u_0+u_t)-(u_0-u_t)e^{2au_t t}}$	$v_f t - u_t t + \frac{1}{a}\ln\left(\frac{(u_0+u_t)-(u_0-u_t)e^{2au_t t}}{2u_t}\right)$
4	<	<	$v_f - u_t \tan\left(\tan^{-1}\left(\frac{u_0}{u_t}\right) + au_t t\right)$	$v_f t + \frac{1}{a}\ln\left(\sqrt{1+\left(\frac{u_0}{u_t}\right)^2}\cos\left(\tan^{-1}\left(\frac{u_0}{u_t}\right) + au_t t\right)\right)$
5	=	>	$v_f - u_0 + bt$	$v_f t - u_0 t + \frac{1}{2}bt^2$
6	=	<	$v_f - u_0 - bt$	$v_f t - u_0 t - \frac{1}{2}bt^2$
7	>	=	$v_f - \frac{u_0}{(1+au_0 t)}$	$v_f t - \frac{1}{a}\ln(1+au_0 t)$
8	<	=	$v_f - \frac{u_0}{(1-au_0 t)}$	$v_f t + \frac{1}{a}\ln(1-au_0 t)$
9	=	=	$v_f - u_0$	$v_f t - u_0 t$

2.6 Collision Detection

Ultimately, the frequency distribution of impacts on the tube sheet along with the amount of energy imparted with each impact is the driving force for this work. Techniques commonly used in the computer gaming industry were used to accurately detect collision locations while plastic deformation correlations dependent on a material's modulus of elasticity, yield strength and Poisson ratio determined the extent of the inelastic collision [Baraff].

2.6.1 Collision Logic

Once the part had been started with initial conditions within the system it would be moved by the governing flow equations for a short time step Δt, generally equal to 1.0E-03 seconds. The new position, velocity and drag coefficient are updated at this time. After each time step it was necessary to check whether or not the part physically remained within the system. It was assumed that the size of the part was large enough that it could not enter into the steam generator tubes; otherwise the part would exit the area without imparting very much energy onto any surface of interest in this research.

To check if the part remained in the system, a series of primitives were constructed in three dimensional space to represent the boundaries. Everything needed for the scaled experiment and the full scale simulation was built using a combination of spheres, cylinders, tori and planes. **Figures 2.12 and 2.13** depict the basic layout of the scaled and full scale boundaries used in the code. The scaled experiment consisted of three boundary planes, one cylinder and one sphere. The full scale model consisted of six boundary planes, two cylinders, one torus and one sphere.

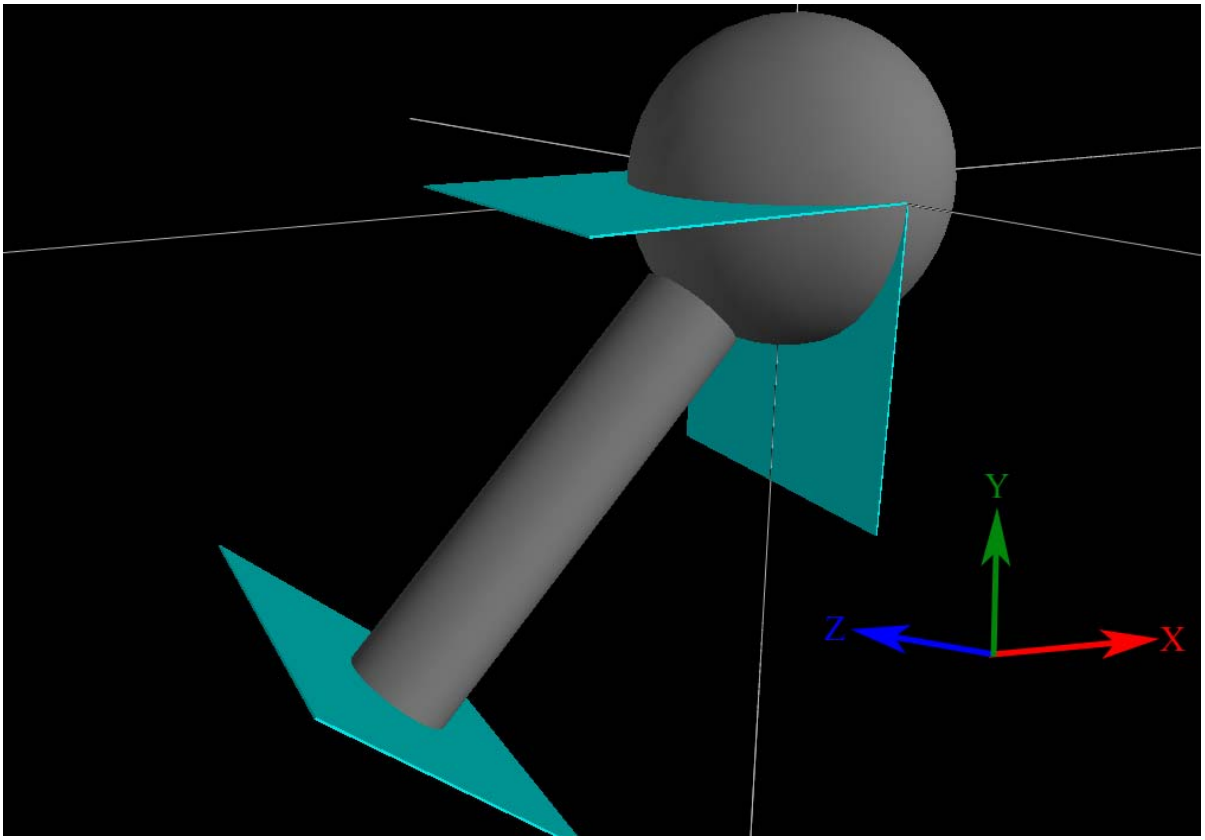

Figure 2.12 Scaled simulation primitive boundaries

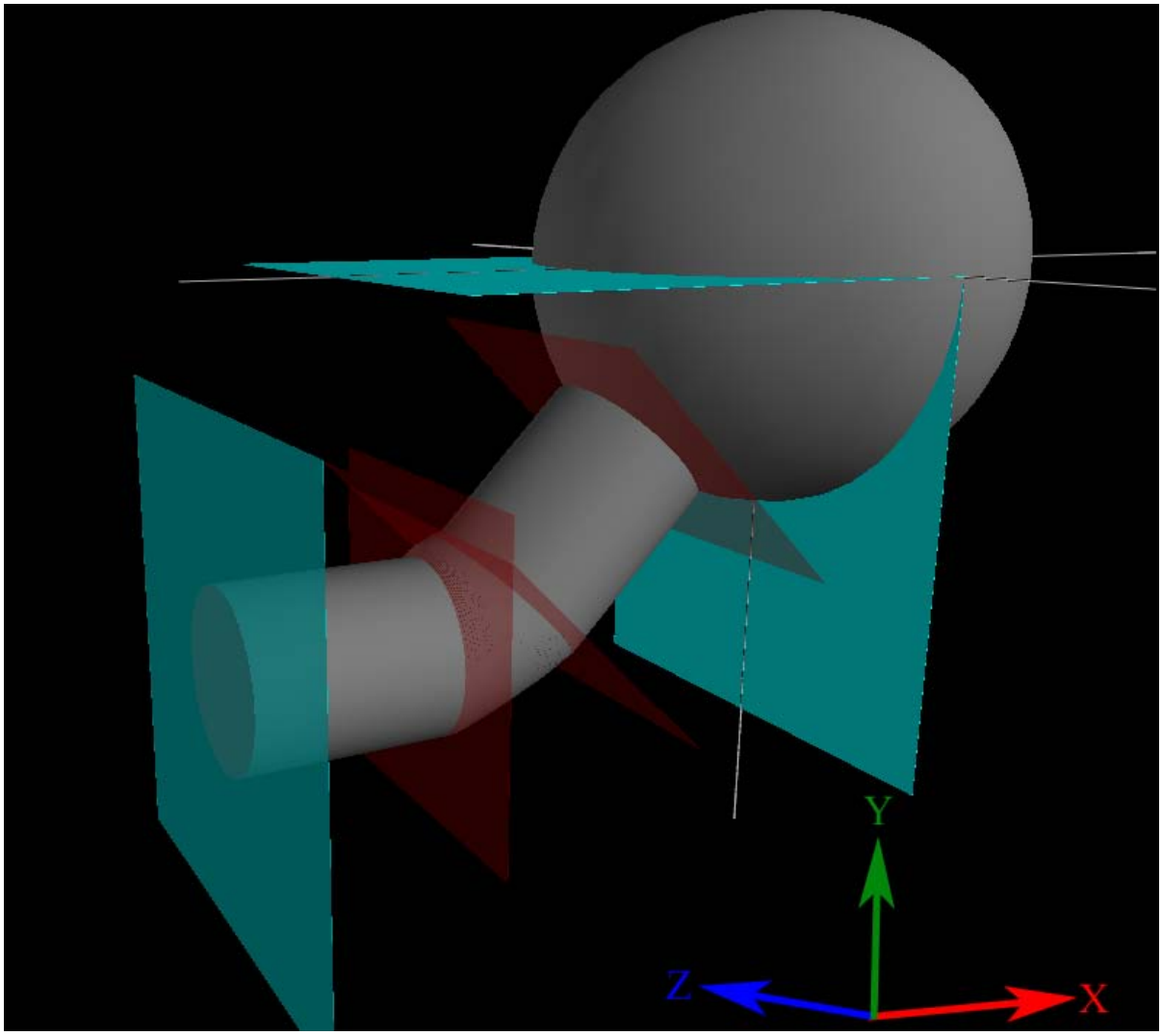

Figure 2.13 Full scale simulation primitive boundaries

The orientation of the primitives in each of these models is arbitrary but set within the FORTRAN code. Therefore if any flow fields were to be generated for the code they would have to be rotated to utilize the already built in geometry. The part was represented for collision purposes as a sphere. The necessary information to detect the collisions correctly was the x-y-z position of the part's centroid, the effective radius of the part and the implicit equations of all the primitives that made up the model.

2.6.1.1 Scaled Experiment Primitives

Specific to the scaled experiment, the implicit equations used are given in **Table 2.6**. R_{eff} is the effective radius of the part, R is the plenum sphere radius and ρ is the inlet plenum radius. Once the part's location was updated for the current time step, the boundary planes were checked. The part must stay on the correct side of these planes at all times; otherwise a non-physical event has occurred. The x-y-z location of the part's centroid can be substituted into any of the given implicit equations to determine if the part is inside or outside an object or if it is on one side or the other in the case of one of the planes.

Table 2.6 Scaled model primitive implicit boundary equations

Physical Boundary	Coordinate Location	Implicit Equation
Tube Sheet	X-Z Plane	$y \le -R_{eff}$
Plenum Divide	Y-Z Plane	$x \le -R_{eff}$
Inlet Pipe Origin	Inlet Pipe Plane	$-2x - 2y - 60\sqrt{2} \ge 0$
Plenum Shell	Sphere, center (0, 0, 0)	$(x - x_c)^2 + (y - y_c)^2 + (z - z_c)^2 \le (R - R_{eff})^2$
Inlet Pipe	Cylinder, along y = x	$2z^2 + x^2 + y^2 - 2xy \le (\rho - R_{eff})^2$

If the part is in fact located on the correct side of all three planes, then a check to see whether the part is inside the inlet pipe or plenum area begins. Note that the cylinder equation is for an infinitely long cylinder so it is possible for the part to be 'inside' the inlet cylinder and plenum sphere at the same time. A non-physical event only would occur if the part managed to find a way outside both the sphere and cylinder.

2.6.1.2 Full Scale Experiment Primitives

Specific to the full scale model implicit equations are given in **Table 2.7**. R_{eff} is the effective radius of the part, R is the plenum sphere radius and ρ is the inlet plenum radius. Once the part's location is updated four boundary planes are checked to verify that the part is indeed in the system. If this is true then two torus planes are checked to identify which of the three regions the part is located in. Region 1 consists of a horizontal segment of the hot leg just before the 45^0 elbow bend. Region 2 is the elbow bend itself made up from the torus segment. Region 3 is comprised of the 45^0 inlet pipe and plenum similar to the scaled experiment. See **Figure 2.17b** for more details about each region.

Table 2.7 Full scale model primitive implicit boundary equations

Physical Boundary	Region	Coordinate Location	Implicit Equation
Tube Sheet	3	X-Z Plane	$y \le -R_{eff}$
Plenum Divide	3	Y-Z Plane	$x \le -R_{eff}$
Sphere Plane	3	Plane, $\perp$ to y = x	$x + y + 77.60 = 0$
Inlet Pipe	3	Cylinder, along y = x	$2z^2 + x^2 + y^2 - 2xy \le \left(\rho - R_{eff}\right)^2$
Torus Plane # 2	3	Plane, $\perp$ to y = x	$x + y + 150.96 = 0$
45^0 Elbow Bend	2	Torus	$\left(\begin{matrix}\left(x-x_c\right)^2+\left(y-y_c\right)^2+z^2 \\ +R^2-\left(\rho-R_{eff}\right)^2\end{matrix}\right)^2 \le 4R^2\left(\left(x-x_c\right)^2+\left(y-y_c\right)^2\right)$
Torus Plane # 1	2	Plane, $\parallel$ to Y-Z Plane	$x + 96.70 = 0$
Hot Leg	1	Cylinder, $\parallel$ to X-axis	$z^2 + \left(y - y_c - 30\right)^2 = \left(\rho - R_{eff}\right)^2$
Hot Leg Plane	1	Plane, $\parallel$ to Y-Z Plane	$x + 144.70 = 0$

x_c and y_c are the coordinates of the center of the torus and are given in inches by

$x_c = -96.6969$ $y_c = -54.2704$.

2.6.2 Collision Impact Location

Generally, the part will be somewhere inside all of the boundaries controlled by the flow equations in **Section 2.5**. In the event of a collision, the part encroaches on a single boundary at time t_0. The following time step $t_1 = t_0 + dt$, the part fails one of the collision detection tests and inter-penetrates the boundary; see **Figure 2.14**. At this point, subroutines are activated to calculate the point of contact on the wall and the fraction of the time step $t_c = t_0 + fdt$ which elapsed before the collision occurred. To do this, the line that intersects both points $\vec{P}_0$ and $\vec{P}_1$ can be given parametrically by

$$\vec{P}_{line} = \vec{P}_0 + u\left(\vec{P}_1 - \vec{P}_0\right) \tag{2.5.1}$$

where $u \in [0,1]$ is the length of the line between $\vec{P}_0$ and $\vec{P}_1$. Somewhere along this line must be an intersection with the surface of interest. The parametric equation of the line can then be substituted into the implicit equation of the surface and the equations solved for an x, y, and z location.

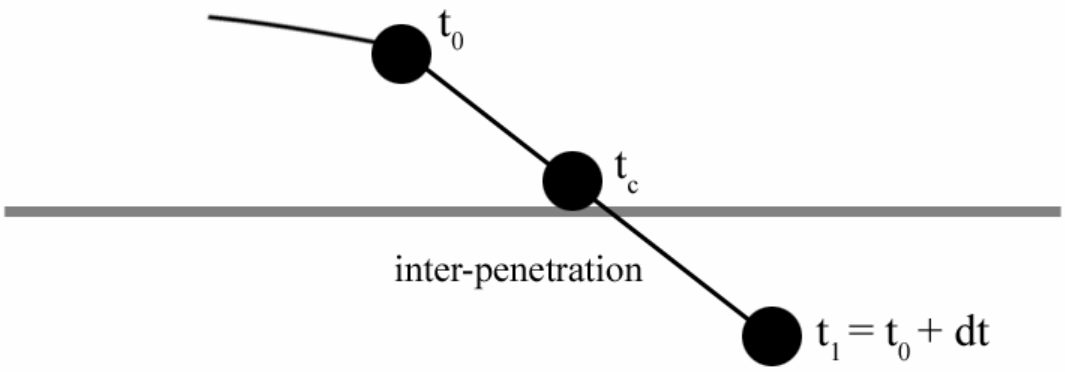

Figure 2.14 Inter-penetration of a surface

This intersection is geometry dependent and must be taken into account for each surface. Spheres, cylinders and tori all being three dimensional objects have the possibility of two different intersection scenarios. The line may intersect and pass through the object exiting out the other side making for two intersections (or four for the torus). The line may be tangent to the surface and will result in only one intersection. Planes and other two dimensional objects will either have one intersection point or they will be contained within the surface resulting in an infinite number of intersections. Given the physics of the model, only the cases of two intersections for the three dimensional objects other than the torus and one intersection for the two dimensional objects should ever occur. Proper error checking is carried out to ensure that only these scenarios are occurring.

2.6.2.1 Sphere Impact Location Derivation

Given the two x, y, z points $\vec{P}_0$ and $\vec{P}_1$ that make up line $\vec{P}_{line}$ and the equation of a sphere centered at (x_c, y_c, z_c) substitute the line equations into the sphere equation.

$$\vec{P}_{line} = \vec{P}_0 + u\left(\vec{P}_1 - \vec{P}_0\right) \qquad \begin{aligned} P_{line}^x &= x_0 + u\left(x_1 - x_0\right) \\ P_{line}^y &= y_0 + u\left(y_1 - y_0\right) \\ P_{line}^z &= z_0 + u\left(z_1 - z_0\right) \end{aligned}$$

and

$$\left(x - x_c\right)^2 + \left(y - y_c\right)^2 + \left(z - z_c\right)^2 = \left(R - R_{eff}\right)^2$$

substituting

$$\left(\left[x_0 + u\left(x_1 - x_0\right)\right] - x_c\right)^2 + \left(\left[y_0 + u\left(y_1 - y_0\right)\right] - y_c\right)^2 + \left(z_0 + u\left(z_1 - z_0\right) - z_c\right)^2 = \left(R - R_{eff}\right)^2$$

collect on terms with u

$$\left[\left(x_1-x_0\right)^2+\left(y_1-y_0\right)^2+\left(z_1-z_0\right)^2\right]u^2+\left[2\left(x_0-x_c\right)\left(x_1-x_0\right)+2\left(y_0-y_c\right)\left(y_1-y_0\right)+2\left(z_0-z_c\right)\left(z_1-z_0\right)\right]u+\left(x_0-x_c\right)^2+\left(y_0-y_c\right)^2+\left(z_0-z_c\right)^2=\left(R-R_{eff}\right)^2$$

which is of the form

$$au^2+bu+c=0$$

where

$$a=\left(x_1-x_0\right)^2+\left(y_1-y_0\right)^2+\left(z_1-z_0\right)^2$$
$$b=2\left(x_0-x_c\right)\left(x_1-x_0\right)+2\left(y_0-y_c\right)\left(y_1-y_0\right)+2\left(z_0-z_c\right)\left(z_1-z_0\right)$$
$$c=\left(x_0-x_c\right)^2+\left(y_0-y_c\right)^2+\left(z_0-z_c\right)^2-\left(R-R_{eff}\right)^2$$

the solution to this quadratic is given by

$$\frac{-b\pm\sqrt{b^2-4ac}}{2a}$$

The two real roots to this equation are the two u parameter values which correspond to the x, y, z points given by the line equation. These require that the determinant be positive. If the determinant is negative then the line does not intersect the sphere and if the determinant is zero then the line is tangent to the sphere. A check can be performed to determine which of the two points the correct intersection point is by simply measuring the magnitudes between $\vec{P}_1$ and the two intersection points. Whichever magnitude is the smallest is the correct intersection point.

2.6.2.2 Torus Impact Location Derivation

Solving for the location of an impact point on the surface of a torus is not a trivial task. This quartic surface can be solved analytically using Ferrari's Method but this is unnecessary. A very good approximation can be found using a numerical root finding

algorithm. For this purpose Brent's Algorithm was implemented. It combines root bracketing, bisection and inverse quadratic interpolation from the Newton-Rhapson and Bisection techniques to solve for a root within a given region.

Setup is similar to the spherical case outlined above except the implicit equation of the torus is used from **Table 2.7**. Given the two x, y, z points $\vec{P}_0$ and $\vec{P}_1$ that make up line $\vec{P}_{line}$ and the equation of a torus radially symmetric about the z-axis and centered at $\left(x_c, y_c, z_c = 0\right)$ substitute the line equations into the torus equation.

$$\vec{P}_{line} = \vec{P}_0 + u\left(\vec{P}_1 - \vec{P}_0\right) \qquad \begin{aligned} P_{line}^x &= x_0 + u\left(x_1 - x_0\right) \\ P_{line}^y &= y_0 + u\left(y_1 - y_0\right) \\ P_{line}^z &= z_0 + u\left(z_1 - z_0\right) \end{aligned}$$

and

$$\left(\left(x - x_c\right)^2 + \left(y - y_c\right)^2 + z^2 + R^2 - \left(\rho - R_{eff}\right)^2\right)^2 = 4R^2\left(\left(x - x_c\right)^2 + \left(y - y_c\right)^2\right)$$

substituting

$$\left(\left(x_0 + u\left(x_1 - x_0\right) - x_c\right)^2 + \left(y_0 + u\left(y_1 - y_0\right) - y_c\right)^2 + \left(z_0 + u\left(z_1 - z_0\right)\right)^2 + R^2 - \left(\rho - R_{eff}\right)^2\right)^2 =$$
$$4R^2\left(\left(x_0 + u\left(x_1 - x_0\right) - x_c\right)^2 + \left(y_0 + u\left(y_1 - y_0\right) - y_c\right)^2\right)$$

collecting on terms with u we end up with a form of

$$au^4 + bu^3 + cu^2 + du + e = 0$$

where

$$a = \left(\left(x_1 - x_0\right)^2 + \left(y_1 - y_0\right)^2 + \left(z_1 - z_0\right)^2\right)^2$$

$$b = 2\sqrt{a}\left(2\left(x_0 - x_c\right)\left(x_1 - x_0\right) + 2\left(y_0 - y_c\right)\left(y_1 - y_0\right) + 2z_0\left(z_1 - z_0\right)\right)$$

$$c = -4R^2\left(\left(x_1 - x_0\right)^2 + \left(y_1 - y_0\right)^2\right) +$$
$$2\sqrt{a}\left(\left(x_0 - x_c\right)^2 + \left(y_0 - y_c\right)^2 + z_0^2 + R^2 - \left(\rho - R_{eff}\right)^2\right) + \frac{b^2}{a}$$

$$d = -4R^2\left(2\left(x_0 - x_c\right)\left(x_1 - x_0\right) + 2\left(y_0 - y_c\right)\left(y_1 - y_0\right)\right) +$$
$$2\frac{b}{\sqrt{a}}\left(\left(x_0 - x_c\right)^2 + \left(y_0 - y_c\right)^2 + z_0^2 + R^2 - \left(\rho - R_{eff}\right)^2\right)$$

$$e = \left(\left(x_0 - x_c\right)^2 + \left(y_0 - y_c\right)^2 + z_0^2 + R^2 - \left(\rho - R_{eff}\right)^2\right)^2 - 4R^2\left(\left(x_0 - x_c\right)^2 + \left(y_0 - y_c\right)^2\right)$$

The quartic function and its derivative can be given as input to Brent's Algorithm along with the upper and lower bounds to search for the root as well as the minimum acceptable tolerance for the solution. Because $\vec{P}_0$ and $\vec{P}_1$ are points chosen inside and outside of the particular impacting surface, this dictates that Brent's Algorithm must find a root for u between 0 and 1. This allows the correct root to be chosen each time there is an impact with the torus.

Between the analytic method described for the sphere and the numerical technique described for the torus all geometrical shapes necessary for the impact location calculation may be solved in a similar fashion.

2.6.3 Collision Physics

Once the point of impact has been located, the time step can be backed up to the correct time t_c. A spatial linear interpolation can be used between points $\vec{P}_0$, $\vec{P}_c$ and $\vec{P}_1$ to find t_c. The next step is to find the surface normal at the point of impact. This can be done

using the implicit equation of the surface $f(x,y,z)$ and the collision point x_c, y_c, z_c and calculating the gradient. The normal vector would then be given by

$$\left(\left.\frac{\partial f(x,y,z)}{\partial x}\right|_{x_c,y_c,z_c}, \left.\frac{\partial f(x,y,z)}{\partial y}\right|_{x_c,y_c,z_c}, \left.\frac{\partial f(x,y,z)}{\partial z}\right|_{x_c,y_c,z_c} \right) \tag{2.5.2}$$

With geometry fixed in the two simulations these equations were hard coded for speed and accuracy. To properly calculate the normal force needed to keep the part inside the bounds of the walls, the total force in the direction opposing the normal vector can be calculated. The normal force is simply the negative of this total force.

At this point, just before the collision occurred, the kinetic energy was written out along with the impact location. Using the impact location as a local origin, the normal vector defined the plane at which a ray trace could be preformed to estimate the trajectory of the part after impact.

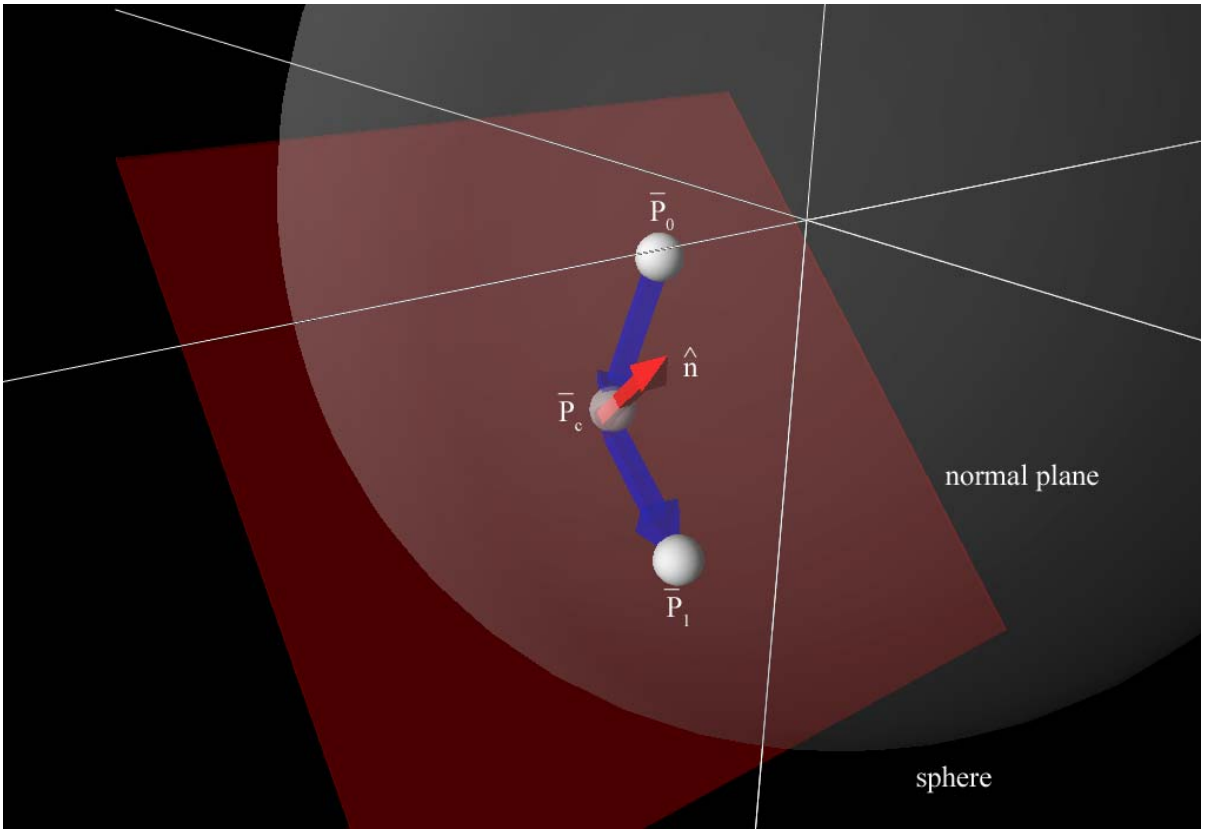

Figure 2.15 Ray trace example for a sphere

The vector created by $\vec{P}_c - \vec{P}_0$ and the normal vector $\hat{n}$ provide enough information to find the point $\vec{P}_1$ using transformations about the impact point and is given by

$$\hat{P}_1 = \hat{P}_0 - 2\hat{n}\left(\hat{P}_0 \cdot \hat{n}\right) \tag{2.5.3}$$

Note that all the vectors in Equation (2.5.3) are unit vectors. To determine the magnitude of $\vec{P}_1$ one may use a parameter called the coefficient of restitution, e. This parameter ranges from zero to one with zero being a completely inelastic collision and one being a completely elastic collision.

2.6.3.1 Coefficient of Restitution

To characterize the behavior of the impacts on the surfaces of the steam generator, results from Wu, Li and Thornton were implemented [Thornton, Wu, Li]. Their work specifically focused on the rebound behavior of spheres for plastic impacts. Using finite element analysis and an extension of Hertz theory they were able to characterize the behavior of the coefficient of restitution through the several relevant regions of elastic-plastic impact scenarios.

The coefficient of restitution e is generally given as the ratio of the rebound velocity to the initial velocity. These velocities are normal to the impact surface.

$$e = \frac{V_r}{V_i} \tag{2.5.4}$$

As an object's velocity increases a collision will transition from fully elastic into elastic-plastic deformation. This transition is dependent on both the wall and object's modulus of elasticity, yield strength and Poisson's ratio. It also depends on the object's velocity and orientation with the surface. Beyond the elastic-plastic region is the onset of finite plastic deformation. The majority of significant damage causing impacts in the steam generator will fall within this region. For the purposes of this research, the correlations developed by Thornton et al. for a sphere will be used regardless of the shape of the part.

The following list of equations give the coefficient of restitution fits produced by Thornton et al. The case for an elastic-perfectly plastic sphere impacting with a rigid wall is used.

$$E^* = \frac{E_1}{1-\nu_1^2} \tag{2.5.5}$$

$$V_y = 5.052\left(\frac{Y^5}{E^{*4}\rho}\right)^{1/2} \tag{2.5.6}$$

$$V_i^* = \frac{0.008 V_y E^*}{Y^2} \tag{2.5.7}$$

$$\bar{p}_y = 1.6Y \tag{2.5.8}$$

$$\bar{V}_y = \left(\frac{\pi}{2E^*}\right)^2 \left(\frac{2}{5\rho}\right)^{1/2} \bar{p}_y^{5/2} \tag{2.5.9}$$

$$m = \left(\frac{1-2.08(100)^{-1/4}}{\bar{V}_y - 100V_y}\right) \tag{2.5.10}$$

where

E_1	-	Young's Modulus of the part
ν_1	-	Poisson's ratio of the part
E^*	-	Representative Young's Modulus
Y	-	Yield Stress of rigid wall
ρ	-	Density of rigid wall
V_y	-	Yield velocity where plastic deformation is initiated
V_i^*	-	Critical velocity at which finite deformation occurs
$\bar{p}_y$	-	Hertzian cut-off pressure
$\bar{V}_y$	-	Yield velocity where elastic-plastic deformation is initiated
m	-	Interpolated slope between elastic and elastic-plastic region

These equations can be used to build a four region piecewise function for the coefficient of restitution. The elastic region begins with the initial impact velocity approaching zero and ends at $\bar{V}_y$. This elastic region is characterized by a full recovery of the

surface and virtually no energy loss to the impacting part. A very small region of initial velocity from $V_i = \bar{V}_y \approx$ 1.6E-05 to $V_i = 100V_y \approx 1.6E-03$ m/s for Inconel 600 at 68^0F represents a linear interpolation between the elastic region and elastic-plastic region. From $V_i = 100V_y$ up to $V_i = V_i^*$ is the elastic-plastic region. Beyond V_y^* is the finite-plastic deformation region. **Figure 2.16** depicts the coefficient of restitution as a function of initial impact velocity.

$$e = \begin{cases} 1 & V_i \le \bar{V}_y \\ m\left(V_i - \bar{V}_y\right) + 1 & \bar{V}_y < V_i \le 100V_y \\ 2.08\left(V_i / V_y\right)^{-1/4} & 100V_y < V_i \le V_i^* \\ 0.62\left(\dfrac{V_i / V_y}{E^* / Y}\right)^{-1/2} & V_i > V_i^* \end{cases} \qquad (2.5.11)$$

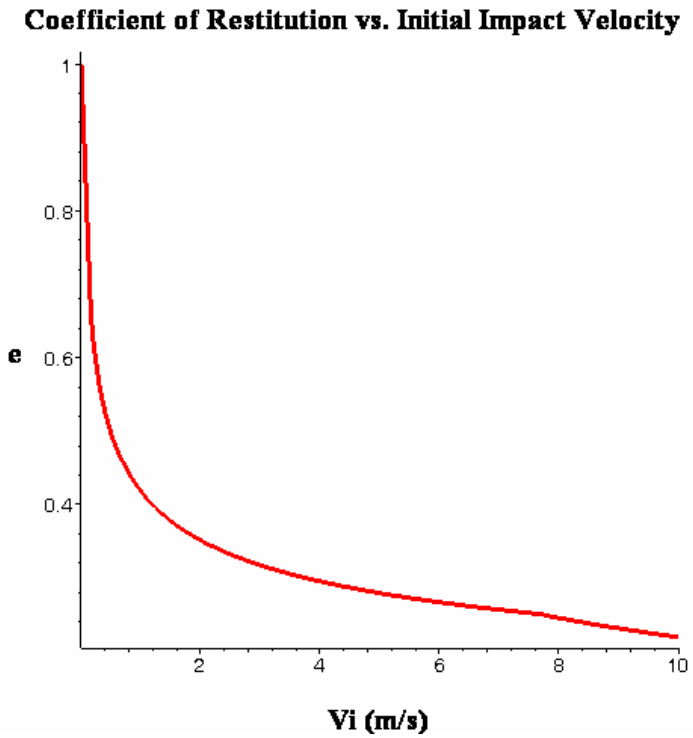

Figure 2.16 Coefficient of restitution versus initial impact velocity

Once the coefficient of restitution is known, it becomes a multiplier on the original incoming velocity of the part to determine the outgoing velocity.

$$\left|\vec{V}_o\right| = e\left|\vec{V}_i\right| \tag{2.5.12}$$

$\vec{P}_1$ can then be calculated by completing the fraction of a time step left $t_1 = t_c + (1 - f)\,dt$.

2.6.4 Special Collision Cases

With the inclusion of gravity in the flow equations and also taking into consideration the geometry of the models, it is possible for the part, if it meets certain criteria, to settle out on a surface. Moreover it is also possible to have more than one collision at a time. For instance, if the part were to find its way into a corner then it is feasible to have two or even three simultaneous collisions.

To minimize the amount of time that a part spent not interacting with the tube sheet, several logic statements were added to the code. Checks for slow or periodic movement that implied the part settling out on a surface were implemented. If a part existed for a set amount of time without having any tube sheet impacts then the history would be terminated and a new part trajectory begun.

Having simultaneous collisions requires the solution of simultaneous equations to determine the resulting normal forces on the particle. For simplicity, this scenario was avoided by backing up to the previous time step t_0 and cutting the Δt in half. This could be repeated until the particle was only impacting one surface instead of two. In some rare cases the time step would be reduced significantly. Eventually a cutoff threshold for the time step would be reached. If this occurred, then the part history was terminated. This eliminated the need to build in a linear equation solver and also kept the program from spending too much time on this event.

2.7 Data Collection

A file structure was created to accommodate the large volume of runs that took place. A hierarchy of types of runs was created based on initial part velocity, starting location, fluid field inlet velocity, fluid temperature and part type.

Without detailed information about possible incoming part velocities it was necessary to sample many possible incoming velocities. Depending on the starting location of the part, the fluid velocity around that location was used as a basis for determining the appropriate initial part velocity for that particular run. Given the x, y and z components of the fluid velocity, a total kinetic energy of a part traveling at this speed could be calculated. Based on

this, energy values starting at 0% and incrementing by 10% all the way up to 100% were used as initial part kinetic energy values. From this initial value, the z and y components of the part's initial velocity were uniformly sampled by rejection such that the part velocities were less than that of the fluid and also returned less than the total amount of kinetic energy needed for that specific run. By choosing the z and y components, this fixed the x component of part initial velocity so that the part initial starting kinetic energy was achieved.

With no information about part origin, it was also necessary to sample various starting locations to see what, if any, difference part origin made for the impact distributions on the tube sheet. In both the scaled and full scale models several different locations were chosen to start the parts. These locations were designated by planes or spheres within the flow volume. Given the implicit equations of these locations, a uniform sampling could occur in each location for an origin point of the part. Coupled with the varying initial velocity distributions of the part, this made for a highly random initial state sampling for the part. Sampling planes for the scaled and full scale models are shown in **Figure 2.17**. Located in **Tables 2.7 and 2.8** are the implicit equations of the initial origin planes for the scaled and full scale models respectively.

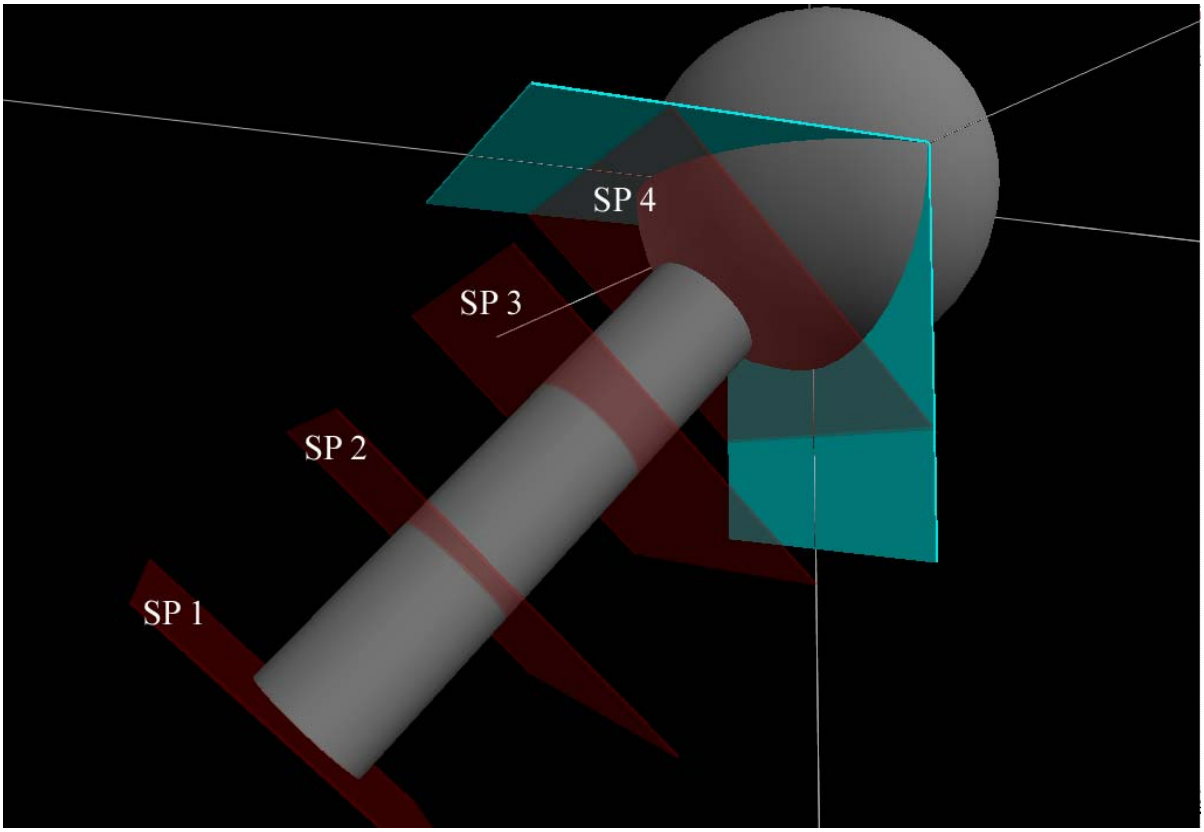

Figure 2.17a Scaled model part initial start plane locations

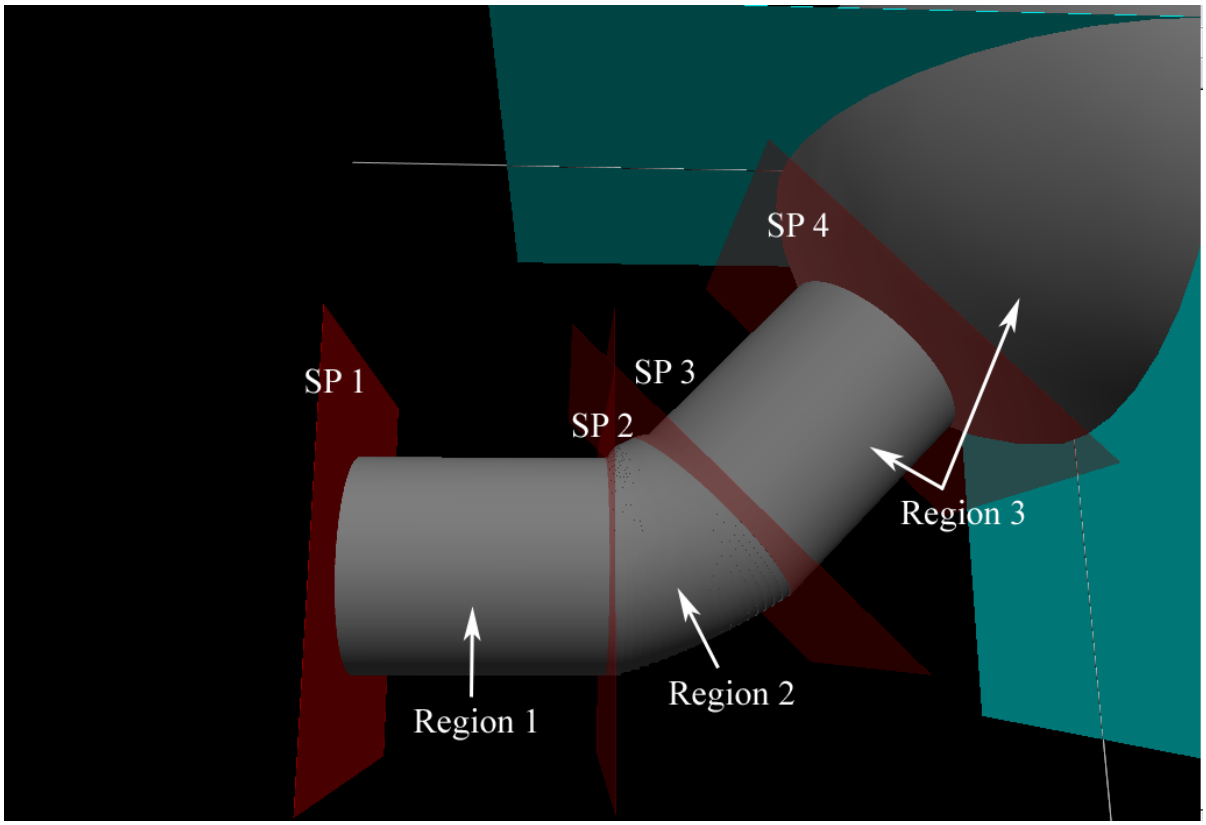

Figure 2.17b Full scale model part initial start plane locations

Table 2.8 Scaled model part initial locations implicit equations

Initial Location	Implicit Equation
SP 1	$2x+2y+55\sqrt{2}=0$
SP 2	$2x+2y+45\sqrt{2}=0$
SP 3	$2x+2y+30\sqrt{2}=0$
SP 4	$2x+2y+15\sqrt{2}=0$

Table 2.9 Full scale model part initial locations implicit equations

Initial Location	Implicit Equation
SP 1	$x+144.70=0$
SP 2	$x+96.70=0$
SP 3	$x+y+150.96=0$
SP 4	$x+y+77.60=0$

Two inlet pipe velocities of 3.6 and 5.3 m/s were run on the scaled model to match the experimental results. On the full scale model a single velocity was run. For the full scale cases, the McGuire 3411 MW 4-loop plant was used as a basis. The hot leg was taken as 42 inches in diameter. The temperature rise across the core was taken to be roughly 58^0F from 558^0F to 615^0F with a mass flow rate of 1.44E+08 lbm/hr. Given this information, the hot leg velocity was about 7.7 m/s.

Temperatures were fixed for the scaled model to 68^0F. The full scale model was run at 614^0F as well as 68^0F to simulate conditions at startup and at hot full power. Pressures were run at 1 atm for the scaled model to emulate the experiment and 2250 psia for the full scale model.

Lastly, 28 different types of loose parts were catalogued by Shi in his work. The scaled experiment only used two of the hexagonal nuts. The nuts were run in addition to other pieces of catalogued parts to try and categorize behaviors based on part size, shape and mass. Along with **Table 2.2**, **Table 2.10** gives all the dimensional information needed for these different types of parts.

Table 2.10 Loose part information

Part Type	Size	Effective Radius (in)	Mass (lbm)	Cross Sectional Area (in^2)	Volume (in^3)	Density (lbm/in^3)	Hydraulic Diameter (in)
Hex Bolt Type 1	1/2''	0.45708	0.05732	0.48038	0.20586	0.27844	0.73259
Hex Bolt Type 1	5/8''	0.57413	0.11023	0.75760	0.40284	0.27363	0.91632
Hex Bolt Type 1	3/4''	0.68495	0.19401	1.06417	0.69896	0.27756	1.10108
Hex Bolt Type 1	7/8''	0.79737	0.29983	1.44200	1.10579	0.27115	1.28299
Hex Bolt Type 1	1''	0.91469	0.45415	1.85509	1.63710	0.27741	1.46226
Hex Bolt Type 2	1/2''	0.58009	0.07496	0.48038	0.27262	0.27495	0.80449
Hex Bolt Type 2	5/8''	0.72382	0.14551	0.75760	0.53476	0.27209	1.00706
Hex Bolt Type 2	3/4''	0.88498	0.25574	1.06417	0.93311	0.27407	1.21240
Hex Bolt Type 2	7/8''	0.99880	0.39242	1.44200	1.43050	0.27433	1.39796
Hex Bolt Type 2	1''	1.14363	0.59084	1.85509	2.11620	0.27920	1.59289
Hex Nut	1/2''	0.49193	0.03527	0.35093	0.15441	0.22844	0.66562
Hex Nut	5/8''	0.60374	0.06614	0.52858	0.28543	0.23171	0.81690
Hex Nut	3/4''	0.71779	0.11464	0.71161	0.46254	0.24785	0.95951
Hex Nut	7/8''	0.83630	0.17637	0.98358	0.72785	0.24232	1.11604
Hex Nut	1''	0.95033	0.27337	1.25500	1.06675	0.25627	1.26771
Rectangular Bar	1/2''	0.55902	0.07055	0.50000	0.25000	0.28219	0.78159
Rectangular Bar	3/4''	0.83853	0.23810	1.12500	0.84375	0.28219	1.17239
Rectangular Bar	7/8''	0.97828	0.37920	1.53125	1.33984	0.28301	1.36779
Rectangular Bar	1''	1.11803	0.56438	2.00000	2.00000	0.28219	1.56319
Cylinder	1/2''	0.55902	0.05732	0.50000	0.19635	0.29193	0.72112
Cylinder	3/4''	0.83853	0.18519	1.12500	0.66268	0.27945	1.08169
Cylinder	7/8''	0.97828	0.29542	1.53125	1.05231	0.28073	1.26197
Cylinder	1''	1.11803	0.44533	2.00000	1.57080	0.28351	1.44225
Sphere	1/2''	0.25000	0.01764	0.19635	0.06545	0.26947	0.50000
Sphere	3/4''	0.37500	0.06173	0.44179	0.22089	0.27945	0.75000
Sphere	9/10''	0.45000	0.12346	0.63617	0.38170	0.32344	0.90000
Sphere	1''	0.50000	0.14551	0.78540	0.52360	0.27789	1.00000
Sphere	3/2''	0.75000	0.49824	1.76715	1.76715	0.28195	1.50000

The effective diameter of a part is given by the longest physical dimension of the part and then divided by two to give effective radius. The cross sectional flow area is taken while at its preferred flow orientation. Volume was found from the given dimensions and the

density found given volume and mass. The hydraulic diameter is computed from the volume as described in **Section 2.5**.

For each run, four different files were output. Other files could also be output for debug purposes but because of the shear volume of data were not recorded.

'info.dat' recorded the run ID number, type of part simulated, size of the part, maximum number of tube sheet impacts to run ~~to~~, maximum number of time steps to run, initial part kinetic energy percentage, initial starting location, fluid density, fluid inlet velocity, fluid temperature, fluid pressure and the fluid information file used for the calculation.

'Collisions.dat' recorded collision locations. It contained sequentially the collision number, x, y, z locations of the collision, the x, y, z velocities of the part at the time of collision, the kinetic energy before and after collision in Joules and the surface name on which the collision occurred.

'TubeSheetImpacts.dat' recorded more specifically each tube sheet impact that occurred in that particular run. It recorded the total tube sheet impact number, the tube sheet impact number for that particular part history, the kinetic energy before collision, the magnitude of the velocity of the part, the x, y, z location of the collision and the x, y, z components of the velocity of the part before impact.

'Stats.dat' recorded the total number of tube sheet impacts, the number of times the part went idle and a new history was started because of it, the average number of tube sheet impacts before the part went idle, the total number of hits on each surface, the average kinetic

energy of impacts on each surface, the average energy loss of hits on each surface and the effective coefficient of restitution on each surface.

The debug files were named ‘position_*****.dat’ and ‘posnum_*****.dat’ where the ‘*****’ represent a file number. The position files recorded a header line of effective radius of the part that was run. Then based on a set interval every X number of time steps the time, time step number, x, y, z positions and velocities of the part were recorded where X could be any positive integer. The posnum files held the corresponding number of time steps recorded in its counterpart position file. After about 50,000 time steps in one file, the visual program VPython would become slow to read in the file, hence the splitting of the files. For complete position files, the number was always set the same in the posnum file. It was only for the last position file did the posnum file become important. By specifying the correct number of time steps this avoided an array out of bounds error in Vpython. This system allowed for a simple visual program in Vpython to read in the data and animate the part as it moved. This served as one of the most helpful checks used to make sure that flow equations were solved correctly and collision physics behaved intuitively as only a visual demonstration could offer.

Figure 2.18 illustrates the file hierarchy written above. With the information from many runs, MATLAB was used to further process and interpret the data. It generated the two dimensional images as well as most of the statistical information given in the results in **Chapter 3**.

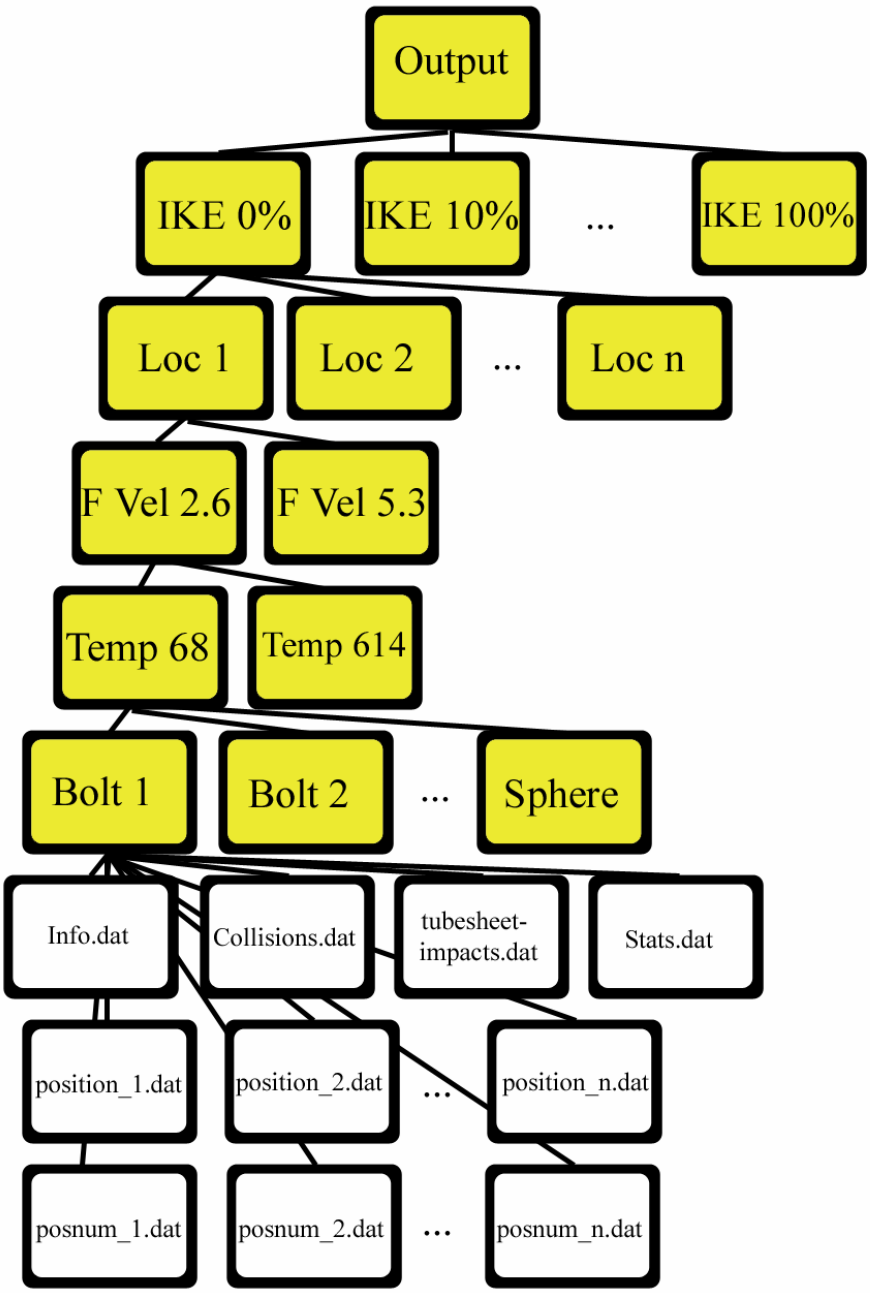

Figure 2.18 Sample output file hierarchy

Chapter 3 Results

3.1 Scaled Simulation Results

The three cases presented in **Table 2.1** were run such that each accumulated a total of 25,000 impacts on the tube sheet surface. The run parameters were as follows:

- 1/2" and 5/8" Hexagonal Nuts were simulated
- Fluid inlet velocities were 3.6 and 5.3 m/s
- Fluid temperature and pressure was 68^0F and 14.696 psia
- Maximum number of tube sheet impacts was 25,000
- Maximum number of time steps at 1.0E-03 seconds was 5,000,000
- Initial kinetic energy of the part ranged from 0% to 100% of the surrounding fluid velocity in increments of 10%
- Initial starting locations included all four start planes in **Figure 2.17a**

A part history was started at the corresponding initial kinetic energy and start plane and the part was allowed to move freely until a total of five impacts occurred on the tube sheet. The reasoning for starting a new history at this point was to try and mimic the behavior seen from Shi's scaled experimental results. The scaled experiment part was launched from a valve and allowed to impact the tube sheet. Either when the part stopped impacting the tube sheet (discerned from the noise it produced) or after a few hits had occurred the flow was turned off and the experiment reset.

In the following figures, the tube sheet impacts generated from the 1/2" nut in the 5.3 m/s flow are displayed as a function of initial kinetic energy from start plane 1.

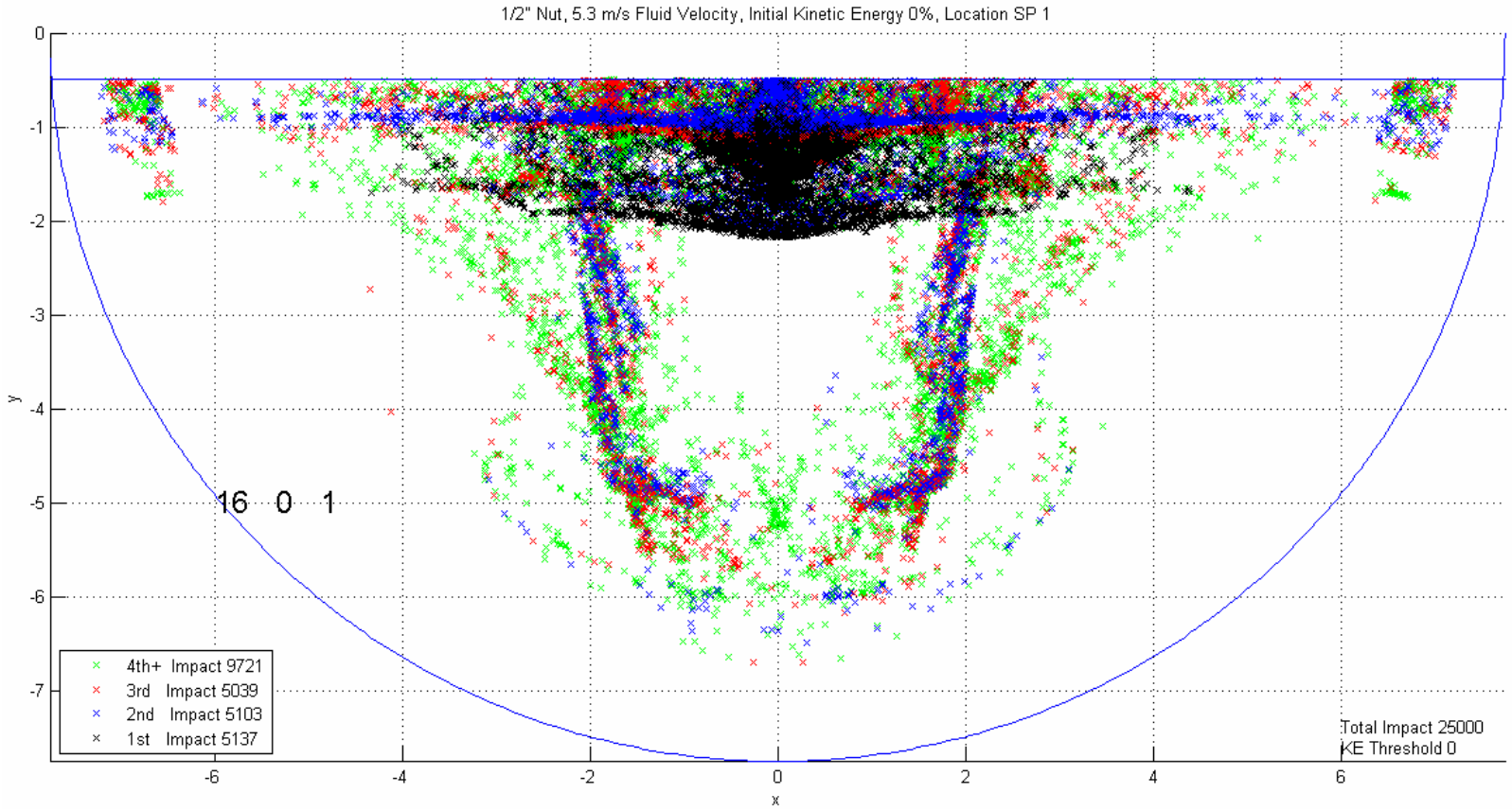

Figure 3.1 1/2" nut, 5.3 m/s fluid velocity, initial kinetic energy 0%, location SP 1

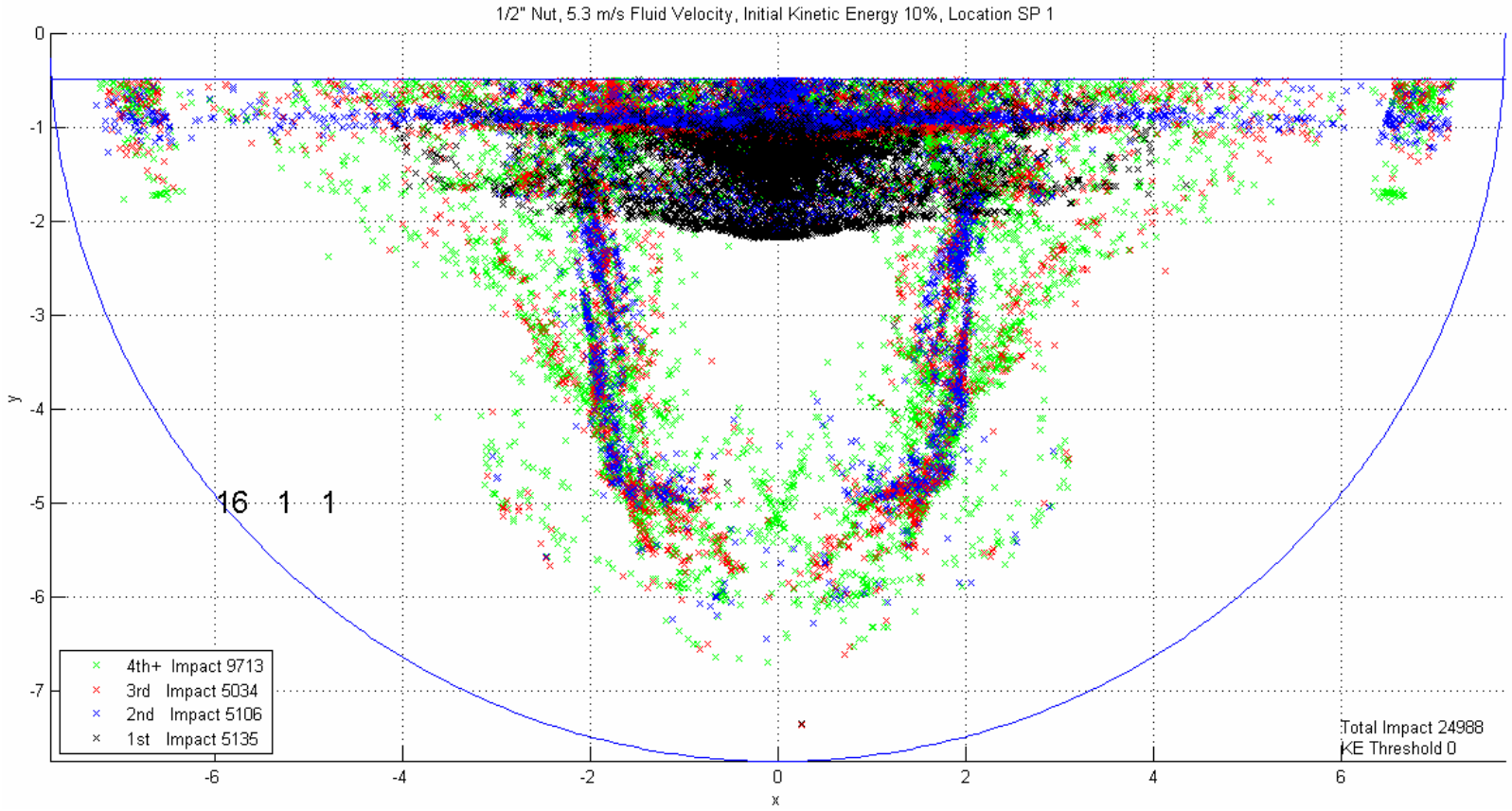

Figure 3.2 1/2" nut, 5.3 m/s fluid velocity, initial kinetic energy 10%, location SP 1

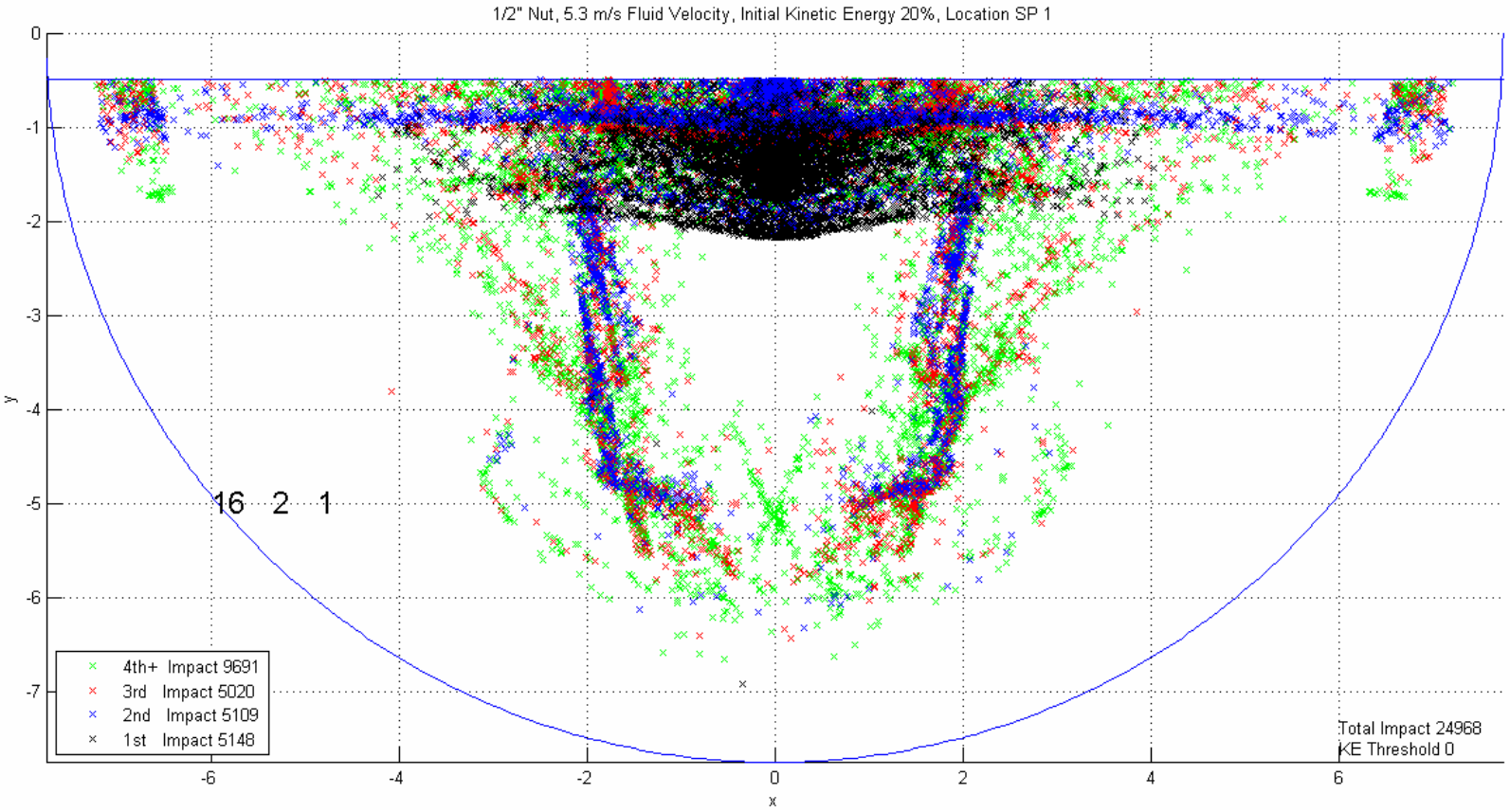

Figure 3.3 1/2" nut, 5.3 m/s fluid velocity, initial kinetic energy 20%, location SP 1

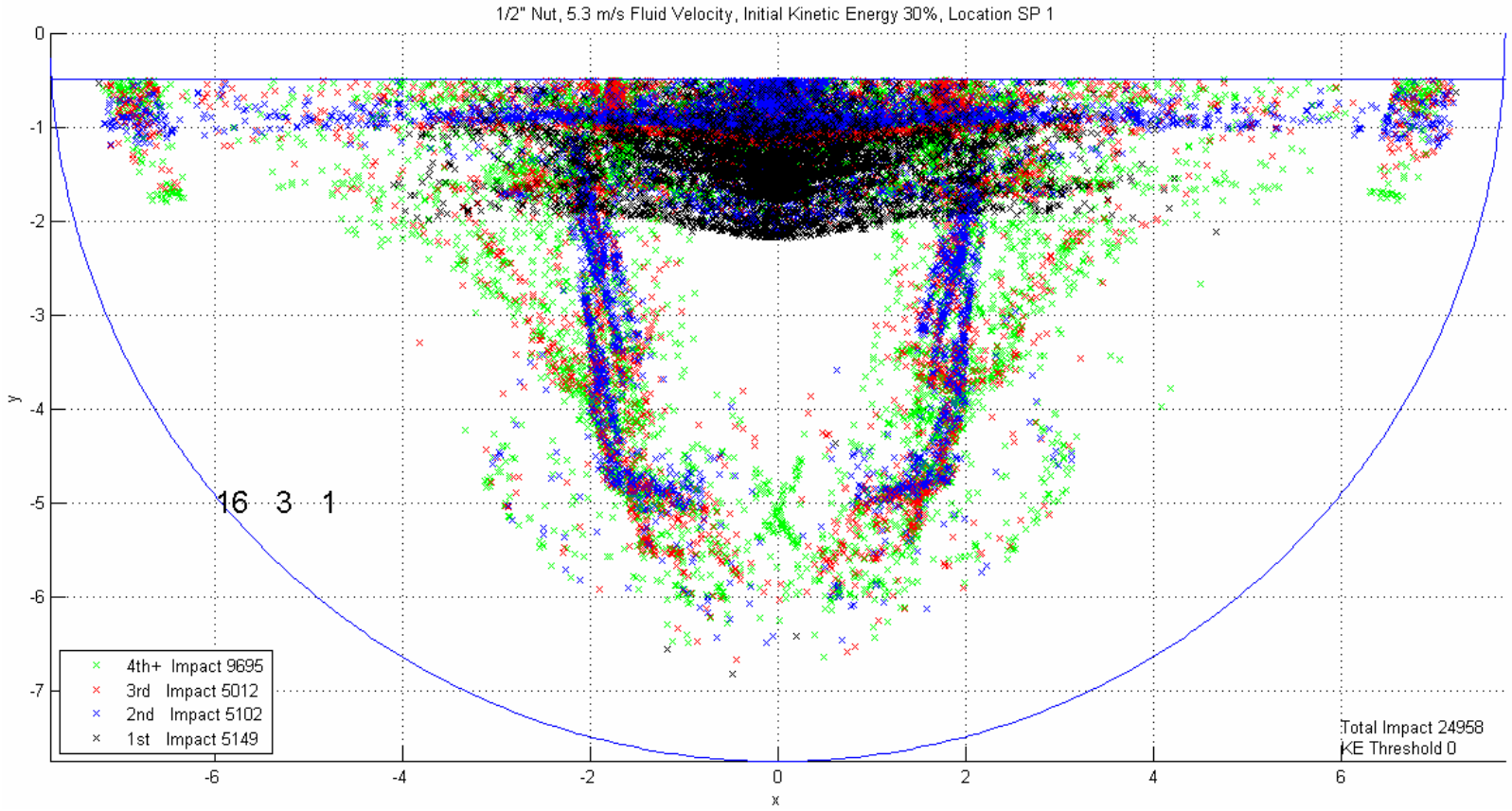

Figure 3.4 1/2" nut, 5.3 m/s fluid velocity, initial kinetic energy 30%, location SP 1

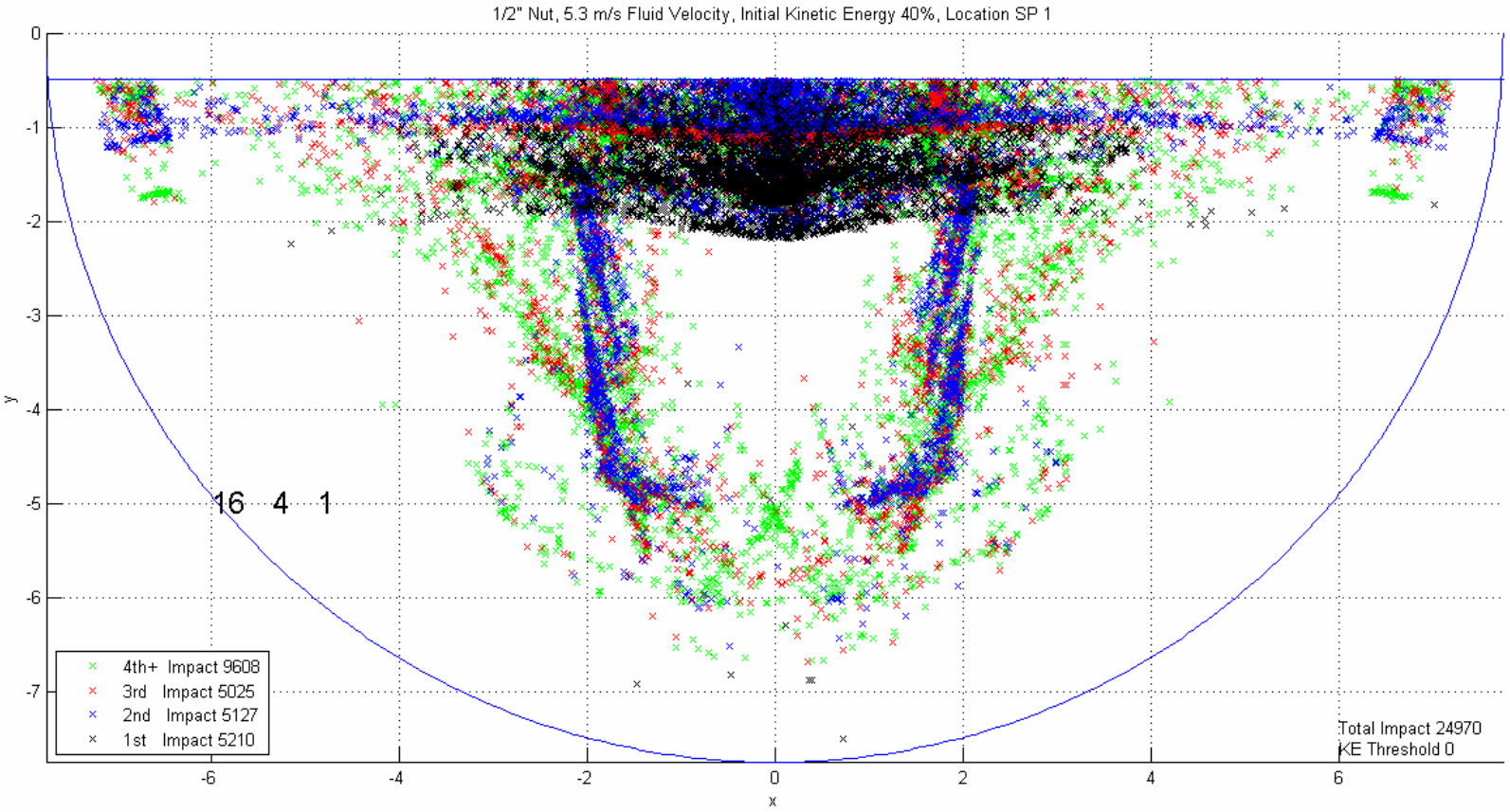

Figure 3.5 1/2" nut, 5.3 m/s fluid velocity, initial kinetic energy 40%, location SP 1

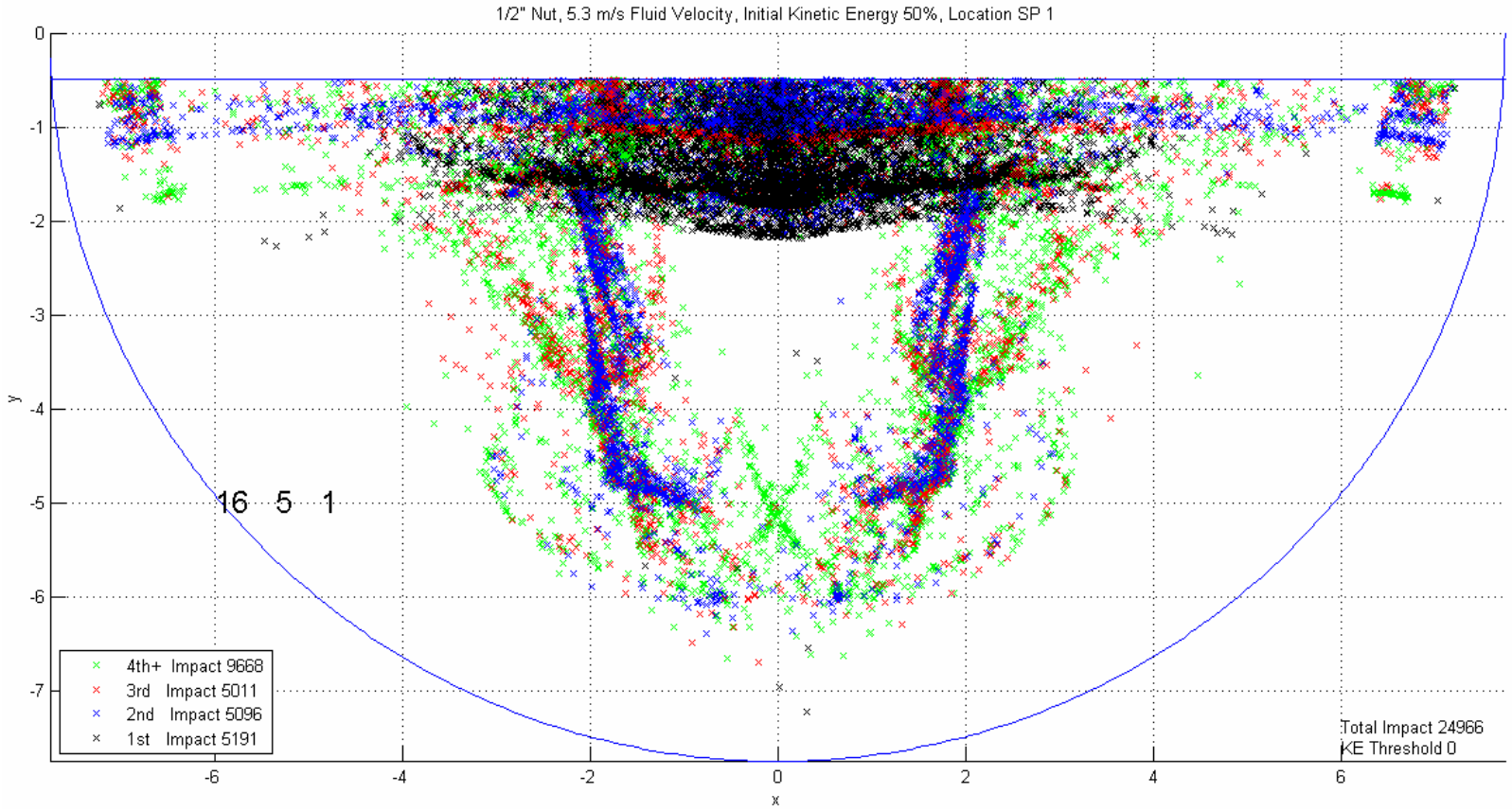

Figure 3.6 1/2" nut, 5.3 m/s fluid velocity, initial kinetic energy 50%, location SP 1

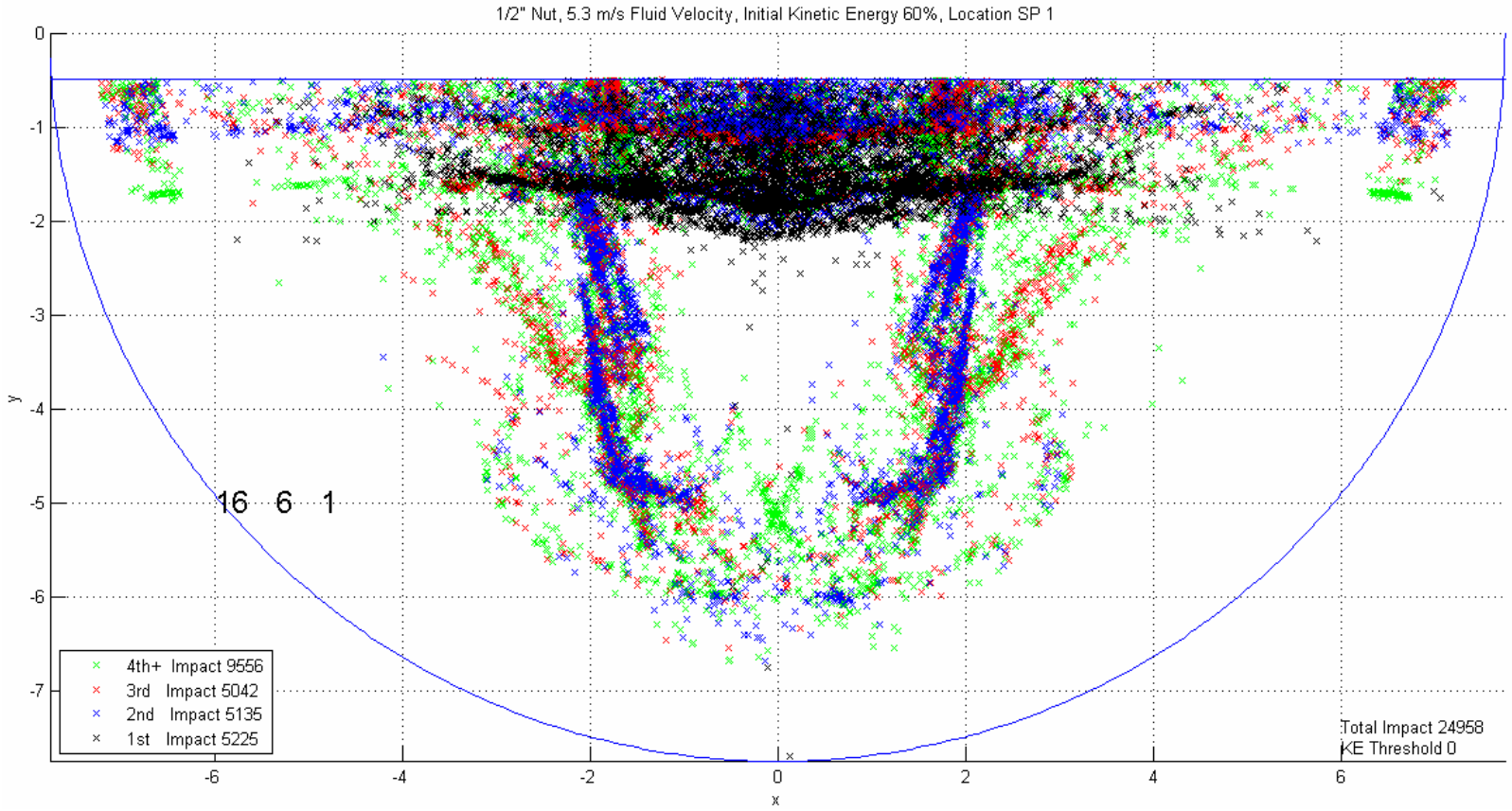

Figure 3.7 1/2" nut, 5.3 m/s fluid velocity, initial kinetic energy 60%, location SP 1

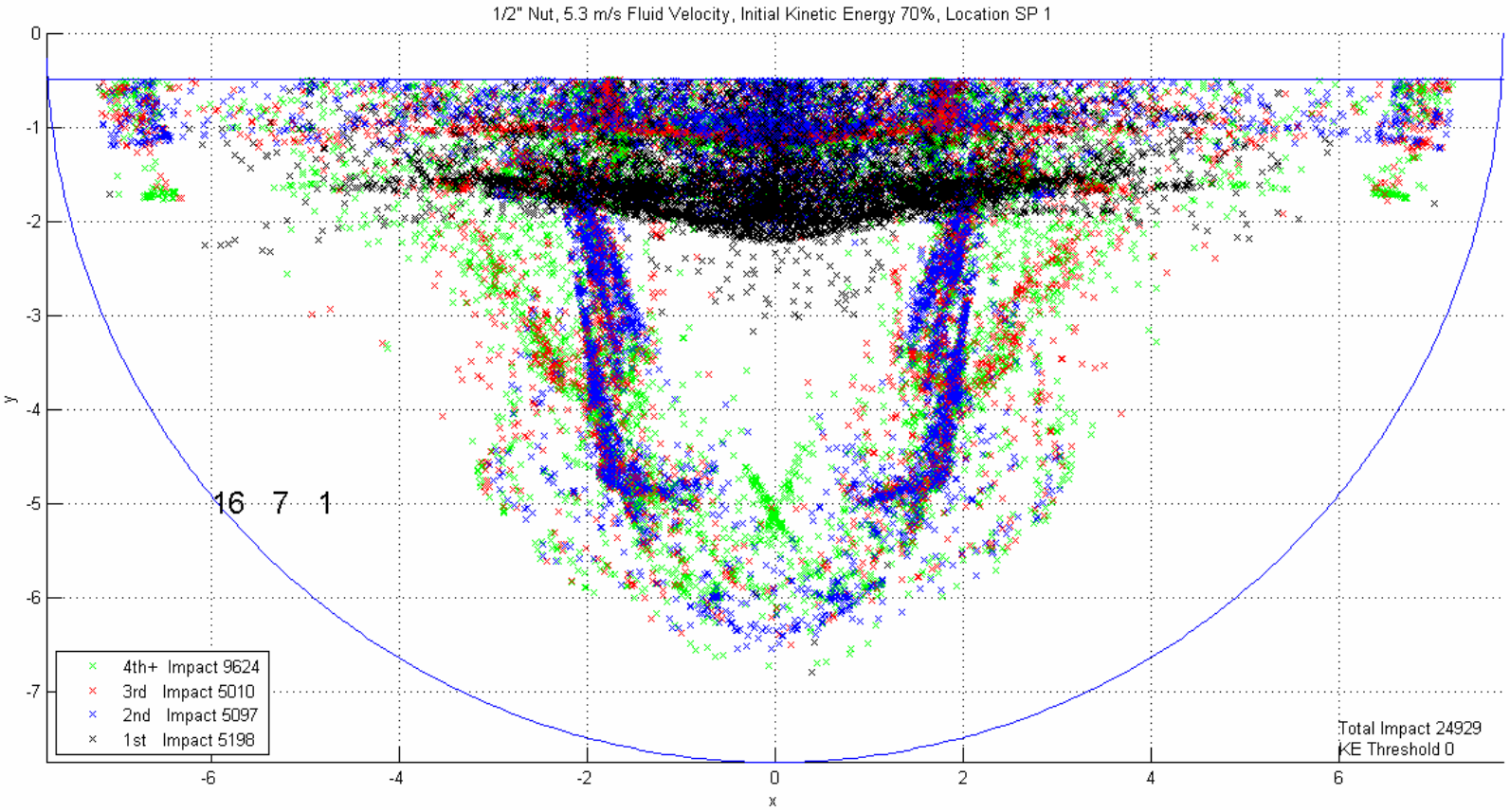

Figure 3.8 1/2" nut, 5.3 m/s fluid velocity, initial kinetic energy 70%, location SP 1

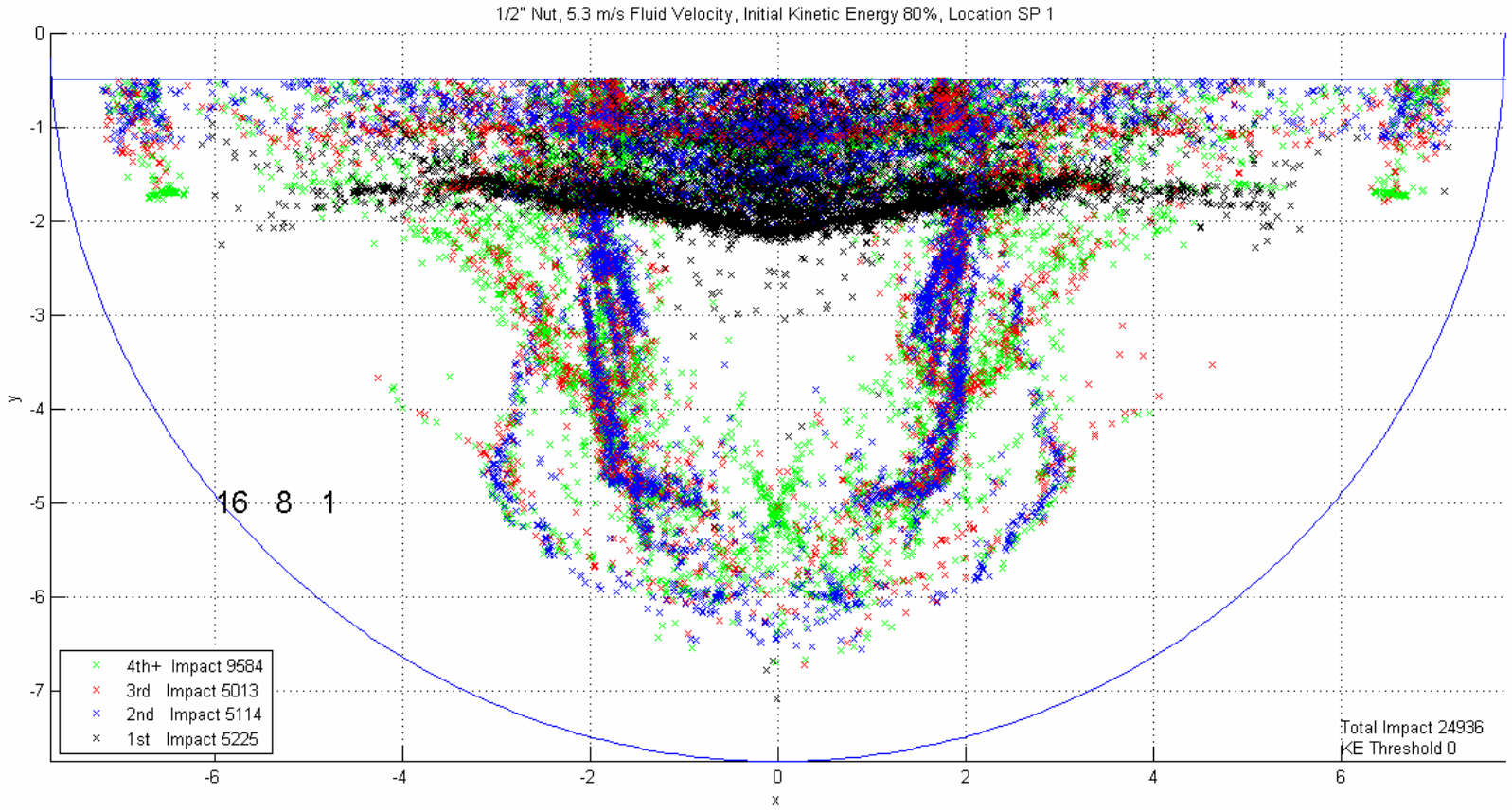

Figure 3.9 1/2" nut, 5.3 m/s fluid velocity, initial kinetic energy 80%, location SP 1

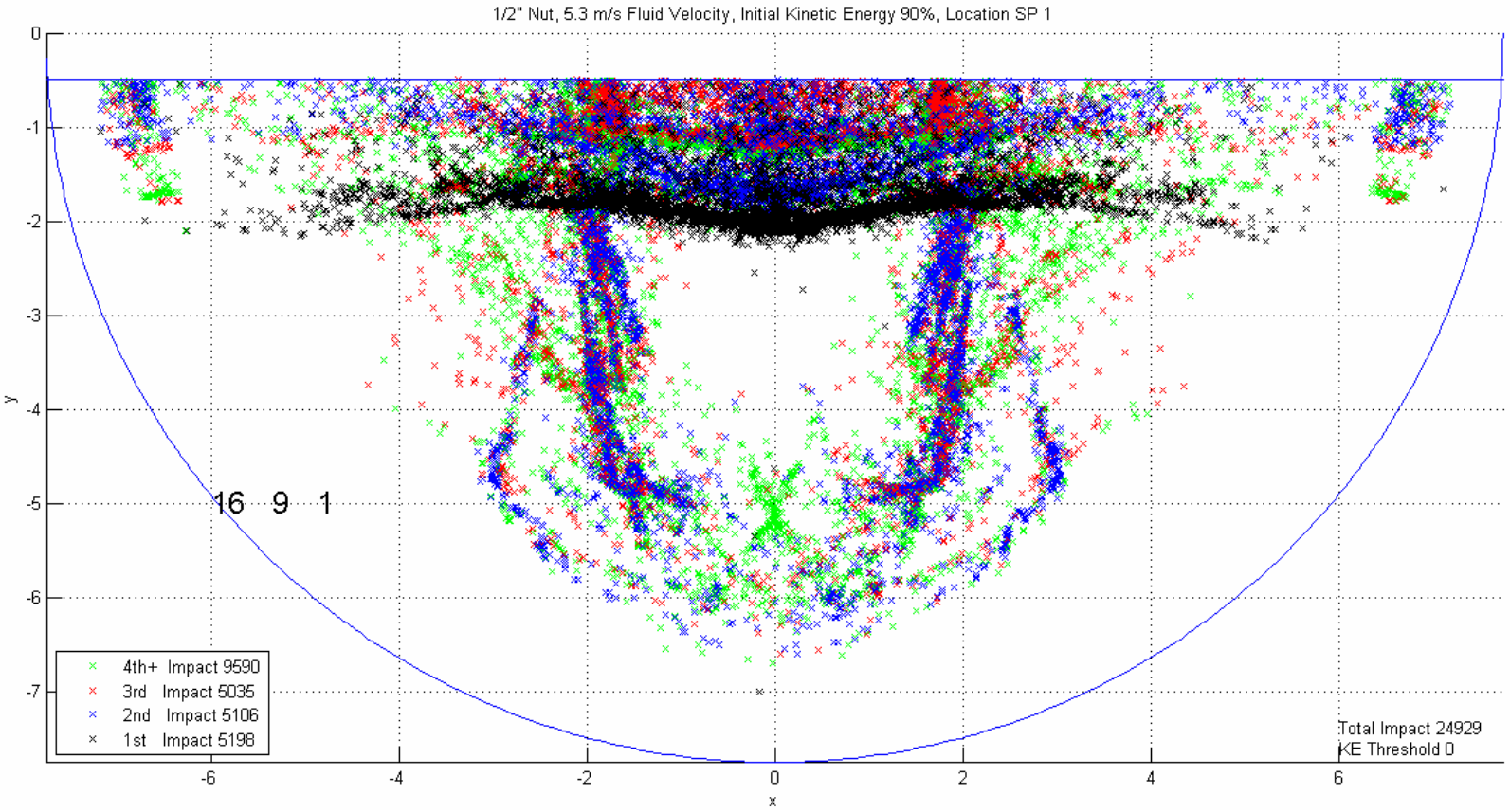

Figure 3.10 1/2" nut, 5.3 m/s fluid velocity, initial kinetic energy 90%, location SP 1

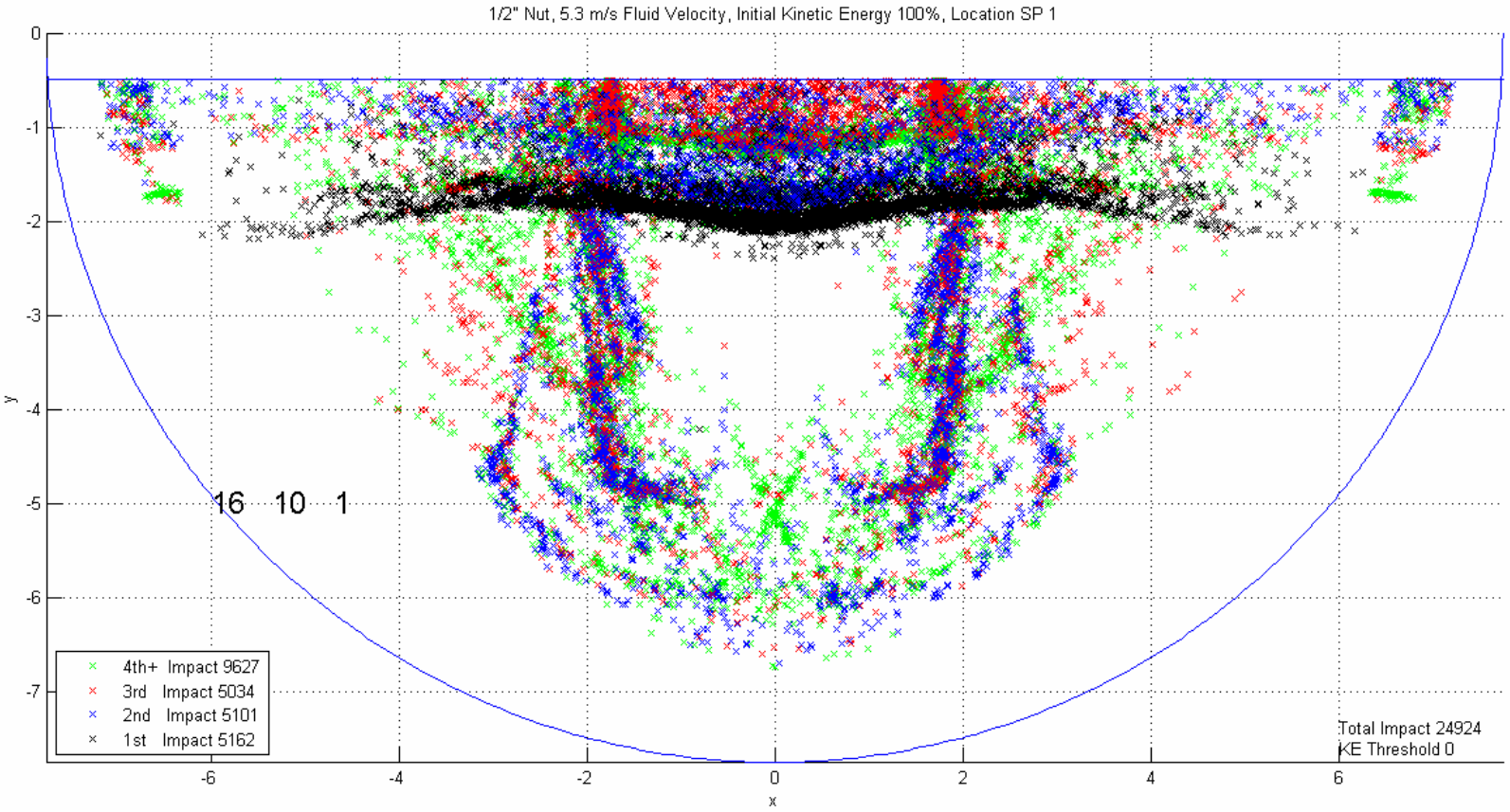

Figure 3.11 1/2" nut, 5.3 m/s fluid velocity, initial kinetic energy 100%, location SP 1

Each of the figures represents a top down perspective on the tube sheet of the scaled setup. There are three distinguishing information areas on each figure. These include the legend in the lower left hand corner, the information in the lower right hand corner and the large set of the three numbers located within the figure itself in the lower left of the tube sheet outline.

Every 'x' is an impact location on the tube sheet. As mentioned previously, these particular figures show roughly 25,000 impacts on each figure. As according to the legend, black represents the first impact of each history, blue the second impact of each history, red the third and green represents the 4^{th} and 5^{th} impacts together for each history. In the legend next to each color impact is the total number of impacts for that color. The total number of impacts is given in the lower right hand corner of the figures as well as a cutoff threshold for the energy of each impact in Joules. Note that since the threshold is set to 0 J in the above figures, all impacts, regardless of impact energy are included. The large set of three numbers in the tube sheet area is a shorthand notation to identify which figure is presented. The number '16' represents the particular ID number of the 1/2" nut and '17' is the ID number of the 5/8" nut. This stems from the fact that there were 28 different types of part catalogued in Shi's work. The ID number simply allows for quick reference to which part run is being displayed.

At first glance, the figures above may appear to be roughly the same, which, in fact they are; but there are subtle differences which will be noted here.

First, there are two different types of initial (1^{st}) impacts that occur here. One possible type of impact, type 1, may occur when the part is launched in such a way that its first

contact is with the tube sheet. The other possible relevant type of impact, type 2, which may also occur, is when the part first impacts the plenum divide before coming into contact with the tube sheet in a secondary impact. **Figure 2.5** in the X-Z cross section profile show two possible trajectories of the part which would lead to the type 1 and the type 2 impact scenarios. Look to the black 1st impacts. As the initial kinetic energy increases, there is a transition from the impacts being mainly focused in the assumed experimental plume region R_p to an impact band extending most of the diameter of the tube sheet.

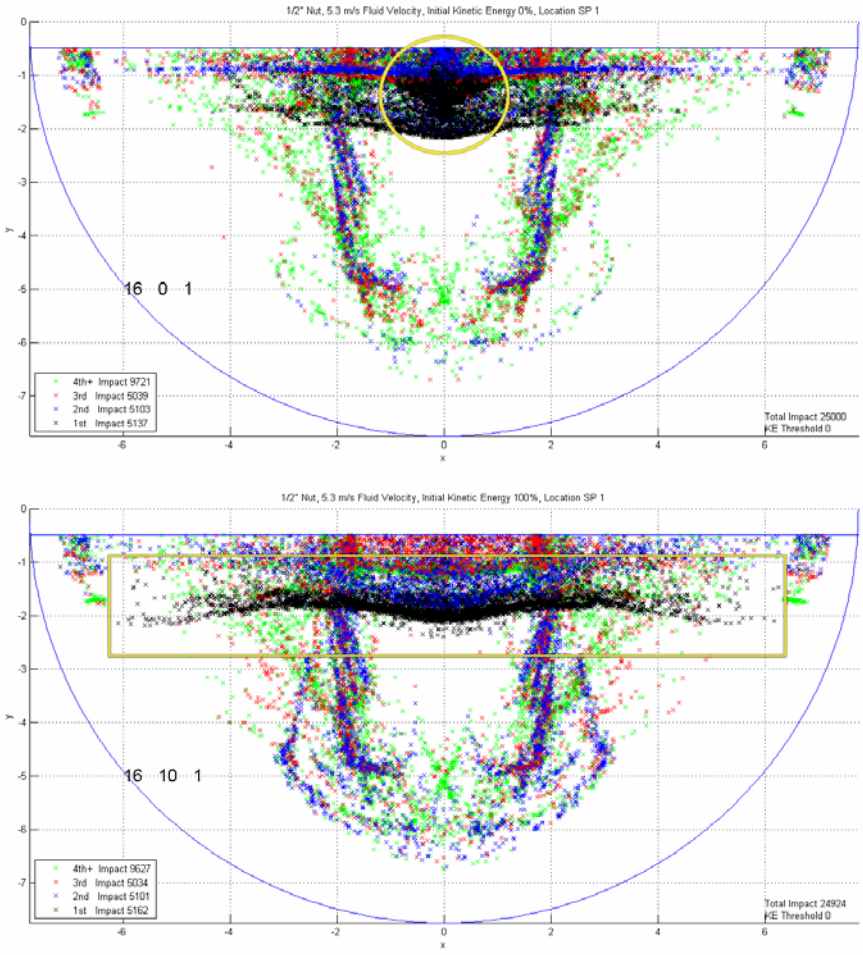

Figure 3.12 First impact changes as a function of initial kinetic energy

The part path deviates more from a stream line started at the same starting location as the part becomes more energetic. The impact band is due to the result of the part first impacting the plenum divide wall and then rebounding to the tube sheet. As there is more energy, the part can travel further from the inlet pipe and still have enough upward momentum to impact the tube sheet away from the assumed flow plume.

It is important to note that the most energetic impacts are not localized to any particular region on the tube sheet. The most energetic impacts occur across the band and in the assumed plume region as well as occasionally in the outward lying regions. The general progression of the spatial distribution of all impact locations as a function of initial kinetic energy accurately depicts the progression for the highest energy impacts as well. As the initial kinetic energy increases and as the start plane increases from one to four there is an increase in the number of higher energy impacts.

The energy distribution for the same figures as above except located at start plane 4 is given in **Figures 3.13** and **3.14**. **Figure 3.13** gives the distribution as a function of the 1st impact. **Figure 3.14** gives the energy distribution as a function of the 2nd through 5th impacts. Start plane 4 is used instead of start plane 1 because the effects are more pronounced and easier to see as the start plane number increases. The same general trend can be seen at any of the start planes.

Impacts with energy above 0.07 J for the 1/2” nut at 5.3 m/s can be associated solely with the 1st impact. The part initially coming up the inlet pipe and into the plenum has the potential to carry much more energy than part that has already entered the plenum. Notice as the initial kinetic energy is increased we see a direct correlation in the 1st impact energy.

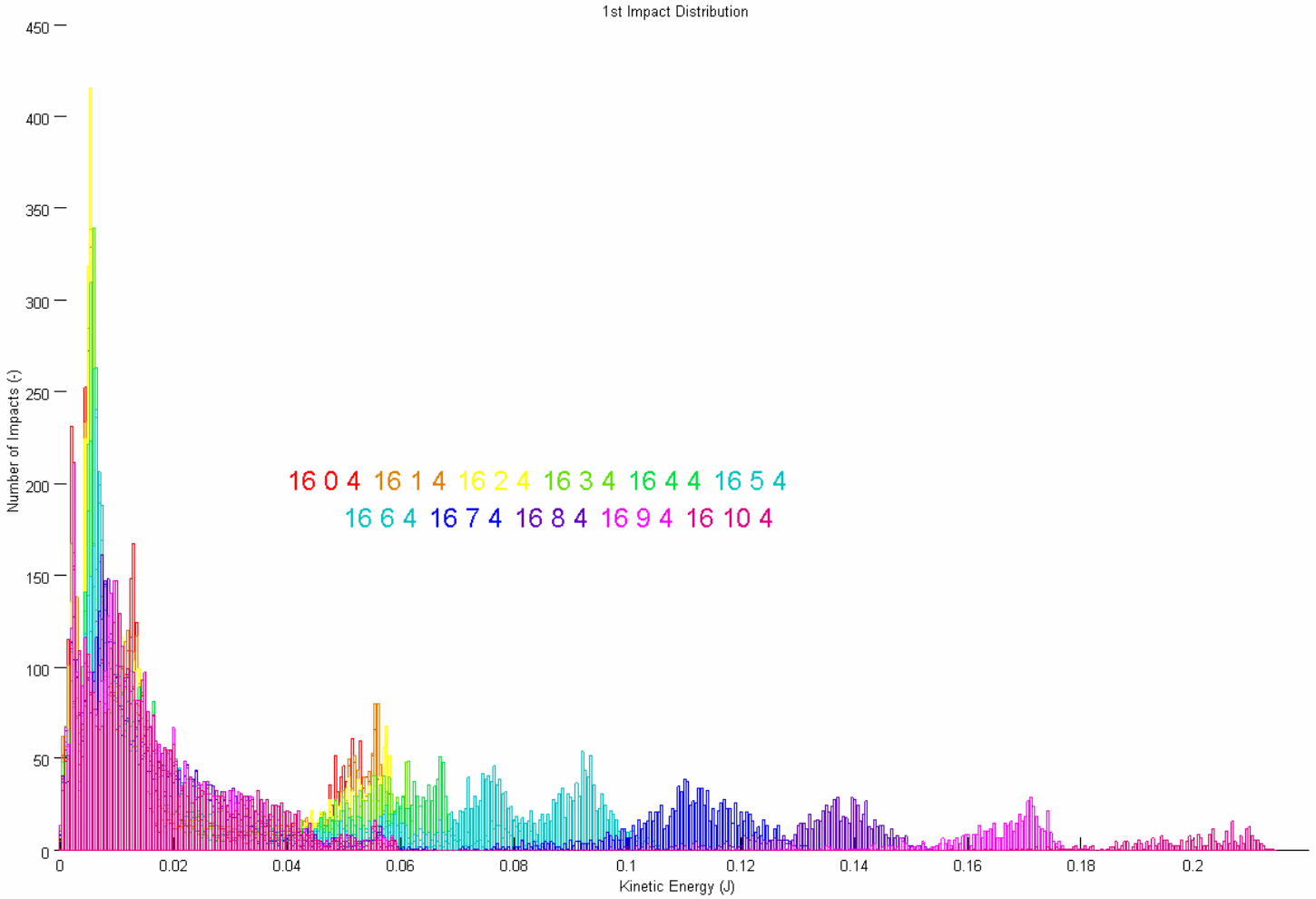

Figure 3.13 1st impact energy distributions

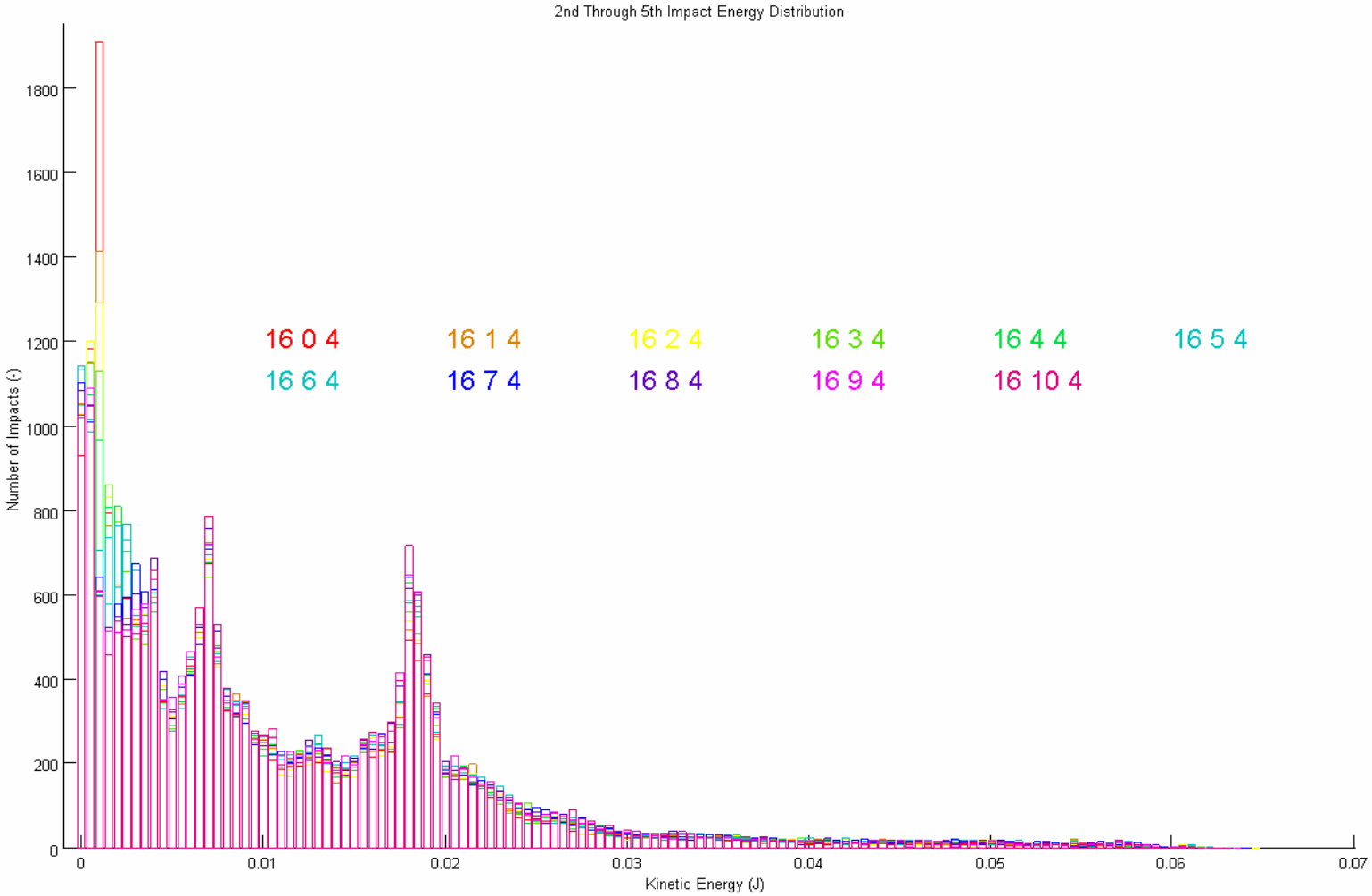

Figure 3.14 2nd through 5th impact energy distributions

The higher initial kinetic energy impacts leads to higher energy 1st impacts on the tube sheet. Beyond the 1st impact the energy distribution is invariant to initial kinetic energy and initial start plane. The sequences of three numbers signify the short hand described earlier. The color of the text matches the color of the corresponding distribution.

The invariance seen in the energy distribution does not hold the same for the spatial distribution. The effects of the initial kinetic energy and initial start plane ripple into the 2nd and 3rd impacts. The effects in the 2nd impacts are more pronounced than the effects in the 3rd impacts. Beyond the 3rd impacts little to no change can be discerned and the invariance due to initial kinetic energy and initial start planes is valid.

Four more figures are given below as a function of initial starting position. These impact distributions are from Case 1 with the 1/2" nut at 5.3 m/s fluid velocity. Each is taken from the same initial kinetic energy of 50% of the surrounding fluid velocity and start planes 1 through 4. These figures are laid out specifically to illustrate the effects of initial starting position as a function of spatial impact distribution.

It is evident from the figures that the initial starting location plays a significant role in the 1st impact location on the tube sheet. Impacts tend to concentrate into the banded formations for the 1st, 2nd and 3rd impacts for parts starting in plane 1. As the start plane number is increased, the distributions tend to disperse in the assumed plume region leaving the outermost impacts largely unaffected. This is seen in the later figures as if the bands have been smeared in a more uniform distribution towards the plenum divide wall.

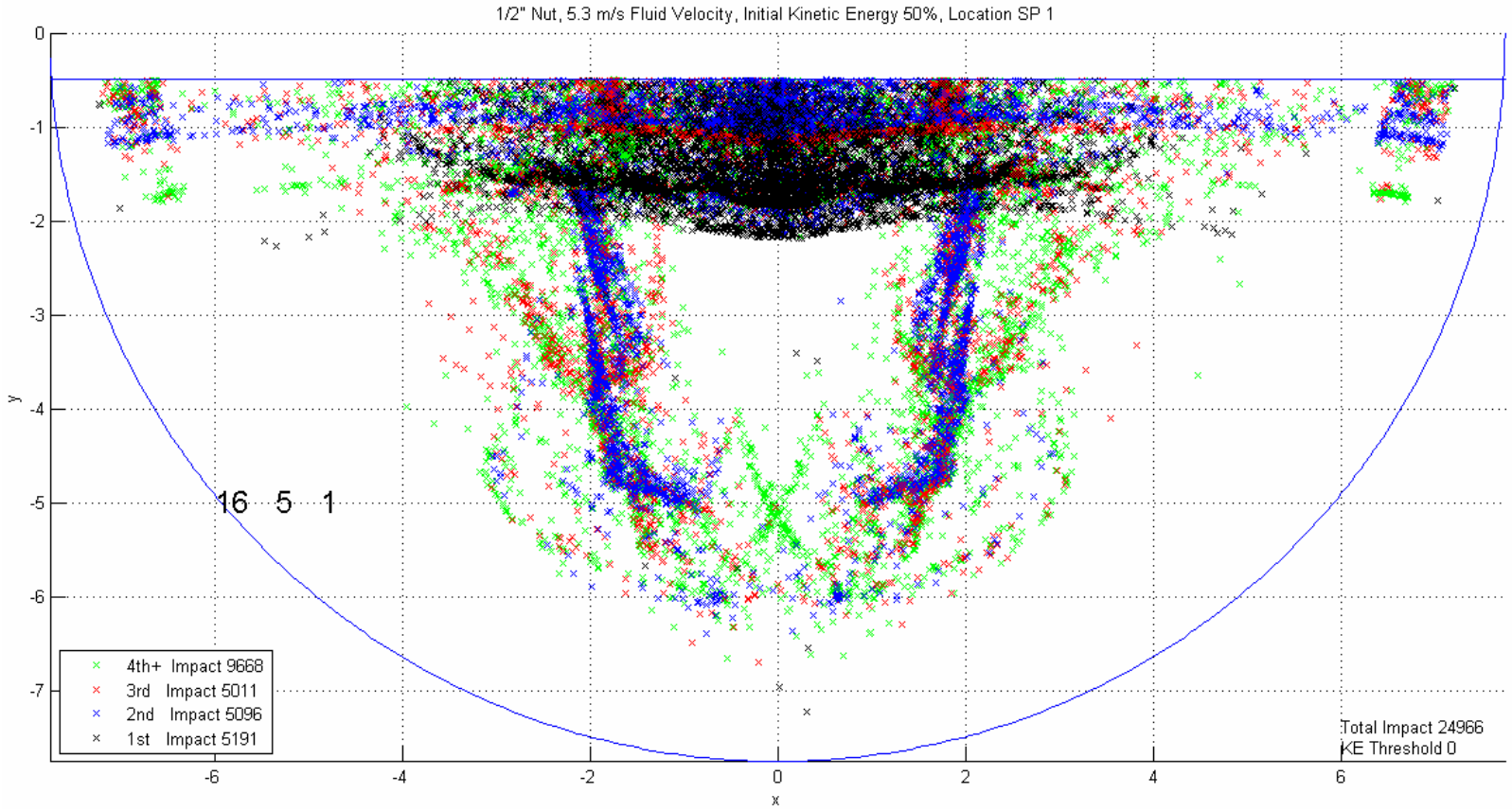

Figure 3.15 1/2" nut, 5.3 m/s fluid velocity, initial kinetic energy 50%, location SP 1

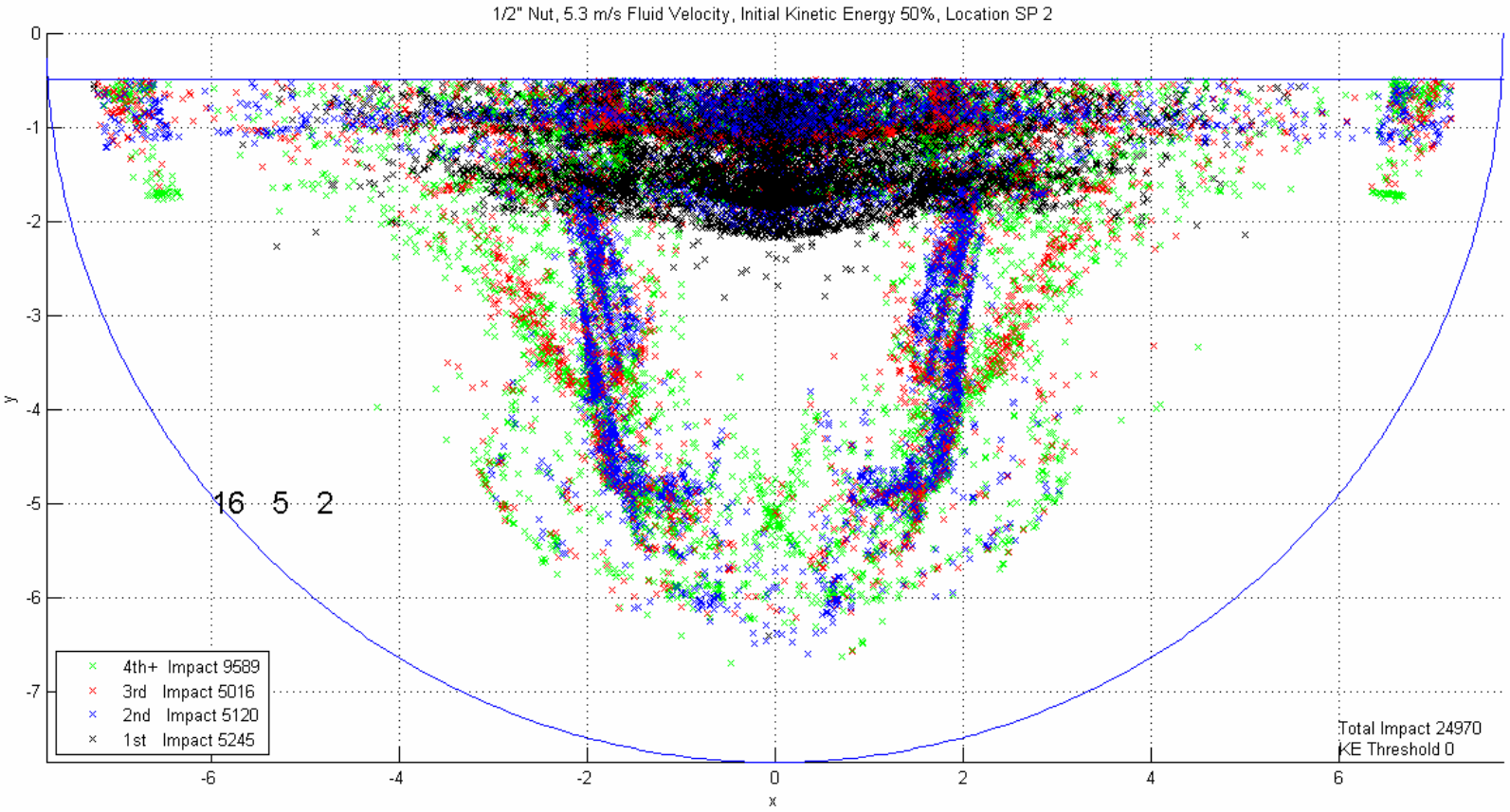

Figure 3.16 1/2" nut, 5.3 m/s fluid velocity, initial kinetic energy 50%, location SP 2

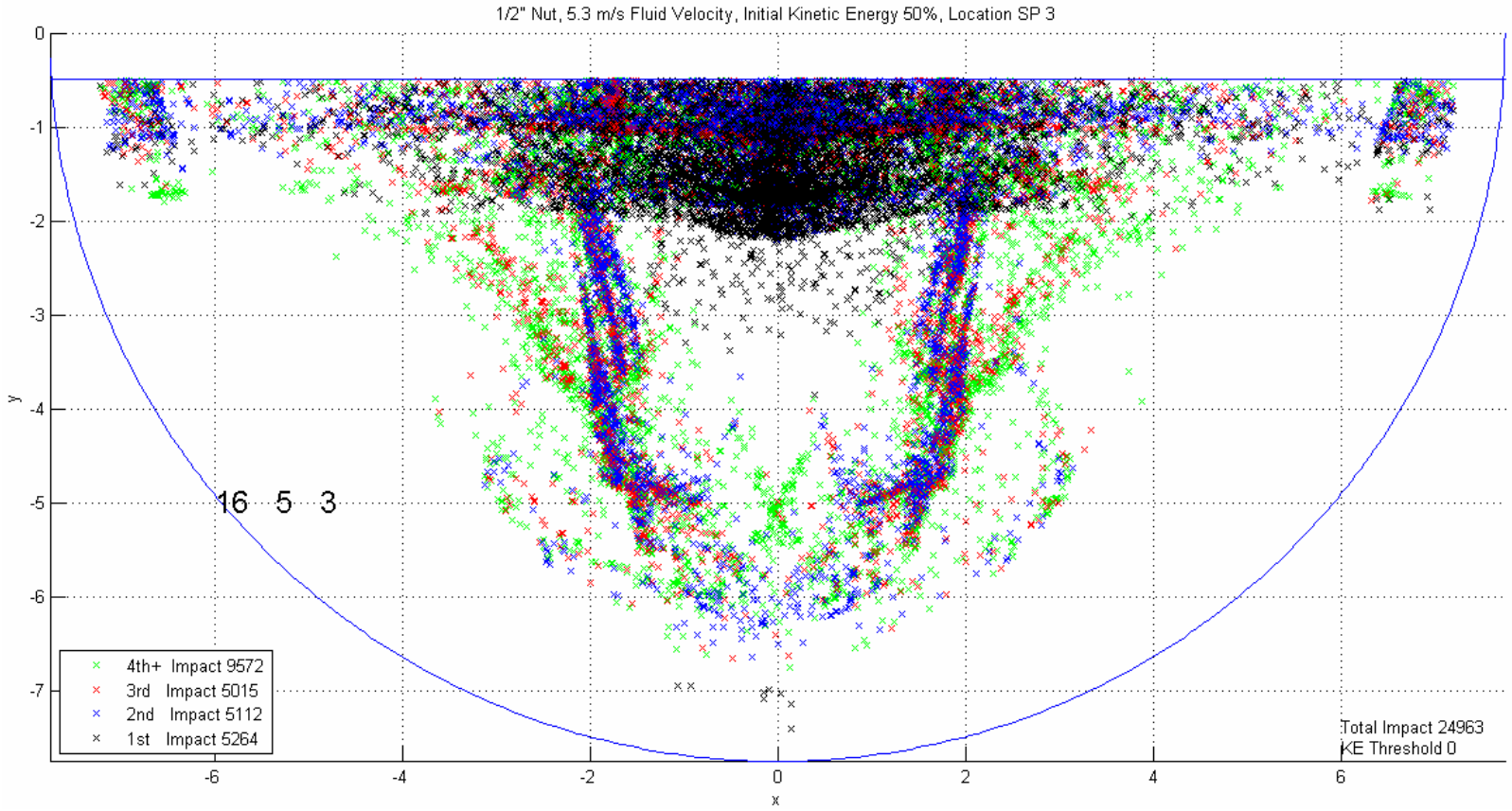

Figure 3.17 1/2" nut, 5.3 m/s fluid velocity, initial kinetic energy 50%, location SP 3

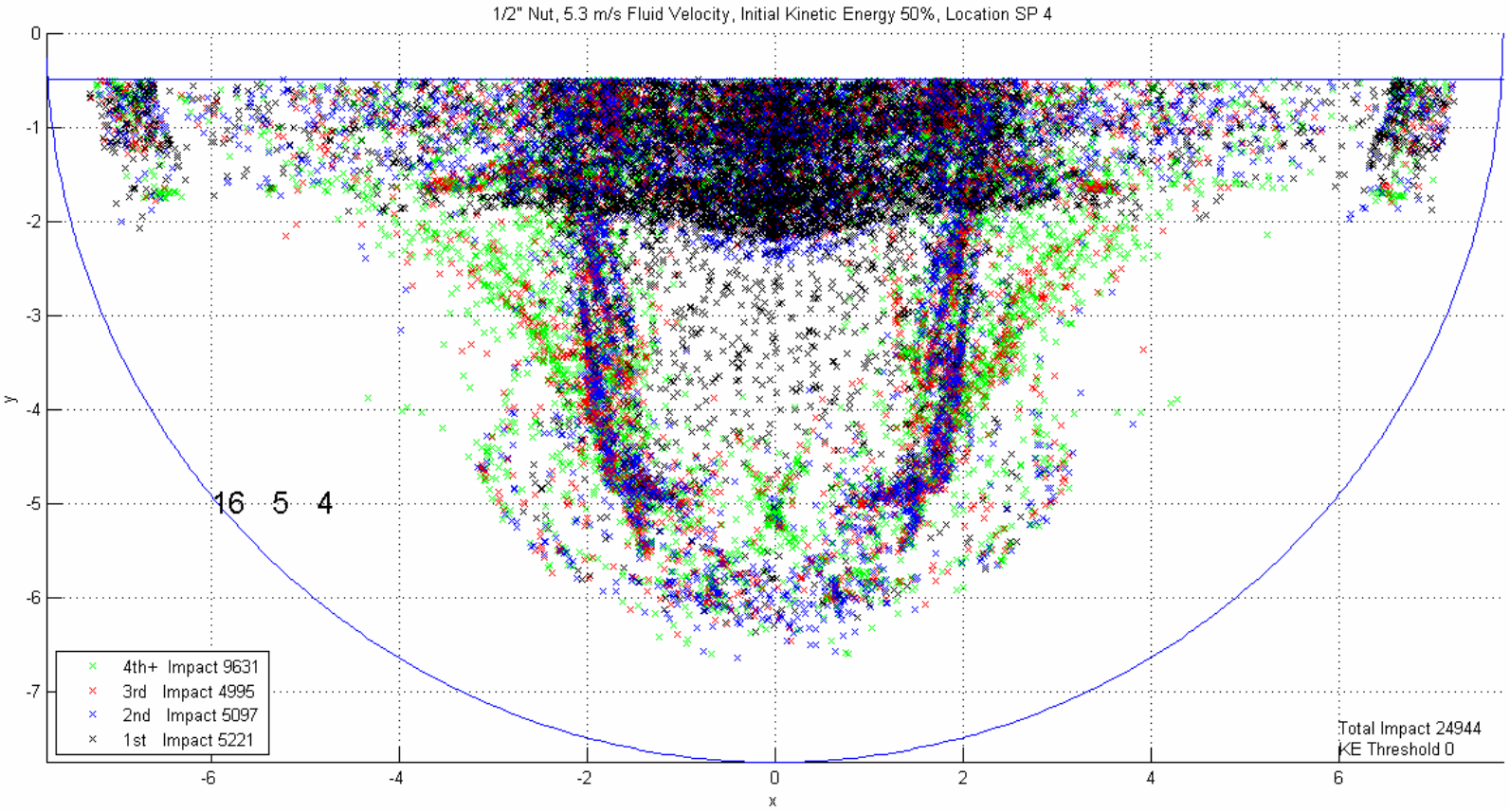

Figure 3.18 1/2" nut, 5.3 m/s fluid velocity, initial kinetic energy 50%, location SP 4

3.1.1 Scaled Experiment and Simulation Comparisons

To compare the data from Shi's experiment and the simulation completed in this project the data must be properly filtered. To fit a 2-D Gaussian function as Shi did only the points within the assumed plume area are used. The experiments revealed that within this area the maximum probabilities were similar. Although these fits do not necessarily reflect the best overall fit of the data they are used to generate a benchmark between the experiment and simulation.

Figure 3.19 depicts the spatial impact distribution for the combined three cases detailed in **Table 2.1**. The fitted Gaussians described by Equation (2.1.1) are composed only of the dots for each individual case. Note that the tube sheet starts at an X-coordinate around zero while the simulation figures start at the effective radius of the part. This is because the simulation assumes the impact is a sphere impact when in fact depending on the orientation of the part it would be possible for the part to impact closer.

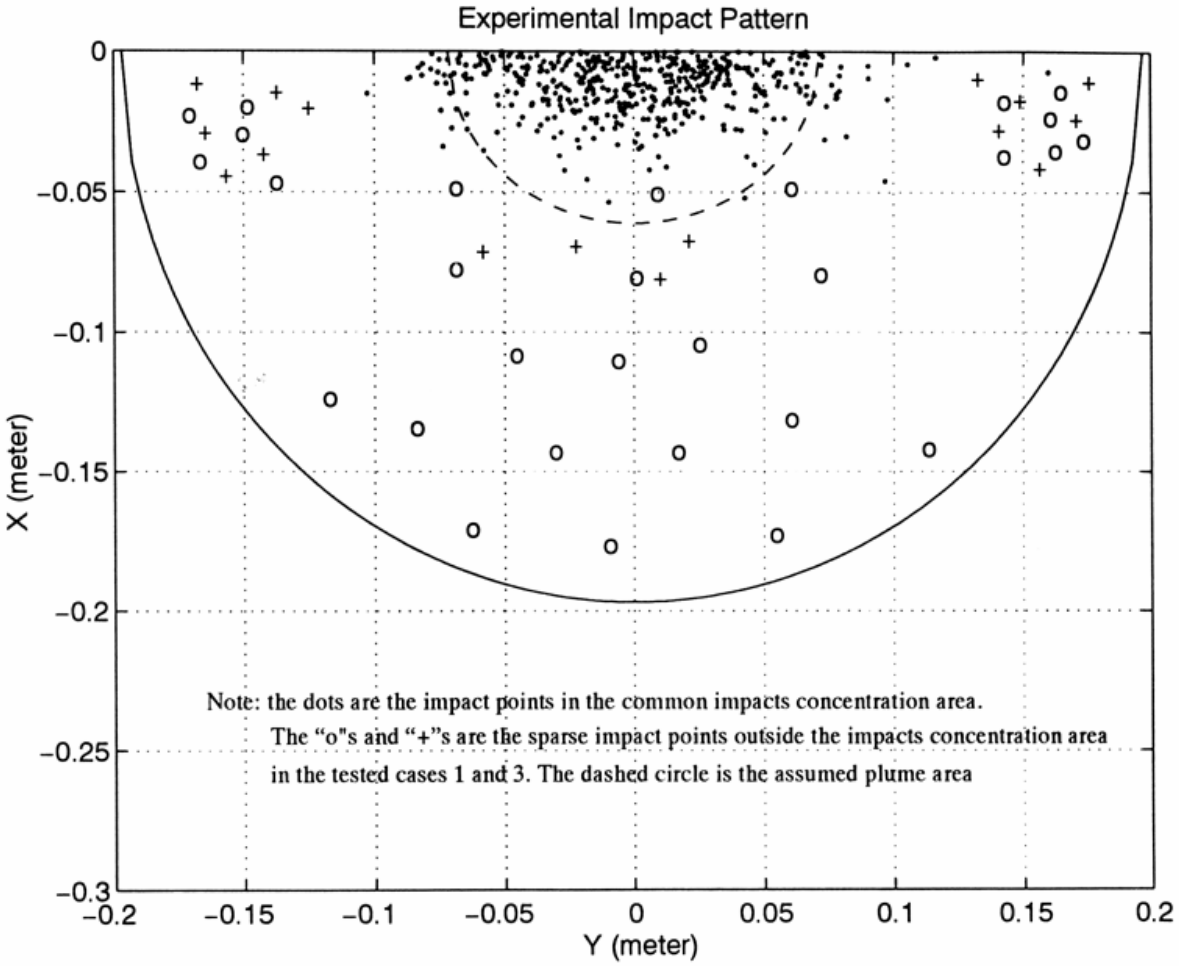

Figure 3.19 Experimental impact patterns combined for the three cases [Shi]

Given that Shi included results that fell within the assumed plume area, R_p, for the Gaussian fit, the scaled simulation data was also trimmed to only include the impacts that occurred within the radius R_p. To fit the data a 20 x 40 2-D square mesh was laid over the radius of the tube sheet. If a particular impact fell within the region of a particular mesh square an impact was scored. All impacts were tallied in this manner and the subsequent distribution function was normalized to provide a probability distribution function over the

mesh laid upon the tube sheet. Given this PDF, the unknown standard deviations, amplitude and center point parameters of a 2-D Gaussian distribution roughly positioned above the center of the assumed flow plume could be found using nonlinear least squares regression. In this particular case, the Levenberg-Marquardt algorithm was used. A modified version of the 2-D Gaussian given in **Chapter 2** was used to account for the translation of the impacts from the X-axis due to the finite volume of the part discussed previously. The Gaussian fit equation is a function centered at the point $(x_c, 0)$ and is given as

$$f(x,y) = Ae^{-\left(\frac{(x+x_c)^2}{2\sigma_x^2}+\frac{y^2}{2\sigma_y^2}\right)} \tag{3.1.1}$$

where A, x_c, σ_x and σ_y are unknown parameters to be fitted.

Results for the three cases are given in **Table 3.1**. Forty-four runs for each case were completed at the various combinations of initial kinetic energies and initial start planes. The standard deviations of each fit are given as a percentage of the tube sheet radius (7.75 inches). Fits were completed for all impacts within the assumed plume radius together. Once the parameters were found the Gaussian was renormalized by

$$A = \frac{1}{\pi\sigma_x\sigma_y\left(1+erf\left(\frac{\sqrt{2}x_c}{2\sigma_x}\right)\right)} \tag{3.1.2}$$

such that

$$\int_{-\infty}^{\infty}\int_{-\infty}^{0} f(x,y)\,dxdy = 1 \tag{3.1.3}$$

Some arbitrary cases are highlighted to draw attention to the particularly close agreement with Shi's previous experimental results.

Table 3.1a Case 1 Gaussian fitting results, start planes 1 & 2, all impacts combined

Case 1 1/2" Nut					
Fluid Velocity 5.3 m/s					
IKE (% FV)	Start Plane	Center (in)	Normalization Constant (-)	σ_x (%TS)	σ_y (%TS)
0	1	0.253	0.636	5.683	19.933
1	1	0.265	0.623	5.382	19.899
2	1	0.263	0.626	5.396	19.997
3	1	0.253	0.625	5.691	20.003
4	1	0.221	0.642	6.750	19.991
5	1	0.202	0.647	7.594	19.978
6	1	0.188	0.662	8.266	20.032
7	1	0.170	0.726	9.252	19.980
8	1	0.160	0.777	9.731	20.017
9	1	0.144	0.872	10.839	20.003
10	1	0.192	0.654	8.633	19.122
0	2	0.231	0.602	6.497	19.977
1	2	0.227	0.614	6.573	20.051
2	2	0.238	0.611	6.185	20.026
3	2	0.228	0.626	6.524	19.962
4	2	0.218	0.607	7.014	20.006
5	2	0.203	0.615	7.691	19.960
6	2	0.191	0.639	8.216	20.020
7	2	0.172	0.696	9.264	19.997
8	2	0.151	0.756	10.750	19.989
9	2	0.138	0.908	11.330	20.019
10	2	0.146	0.964	10.203	19.971

Table 3.1b Case 1 Gaussian fitting results, start planes 3 & 4, all impacts combined

Case 1 1/2" Nut					
Fluid Velocity 5.3 m/s					
IKE (% FV)	Start Plane	Center (in)	Normalization Constant (-)	σ_x (%TS)	σ_y (%TS)
0	3	0.206	0.476	8.346	20.004
1	3	0.201	0.458	8.798	20.015
2	3	0.196	0.528	8.585	20.029
3	3	0.206	0.600	7.612	20.034
4	3	0.210	0.614	7.356	19.999
5	3	0.195	0.613	8.160	19.957
6	3	0.189	0.611	8.490	20.031
7	3	0.165	0.599	10.389	20.013
8	3	0.158	0.666	10.587	19.992
9	3	0.169	0.738	9.195	20.033
10	3	0.180	0.734	8.507	19.990
0	4	0.145	0.355	14.848	19.791
1	4	0.142	0.010	18.775	19.765
2	4	0.154	0.321	13.968	20.038
3	4	0.162	0.474	11.908	19.742
4	4	0.159	0.459	12.078	20.021
5	4	0.162	0.376	12.555	20.003
6	4	0.171	0.370	11.811	20.015
7	4	0.181	0.214	12.763	19.605
8	4	0.182	0.353	11.037	19.963
9	4	0.185	0.311	11.149	20.033
10	4	0.188	0.304	11.724	19.014

Table 3.1c Case 2 Gaussian fitting results, start planes 1 & 2, all impacts combined

Case 2 1/2" Nut					
Fluid Velocity 3.6 m/s					
IKE (% FV)	Start Plane	Center (in)	Normalization Constant (-)	σ_x (%TS)	σ_y (%TS)
0	1	0.394	1.094	1.249	19.396
1	1	0.025	0.258	10.006	19.997
2	1	0.053	0.316	7.804	20.062
3	1	0.087	0.346	6.781	19.973
4	1	0.071	0.284	8.620	19.980
5	1	0.098	0.303	7.728	20.003
6	1	0.029	0.313	12.374	13.353
7	1	0.000	0.120	20.978	20.978
8	1	0.005	0.340	12.445	12.464
9	1	0.394	0.232	7.642	19.965
10	1	0.559	0.234	6.547	20.027
0	2	0.000	0.734	8.496	8.496
1	2	0.111	0.856	4.911	10.253
2	2	0.190	0.509	4.563	16.183
3	2	0.133	0.312	7.472	19.213
4	2	0.115	0.158	16.005	19.517
5	2	0.000	0.146	18.651	19.526
6	2	1.534	0.509	8.517	6.179
7	2	0.857	0.490	7.326	7.896
8	2	0.375	0.153	13.514	19.985
9	2	0.671	0.230	6.275	20.001
10	2	0.946	0.215	6.346	19.977

Table 3.1d Case 2 Gaussian fitting results, start planes 3 & 4, all impacts combined

Case 2 1/2" Nut					
Fluid Velocity 3.6 m/s					
IKE (% FV)	Start Plane	Center (in)	Normalization Constant (-)	σ_x (%TS)	σ_y (%TS)
0	3	1.434	0.127	10.971	20.000
1	3	1.139	0.155	8.984	19.995
2	3	1.630	0.120	11.357	20.007
3	3	1.466	0.170	8.285	19.073
4	3	1.946	0.121	11.006	20.113
5	3	0.730	0.142	9.914	22.730
6	3	0.787	0.208	7.308	18.957
7	3	1.471	0.104	14.011	20.009
8	3	1.289	0.136	10.319	20.001
9	3	1.401	0.173	7.720	19.996
10	3	1.428	0.329	4.009	20.078
0	4	1.560	0.197	6.716	20.012
1	4	1.563	0.229	5.788	19.981
2	4	1.574	0.159	8.371	20.018
3	4	1.617	0.121	11.329	20.003
4	4	1.485	0.130	10.535	19.998
5	4	1.830	0.097	14.340	20.000
6	4	1.674	0.095	14.973	20.043
7	4	1.747	0.107	12.877	19.996
8	4	1.664	0.133	9.522	21.156
9	4	1.835	0.133	10.661	18.902
10	4	1.788	0.110	12.383	19.996

Table 3.1e Case 3 Gaussian fitting results, start planes 1 & 2, all impacts combined

Case 3 5/8" Nut					
Fluid Velocity 5.3 m/s					
IKE (% FV)	Start Plane	Center (in)	Normalization Constant (-)	σ_x (%TS)	σ_y (%TS)
0	1	0.564	0.229	6.748	19.947
1	1	0.571	0.238	6.298	20.072
2	1	0.580	0.215	7.265	20.002
3	1	0.639	0.208	7.348	19.982
4	1	0.704	0.192	7.908	19.971
5	1	0.744	0.154	10.449	20.006
6	1	0.763	0.139	12.037	19.994
7	1	0.804	0.114	15.608	19.995
8	1	0.909	0.118	14.128	20.001
9	1	1.047	0.138	10.719	20.001
10	1	1.097	0.147	9.751	19.988
0	2	0.594	0.204	7.719	20.015
1	2	0.544	0.216	7.394	20.012
2	2	0.572	0.221	7.074	19.934
3	2	0.597	0.204	7.696	20.057
4	2	0.579	0.182	9.146	20.036
5	2	0.655	0.158	10.667	19.984
6	2	0.573	0.133	14.226	20.125
7	2	0.721	0.132	13.149	20.020
8	2	0.844	0.162	8.071	22.238
9	2	0.983	0.162	8.870	20.001
10	2	0.939	0.167	8.640	20.027

Table 3.1f Case 3 Gaussian fitting results, start planes 3 & 4, all impacts combined

Case 3 5/8" Nut					
Fluid Velocity 5.3 m/s					
IKE (% FV)	Start Plane	Center (in)	Normalization Constant (-)	σ_x (%TS)	σ_y (%TS)
0	3	0.000	0.274	13.899	13.899
1	3	0.012	0.230	15.011	15.235
2	3	0.113	0.209	11.538	20.001
3	3	0.484	0.211	8.020	19.997
4	3	0.494	0.193	9.015	19.986
5	3	0.352	0.172	11.902	19.988
6	3	0.129	0.144	17.021	19.997
7	3	0.363	0.140	14.435	20.918
8	3	0.694	0.153	10.935	20.008
9	3	0.662	0.151	11.320	19.992
10	3	0.522	0.143	13.391	20.007
0	4	0.253	0.174	12.663	19.941
1	4	0.000	0.190	16.715	16.715
2	4	0.000	0.189	16.727	16.727
3	4	0.451	0.177	10.540	20.030
4	4	0.397	0.176	11.097	20.008
5	4	0.248	0.173	12.742	20.035
6	4	0.000	0.186	16.900	16.900
7	4	0.000	0.183	17.001	17.001
8	4	0.000	0.179	17.225	17.225
9	4	0.000	0.177	17.313	17.313
10	4	0.100	0.180	14.723	18.709

Overall fitting results are also given visually in **Figures 3.20** through **3.25**. The movement of the center point as a function of initial kinetic energy is given in **Figures 3.20** through **3.22** for each of the three cases. The standard deviations as a function of initial kinetic energy are given in **Figures 3.23** through **3.25** for each of the three cases. In each figure legend "Plane" stands for Start Plane and "XSP" or "YSP" stand for the X-coordinate or Y-coordinate standard deviation from the corresponding Start Plane. The axes are scaled such that each of the three cases is directly comparable.

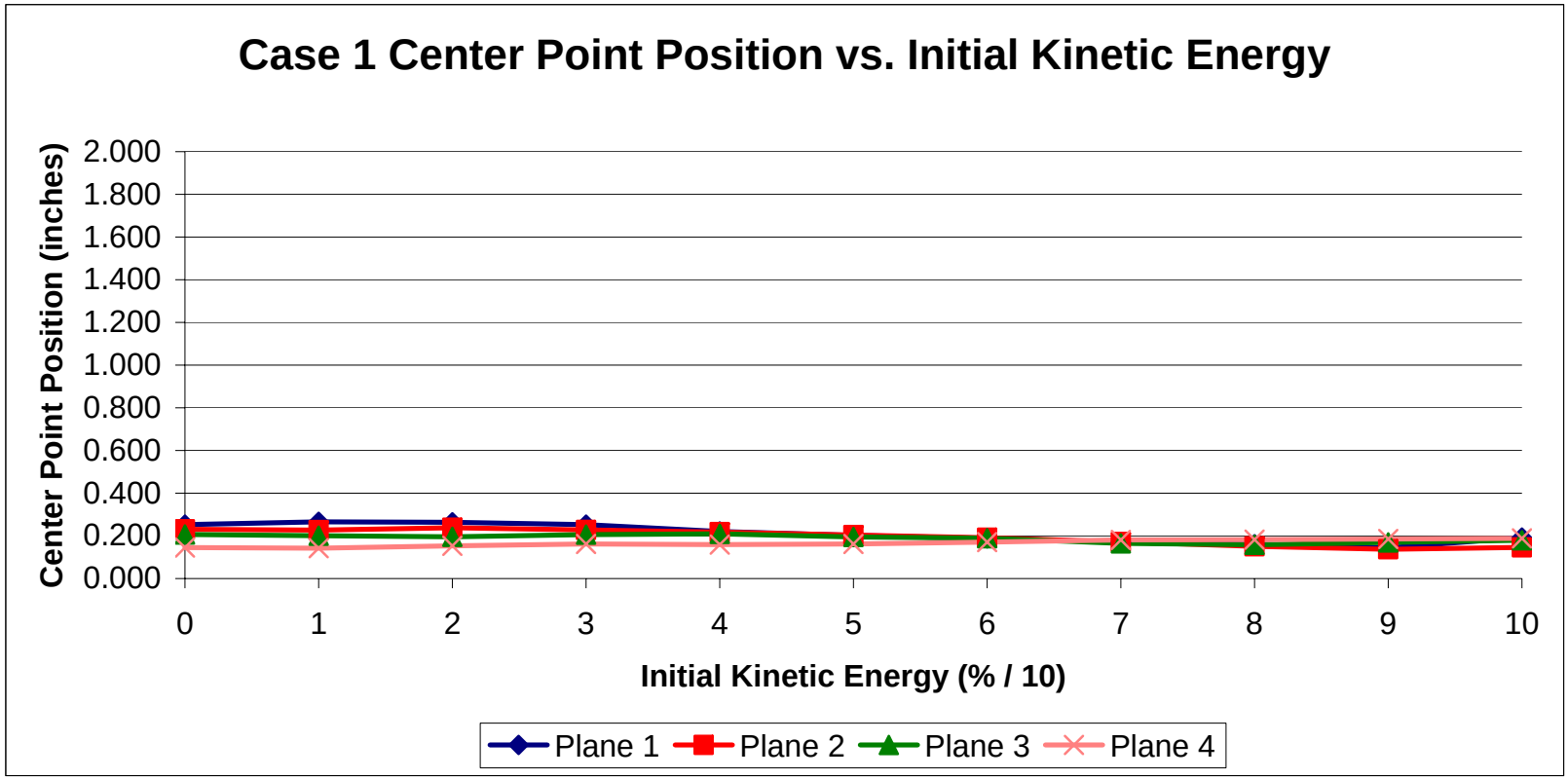

Figure 3.20 Case 1, center point position vs. initial kinetic energy

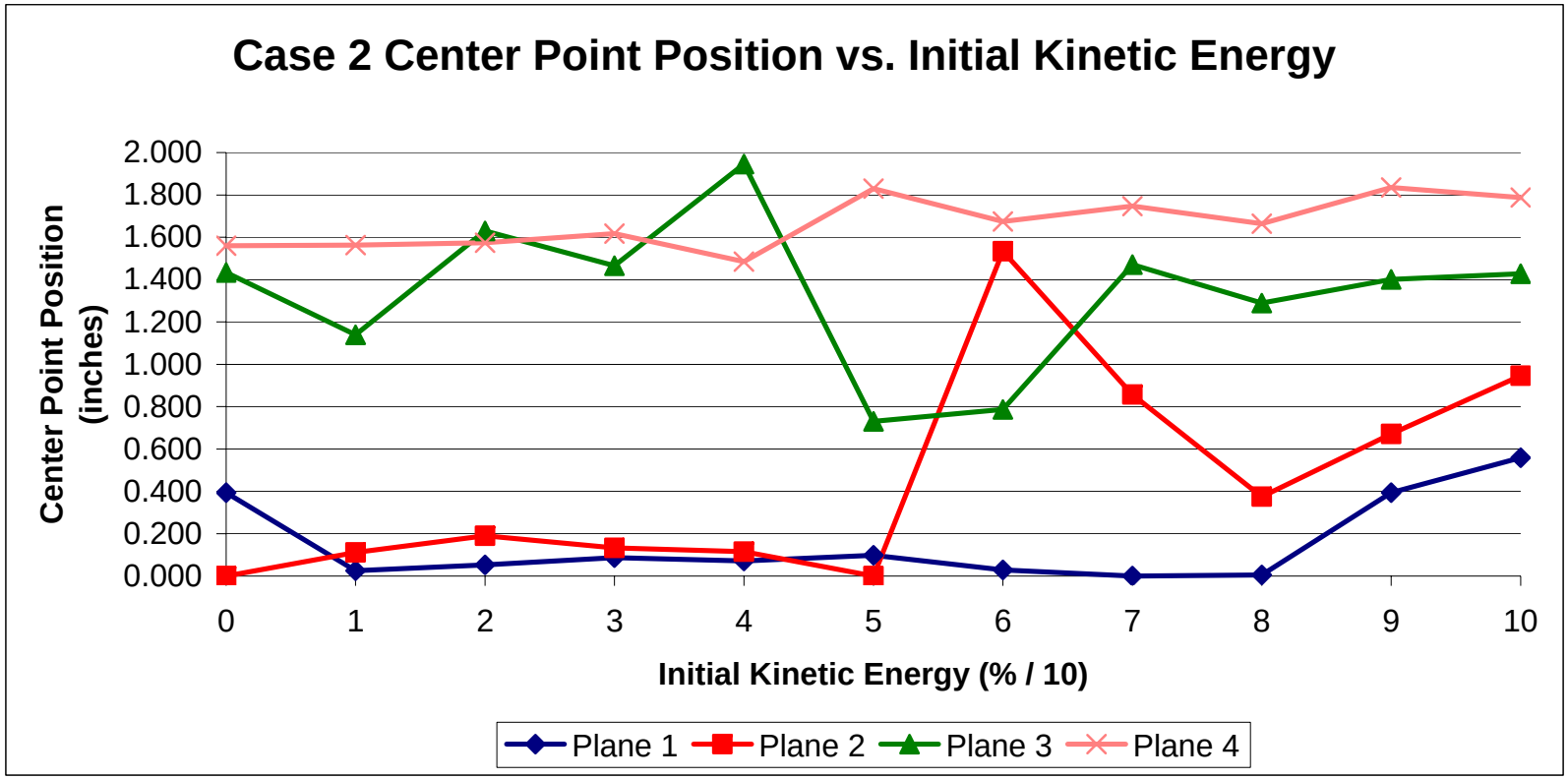

Figure 3.21 Case 2, center point position vs. initial kinetic energy

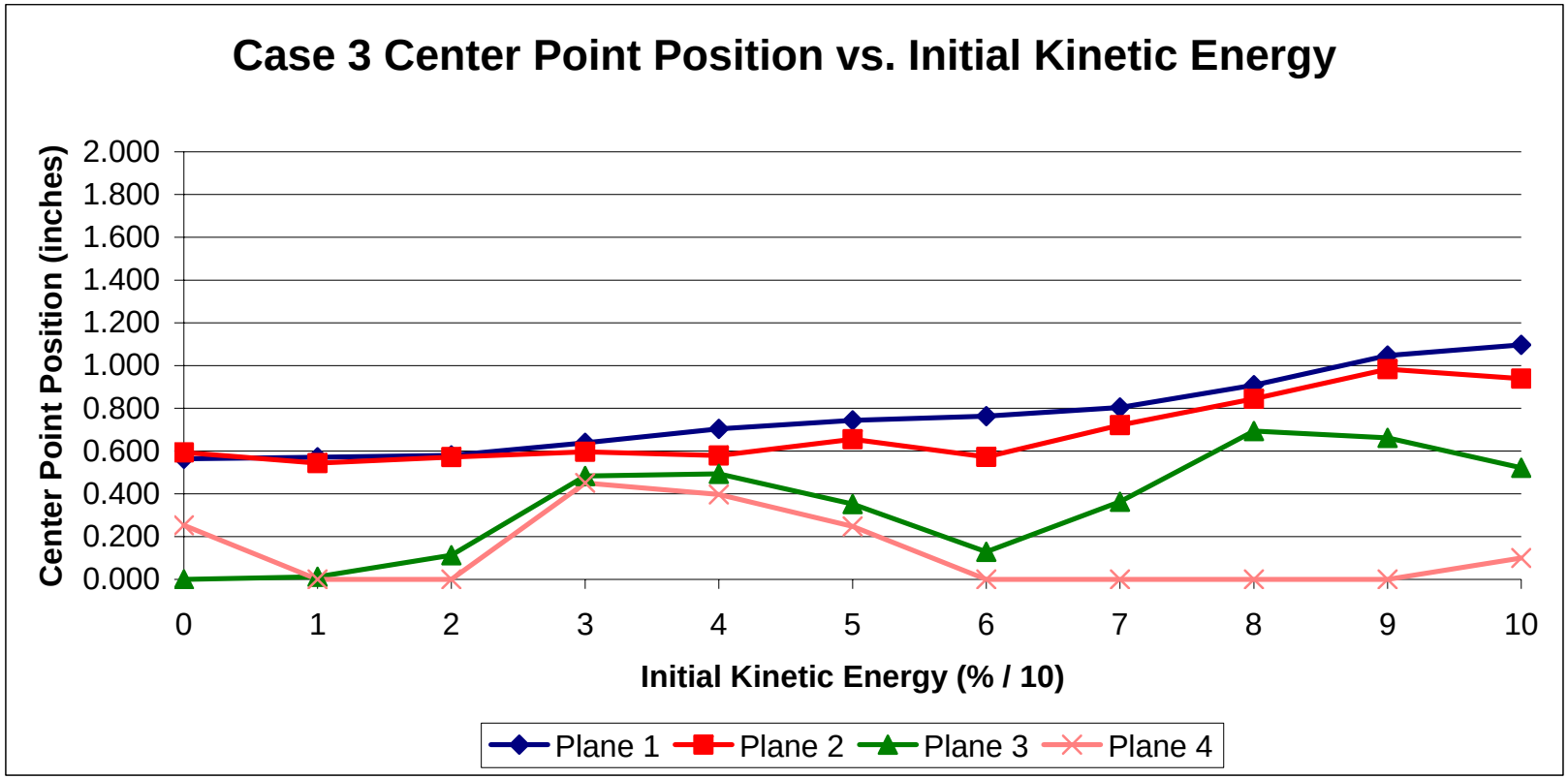

Figure 3.22 Case 3, center point position vs. initial kinetic energy

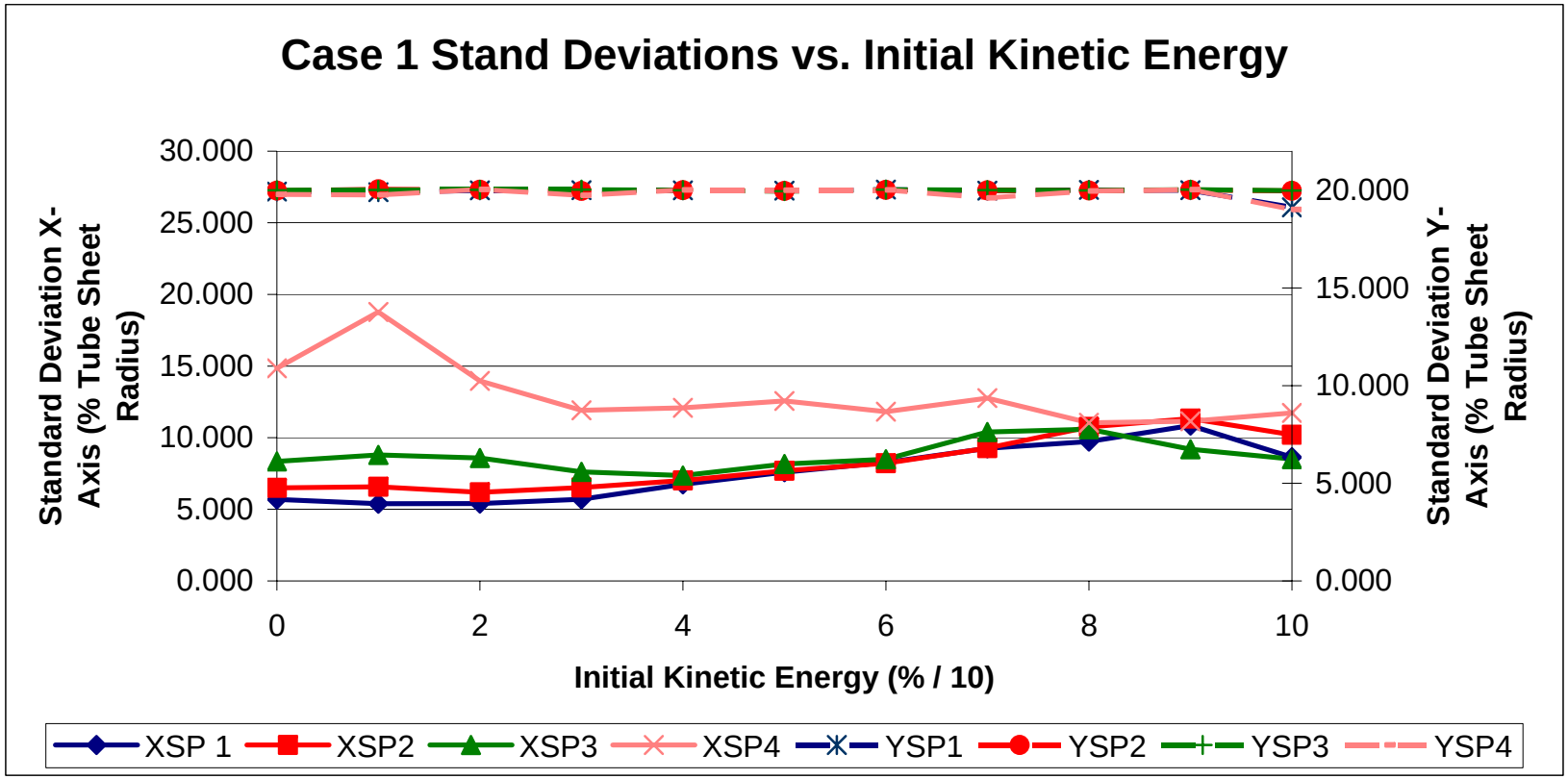

Figure 3.23 Case 1, Gaussian standard deviations vs. initial kinetic energy

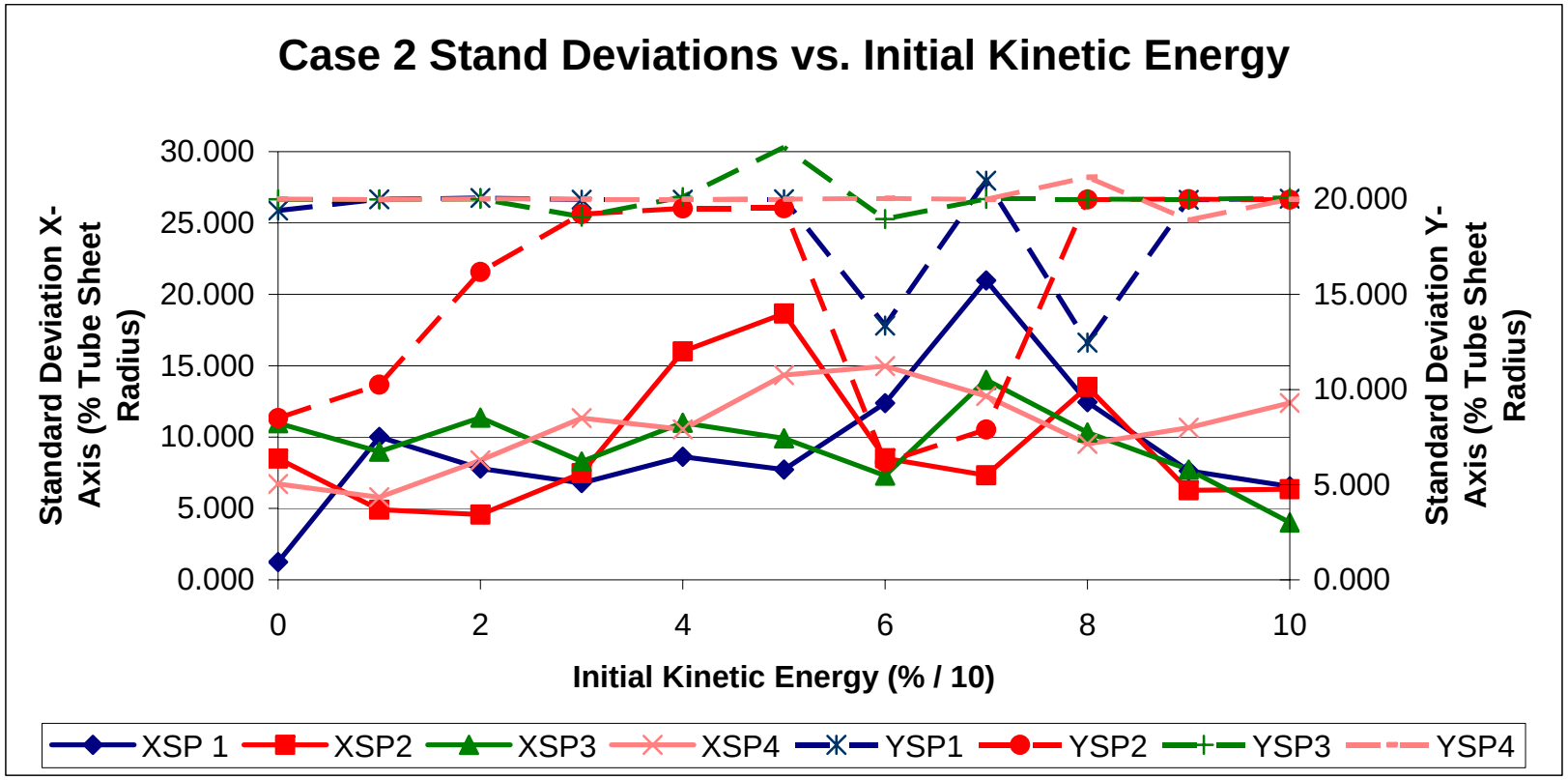

Figure 3.24 Case 2, Gaussian standard deviations vs. initial kinetic energy

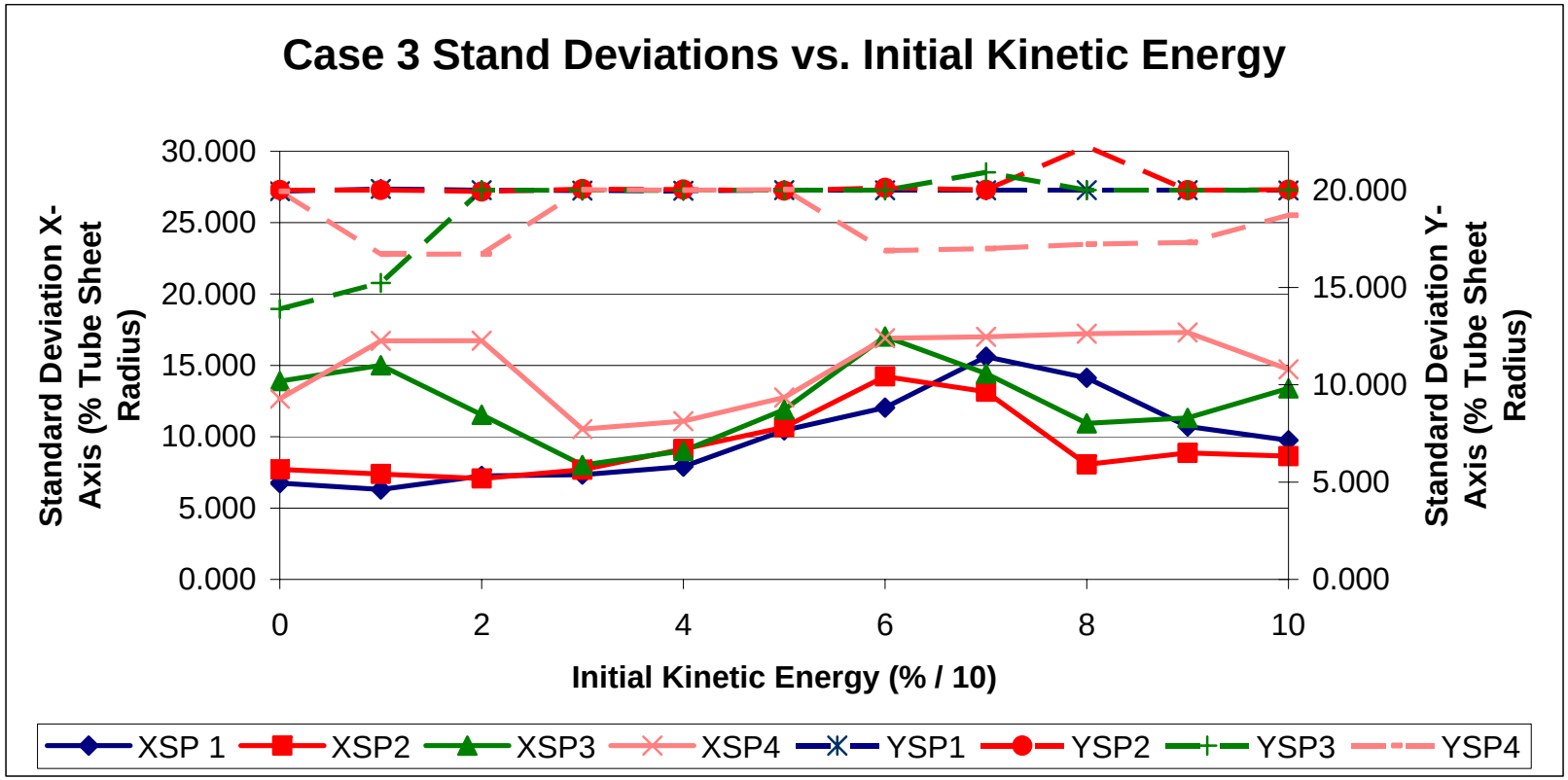

Figure 3.25 Case 3, Gaussian standard deviations vs. initial kinetic energy

3.2 Full Scale Simulation Results

Full scale simulations were carried out for all 28 parts while varying the fluid temperature, initial starting location and initial kinetic energy. Simulations were run looking specifically at the spatial and energetic distributions corresponding to the 1^{st}, 2^{nd} through 5^{th}, and beyond 5^{th} impacts. The run parameters were as follows:

- All 28 Parts were simulated
- Fluid inlet velocity was 26 ft/s
- Fluid temperatures were 68^0F and 614^0F at 2250 psia
- Maximum number of tube sheet impacts was 10,000 or 25,000 (see below)
- Maximum number of time steps at 1.0E-03 seconds was 200,000,000
- Initial kinetic energy of the part ranged from 0% to 100% of the surrounding fluid velocity in increments of 10%
- Initial starting locations included all four start planes in **Figure 2.17b**

Two cases were considered. Case 1 focused on the first five impacts on the tube sheet. Once five impacts had occurred that particular history was terminated and the next part was initiated at the given starting parameters. Ten thousand tube sheet impacts were recorded for this case. Case 2 focused on the long term behavior of the part. The first five impacts were ignored in the results and the part was allowed to continue to move about the system until the maximum number of collisions was reached, time was up or the simulation experienced a 'stuck' part in which case a new history was begun. This case recorded 25,000 tube sheet impacts. In both cases, if after a significant amount of simulation time, the part

was no longer impacting the tube sheet, the simulation was terminated before the maximum simulation time occurred.

In terms of full scale versus scaled results, the distributions did not scale. What was found to be true in the scaled simulations do not hold in the full scale simulations. One major factor in this has to do with the part sizes. From scaled to full scale model, the part sizes remained equivalent. This relative change in size of loose parts to inlet plenum geometry led to different part movement behaviors.

3.2.1 Full Scale Case 1 Results

Case 1 includes the first five impacts of each part history before the part is terminated. The first five impacts are almost always the largest grouping of high energy impacts throughout the simulations and are why significant attention is given here. Generally speaking, once a loose part has been introduced into the inlet plenum, the part is trapped if it cannot fit through the tubes. The particular distributions in this section only describe the spatial and energetic impact distributions for those parts which originate from the hot leg of the primary system. **Section 3.2.2** will go into detail for those distributions once the part is trapped in the inlet plenum.

The following six tables, **Tables 3.2** through **3.7** represent the mean and maximum kinetic energies of the first impact as well as the second through fifth impacts for temperatures of 68^0F and 614^0F for all loose parts initially located at start plane 1 for initial kinetic energies of 0, 50 and 100%. There were a total of 10,000 hits per simulation on the tube sheet implying 2,000 first impact hits and 8,000 second through fifth impact hits. Note that hyphens indicate no hits occurred on the tube sheet for that particular simulation. Also, if

the loose part managed to settle out or get 'stuck', then the number of first impacts may increase to reflect this.

The six figures beyond the table represent a graphical illustration of the same data. In this case, data from all initial kinetic energies (0% through 100%) are depicted. Mean values of the impact kinetic energies are represented by the bar graphs while the maximums are represented as triangles or diamonds. The diamonds correspond to the first impact while the triangles correspond to the second through fifth impacts. Bar colors match up with the appropriate data point colors so that the mean and max of the same simulation are the same color.

Some observations include that the maximum of the mean impact kinetic energies was not necessarily the heaviest part in each class. Notably for the sphere, bolt #2, cylinder and rectangular bar classes it was 3rd or 4th heaviest in the part class. The maximum of the max impact kinetic energies was dominated by the heaviest loose parts in each class. The impact kinetic energy for both max and mean values remained relatively invariant to the initial kinetic energy of the part. Exceptions include the sphere and bolt #2 classes where the max first impacts of the heaviest part in the class did have notable variations. In general, there was a slight downward trend in mean impact kinetic energy as a function of initial kinetic energy, if the parts made it to the tube sheet. This means that the part with the most momentum will likely not impart its full energy onto the tube sheet. Most likely, the part impacts with the plenum divide first before hitting the tube sheet because its momentum does not allow it to continue on a streamline path to the tube sheet directly. A part with less mass or momentum would be more likely to impart more energy initially on the tube sheet.

Table 3.2 Mean and maximum impact kinetic energies for sphere class; 1st – 5th impacts

Start Plane 1 (Energy in Joules)			Fluid Temperature: 68 F				Fluid Temperature: 614 F			
			First Impact (2000 hits)		2nd - 5th Impacts (8000 hits)		First Impact (2000 hits)		2nd - 5th Impacts (8000 hits)	
Part # Part Type	Size	IKE (%)	Mean KE	Max KE	Mean KE	Max KE	Mean KE	Max KE	Mean KE	Max KE
1 Sphere	1/2''									
		0	0.050260	0.148348	0.016154	0.132723	0.021970	0.128637	0.010700	0.119071
		50	0.049726	0.148245	0.014677	0.131616	0.021796	0.122081	0.010501	0.093206
		100	0.050675	0.148245	0.015338	0.131707	0.021255	0.126961	0.008622	0.093372
2 Sphere	3/4''									
		0	0.126834	0.439800	0.054247	0.410231	-	-	-	-
		50	0.127299	0.440357	0.054062	0.412011	-	-	-	-
		100	0.130510	0.439602	0.059192	0.412597	-	-	-	-
3 Sphere	9/10''									
		0	0.264361	0.703989	0.098760	0.738398	-	-	-	-
		50	0.265924	0.707366	0.096961	0.731793	-	-	-	-
		100	0.265776	0.707935	0.103739	0.725233	-	-	-	-
4 Sphere	1''									
		0	0.301351	0.824778	0.129784	0.891541	-	-	-	-
		50	0.297339	0.839459	0.131529	0.894031	-	-	-	-
		100	0.313492	0.836947	0.148999	0.901839	-	-	-	-
5 Sphere	3/2''									
		0	0.206142	1.212410	0.112113	2.396261	-	-	-	-
		50	0.206123	2.145491	0.111311	2.431100	-	-	-	-
		100	0.210818	1.665081	0.113203	2.501051	-	-	-	-

Table 3.3 Mean and maximum impact kinetic energies for hex bolt #1 class; 1^{st} – 5^{th} impacts

Start Plane 1 (Energy in Joules)				Fluid Temperature: 68 F				Fluid Temperature: 614 F			
				First Impact (2000 hits)		2nd - 5th Impacts (8000 hits)		First Impact (2000 hits)		2nd - 5th Impacts (8000 hits)	
Part #	Part Type	Size	IKE (%)	Mean KE	Max KE	Mean KE	Max KE	Mean KE	Max KE	Mean KE	Max KE
6	Hex Bolt Type 1	1/2''									
			0	0.190835	0.446702	0.104895	0.415797	-	-	-	-
			50	0.190017	0.448235	0.102447	0.415573	-	-	-	-
			100	0.182656	0.444311	0.091761	0.414642	-	-	-	-
7	Hex Bolt Type 1	5/8''									
			0	0.239456	0.810605	0.075829	0.733175	-	-	-	-
			50	0.245517	0.807931	0.080738	0.742939	-	-	-	-
			100	0.259773	0.809951	0.094171	0.732434	-	-	-	-
8	Hex Bolt Type 1	3/4''									
			0	0.386987	1.163191	0.151431	1.158431	-	-	-	-
			50	0.391132	1.140751	0.147189	1.158661	-	-	-	-
			100	0.378511	1.179071	0.158818	1.157281	-	-	-	-
9	Hex Bolt Type 1	7/8''									
			0	0.614414	1.701121	0.372831	1.765091	-	-	-	-
			50	0.604736	1.693531	0.356251	1.758810	-	-	-	-
			100	0.549189	1.716671	0.292908	1.752771	-	-	-	-
10	Hex Bolt Type 1	1''									
			0	0.583232	2.545810	0.175712	2.530351	-	-	-	-
			50	0.584286	2.535121	0.194025	2.538041	-	-	-	-
			100	0.569558	2.543791	0.152345	2.530191	-	-	-	-

Table 3.4 Mean and maximum impact kinetic energies for hex bolt #2 class; 1^{st} – 5^{th} impacts

Start Plane 1 (Energy in Joules)			Fluid Temperature: 68 F				Fluid Temperature: 614 F			
			First Impact (2000 hits)		2nd - 5th Impacts (8000 hits)		First Impact (2000 hits)		2nd - 5th Impacts (8000 hits)	
Part # Part Type	Size	IKE (%)	Mean KE	Max KE	Mean KE	Max KE	Mean KE	Max KE	Mean KE	Max KE
11 Hex Bolt Type 2	1/2''									
		0	0.148361	0.522431	0.050643	0.492404	-	-	-	-
		50	0.140302	0.526551	0.048060	0.491945	-	-	-	-
		100	0.155595	0.525627	0.052916	0.490853	-	-	-	-
12 Hex Bolt Type 2	5/8''									
		0	0.277641	0.834952	0.094011	0.847735	-	-	-	-
		50	0.277372	0.835656	0.096234	0.847671	-	-	-	-
		100	0.263366	0.837704	0.095125	0.848014	-	-	-	-
13 Hex Bolt Type 2	3/4''									
		0	0.398261	1.375722	0.157251	1.406341	-	-	-	-
		50	0.404446	1.383175	0.157769	1.386981	-	-	-	-
		100	0.380096	1.364962	0.132466	1.427831	-	-	-	-
14 Hex Bolt Type 2	7/8''									
		0	0.456292	2.056903	0.186474	2.045591	-	-	-	-
		50	0.463866	2.052362	0.193638	2.046710	-	-	-	-
		100	0.313797	2.065722	0.136329	2.033521	-	-	-	-
15 Hex Bolt Type 2	1''									
		0	0.258826	2.607684	0.244634	3.094831	-	-	-	-
		50	0.260089	3.061803	0.245512	3.087241	-	-	-	-
		100	0.256657	2.972454	0.284507	3.090161	-	-	-	-

Table 3.5 Mean and maximum impact kinetic energies for hex nut class; 1^{st} – 5^{th} impacts

Start Plane 1 (Energy in Joules)			Fluid Temperature: 68 F				Fluid Temperature: 614 F			
			First Impact (2000 hits)		2nd - 5th Impacts (8000 hits)		First Impact (2000 hits)		2nd - 5th Impacts (8000 hits)	
Part # Part Type	Size	IKE (%)	Mean KE	Max KE	Mean KE	Max KE	Mean KE	Max KE	Mean KE	Max KE
16 Hex Nut	1/2''									
		0	0.093008	0.287772	0.031000	0.258134	-	-	-	-
		50	0.095098	0.287729	0.034549	0.258489	0.017354	0.029814	0.015471	0.038055
		100	0.094992	0.287744	0.034264	0.255802	0.017379	0.030482	0.015269	0.038083
17 Hex Nut	5/8''									
		0	0.146674	0.508538	0.063461	0.455822	-	-	-	-
		50	0.144144	0.508047	0.061000	0.456821	-	-	-	-
		100	0.144791	0.507885	0.063327	0.458671	-	-	-	-
18 Hex Nut	3/4''									
		0	0.171508	0.743226	0.052814	0.734651	-	-	-	-
		50	0.177214	0.737008	0.056397	0.740453	-	-	-	-
		100	0.185472	0.759249	0.060546	0.751941	-	-	-	-
19 Hex Nut	7/8''									
		0	0.232456	1.042996	0.068094	1.059331	-	-	-	-
		50	0.227665	1.048387	0.071440	1.059331	-	-	-	-
		100	0.239271	1.045078	0.073259	1.057281	-	-	-	-
20 Hex Nut	1''									
		0	0.401412	1.559531	0.162053	1.572691	-	-	-	-
		50	0.388721	1.527251	0.152379	1.571021	-	-	-	-
		100	0.345271	1.535081	0.128446	1.576651	-	-	-	-

Table 3.6 Mean and maximum impact kinetic energies for cylinder class; 1st – 5th impacts

Start Plane 1 (Energy in Joules)				Fluid Temperature: 68 F				Fluid Temperature: 614 F			
				First Impact (2000 hits)		2nd - 5th Impacts (8000 hits)		First Impact (2000 hits)		2nd - 5th Impacts (8000 hits)	
Part #	Part Type	Size	IKE (%)	Mean KE	Max KE	Mean KE	Max KE	Mean KE	Max KE	Mean KE	Max KE
21	Cylinder	1/2''									
			0	0.126451	0.415936	0.042392	0.398573	-	-	-	-
			50	0.124846	0.416629	0.044539	0.398411	-	-	-	-
			100	0.125141	0.417983	0.043236	0.396812	-	-	-	-
22	Cylinder	3/4''									
			0	0.330786	1.037467	0.142649	1.081331	-	-	-	-
			50	0.338687	1.091844	0.142272	1.079491	-	-	-	-
			100	0.311607	1.037743	0.118861	1.073671	-	-	-	-
23	Cylinder	7/8''									
			0	0.462045	1.620975	0.154763	1.632571	-	-	-	-
			50	0.461071	1.616294	0.163402	1.622411	-	-	-	-
			100	0.418525	1.602472	0.131531	1.613871	-	-	-	-
24	Cylinder	1''									
			0	0.273948	2.318919	0.225481	2.326100	-	-	-	-
			50	0.271066	2.325130	0.231952	2.321161	-	-	-	-
			100	0.255499	2.311067	0.248213	2.326621	-	-	-	-

Table 3.7 Mean and maximum impact kinetic energies for rectangular bar class; 1st – 5th impacts

Start Plane 1 (Energy in Joules)			Fluid Temperature: 68 F				Fluid Temperature: 614 F			
			First Impact (2000 hits)		2nd - 5th Impacts (8000 hits)		First Impact (2000 hits)		2nd - 5th Impacts (8000 hits)	
Part #	Part Type	Size IKE (%)	Mean KE	Max KE	Mean KE	Max KE	Mean KE	Max KE	Mean KE	Max KE
25	Rectangular Bar	1/2''								
		0	0.144620	0.465612	0.051534	0.426586	-	-	-	-
		50	0.139938	0.467745	0.050296	0.426519	-	-	-	-
		100	0.137566	0.468689	0.051200	0.428915	-	-	-	-
26	Rectangular Bar	3/4''								
		0	0.399613	1.359293	0.221281	1.396841	-	-	-	-
		50	0.388145	1.359094	0.213781	1.373691	-	-	-	-
		100	0.359266	1.352680	0.169199	1.346211	-	-	-	-
27	Rectangular Bar	7/8''								
		0	0.432475	2.047449	0.165672	2.109281	-	-	-	-
		50	0.408947	2.048752	0.161759	2.075131	-	-	-	-
		100	0.334867	2.022557	0.120149	2.140371	-	-	-	-
28	Rectangular Bar	1''								
		0	0.388793	2.991558	0.156231	2.940931	-	-	-	-
		50	0.384661	2.999462	0.168057	2.956671	-	-	-	-
		100	0.382486	3.028646	0.159076	2.980171	-	-	-	-

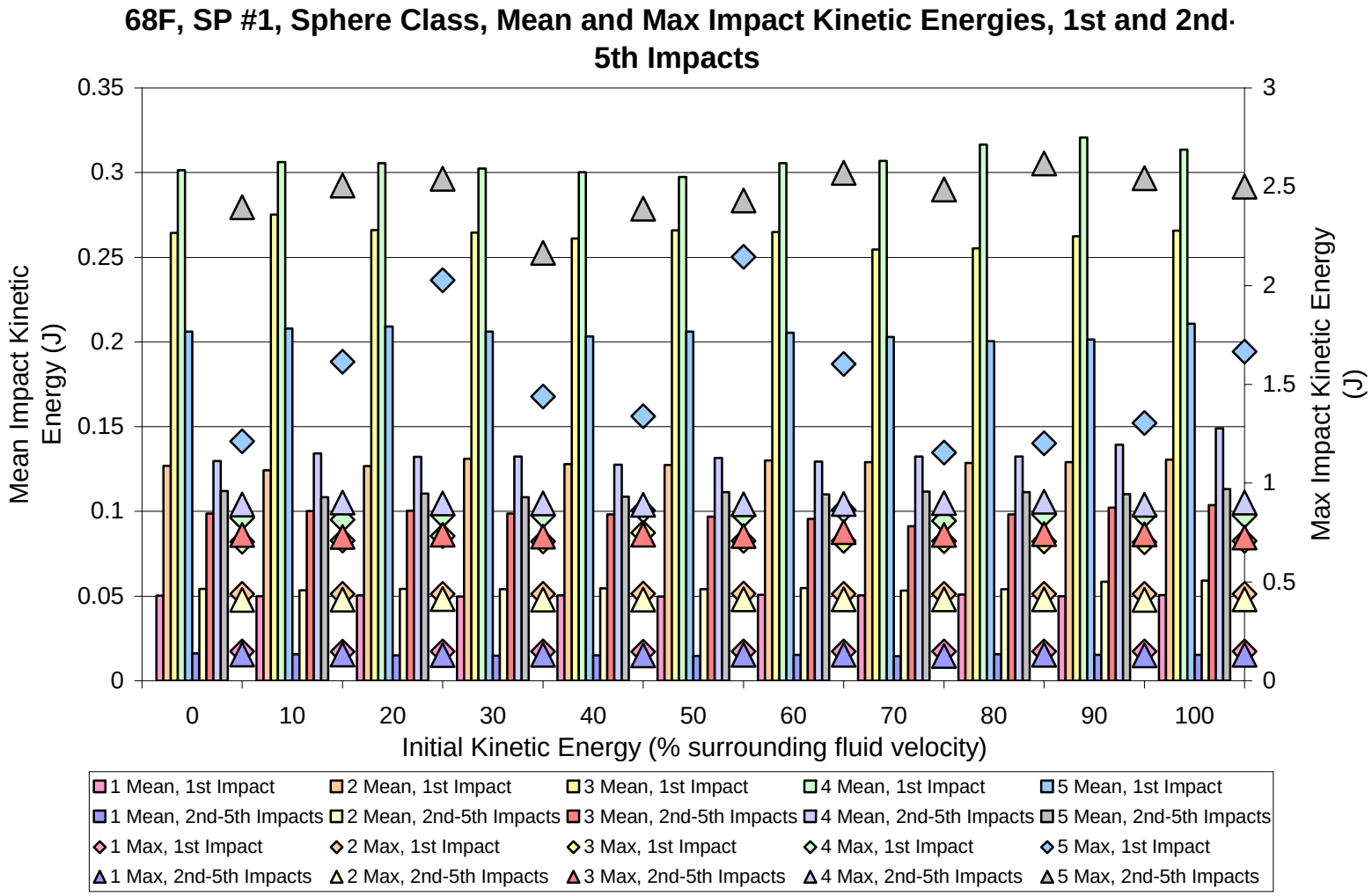

Figure 3.26 Mean and maximum impact kinetic energies for sphere class; 1^{st} – 5^{th} impacts

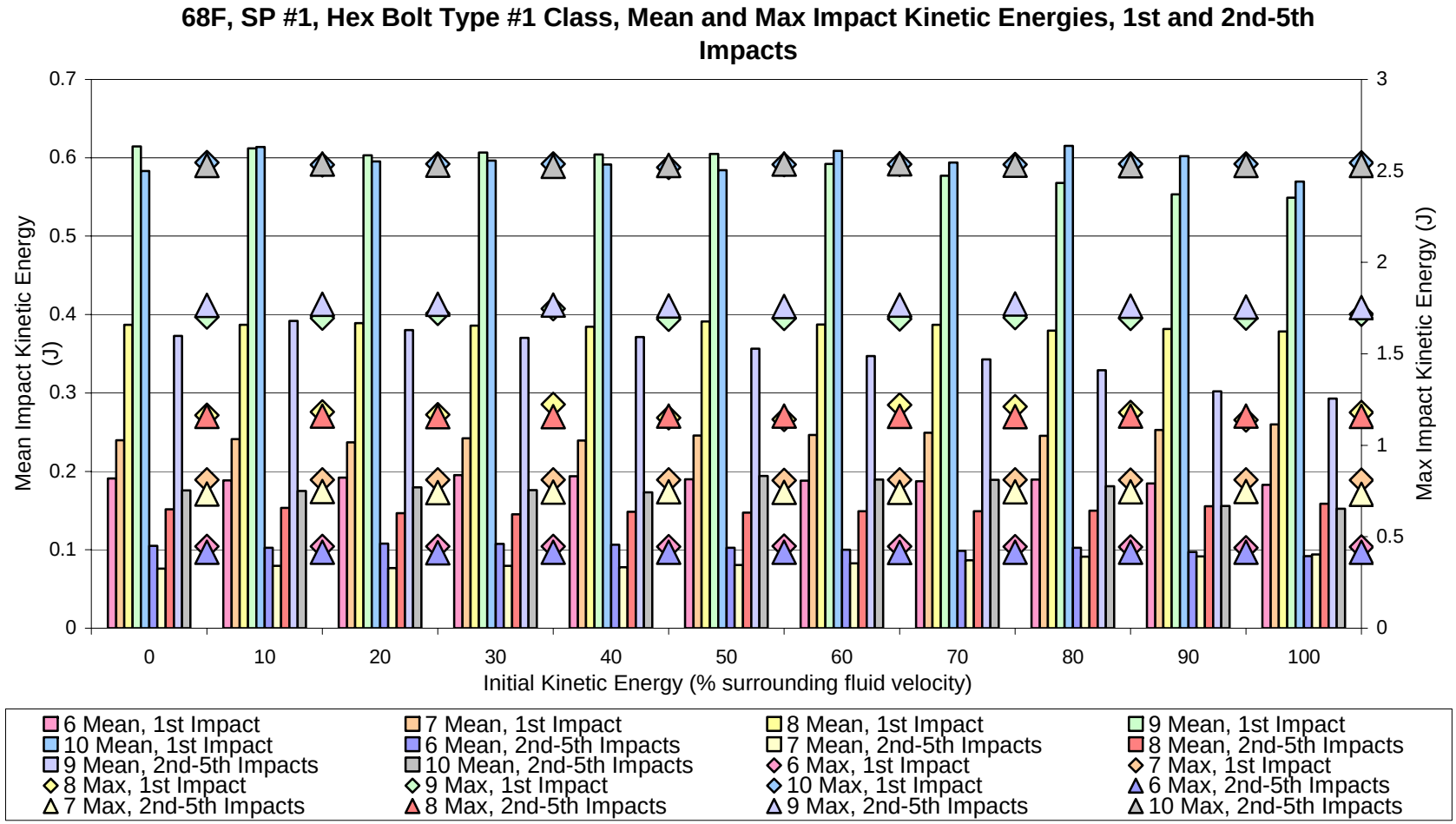

Figure 3.27 Mean and maximum impact kinetic energies for hex bolt type #1 class; 1^{st} – 5^{th} impacts

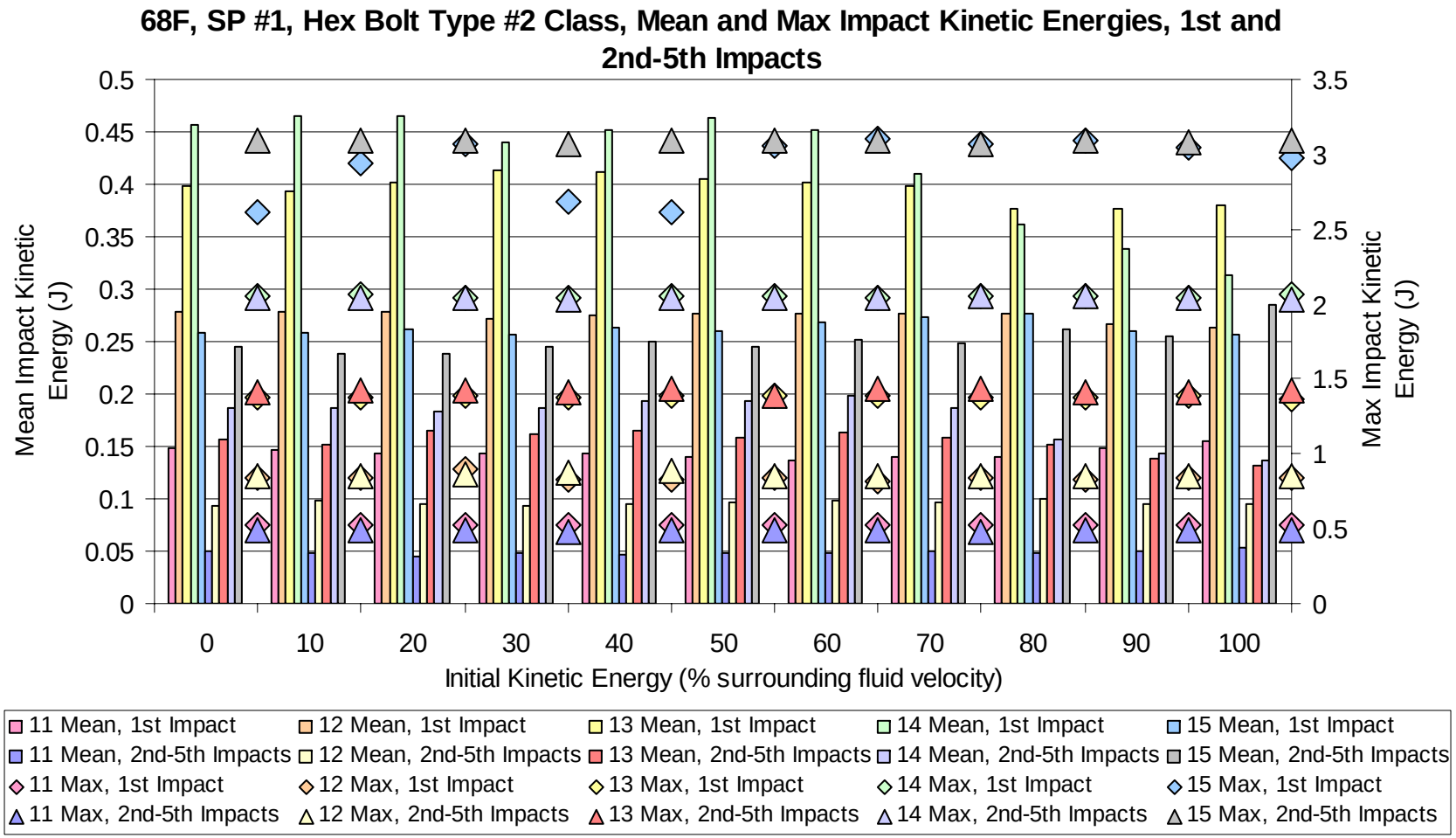

Figure 3.28 Mean and maximum impact kinetic energies for hex bolt type #2 class; 1^{st} – 5^{th} impacts

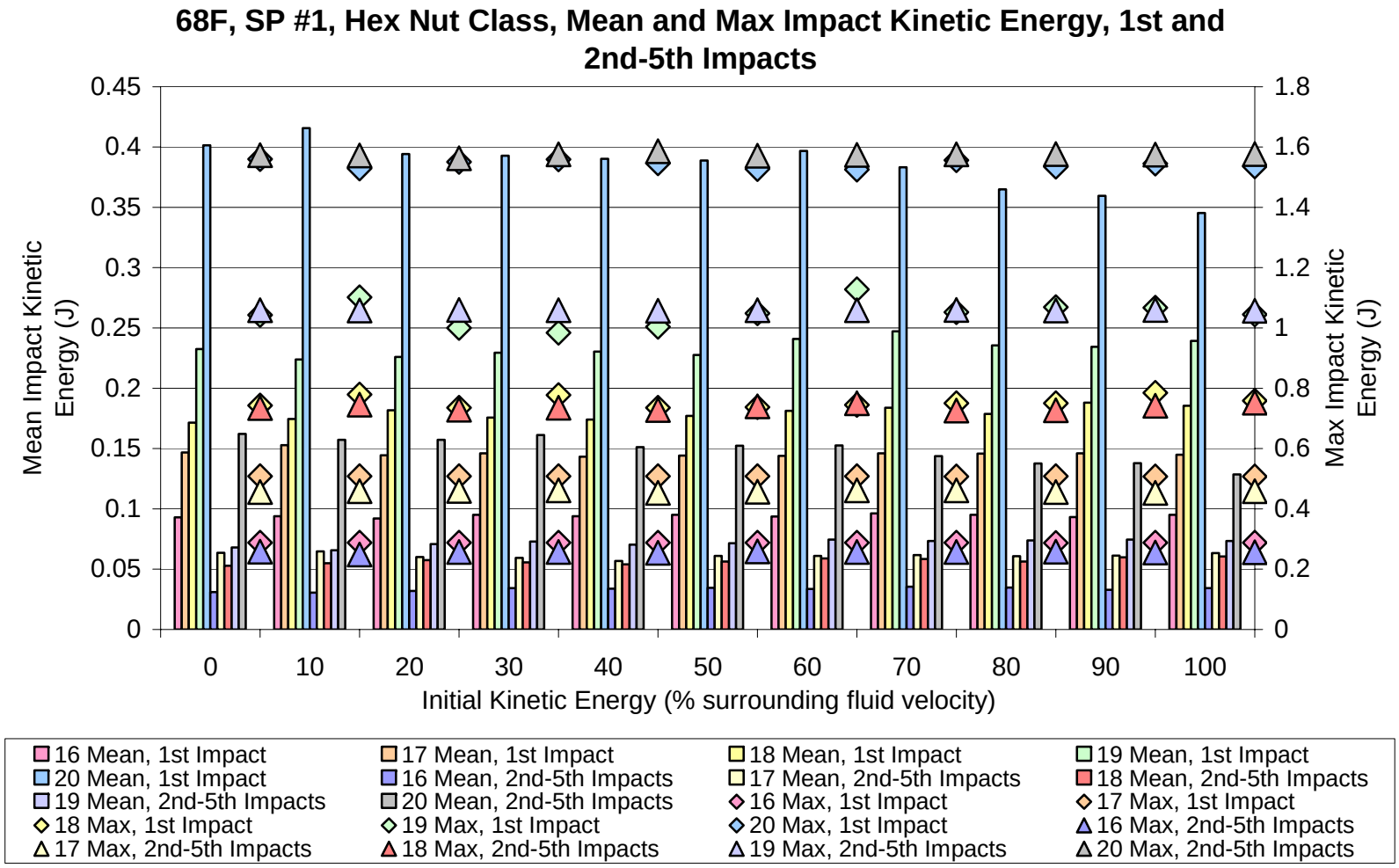

Figure 3.29 Mean and maximum impact kinetic energies for hex nut class; 1^{st} – 5^{th} impacts

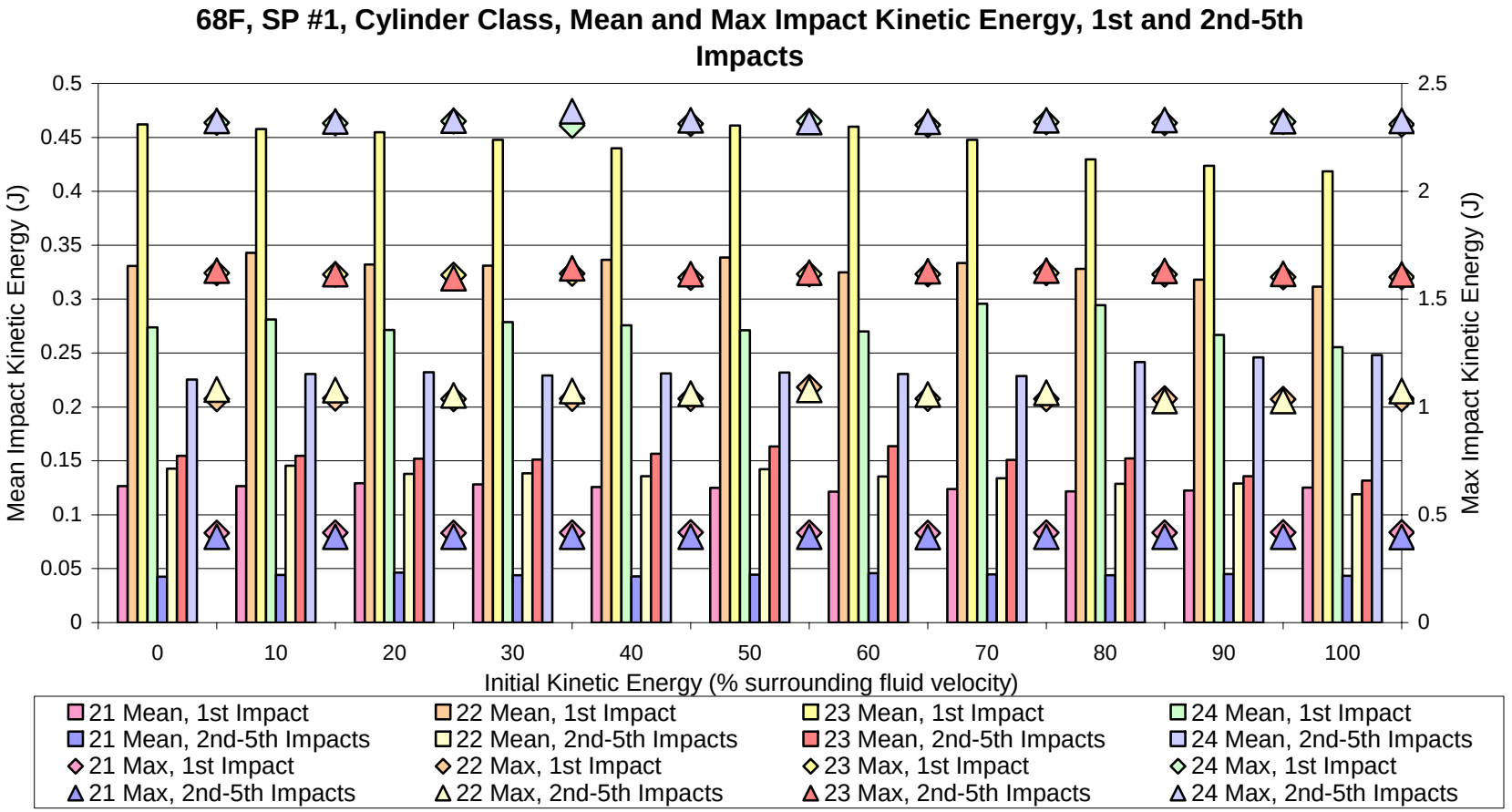

Figure 3.30 Mean and maximum impact kinetic energies for cylinder class; 1^{st} – 5^{th} impacts

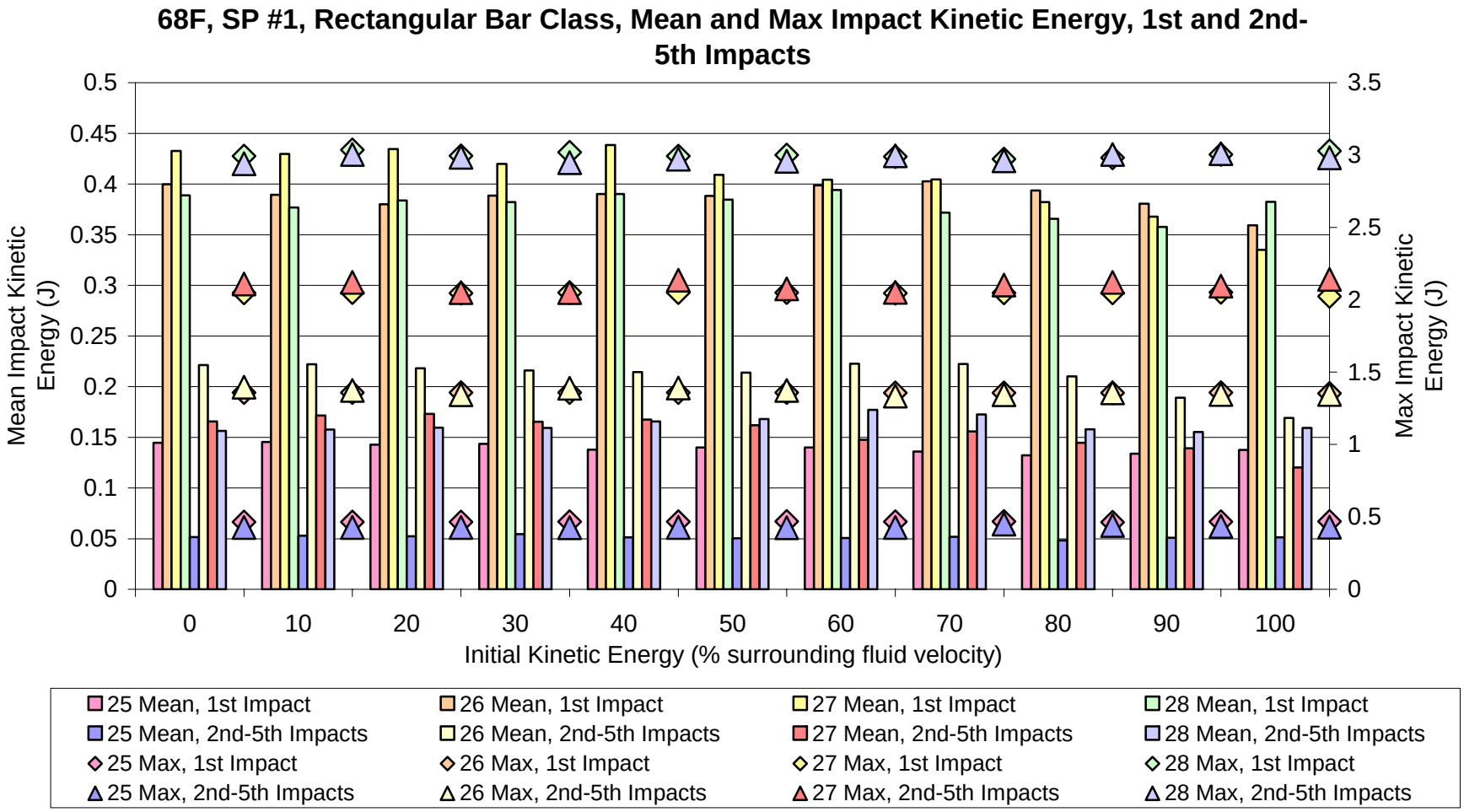

Figure 3.31 Mean and maximum impact kinetic energies for rectangular bar class; 1^{st} – 5^{th} impacts

Interestingly enough, only the lightest of the spheres and hex nuts were able to reach the tube sheet for a fluid temperature of 614^0F. Under these conditions, the viscosity of the fluid was reduced significantly to the point that most of the parts were too heavy for their particular cross section to be lifted all the way to the tube sheet. Behaviors of loose parts in the full scale system showed that most parts had to scale the walls of the plenum in order to position themselves in a manner that would allow them to be launched upwards with enough momentum to make it to the tube sheet. The energies imparted at fluid temperatures of 614^0F were only fractions of the room temperature case but stand to be of most concern since the reactor will remain at hot full power conditions for long periods of time. More analysis will be given to the 614^0F scenario in Case 2 in **Section 3.2.2**.

The following 14 Figures represent the spatial distribution of all five impacts over the course of many histories for the largest and smallest loose parts in each class for initial kinetic energies of 0% and 100% of local fluid velocity. Each color represents a different order impact with the first impact as black, second impact as blue, third impact as red, fourth impact as green and fifth impact as magenta. Each part has a unique distribution that tends to be invariant to initial kinetic energy, as the figures suggest, as well as invariant to starting positions as long as the starting location happens before the 45^0 upward bend in the hot leg. In all cases, as the mass of the part increases, the grouping of impacts tends toward the center flow plume. The lighter parts tend to spread more over the tube sheet surface.

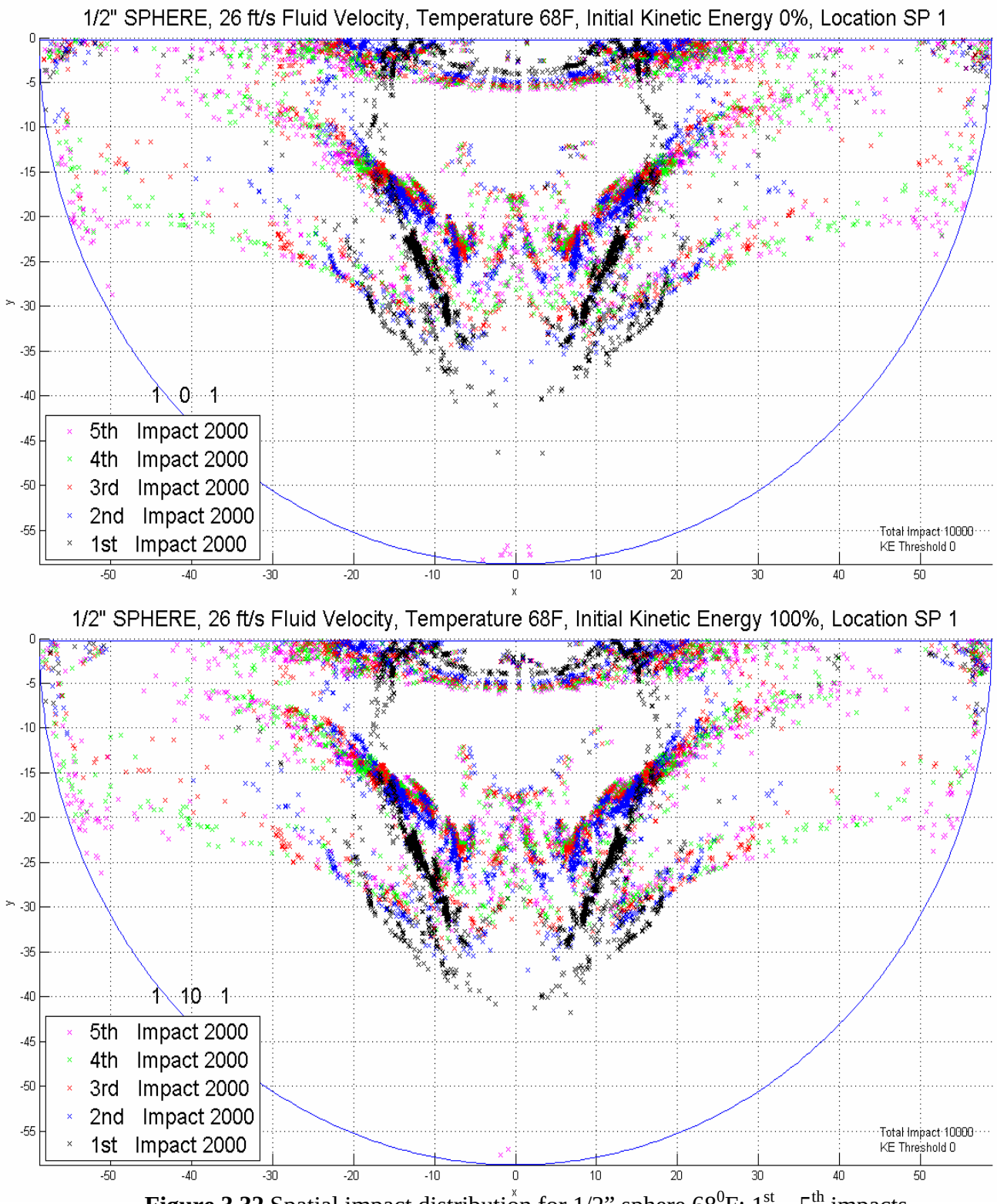

Figure 3.32 Spatial impact distribution for 1/2" sphere 68^0F; 1^{st} – 5^{th} impacts

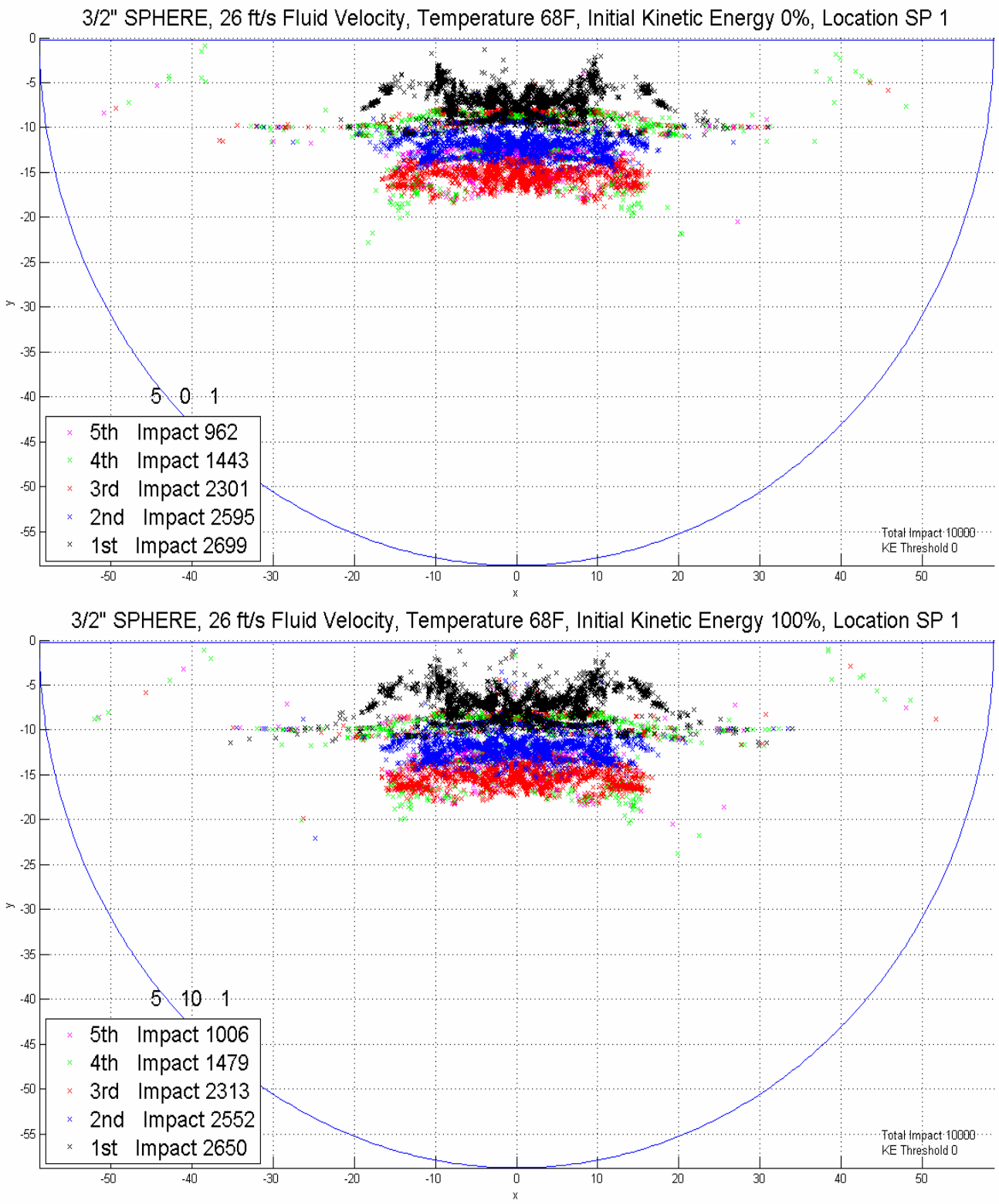

Figure 3.33 Spatial impact distribution for 3/2" sphere 68^0F; 1^{st} – 5^{th} impacts

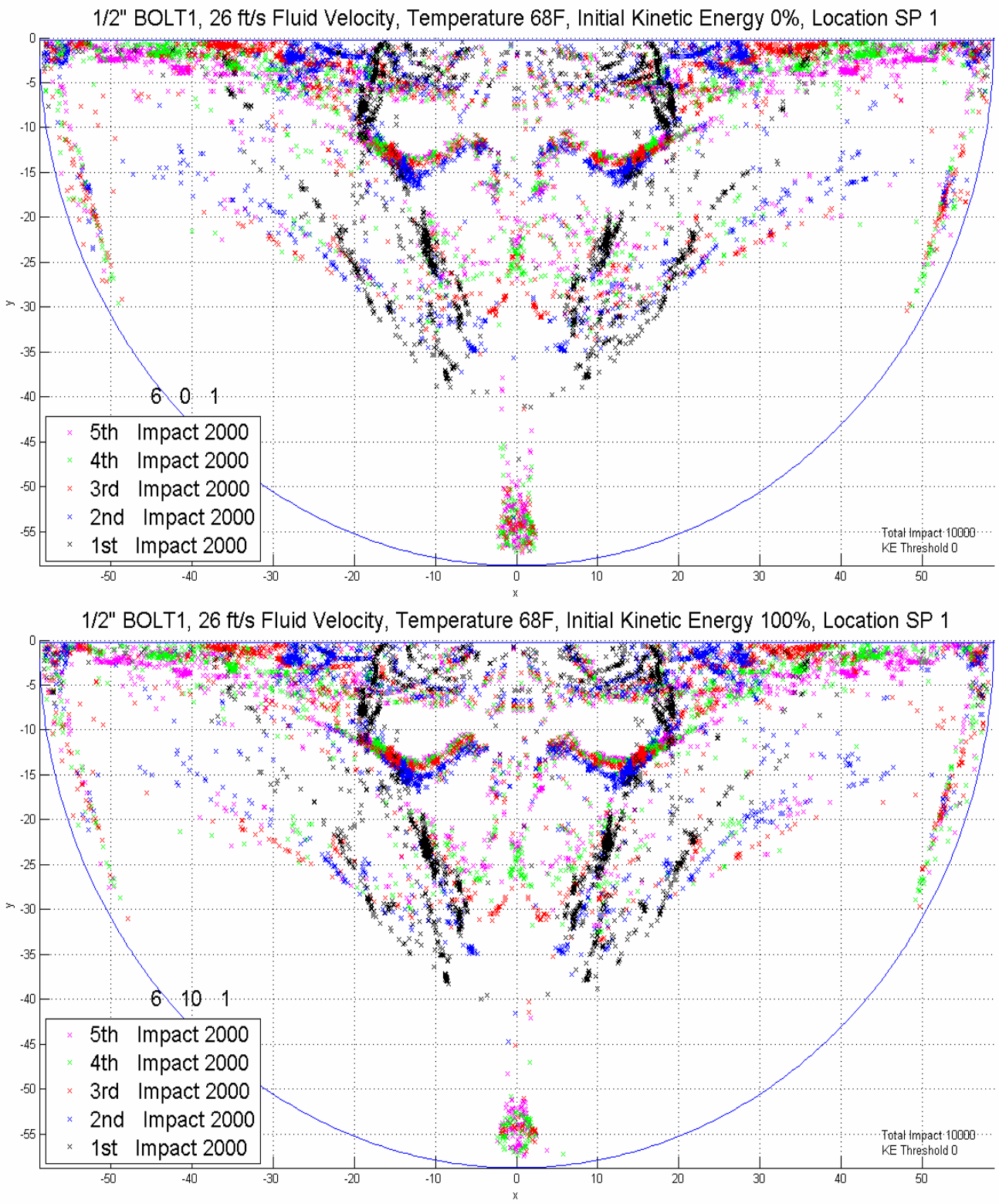

Figure 3.34 Spatial impact distribution for 1/2" hex bolt #1 68^0F; 1^{st} – 5^{th} impacts

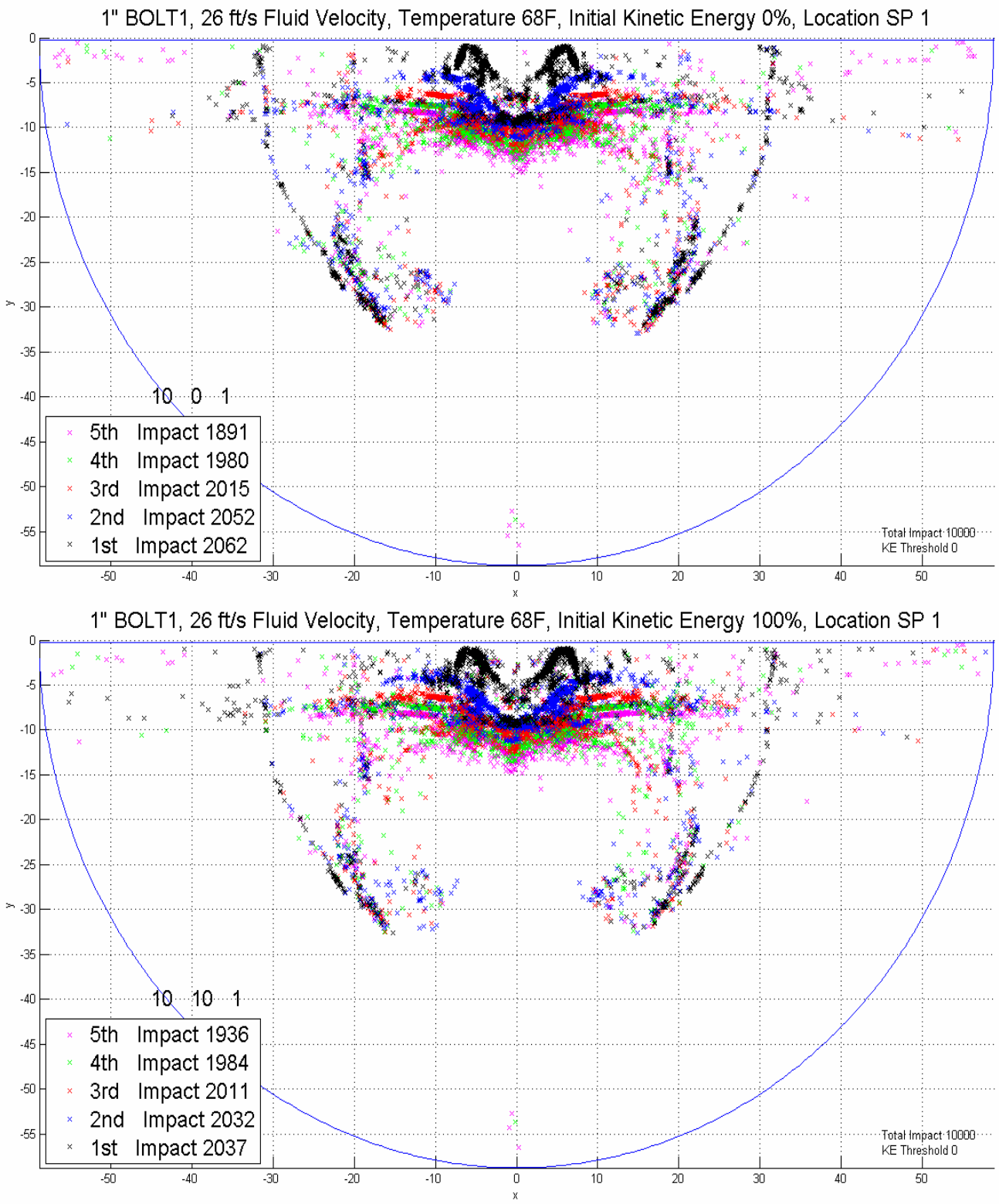

Figure 3.35 Spatial impact distribution for 1" hex bolt #1 68^0F; 1^{st} – 5^{th} impacts

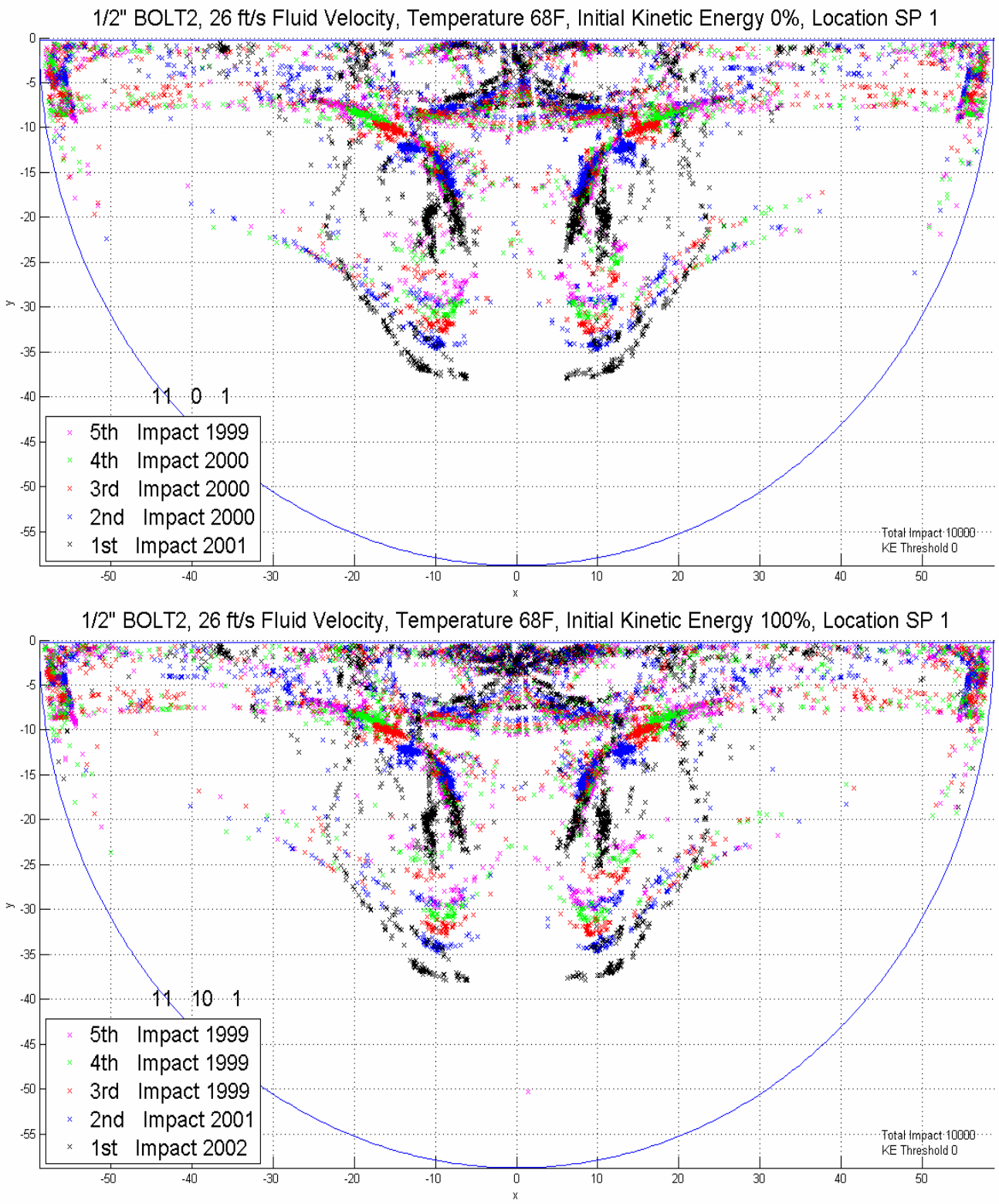

Figure 3.36 Spatial impact distribution for 1/2" hex bolt #2 68^0F; 1^{st} – 5^{th} impacts

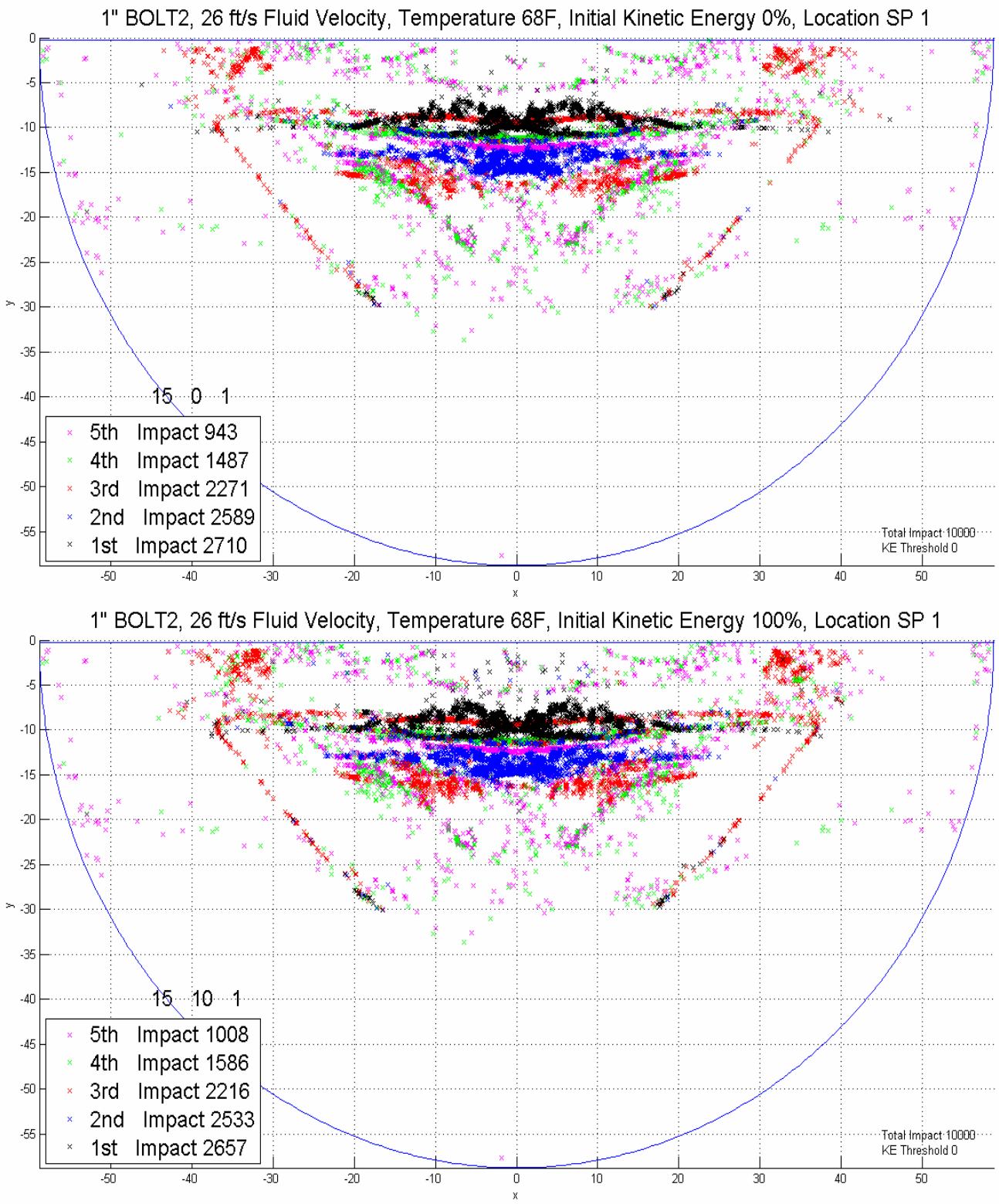

Figure 3.37 Spatial impact distribution for 1" hex bolt #2 68^0F; 1^{st} – 5^{th} impacts

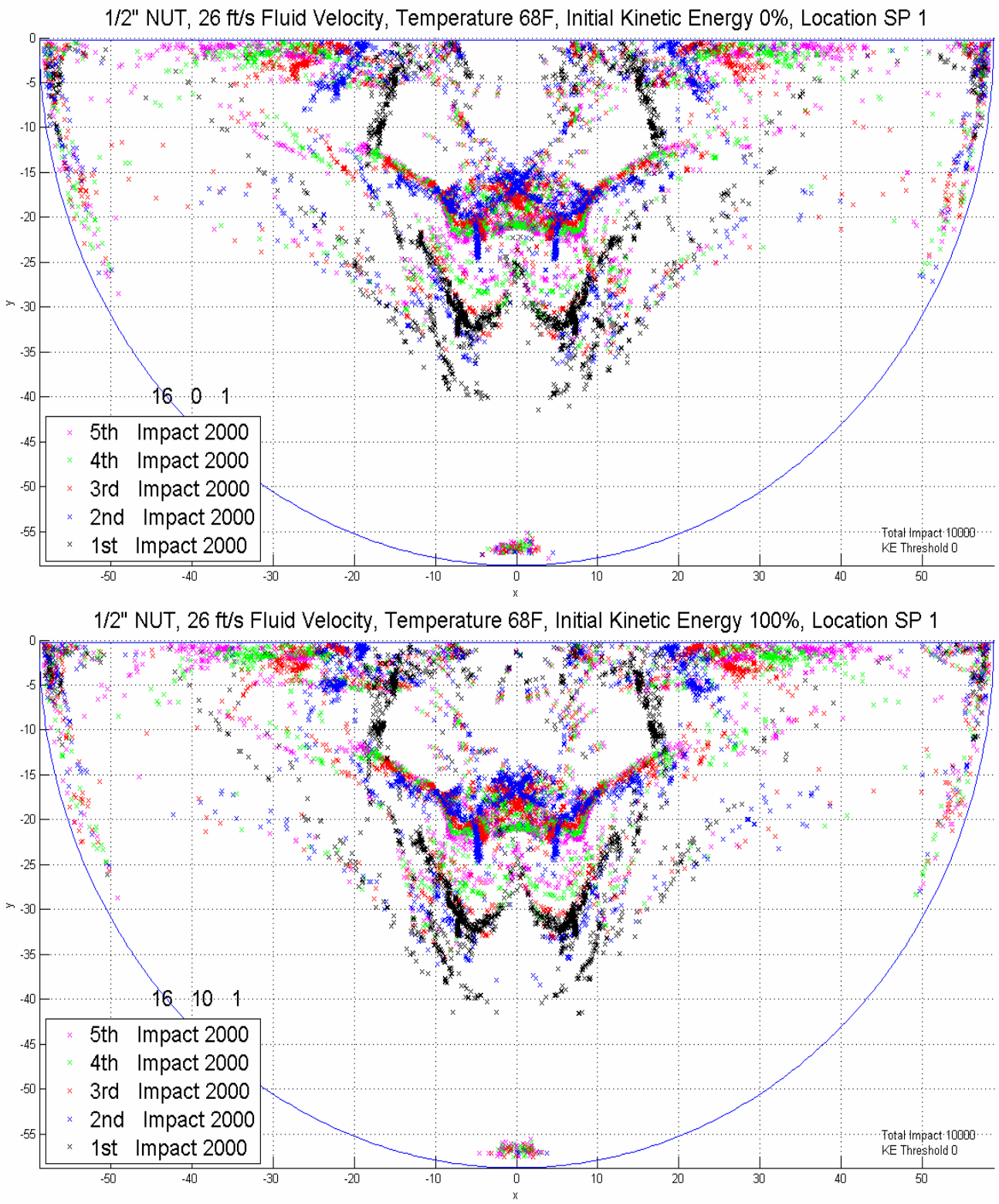

Figure 3.38 Spatial impact distribution for 1/2" hex nut 68^0F; 1^{st} – 5^{th} impacts

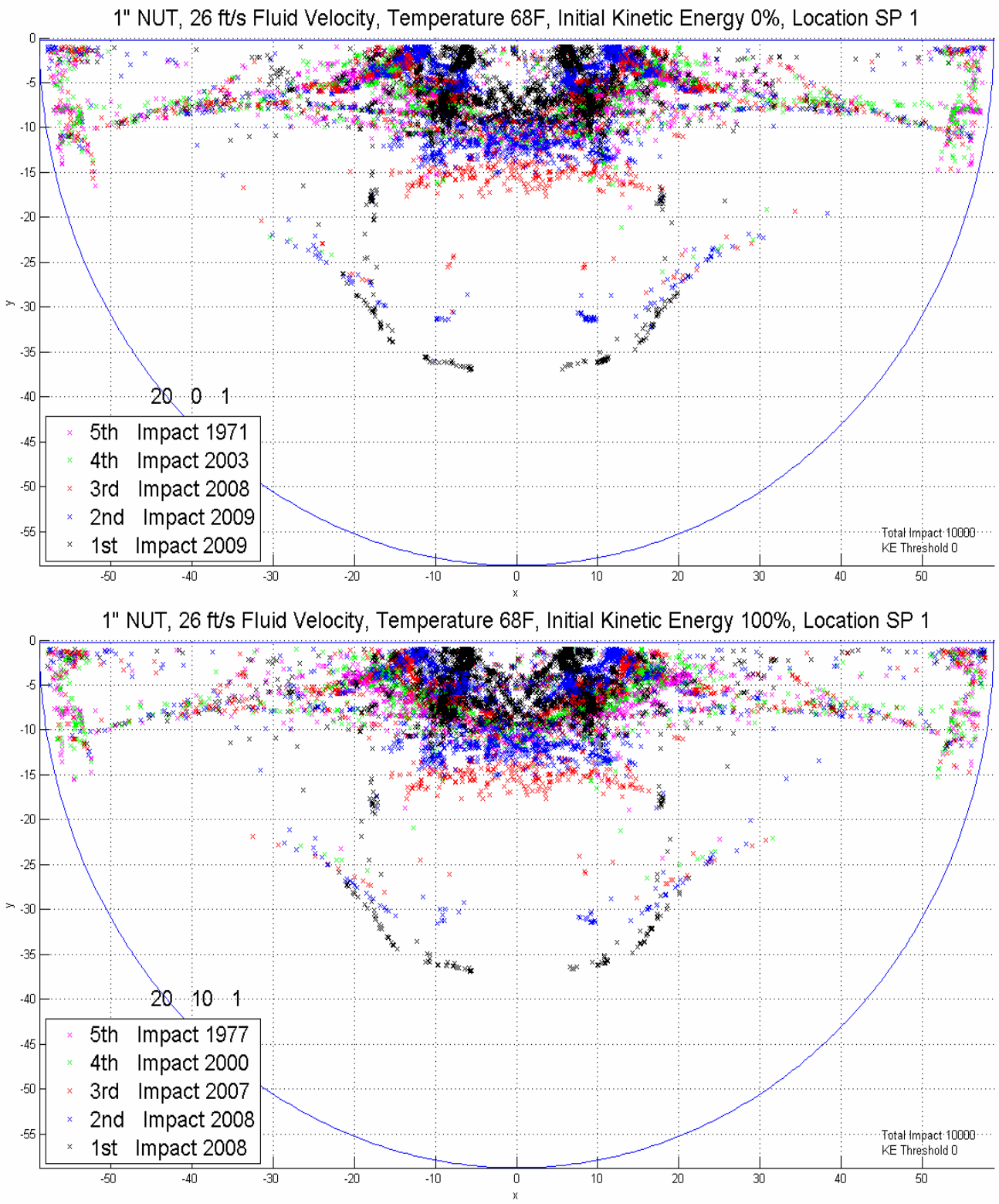

Figure 3.39 Spatial impact distribution for 1" hex nut 68^0F; $1^{st} - 5^{th}$ impacts

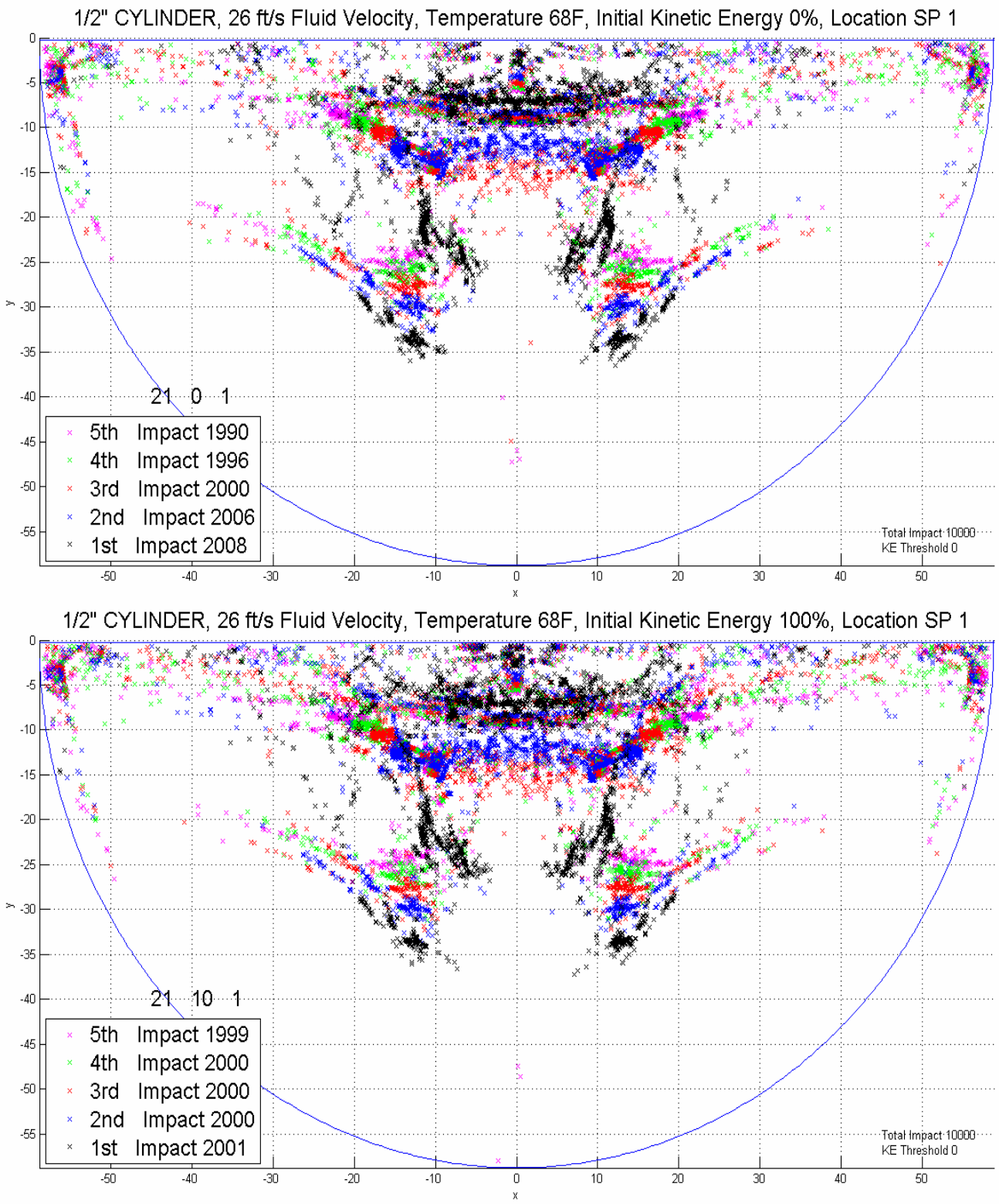

Figure 3.40 Spatial impact distribution for 1/2" cylinder 68^0F; 1^{st} – 5^{th} impacts

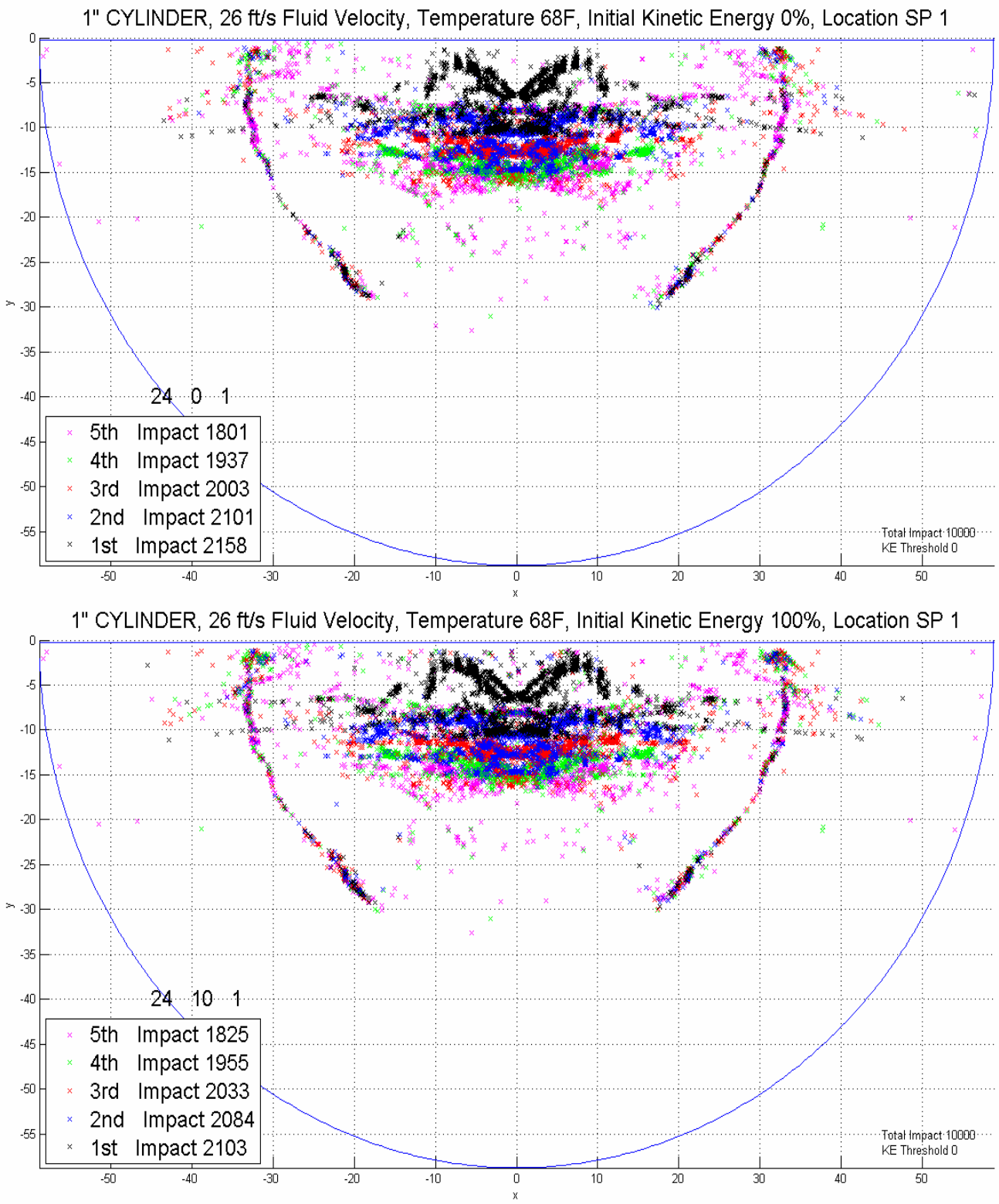

Figure 3.41 Spatial impact distribution for 1" cylinder 68^0F; $1^{st} - 5^{th}$ impacts

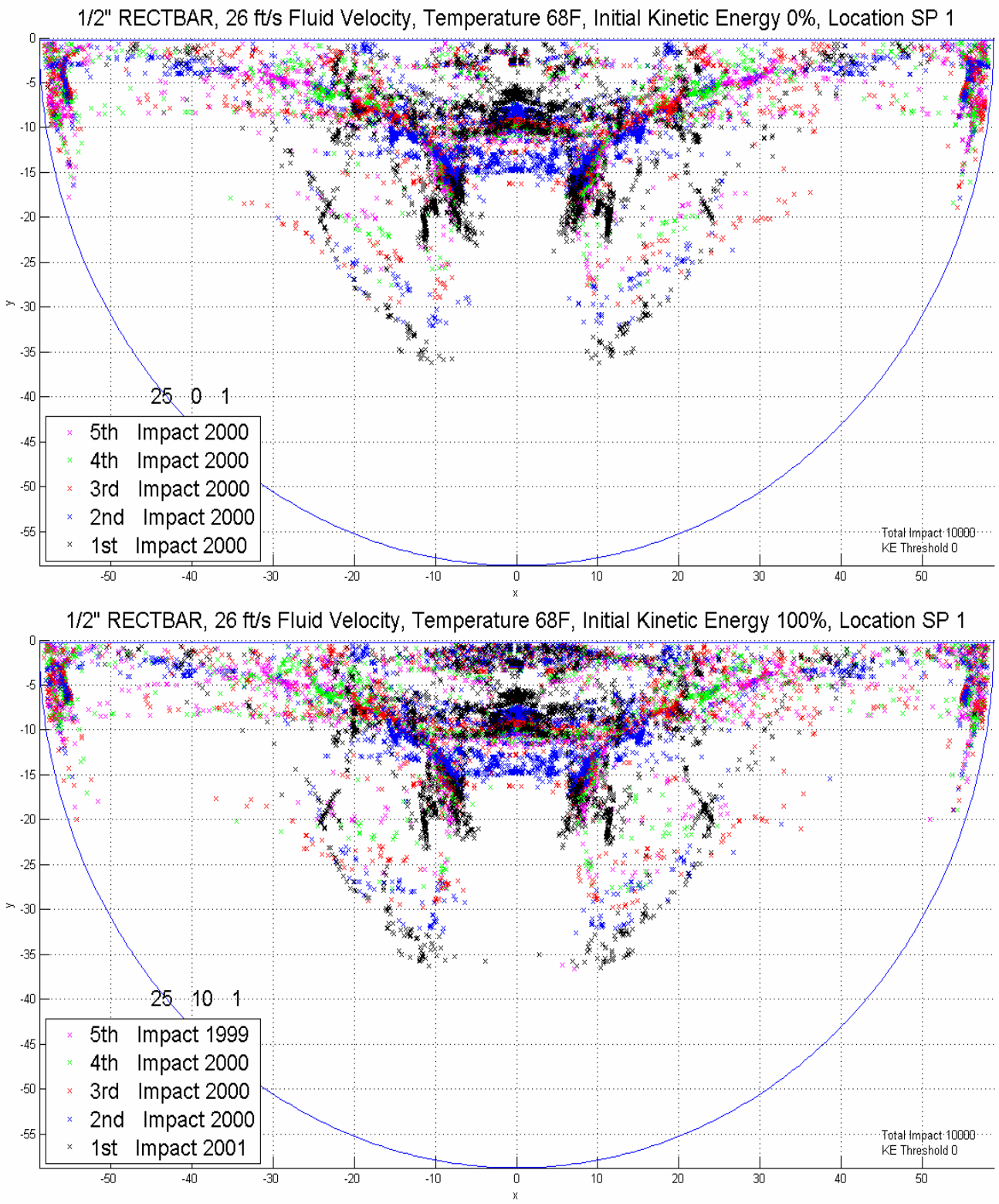

Figure 3.42 Spatial impact distribution for 1/2" rectangular bar 68^0F; $1^{st} - 5^{th}$ impacts

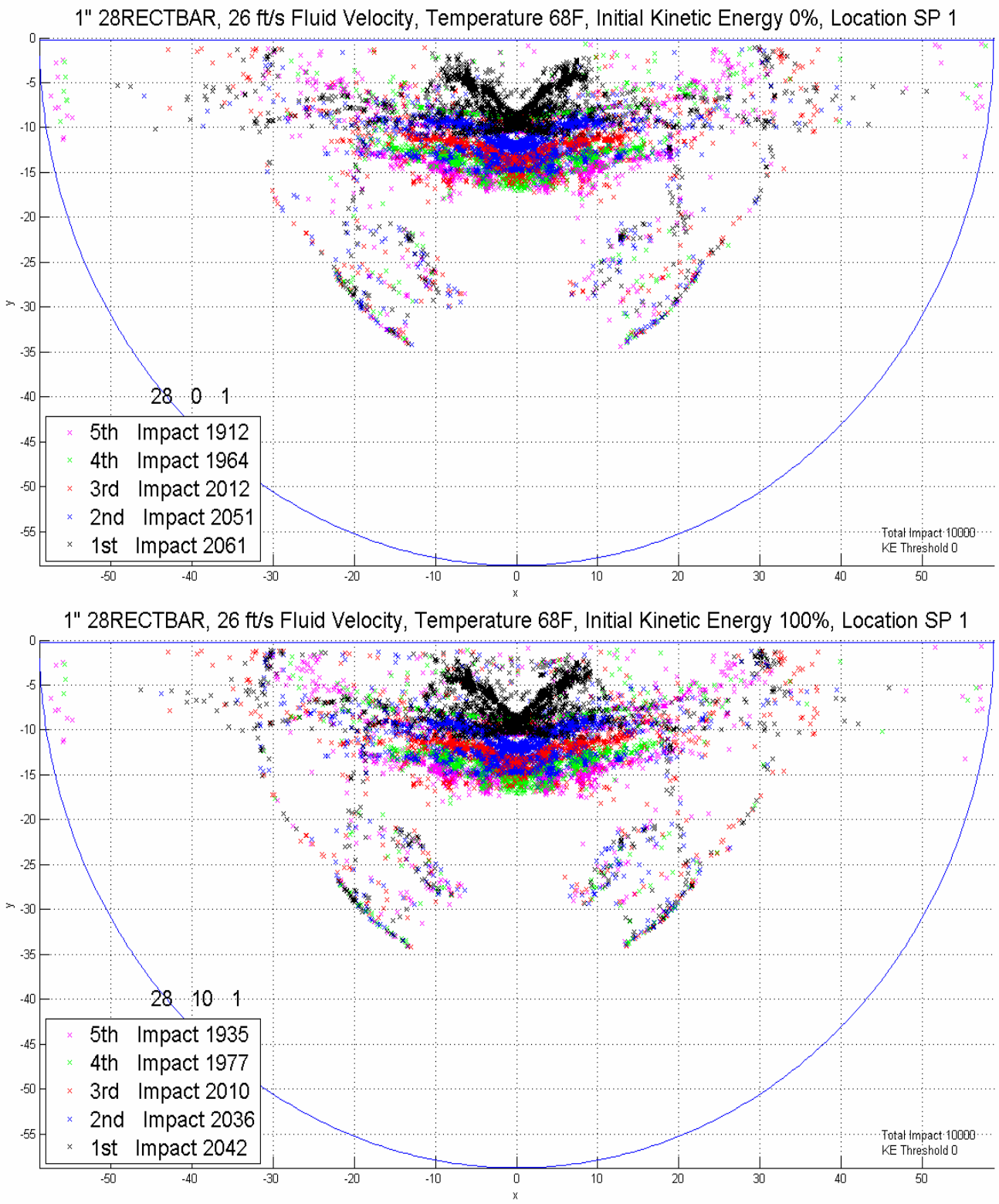

Figure 3.43 Spatial impact distribution for 1" rectangular bar 68^0F; 1^{st} – 5^{th} impacts

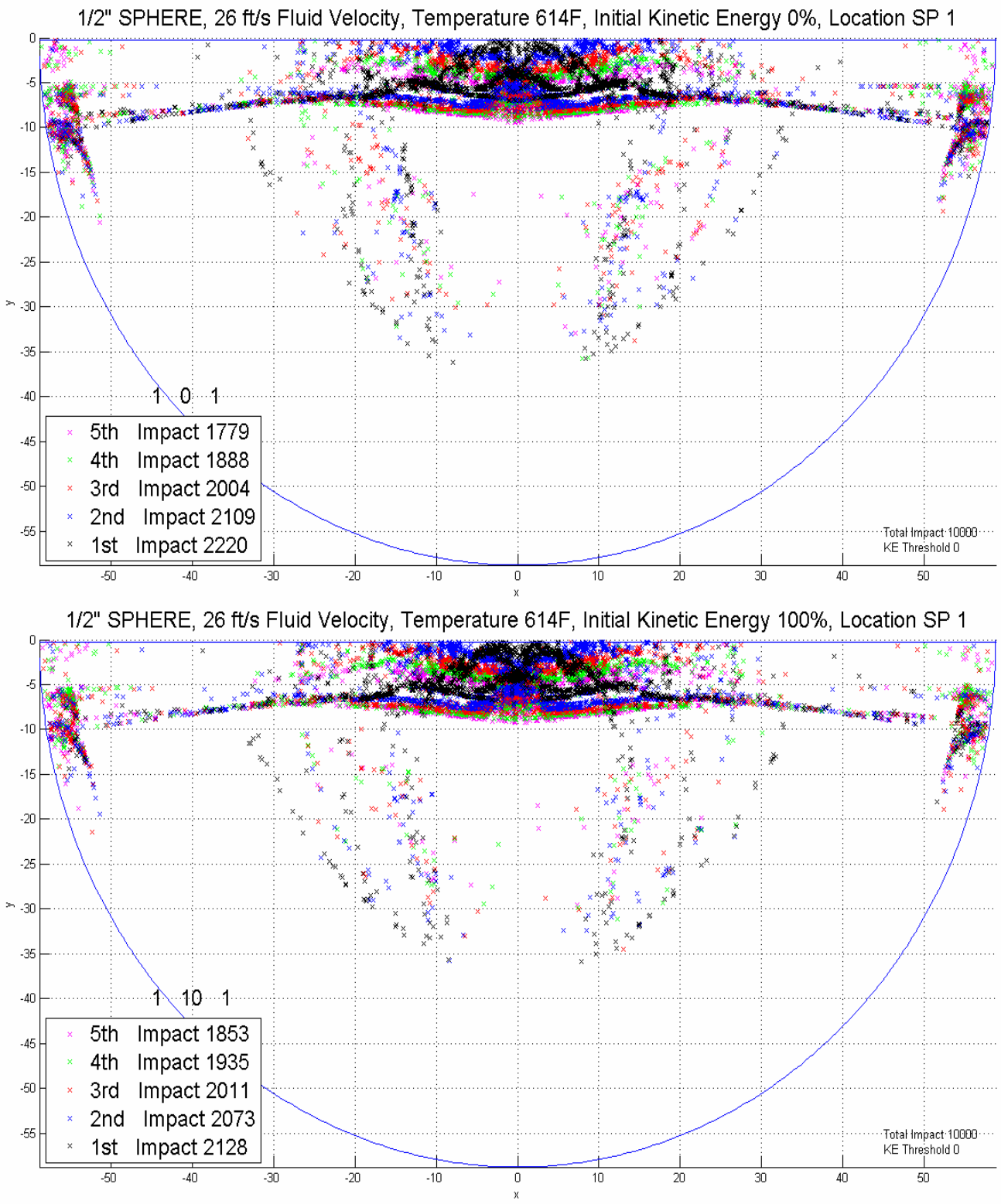

Figure 3.44 Spatial impact distribution for 1/2" sphere 614^0F; 1^{st} – 5^{th} impacts

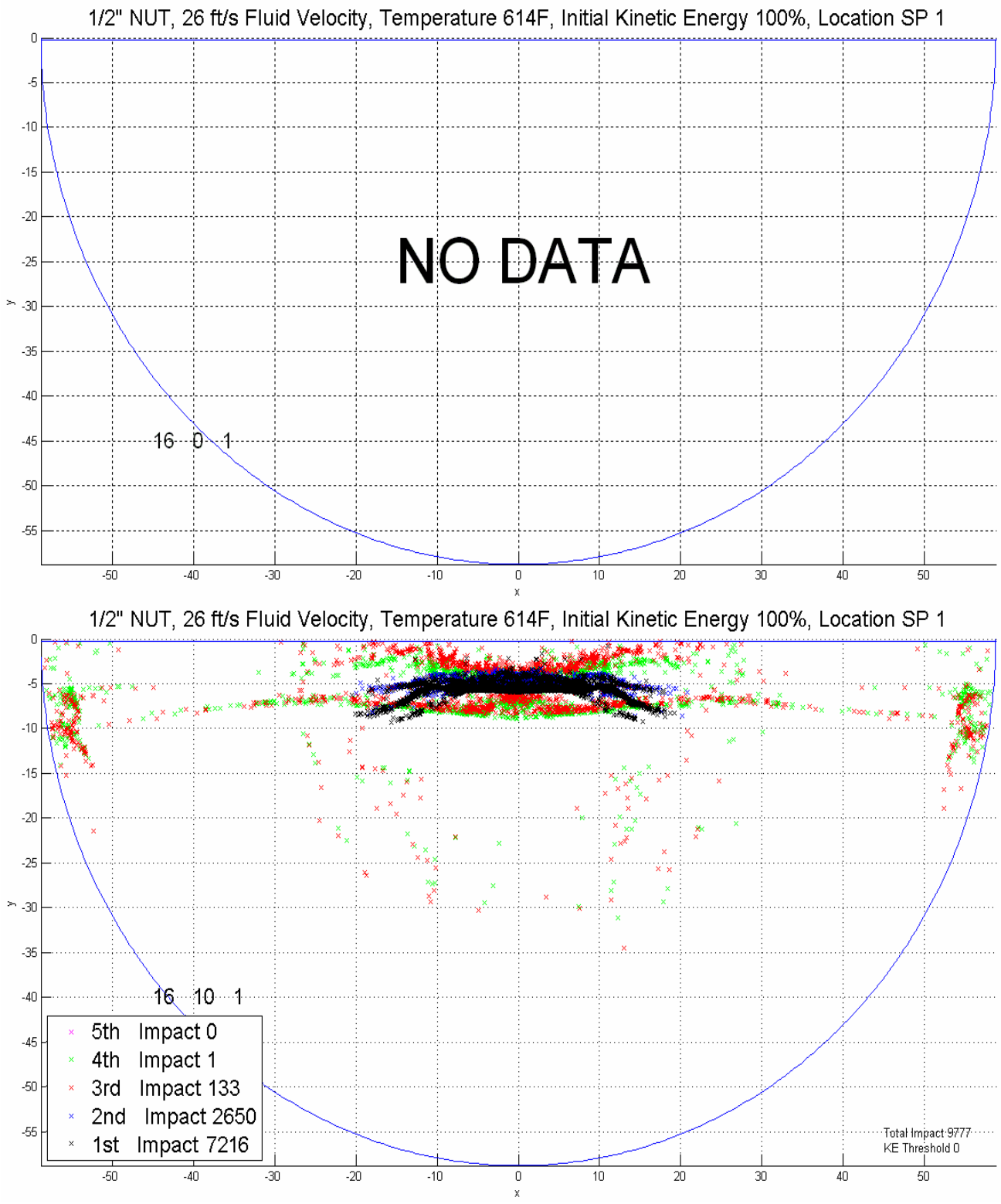

Figure 3.45 Spatial impact distribution for 1/2" hex nut 614^0F; $1^{st} - 5^{th}$ impacts

The next 14 figures represent the same data as the previous 14 figures only now the data has been placed into spatial bins along a 20 x 40 rectangular mesh encompassing the tube sheet. The largest graph in each figure represents the total impacts on the tube sheet for Case 1. The smaller eight graphs that are located in the lower portion of each figure represent impacts as a function of impact energy. Starting from the upper left and continuing to the lower right, the energy ranges are 0 to 1%, 1 to 2%, 2 to 5%, 5 to 10%, 10 to 25%, 25 to 50% 50 to 90% and 90 to 100% of the maximum impact kinetic energy for that particular loose part simulation. The maximum impact kinetic energy is given in the title of the figures. Note that the graph axes are not to scale with one another. This was done to give a more accurate representation of the number of impacts in a particular energy region. All figures are given at 0% initial kinetic energy except for the 1/2" hex nut at 614^0F which is given at 100% initial kinetic energy.

Again, it is evident that spatial distributions tend to group more towards the center of the tube sheet for the first five impacts as the part gets heavier. This behavior also seems to carry over as the temperature increases. This general concept suggests that some of the highest energy impacts will tend to group towards the central flow plume. Beyond a certain threshold initial kinetic energy for a particular loose part, its momentum will carry it out of the flow plume to collide with the plenum divide leading to a lower energy impact on the tube sheet.

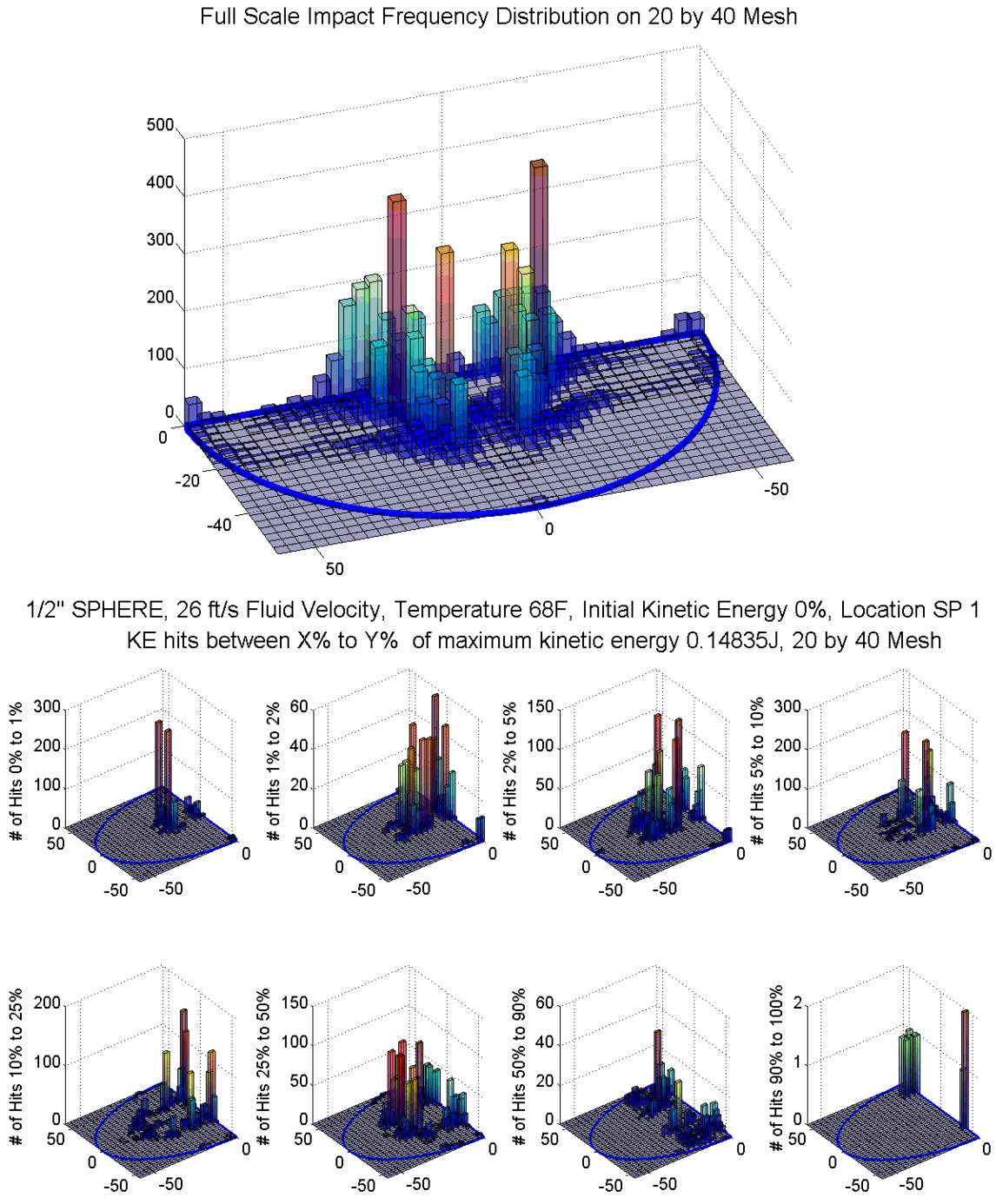

Figure 3.46 Spatial impact distribution as a function of impact energy on 20 x 40 mesh for 1/2" sphere 68^0F; $1^{st} - 5^{th}$ impacts

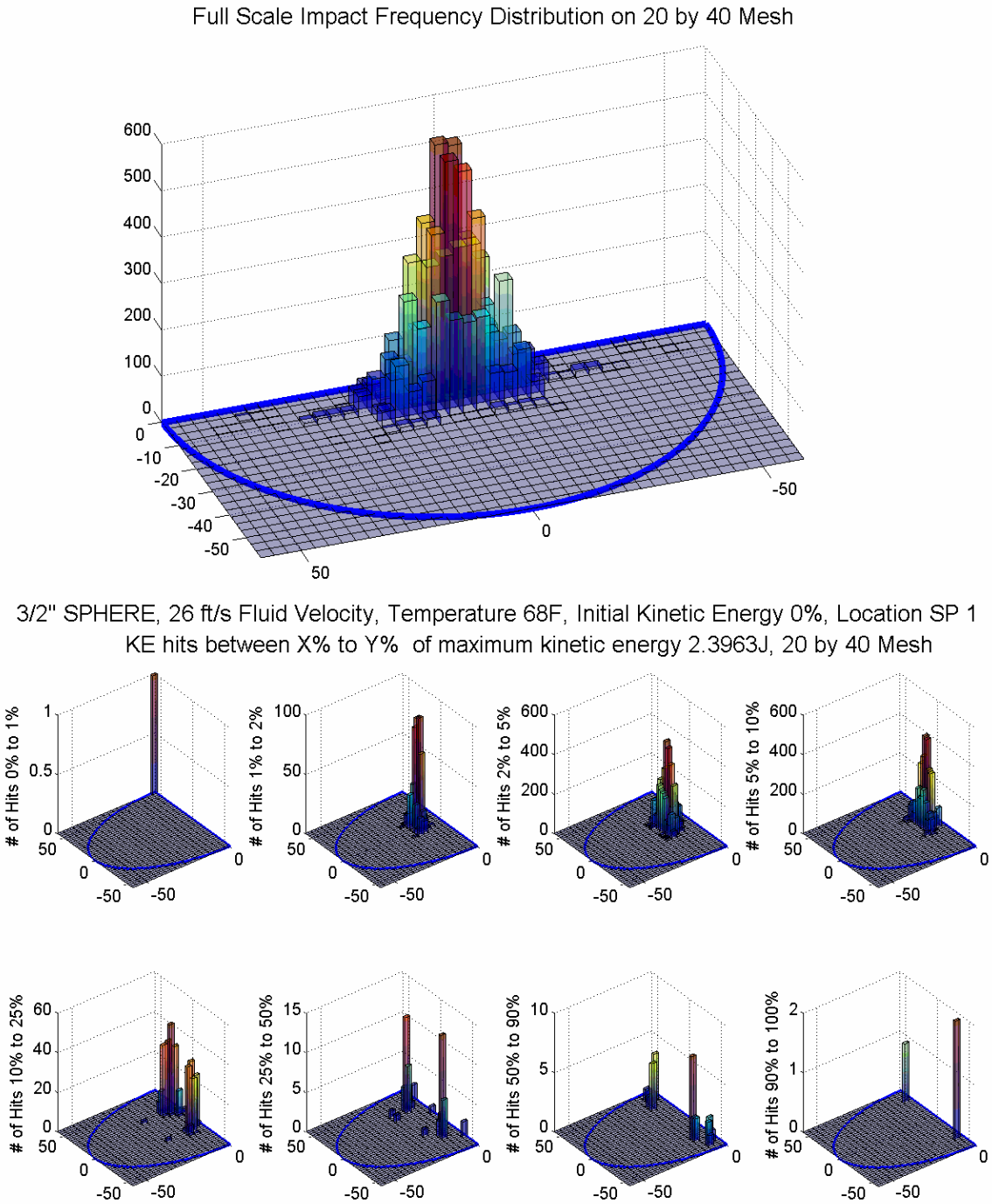

Figure 3.47 Spatial impact distribution as a function of impact energy on 20 x 40 mesh for 3/2" sphere 68^0F; 1^{st} – 5^{th} impacts

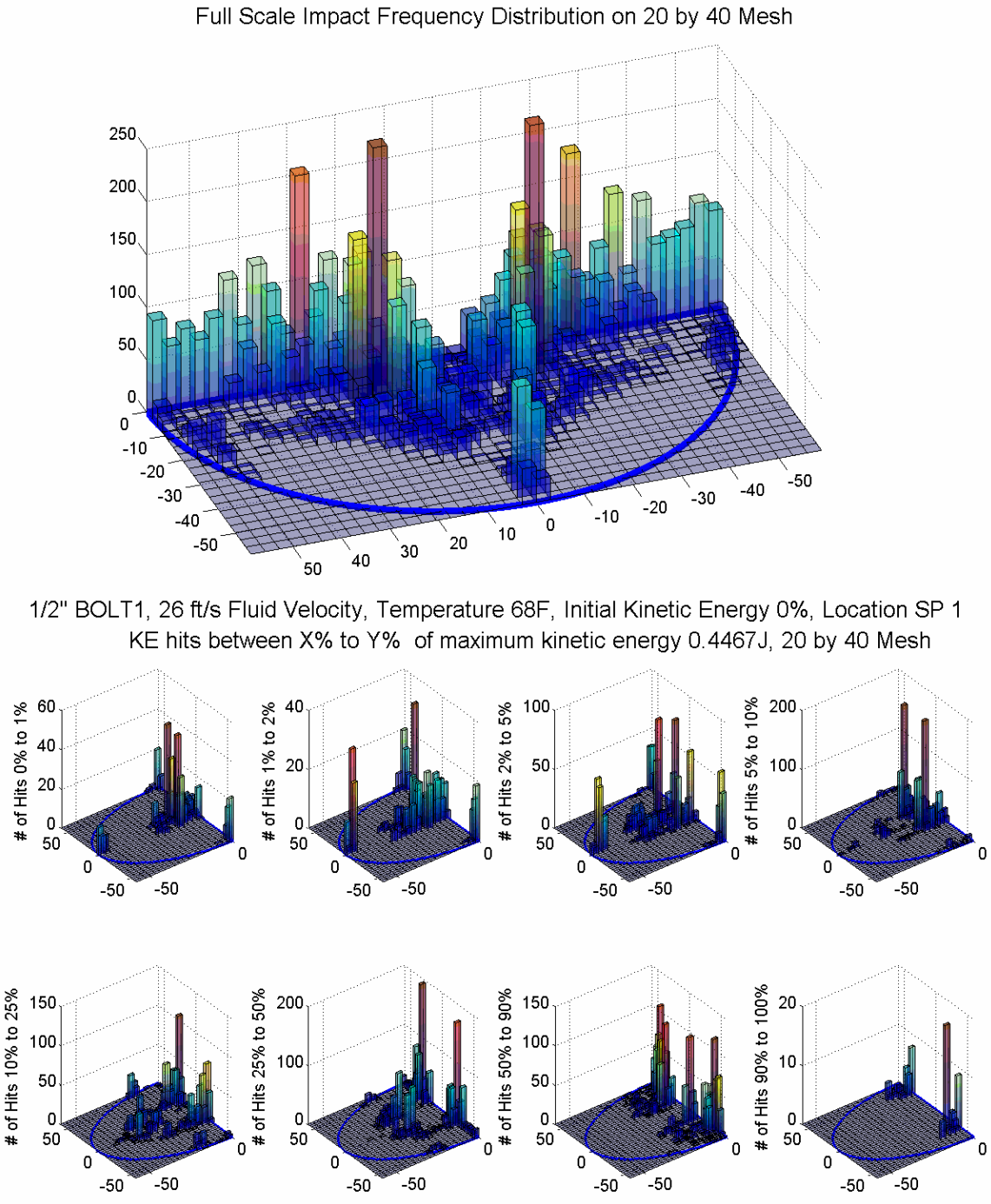

Figure 3.48 Spatial impact distribution as a function of impact energy on 20 x 40 mesh for 1/2" bolt type #1 68^0F; 1^{st} – 5^{th} impacts

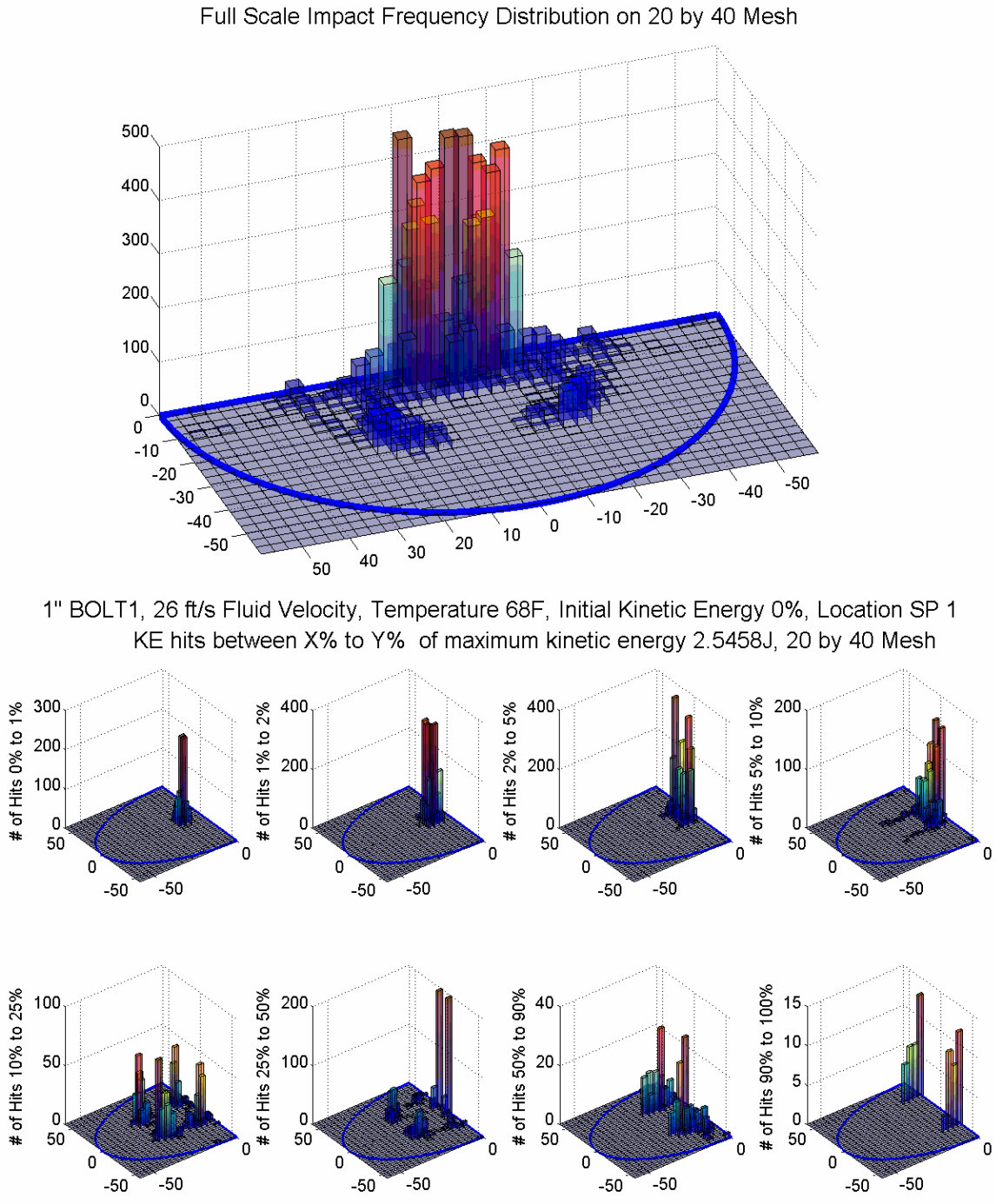

Figure 3.49 Spatial impact distribution as a function of impact energy on 20 x 40 mesh for 1" bolt type #1 68^0F; 1^{st} – 5^{th} impacts

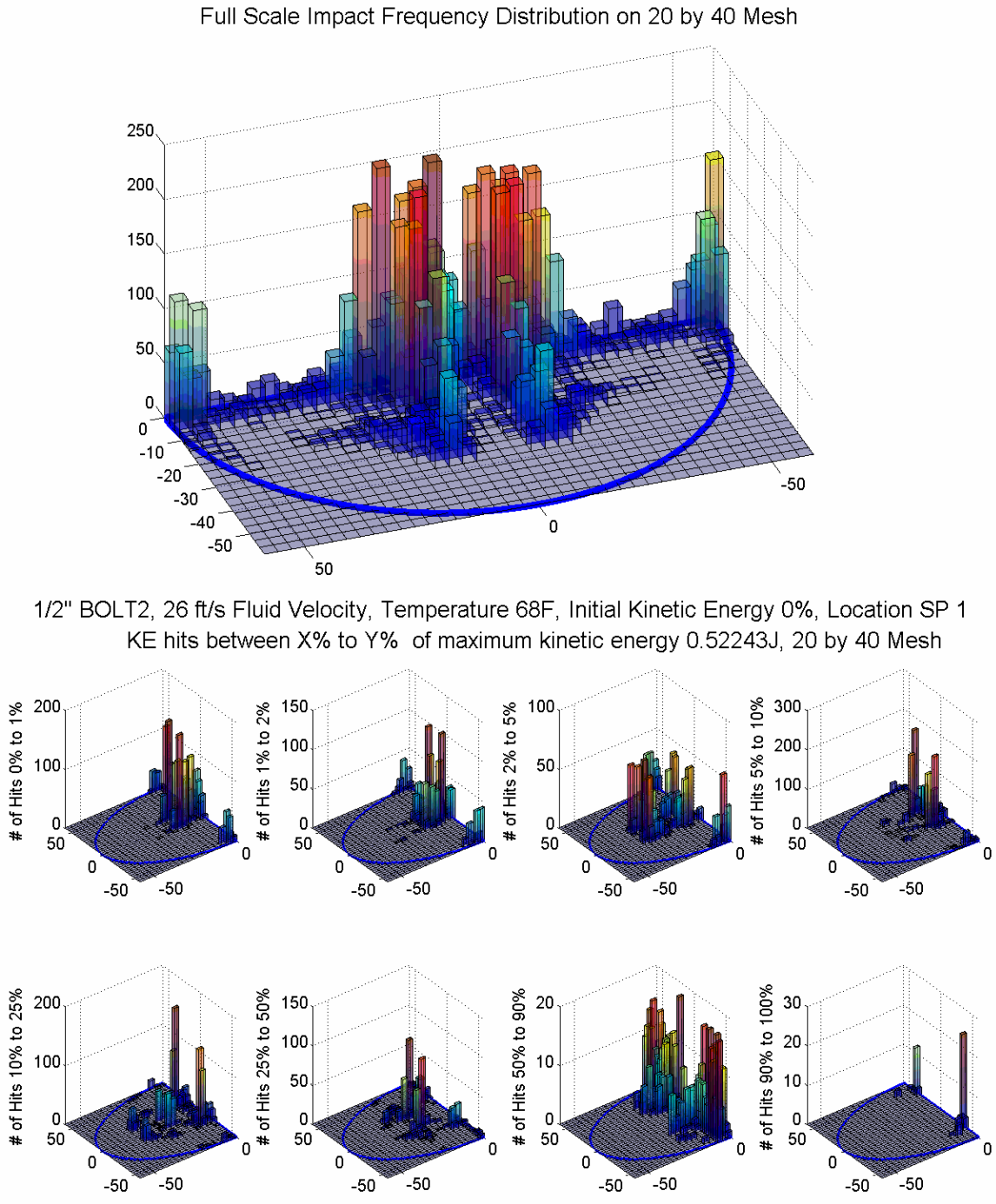

Figure 3.50 Spatial impact distribution as a function of impact energy on 20 x 40 mesh for 1/2" bolt type #2 68^0F; 1^{st} – 5^{th} impacts

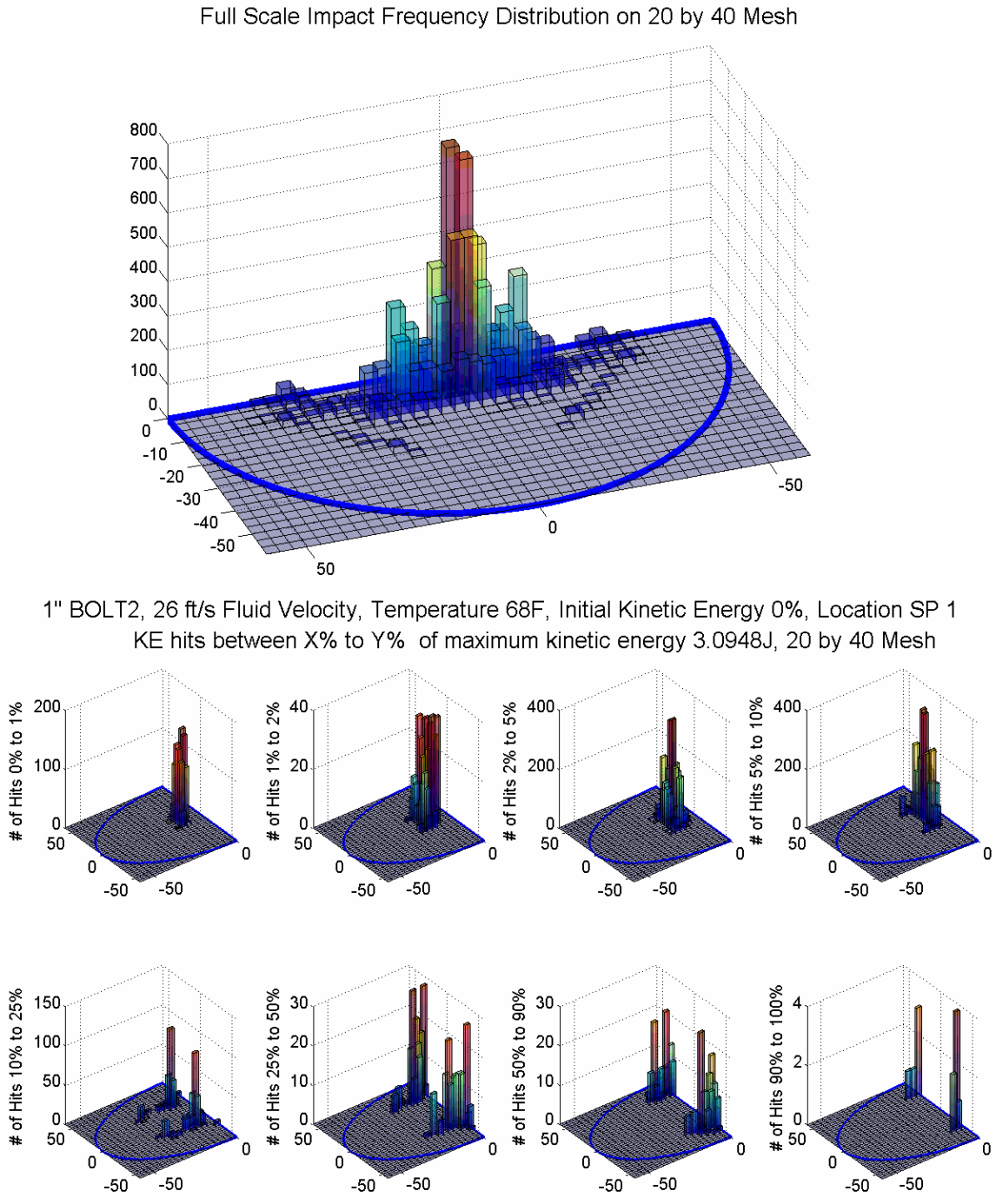

Figure 3.51 Spatial impact distribution as a function of impact energy on 20 x 40 mesh for 1" bolt type #2 68^0F; 1^{st} – 5^{th} impacts

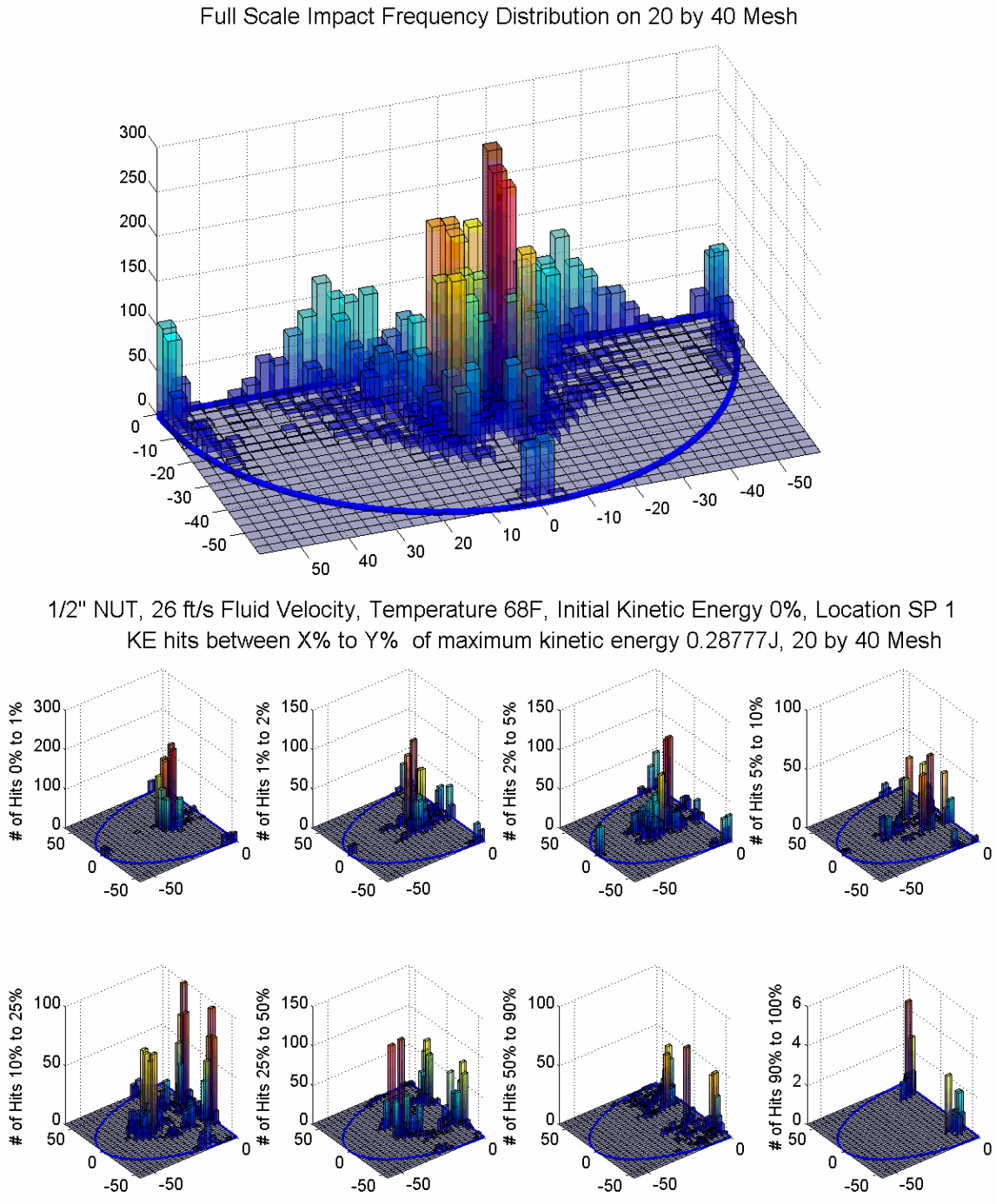

Figure 3.52 Spatial impact distribution as a function of impact energy on 20 x 40 mesh for 1/2" hex nut 68^0F; 1^{st} – 5^{th} impacts

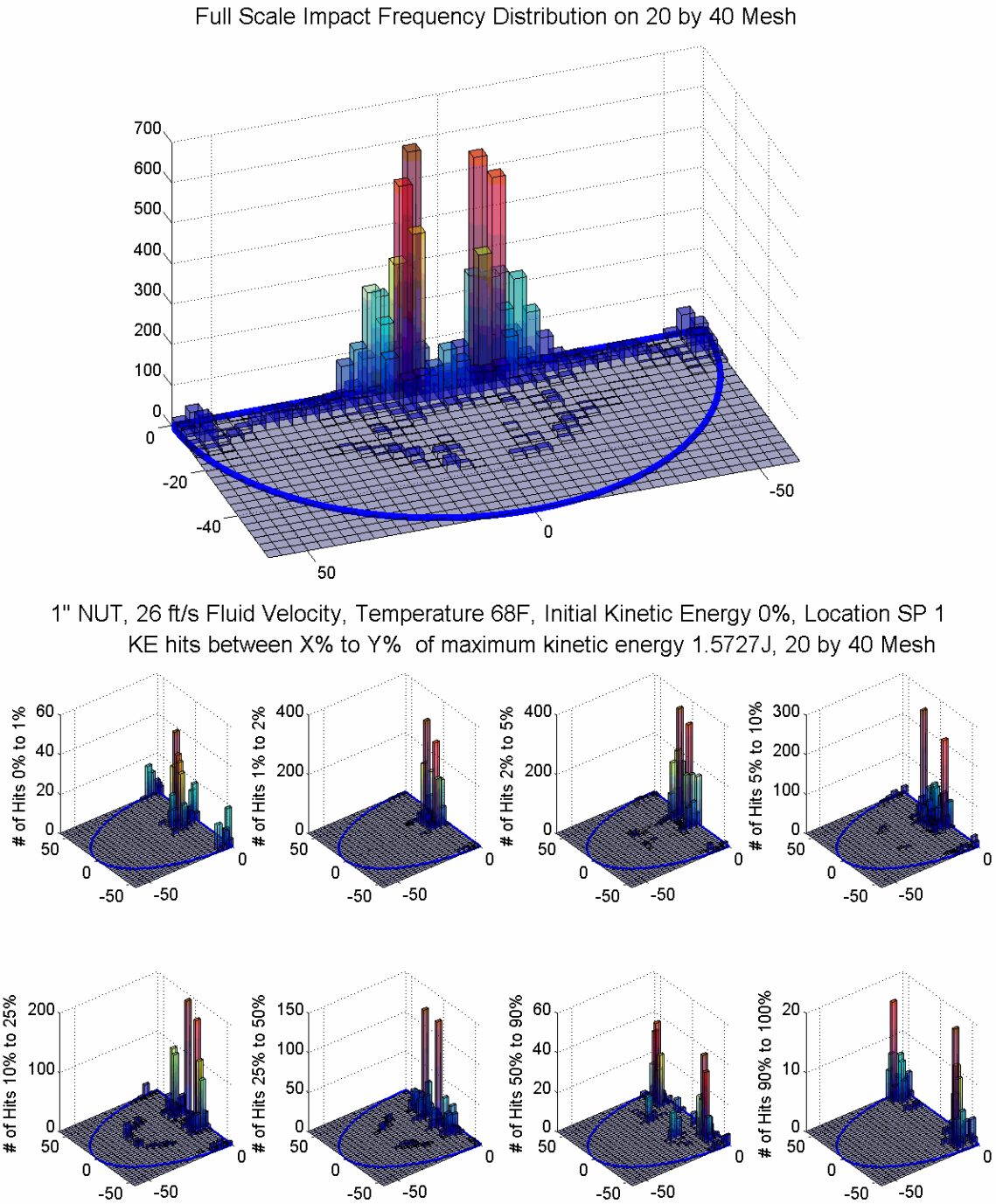

Figure 3.53 Spatial impact distribution as a function of impact energy on 20 x 40 mesh for 1" hex nut 68^0F; 1^{st} – 5^{th} impacts

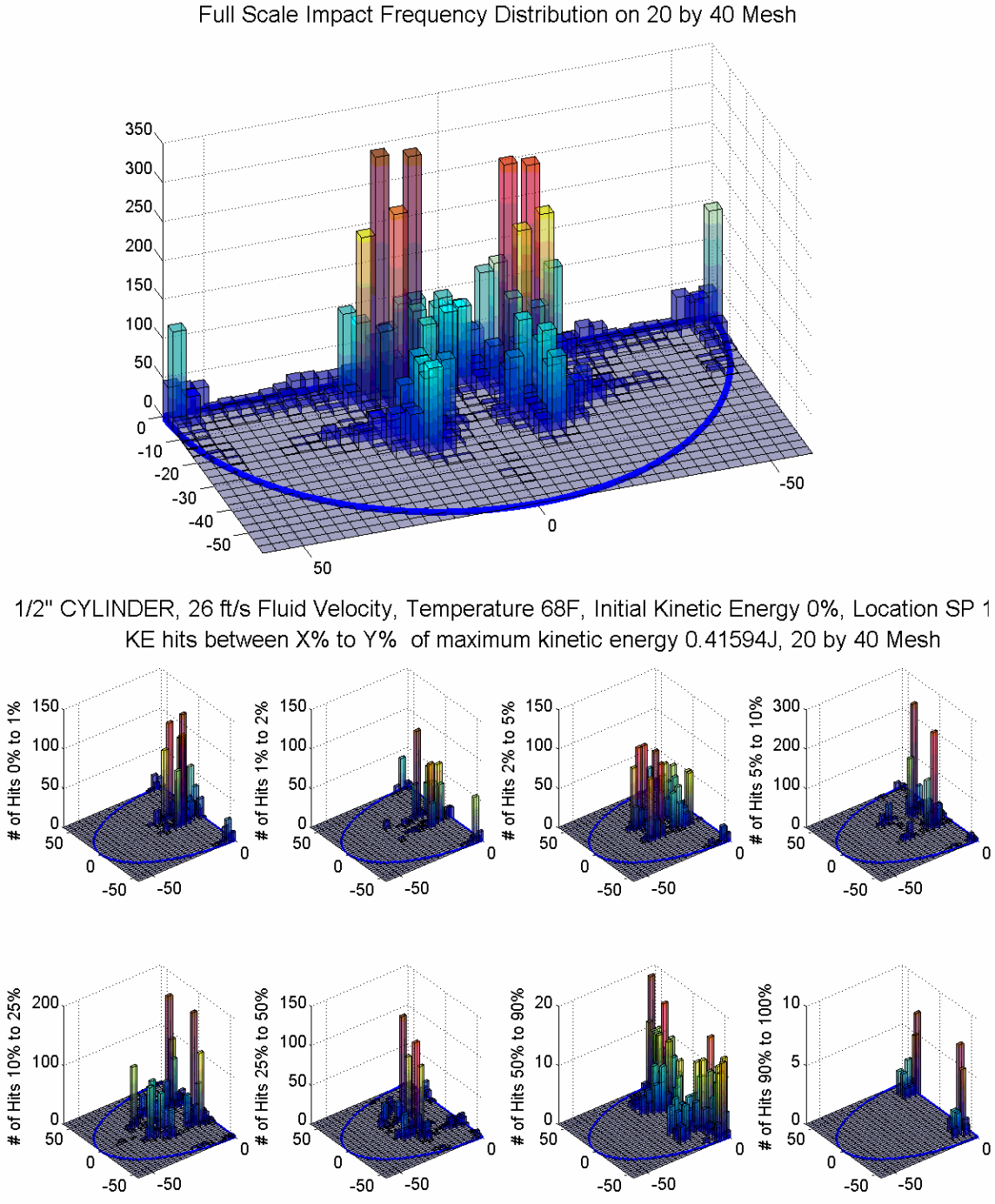

Figure 3.54 Spatial impact distribution as a function of impact energy on 20 x 40 mesh for 1/2" cylinder 68^0F; 1^{st} – 5^{th} impacts

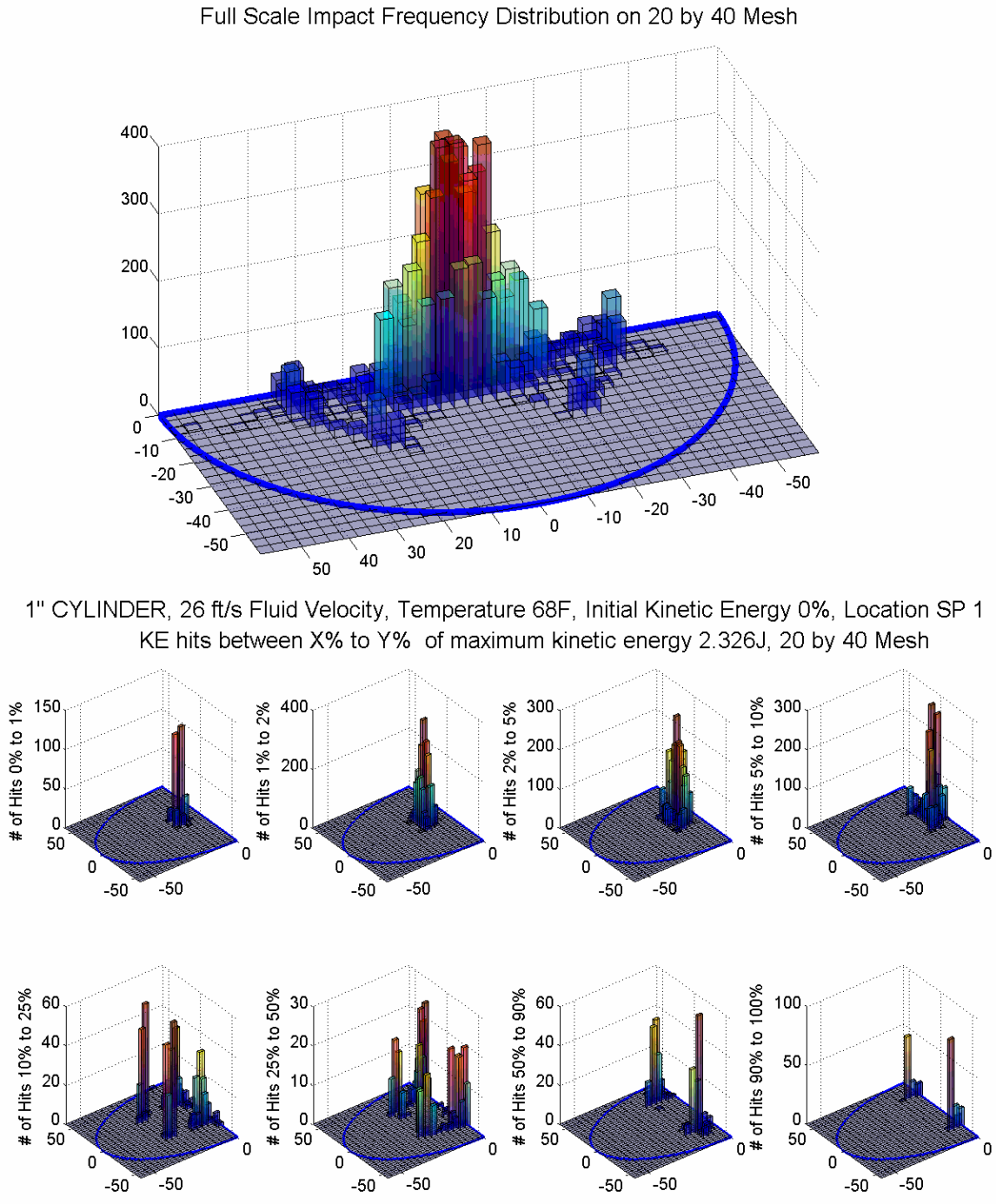

Figure 3.55 Spatial impact distribution as a function of impact energy on 20 x 40 mesh for 1" cylinder 68^0F; $1^{st} - 5^{th}$ impacts

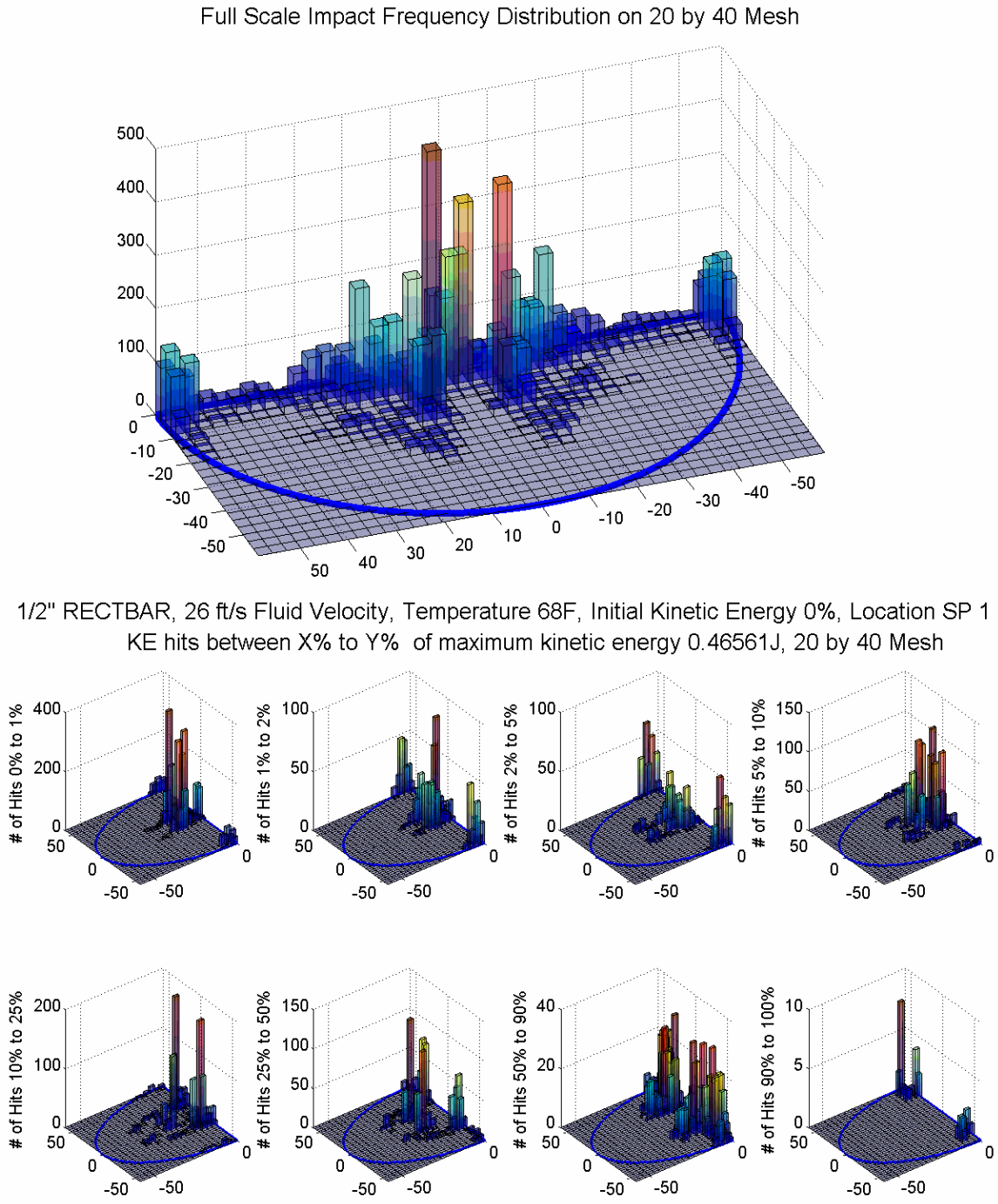

Figure 3.56 Spatial impact distribution as a function of impact energy on 20 x 40 mesh for 1/2" rectangular bar 68^0F; 1^{st} – 5^{th} impacts

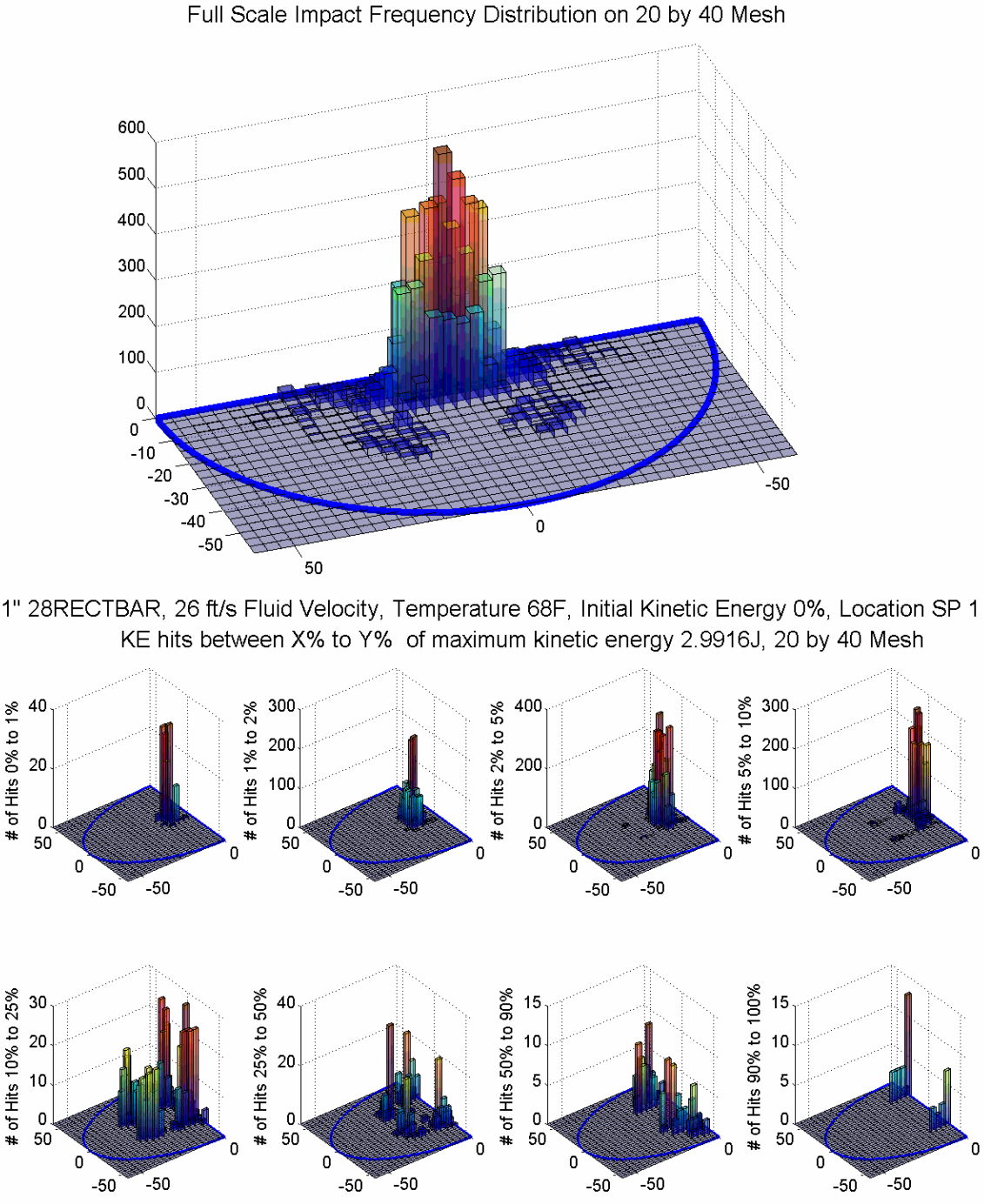

Figure 3.57 Spatial impact distribution as a function of impact energy on 20 x 40 mesh for 1" rectangular bar 68^0F; $1^{st} - 5^{th}$ impacts

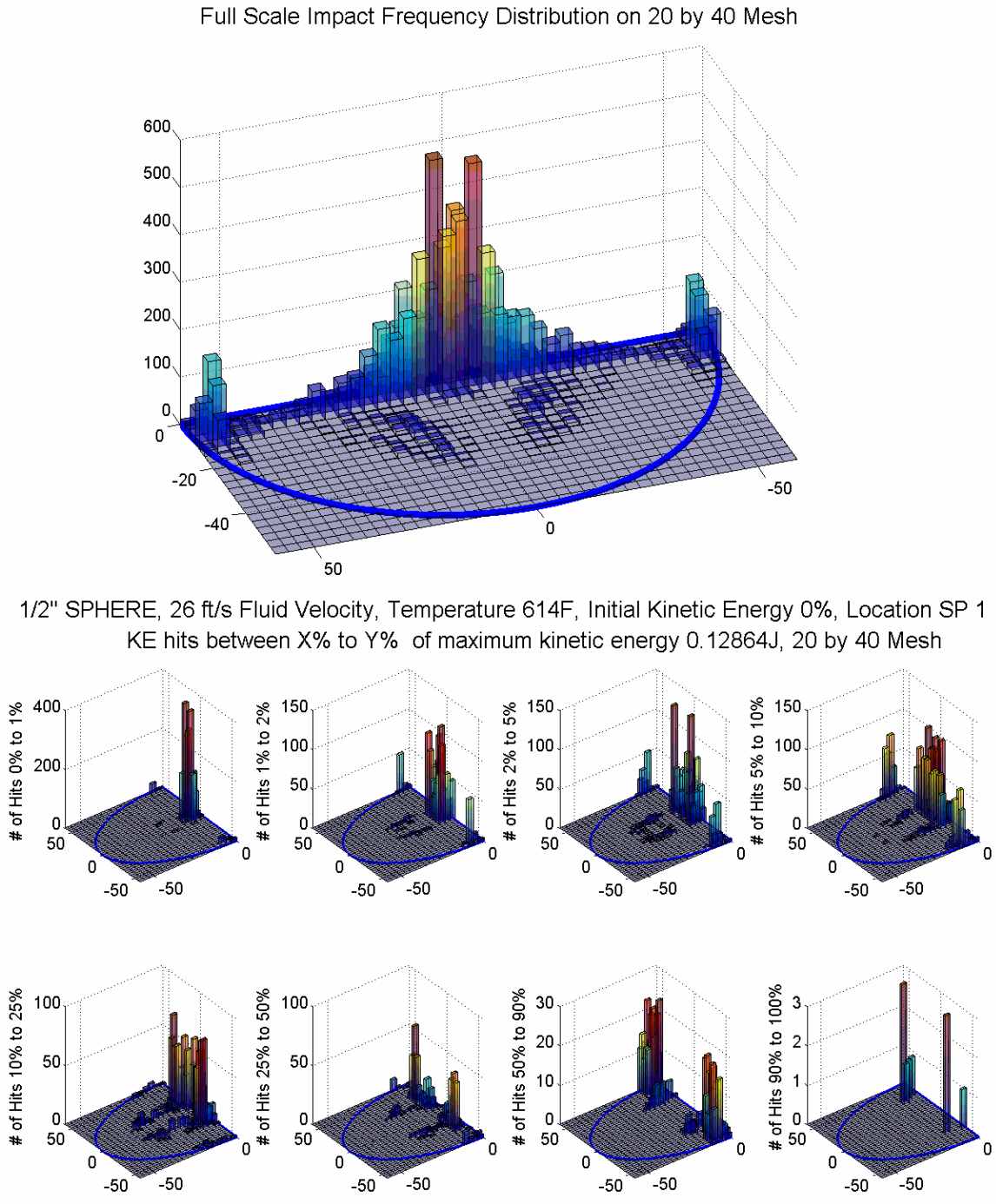

Figure 3.58 Spatial impact distribution as a function of impact energy on 20 x 40 mesh for 1/2" sphere 614^0F; $1^{st} - 5^{th}$ impacts

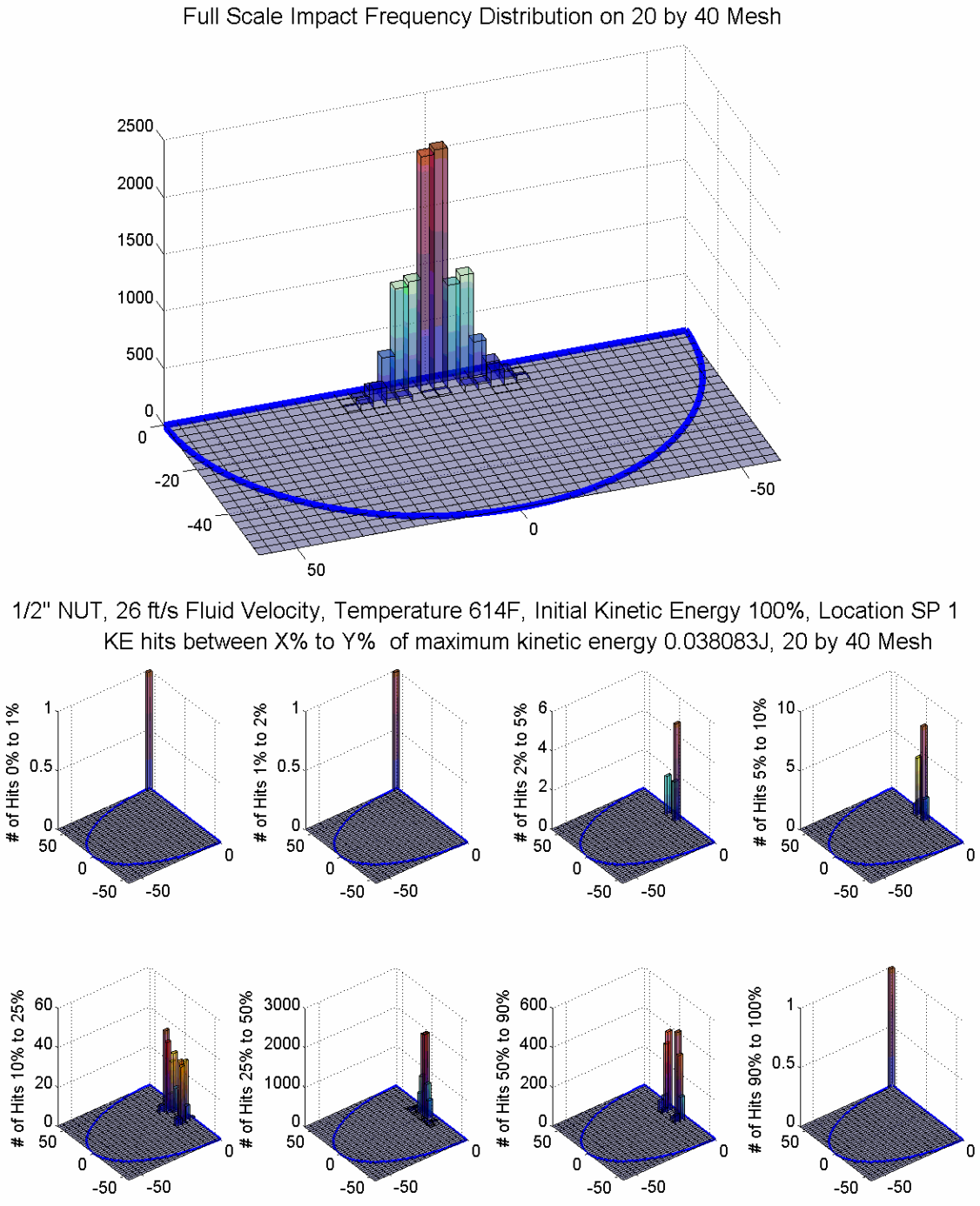

Figure 3.59 Spatial impact distribution as a function of impact energy on 20 x 40 mesh for 1/2" hex nut 614^0F; $1^{st} - 5^{th}$ impacts

Lastly, for Case 1, the next six figures are histograms of impact kinetic energy as a function of part type. For sake of clarity, the parts have been broken down into figures representing each part class. The kinetic energy axes are all scaled identically to the maximum impact kinetic energy for all loose parts for the first five impacts. Note that the 614^0F runs for the 1/2" sphere and 1/2" hex nut are combined in with the 68^0F runs for the sphere and hex nut figures repsectively. In all, there are a total of thirty histograms to compare. The Z-axis is scaled logarithmically and reflects the maximum cutoff for each run of 10,000 tube sheet impacts.

The heaviest part in each class was responsible for the largest number of high energy impacts. Overall, the 1" hex bolt type #2 impacts with the maximum force at 3.095 Joules which matches with the data shown in **Table 3.4**. The 7/8" hex bolt type #1 is responsible for the highest mean impact kinetic energy for the first five impacts at 0.373 Joules.

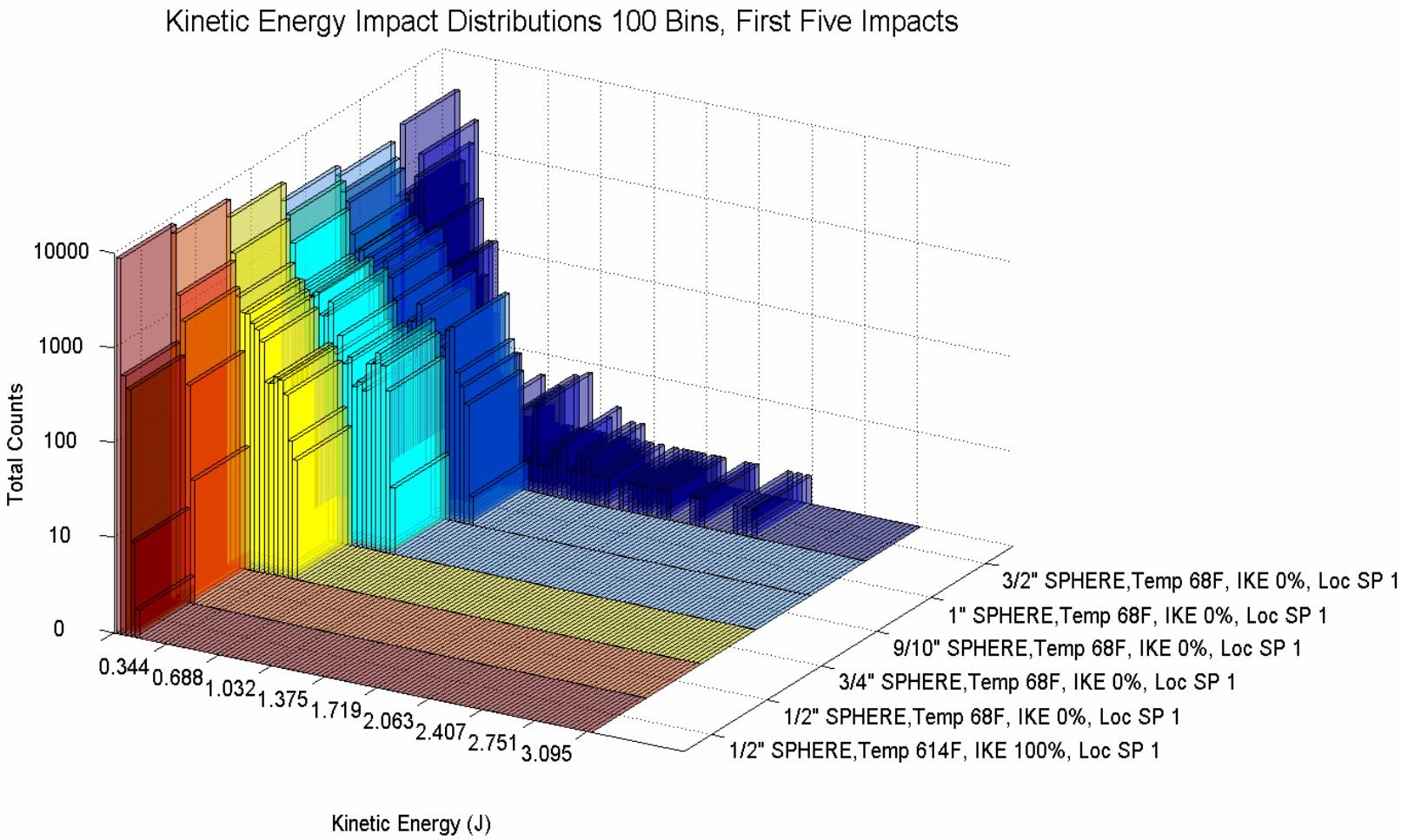

Figure 3.60 Sphere class impact kinetic energy distribution; 1st – 5th impacts

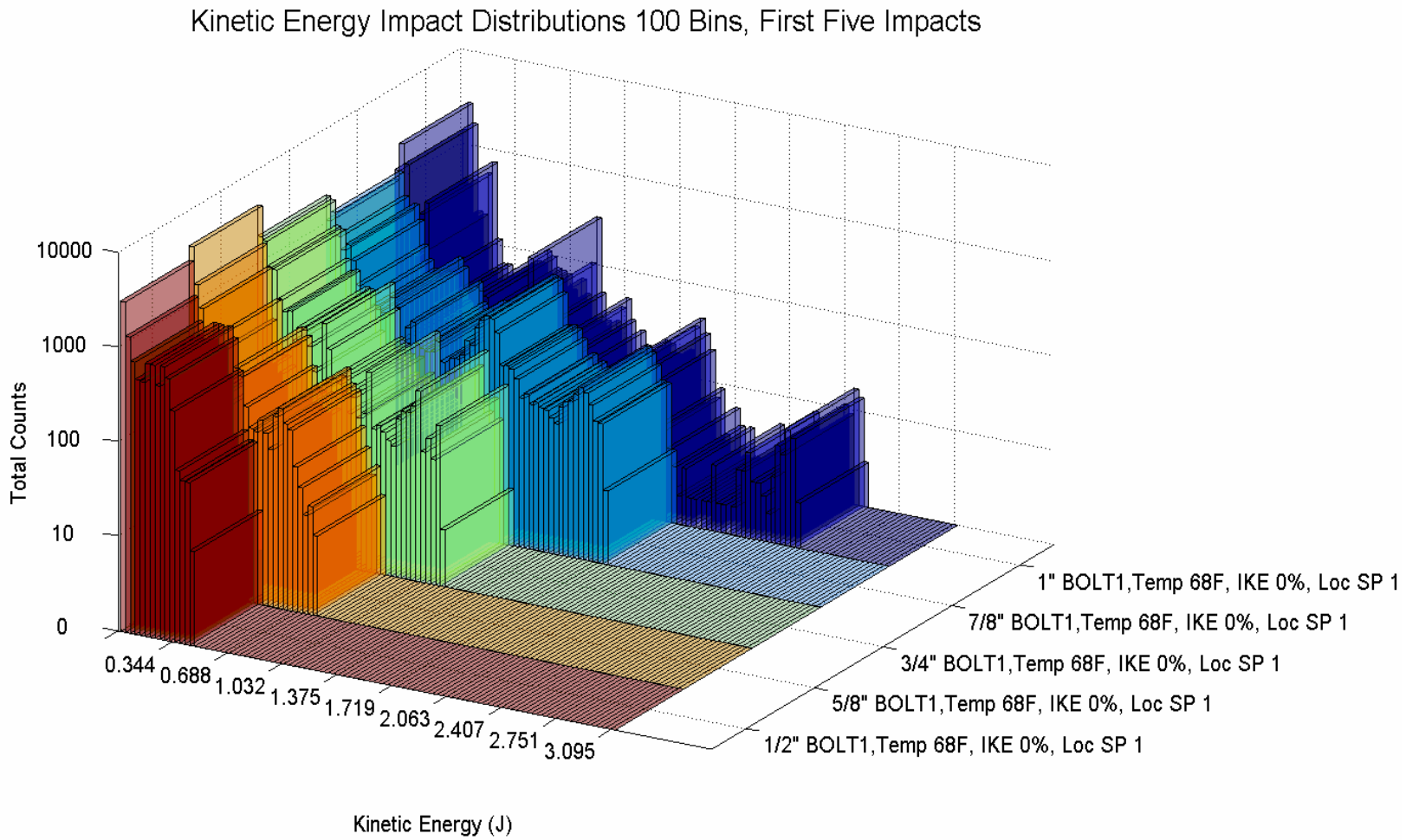

Figure 3.61 Bolt type #1 class impact kinetic energy distribution; 1st – 5th impacts

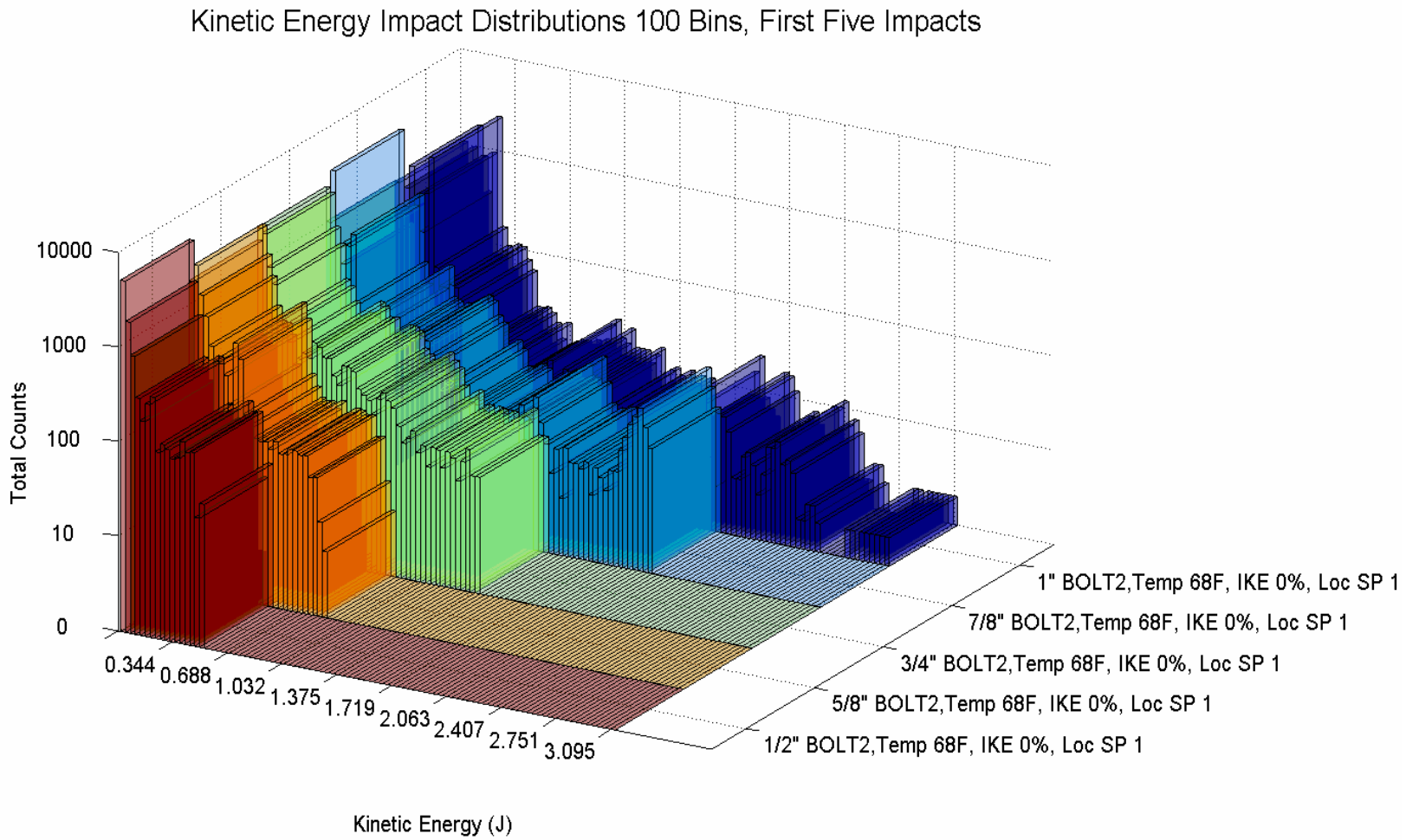

Figure 3.62 Bolt type #2 class impact kinetic energy distribution; 1st – 5th impacts

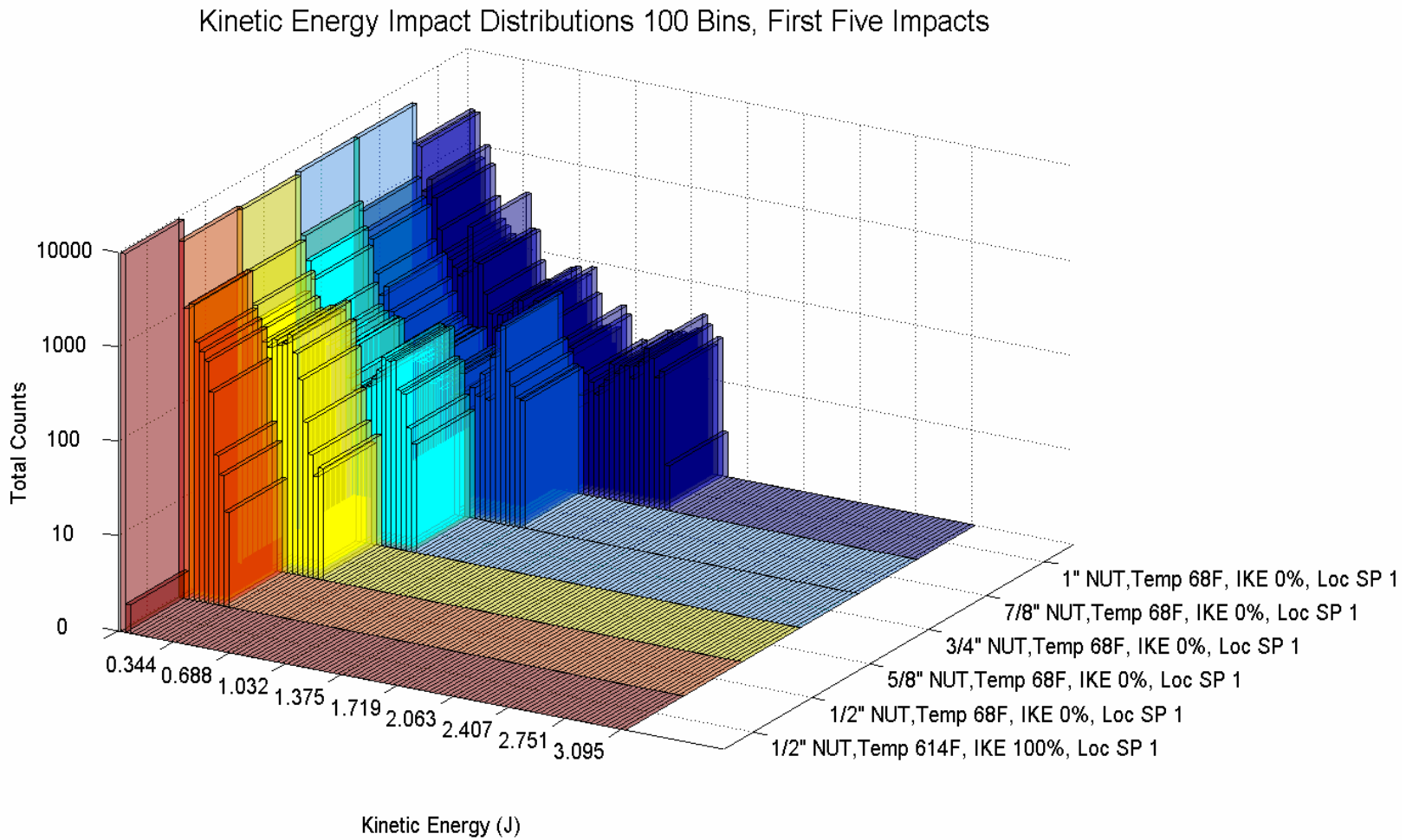

Figure 3.63 Hex nut class impact kinetic energy distribution; 1st – 5th impacts

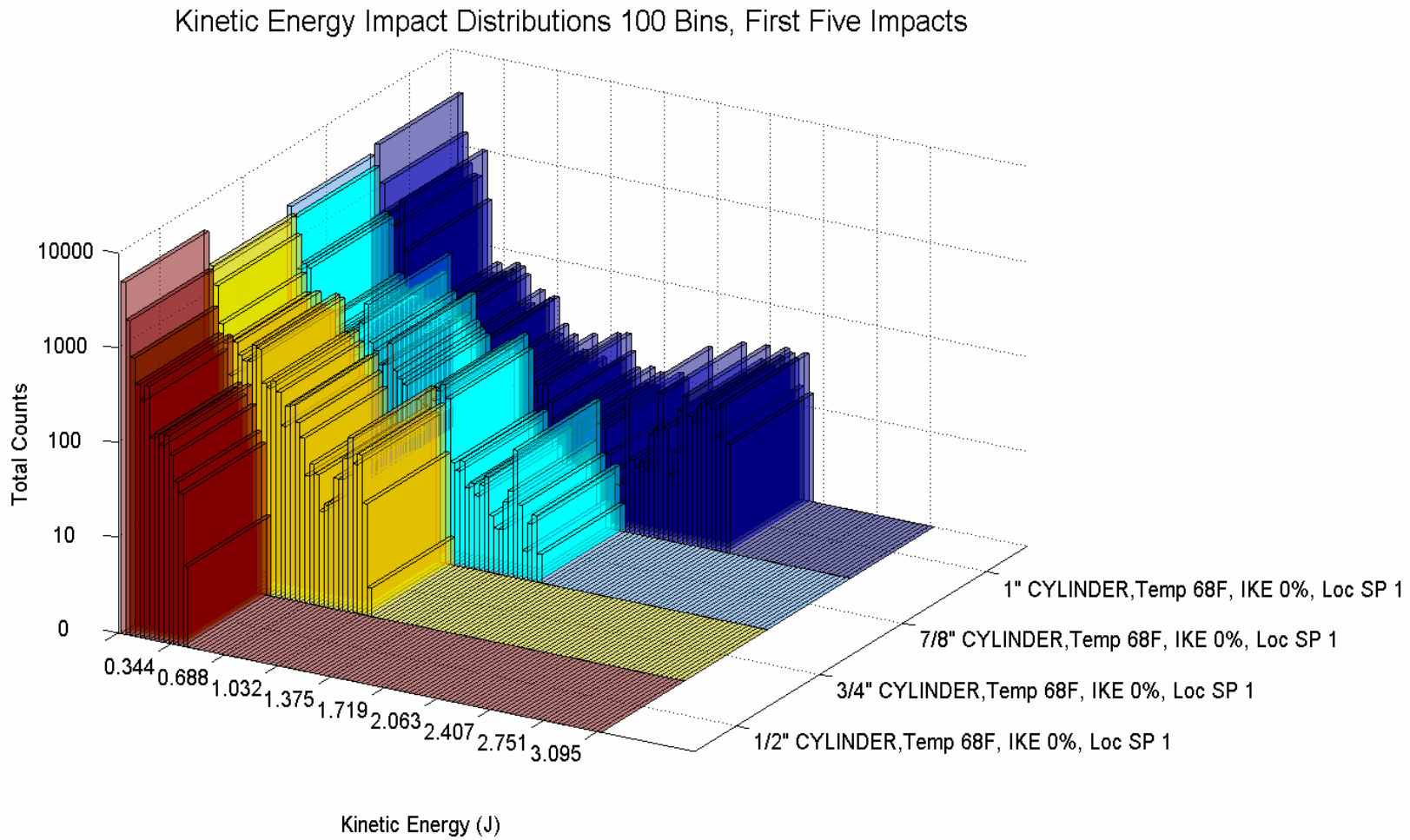

Figure 3.64 Cylinder class impact kinetic energy distribution; 1^{st} – 5^{th} impacts

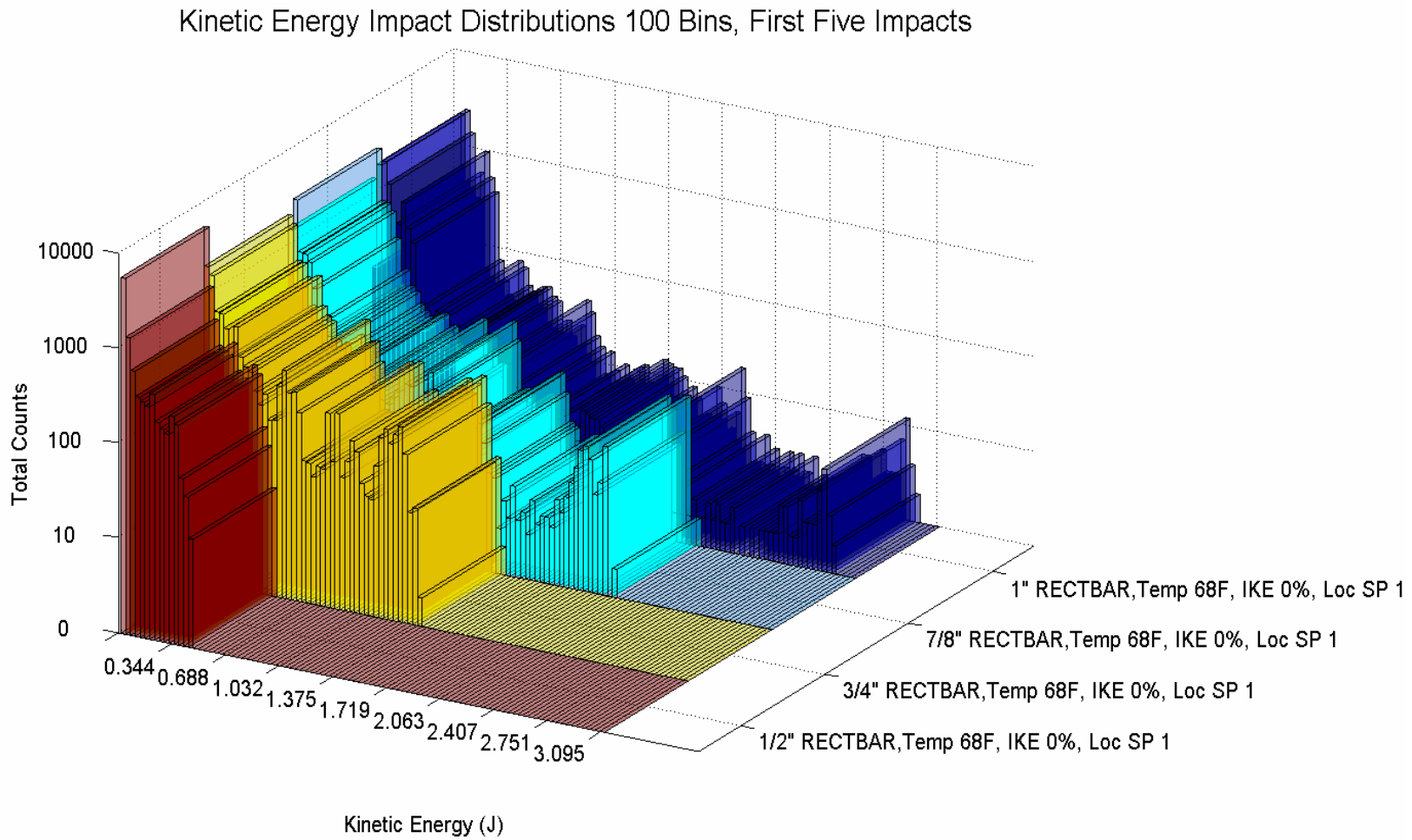

Figure 3.65 Sphere class impact kinetic energy distribution; 1st – 5th impacts

3.2.2 Full Scale Case 2 Results

Case 2 was conducted to capture the long term behavior of the loose parts once they had been introduced into the inlet plenum. These simulations ignore the first five impact locations and energies and continue on for up to 25,000 tube sheet impacts. The only occurrences of multiple histories were due to loose parts that were impacting multiple surfaces in a time frame of less than 1.0E-06 seconds, i.e. 'stuck'. If the part was not impacting the tube sheet at all and became idle for one hundred separate histories the simulation time was cut short to reduce computation time.

Case 2 results are displayed in a manner similar to the Case 1 results with the exception that on some figures data was combined from all the initial kinetic energy simulations as well as from start plane 1 and 2 (the two locations occurring before the 45^0 elbow bend). The first set of six tables give the mean and max impact kinetic energies for each part starting from start plane 1 for initial kinetic energies of 0, 50 and 100% the local fluid velocity for all impacts beyond the fifth impact for temperatures of 68^0F and 614^0F. Overall, the 1" cylinder had the highest mean impact kinetic energy at 0.451 Joules while the 1" hex bolt type #2 had the maximum of the max impact kinetic energies at 3.09 Joules. The six figures beyond the tables represent a graphical illustration of the same data. In this case, data from all initial kinetic energies (0% through 100%) are depicted. Mean values of the impact kinetic energies are represented by the bar graphs while the maximums are represented as diamonds. The diamonds correspond to all impacts beyond the fifth impact. Bar colors match up with the appropriate data point colors so that the mean and max of the same simulation are the same color.

Table 3.8 Mean and maximum impact kinetic energies for sphere class; beyond 5th impact

Start Plane 1 (Energy in Joules)			(25000 hits)	Fluid Temperature: 68 F After 5th Impact		Fluid Temperature: 614 F After 5th Impact	
Part #	Part Type	Size	IKE (%)	Mean KE	Max KE	Mean KE	Max KE
1	Sphere	1/2''					
			0	0.000243	0.118725	0.000918	0.092668
			50	0.000243	0.126426	0.000951	0.131308
			100	0.000150	0.116255	0.000572	0.092774
2	Sphere	3/4''					
			0	0.014558	0.402424	-	-
			50	0.003620	0.399261	-	-
			100	0.003867	0.357225	-	-
3	Sphere	9/10''					
			0	0.012799	0.718973	-	-
			50	0.011599	0.685061	-	-
			100	0.010392	0.626827	-	-
4	Sphere	1''					
			0	0.037200	0.865713	-	-
			50	0.031671	0.856257	-	-
			100	0.029414	0.855773	-	-
5	Sphere	3/2''					
			0	0.156052	2.623621	-	-
			50	0.152958	2.593971	-	-
			100	0.159274	2.621141	-	-

Table 3.9 Mean and maximum impact kinetic energies for hex bolt type #1 class; beyond 5th impact

Start Plane 1 (Energy in Joules)			(25000 hits)	Fluid Temperature: 68 F After 5th Impact		Fluid Temperature: 614 F After 5th Impact	
Part #	Part Type	Size	IKE (%)	Mean KE	Max KE	Mean KE	Max KE
6	Hex Bolt Type 1	1/2''					
			0	0.023799	0.414091	-	-
			50	0.042864	0.415146	-	-
			100	0.024259	0.430285	-	-
7	Hex Bolt Type 1	5/8''					
			0	0.029998	0.709089	-	-
			50	0.038149	0.702845	-	-
			100	0.022749	0.702588	-	-
8	Hex Bolt Type 1	3/4''					
			0	0.024671	1.156891	-	-
			50	0.024481	1.150731	-	-
			100	0.022451	1.031191	-	-
9	Hex Bolt Type 1	7/8''					
			0	0.060848	1.683891	-	-
			50	0.078040	1.717131	-	-
			100	0.059115	1.686331	-	-
10	Hex Bolt Type 1	1''					
			0	0.126752	2.537341	-	-
			50	0.132524	2.536331	-	-
			100	0.161711	2.539011	-	-

Table 3.10 Mean and maximum impact kinetic energies for hex bolt type #2 class; beyond 5th impact

Start Plane 1 (Energy in Joules)			(25000 hits)	Fluid Temperature: 68 F After 5th Impact		Fluid Temperature: 614 F After 5th Impact	
Part #	Part Type	Size	IKE (%)	Mean KE	Max KE	Mean KE	Max KE
11	Hex Bolt Type 2	1/2''					
			0	0.012477	0.466562	-	-
			50	0.016501	0.472177	-	-
			100	0.009049	0.467939	-	-
12	Hex Bolt Type 2	5/8''					
			0	0.022789	0.847076	-	-
			50	0.023741	0.848725	-	-
			100	0.022653	0.847697	-	-
13	Hex Bolt Type 2	3/4''					
			0	0.039110	1.384241	-	-
			50	0.043841	1.383411	-	-
			100	0.040453	1.384071	-	-
14	Hex Bolt Type 2	7/8''					
			0	0.311266	2.053731	-	-
			50	0.320351	2.065541	-	-
			100	0.315672	2.046211	-	-
15	Hex Bolt Type 2	1''					
			0	0.278992	3.088061	-	-
			50	0.278063	3.086061	-	-
			100	0.286047	3.090161	-	-

Table 3.11 Mean and maximum impact kinetic energies for hex nut class; beyond 5th impact

Start Plane 1 (Energy in Joules)			(25000 hits)	Fluid Temperature: 68 F After 5th Impact		Fluid Temperature: 614 F After 5th Impact	
Part #	Part Type	Size	IKE (%)	Mean KE	Max KE	Mean KE	Max KE
16	Hex Nut	1/2''					
			0	0.004093	0.243100	0.018247	0.031925
			50	0.003548	0.240595	0.018519	0.035113
			100	0.004671	0.263094	0.018416	0.038083
17	Hex Nut	5/8''					
			0	0.024499	0.456262	-	-
			50	0.017156	0.455724	-	-
			100	0.021962	0.456643	-	-
18	Hex Nut	3/4''					
			0	0.011474	0.701135	-	-
			50	0.027315	0.718827	-	-
			100	0.018630	0.707023	-	-
19	Hex Nut	7/8''					
			0	0.025107	1.063971	-	-
			50	0.026214	1.068910	-	-
			100	0.019092	1.052671	-	-
20	Hex Nut	1''					
			0	0.054476	1.561481	-	-
			50	0.040467	1.557410	-	-
			100	0.050080	1.561210	-	-

Table 3.12 Mean and maximum impact kinetic energies for cylinder class; beyond 5th impact

Start Plane 1 (Energy in Joules)			(25000 hits)	Fluid Temperature: 68 F After 5th Impact		Fluid Temperature: 614 F After 5th Impact	
Part #	Part Type	Size	IKE (%)	Mean KE	Max KE	Mean KE	Max KE
21	Cylinder	1/2''					
			0	0.014971	0.372122	-	-
			50	0.024313	0.386641	-	-
			100	0.037631	0.384216	-	-
22	Cylinder	3/4''					
			0	0.021722	1.020551	-	-
			50	0.028425	1.030011	-	-
			100	0.023615	1.018510	-	-
23	Cylinder	7/8''					
			0	0.073818	1.637531	-	-
			50	0.081204	1.624891	-	-
			100	0.089797	1.632541	-	-
24	Cylinder	1''					
			0	0.451153	2.333110	-	-
			50	0.445883	2.346331	-	-
			100	0.448881	2.352921	-	-

Table 3.13 Mean and maximum impact kinetic energies for rectangular bar class; beyond 5th impact

Start Plane 1 (Energy in Joules)			(25000 hits)	Fluid Temperature: 68 F After 5th Impact		Fluid Temperature: 614 F After 5th Impact	
Part #	Part Type	Size	IKE (%)	Mean KE	Max KE	Mean KE	Max KE
25	Rectangular Bar	1/2''					
			0	0.015378	0.461239	-	-
			50	0.010657	0.428536	-	-
			100	0.008984	0.426893	0.080265	0.463801
26	Rectangular Bar	3/4''					
			0	0.081679	1.342371	-	-
			50	0.055483	1.391231	-	-
			100	0.062202	1.345310	-	-
27	Rectangular Bar	7/8''					
			0	0.138666	2.114851	-	-
			50	0.199695	2.120731	-	-
			100	0.132058	2.115831	-	-
28	Rectangular Bar	1''					
			0	0.384486	3.010381	-	-
			50	0.382457	2.989281	-	-
			100	0.387410	3.028651	-	-

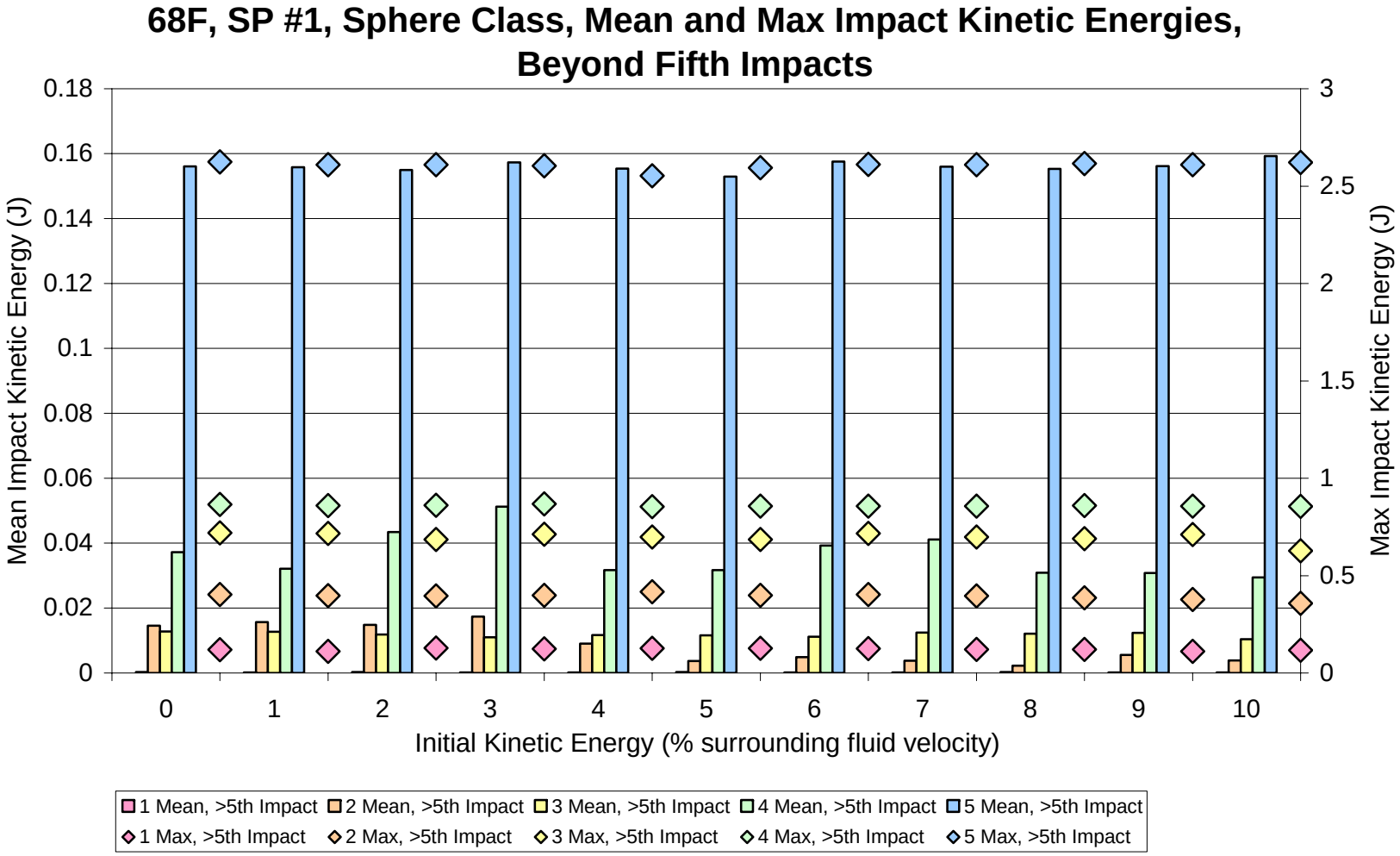

Figure 3.66 Mean and maximum impact kinetic energies for sphere class; beyond 5th impacts

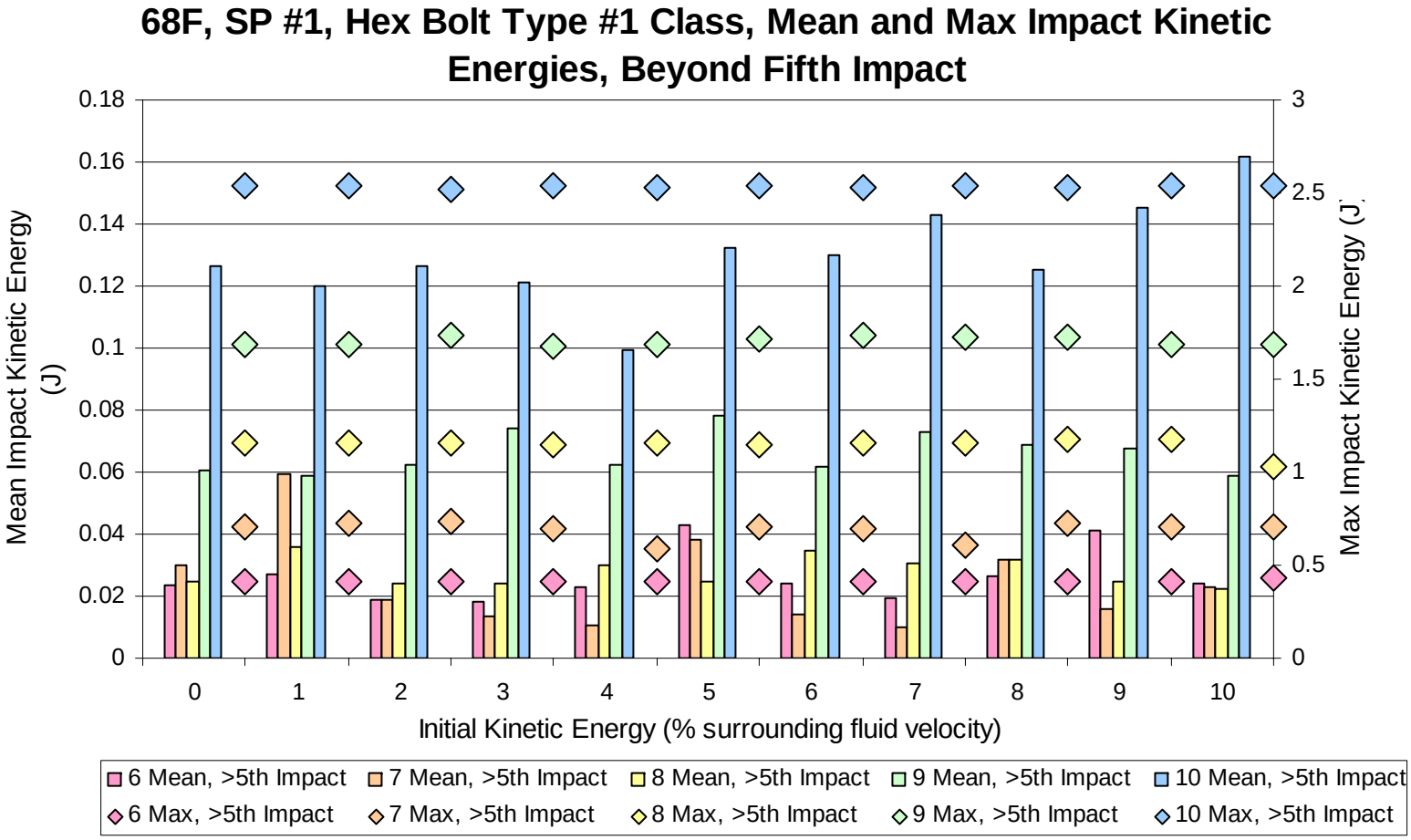

Figure 3.67 Mean and maximum impact kinetic energies for hex bolt #1 class; beyond 5th impacts

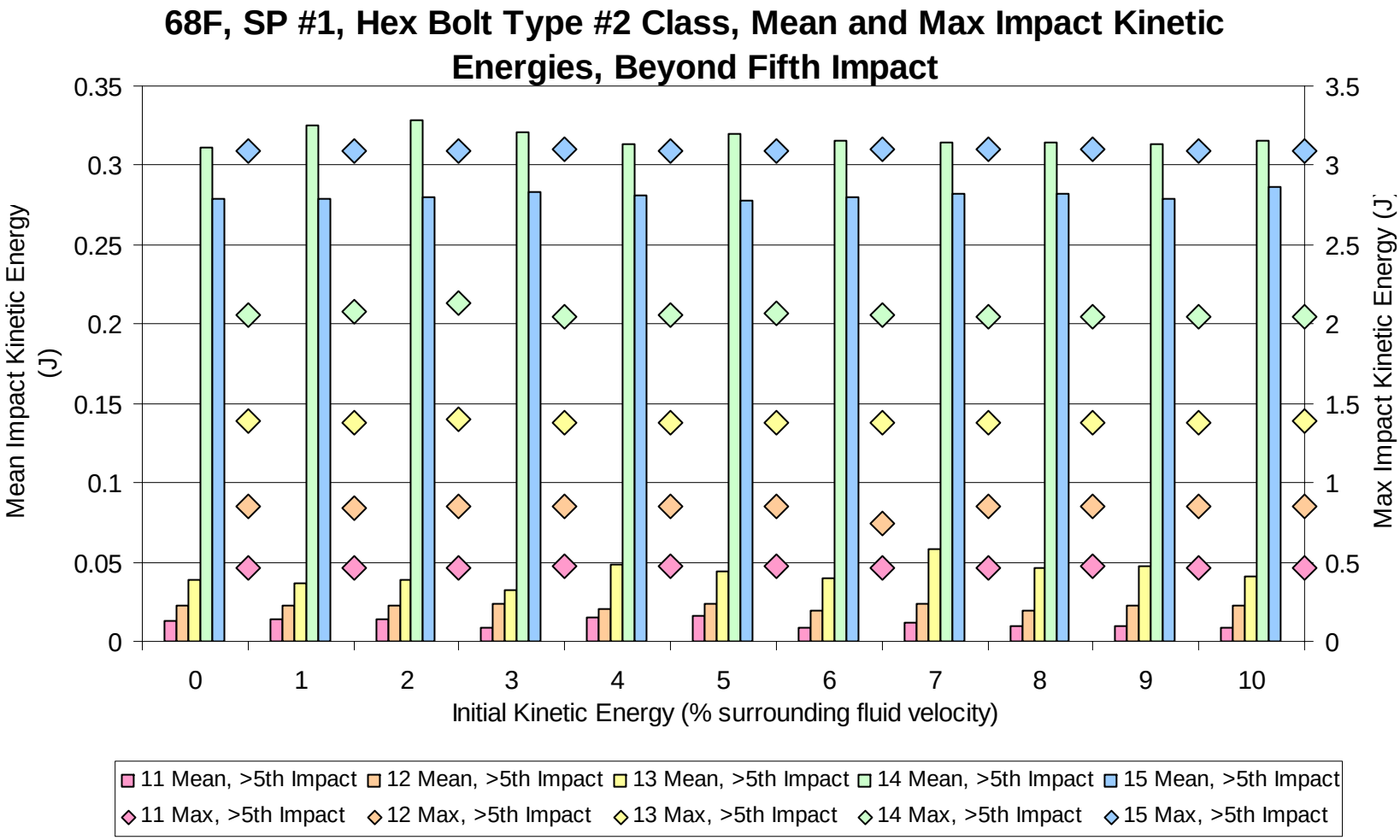

Figure 3.68 Mean and maximum impact kinetic energies for hex bolt #2 class; beyond 5th impacts

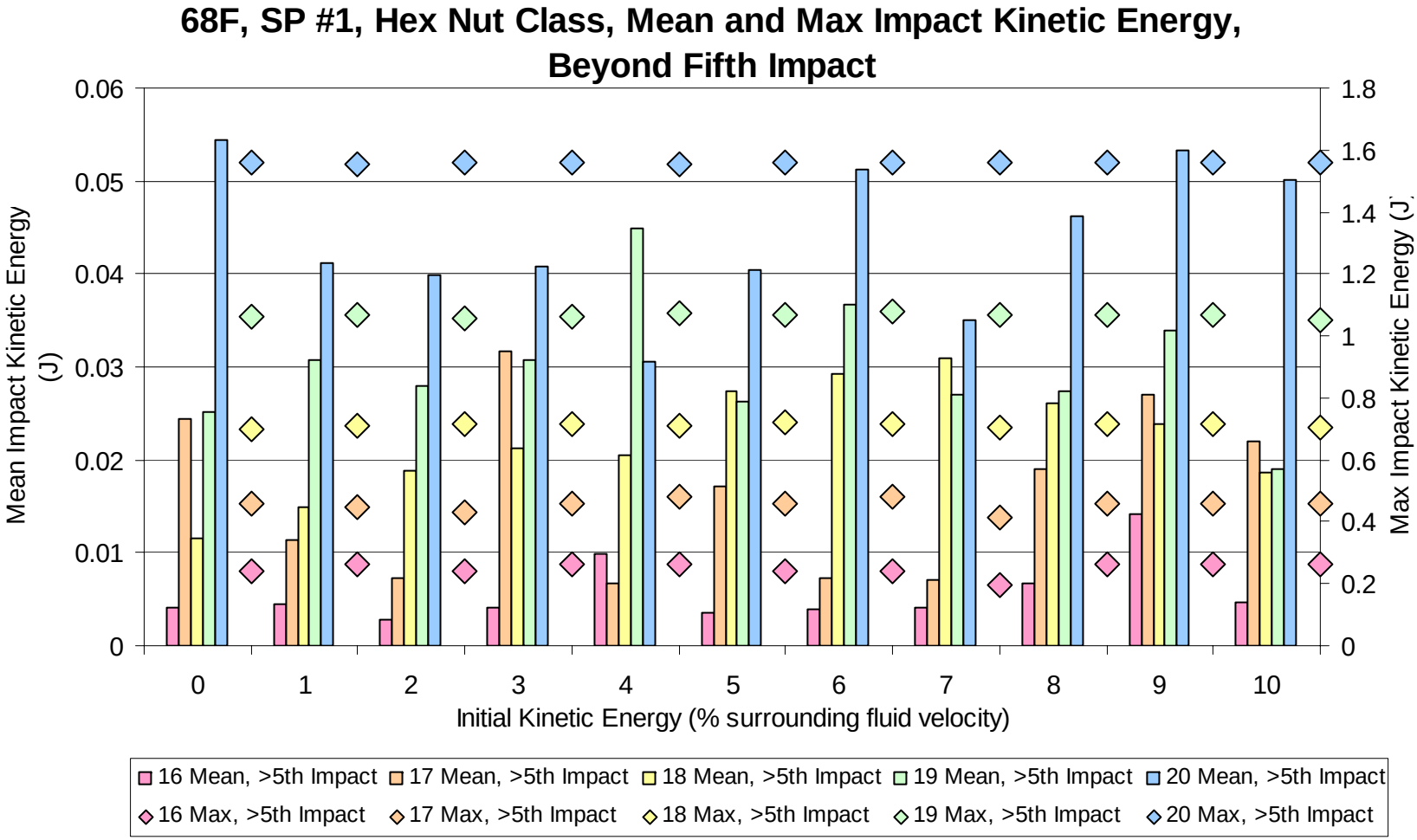

Figure 3.69 Mean and maximum impact kinetic energies for hex nut class; beyond 5th impacts

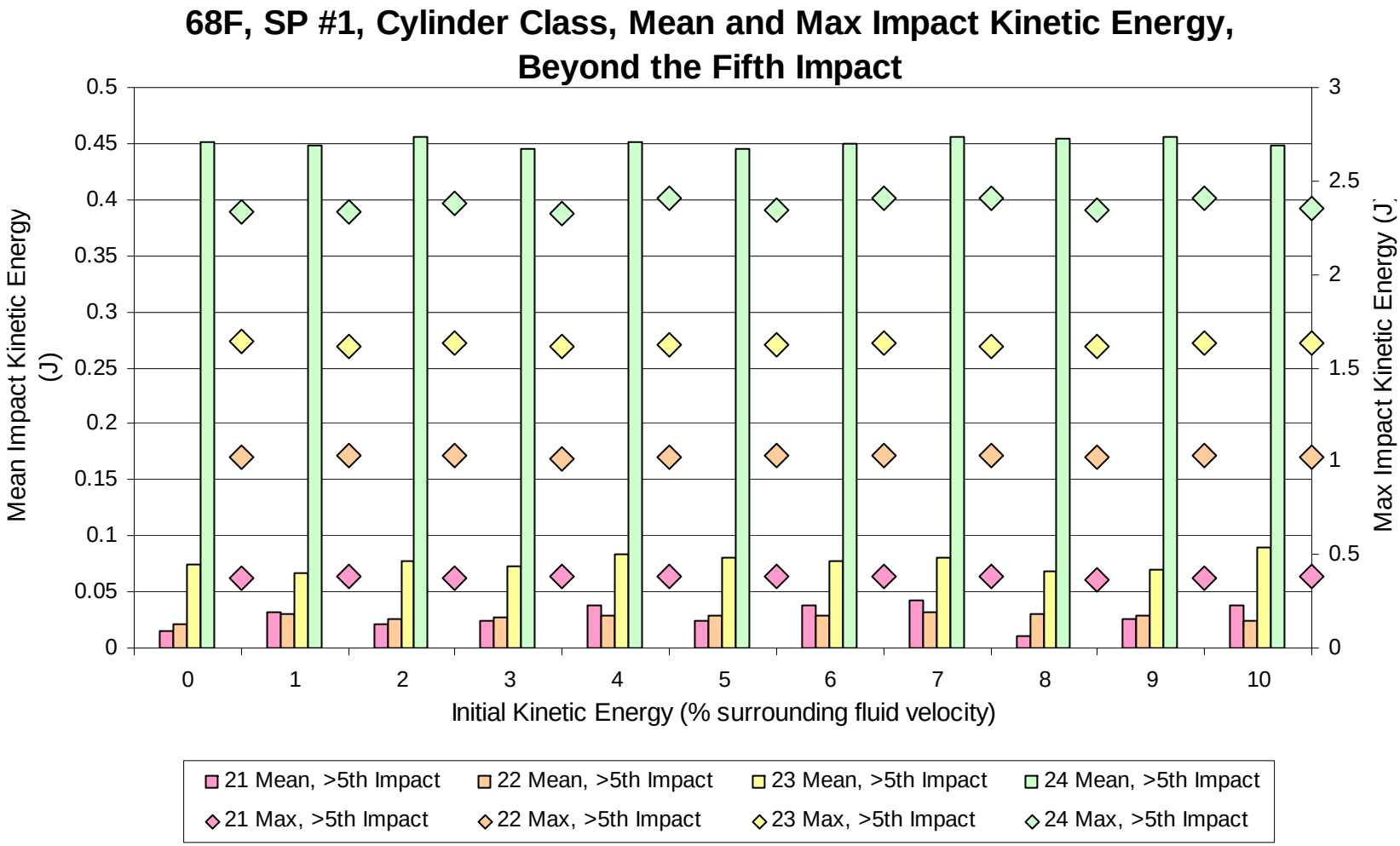

Figure 3.70 Mean and maximum impact kinetic energies for cylinder class; beyond 5th impacts

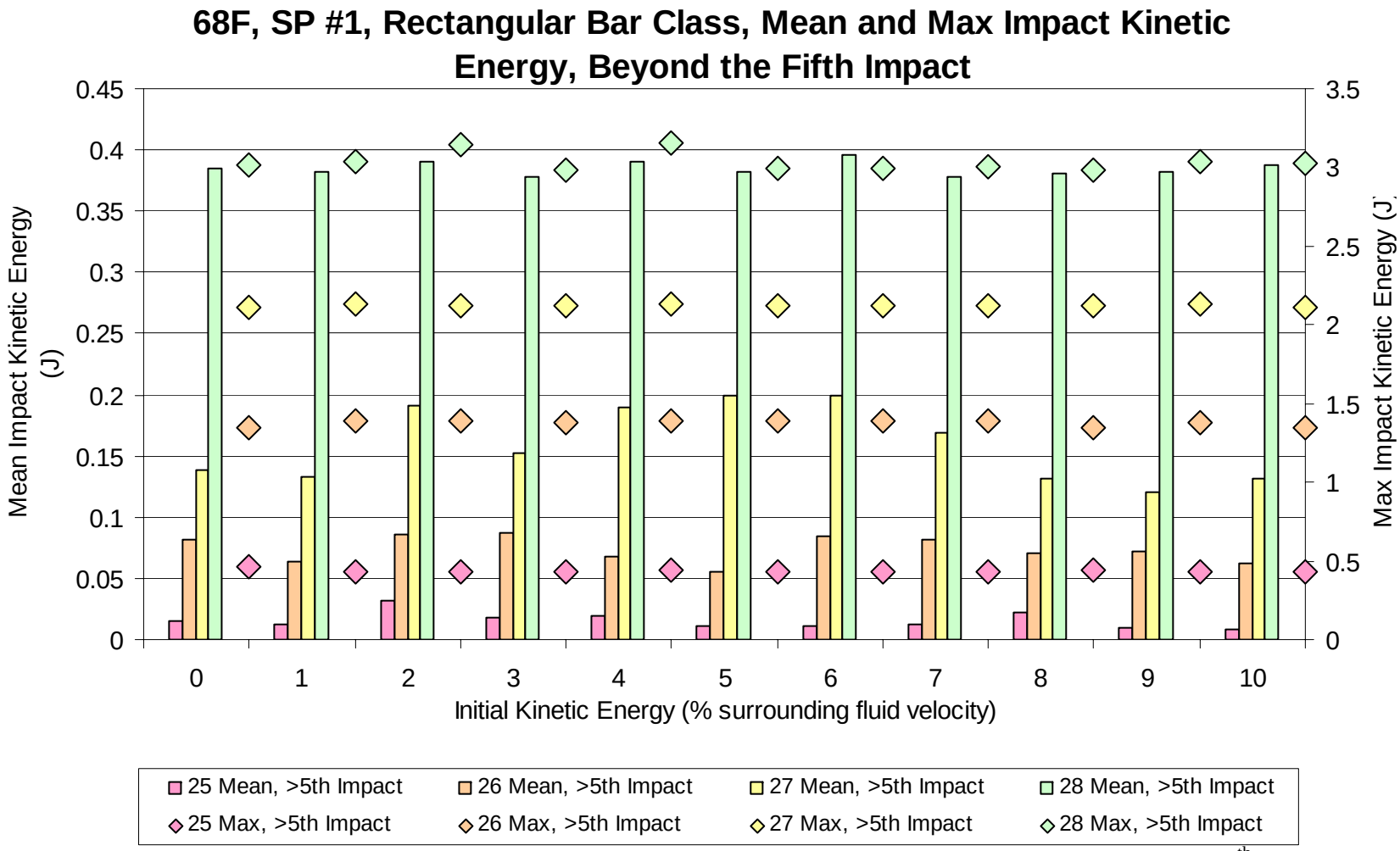

Figure 3.71 Mean and maximum impact kinetic energies for rectangular bar class; beyond 5th impacts

Tables 3.14 and **3.15** depict sorted mean and max kinetic energies as a function of part number respectively. Not necessarily the largest part in each class has the highest mean kinetic energy but the largest in each class has the highest maximum kinetic energy.

Table 3.14 Sorted mean kinetic energies as a function of part number

Rank	Mean KE (J)	Part Number	Rank	Mean KE (J)	Part Number
1	0.44864	24	15	0.03030	7
2	0.38478	28	16	0.02564	21
3	0.31576	14	17	0.02459	22
4	0.28103	15	18	0.02387	8
5	0.15681	27	19	0.02347	19
6	0.15609	5	20	0.02306	12
7	0.14033	10	21	0.02121	17
8	0.08161	23	22	0.01914	18
9	0.06645	26	23	0.01268	11
10	0.06600	9	24	0.01167	25
11	0.04834	20	25	0.01160	3
12	0.04113	13	26	0.00735	2
13	0.03276	4	27	0.00410	16
14	0.03031	6	28	0.00021	1

Table 3.15 Sorted max kinetic energies as a function of part number

Rank	Max KE (J)	Part Number	Rank	Max KE (J)	Part Number
1	3.09016	15	15	1.03001	22
2	3.02865	28	16	0.86571	4
3	2.62362	5	17	0.84873	12
4	2.53901	10	18	0.71897	3
5	2.35292	24	19	0.71883	18
6	2.12073	27	20	0.70909	7
7	2.06554	14	21	0.47218	11
8	1.71713	9	22	0.46124	25
9	1.63753	23	23	0.45664	17
10	1.56148	20	24	0.43029	6
11	1.39123	26	25	0.40242	2
12	1.38424	13	26	0.38664	21
13	1.15689	8	27	0.26309	16
14	1.06891	19	28	0.12643	1

The following figures represent a compilation of multiple simulations on one figure. Each depicts the spatial impact distribution on the tube sheet of the lightest and heaviest part for each class at initial kinetic energies 0% through 100% and starting locations 1 and 2 for temperatures 68^0F and 614^0F. Note the total number of impacts in the lower right corner of each figure. For some of the parts, a majority of impacts occur in small regions of the tube sheet. Generally, the impacts tend to be the less energetic impacts because a part will tend to stay contained in this region without the ability to build up much kinetic energy to impart on the tube sheet. These regions tend to be the two corners and the back end of the tube sheet away from the plenum divide. The lighter parts generally tend to end up in these three regions where the heavier parts have enough mass to drop out of the flow and reenter the main flow plume to come up and hit with higher impact kinetic energies.

Beyond, there are figures which represent the spatial impact distribution as a function of impact kinetic energy. These plots represent the same data as described in the previous paragraph except the data has been partitioned into a 20 x 40 rectangular mesh of spatial bins spanning the radius of the tube sheet. The largest graph on each of these figures represents the total impact frequency. The smaller graphs show the impact frequency for the energy ranges of 0% to 1%, 1% to 2%, 2% to 5%, 5% to 10%, 10% to 25%, 25% to 50%, 50% to 90% and 90% to 100% of the maximum impact kinetic energy for that group of simulations. Note that the scaling for each graph is not the same. The grouping of the heavier parts is noticeably in the center of the tube sheet with a fairly regular pattern. The lighter parts tend to have more sporadic distributions depending on where the part was pinned to the tube sheet.

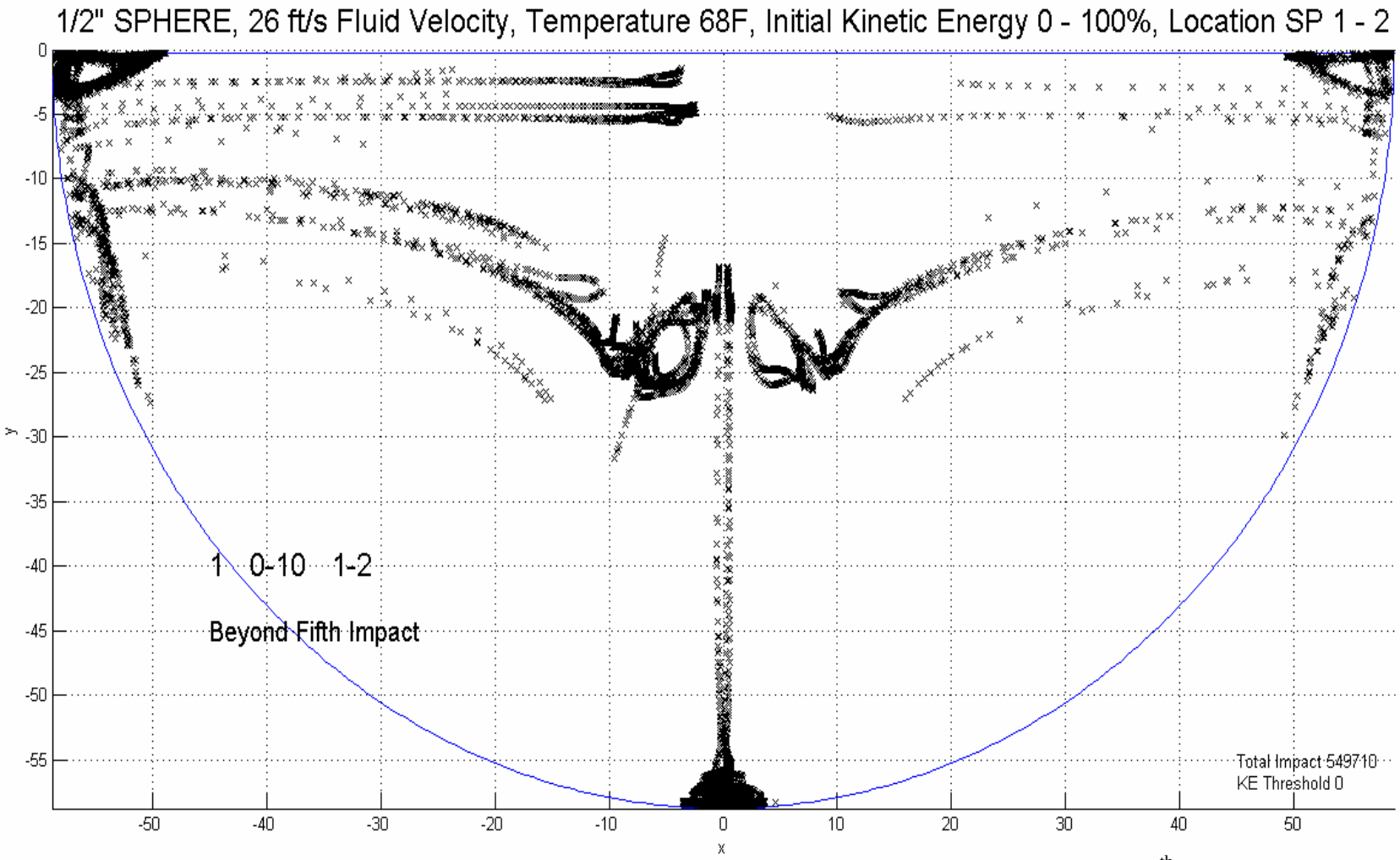

Figure 3.72 1/2" sphere combined spatial impact kinetic energy distribution; beyond 5th impacts

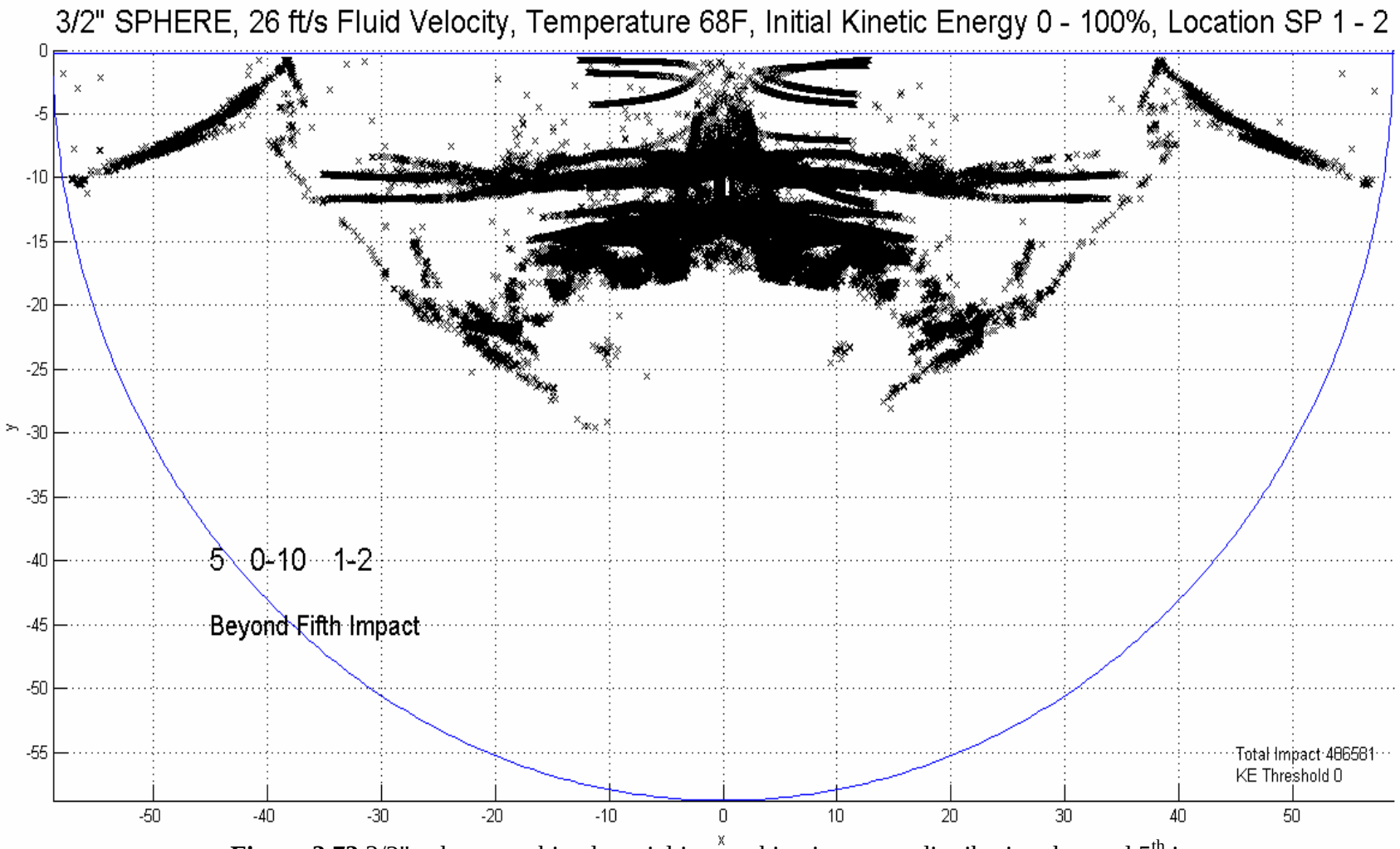

Figure 3.73 3/2" sphere combined spatial impact kinetic energy distribution; beyond 5th impacts

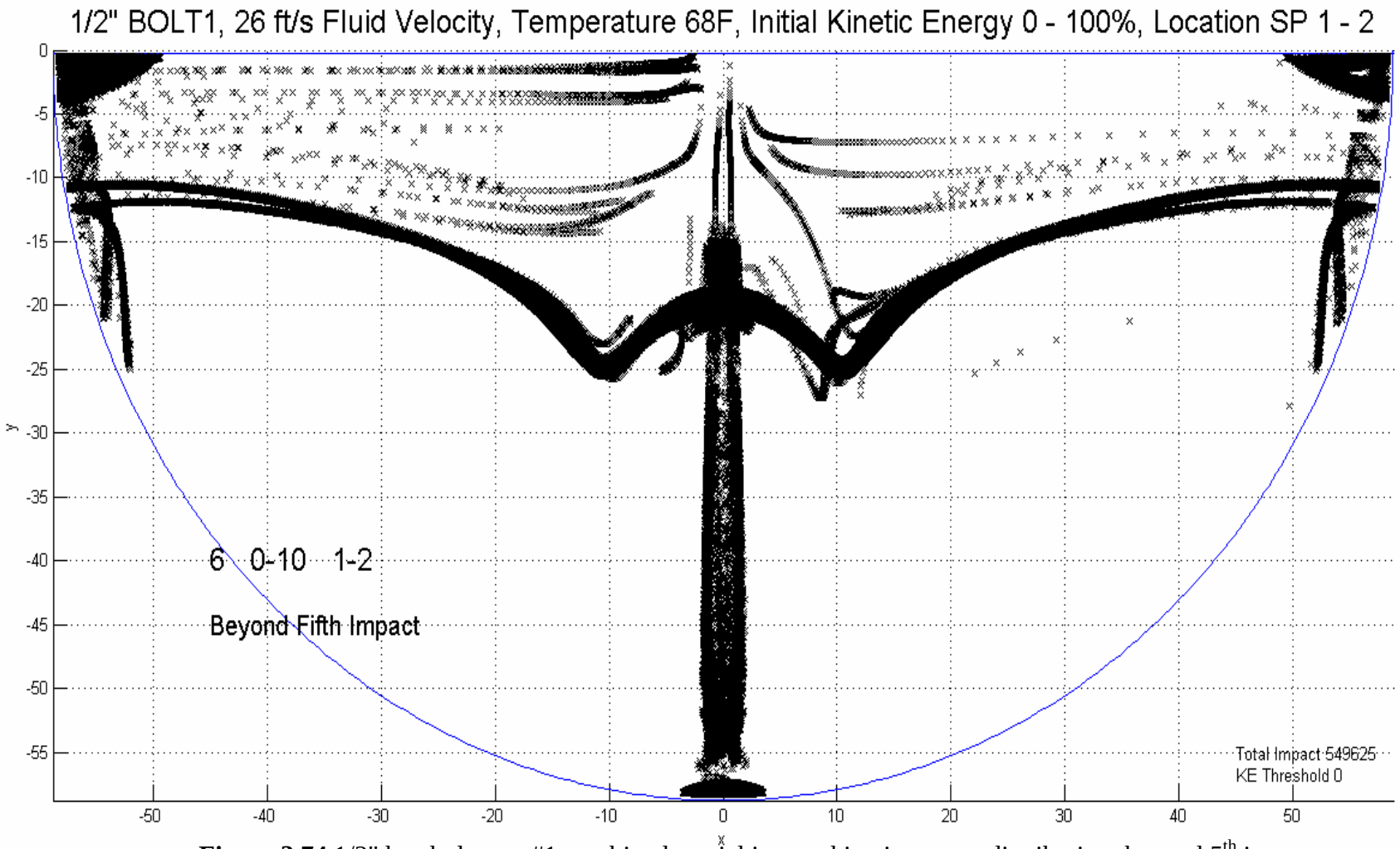

Figure 3.74 1/2" hex bolt type #1 combined spatial impact kinetic energy distribution; beyond 5th impacts

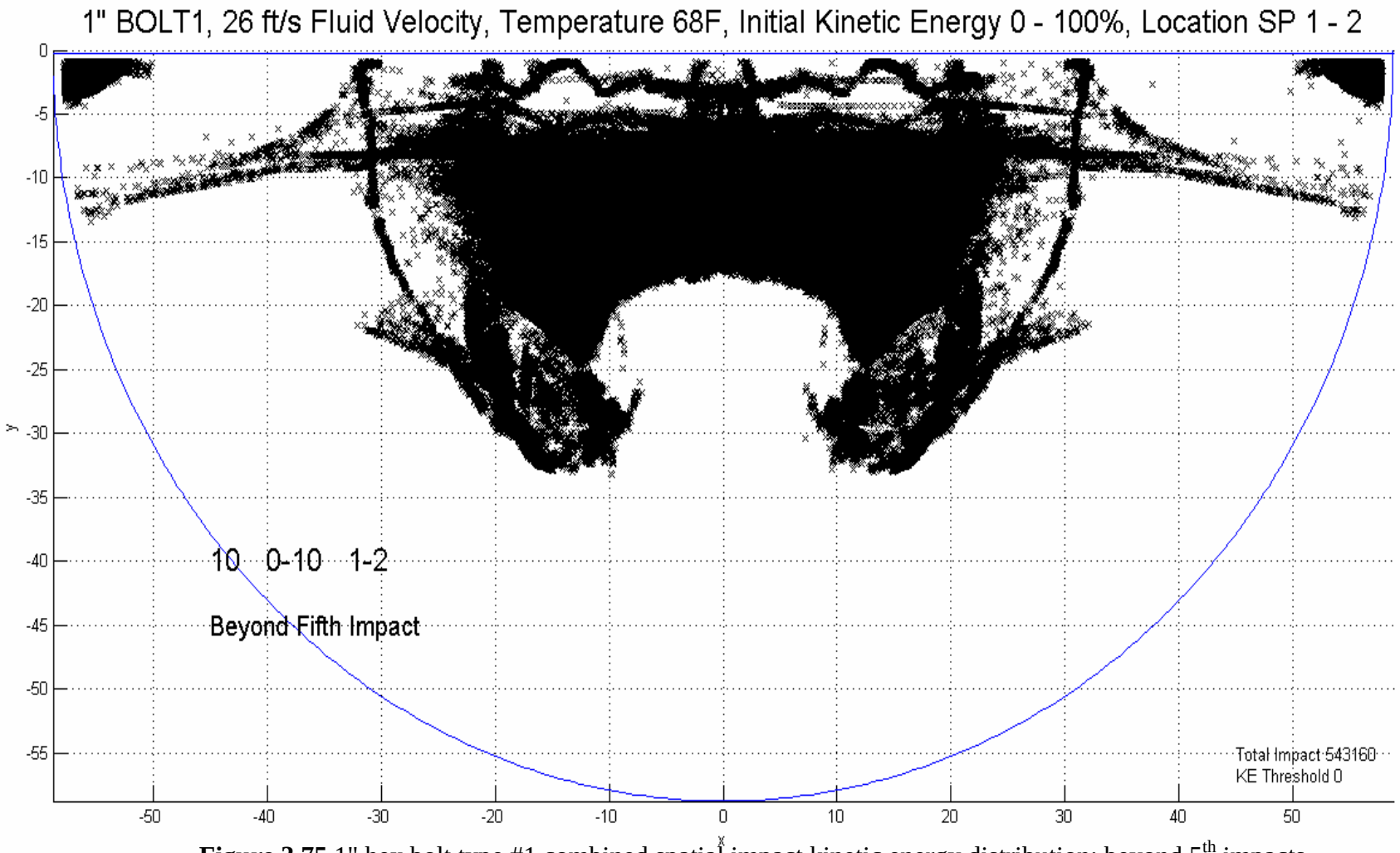

Figure 3.75 1" hex bolt type #1 combined spatial impact kinetic energy distribution; beyond 5th impacts

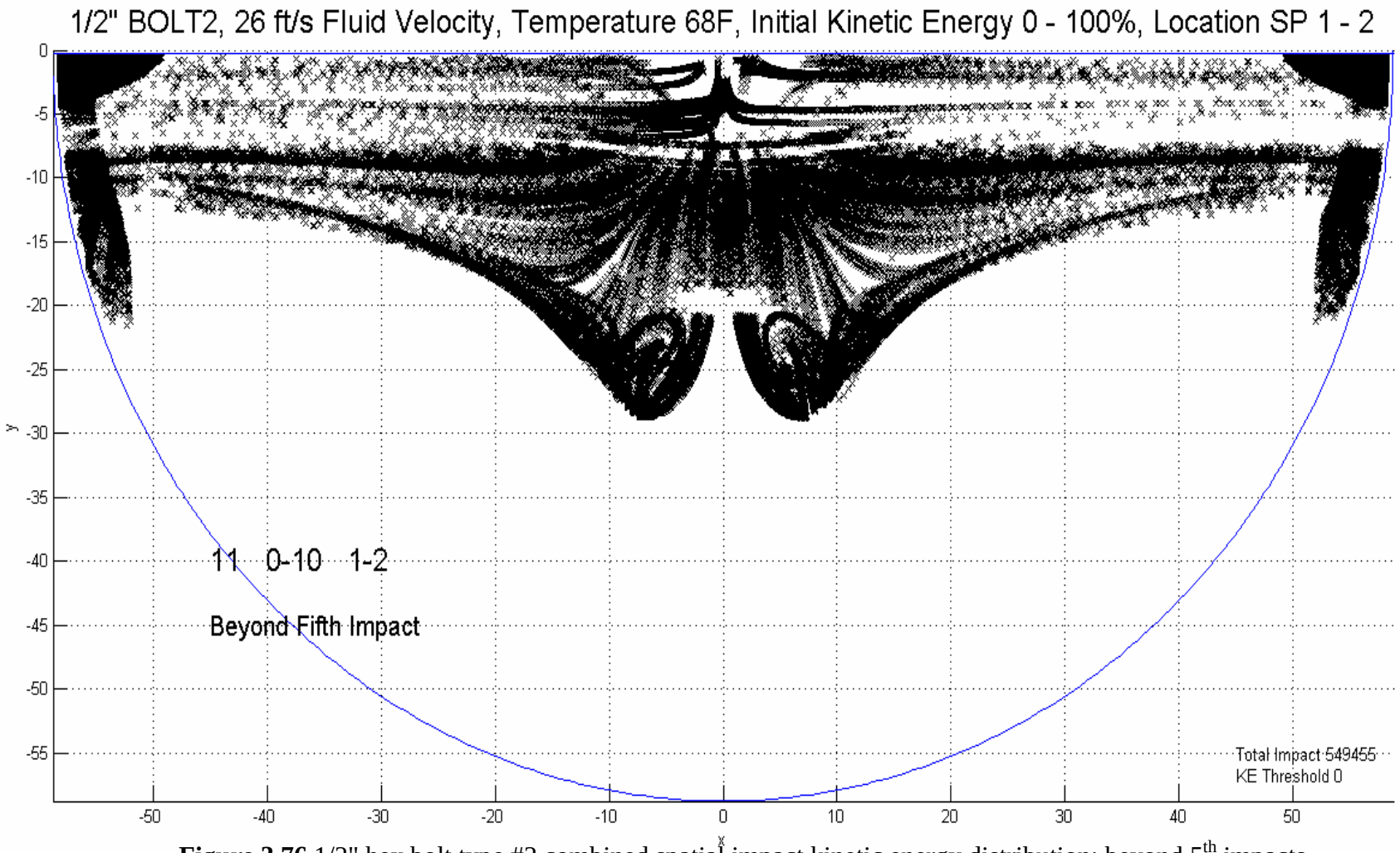

Figure 3.76 1/2" hex bolt type #2 combined spatial impact kinetic energy distribution; beyond 5th impacts

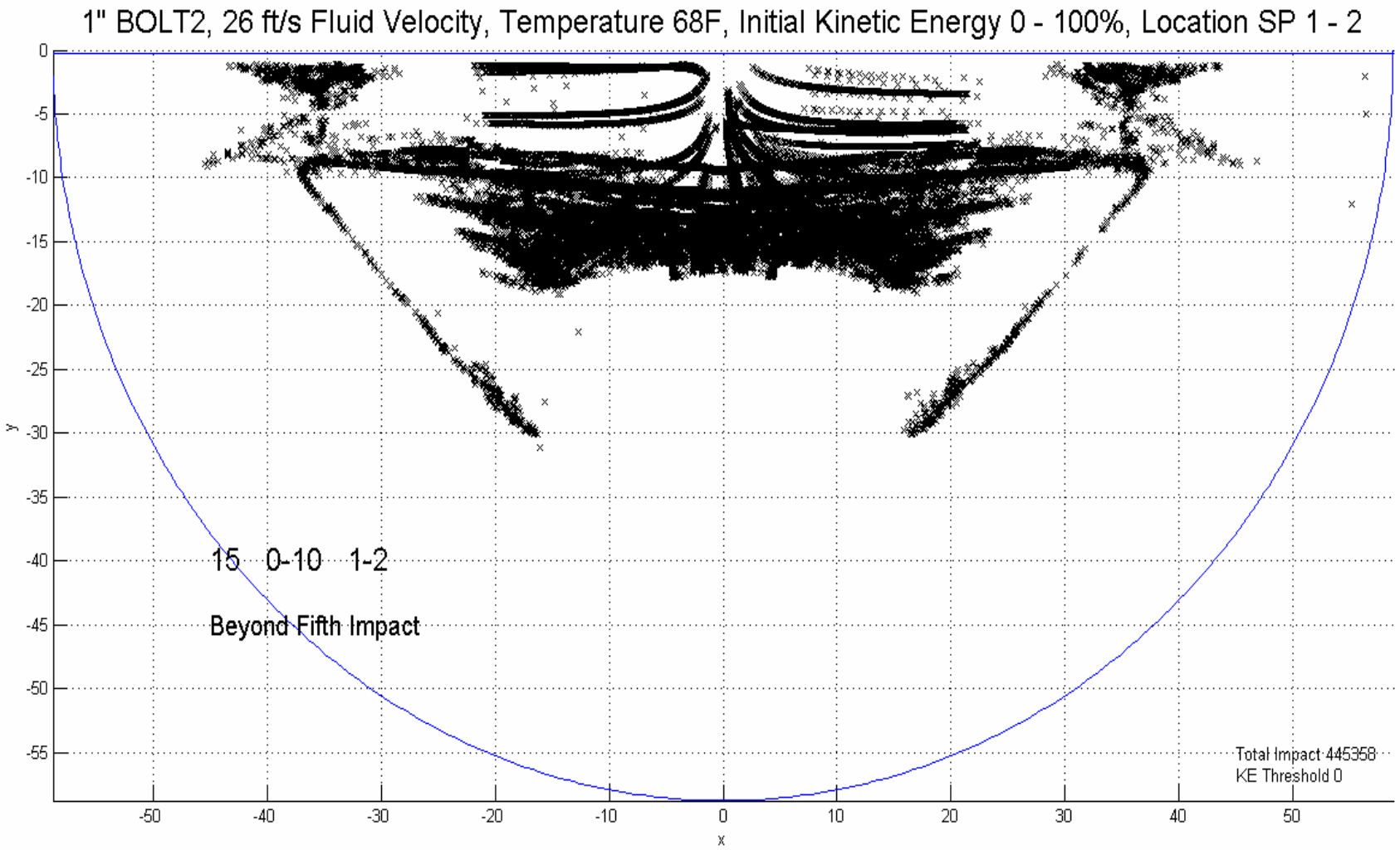

Figure 3.77 1" hex bolt type #2 combined spatial impact kinetic energy distribution; beyond 5th impacts

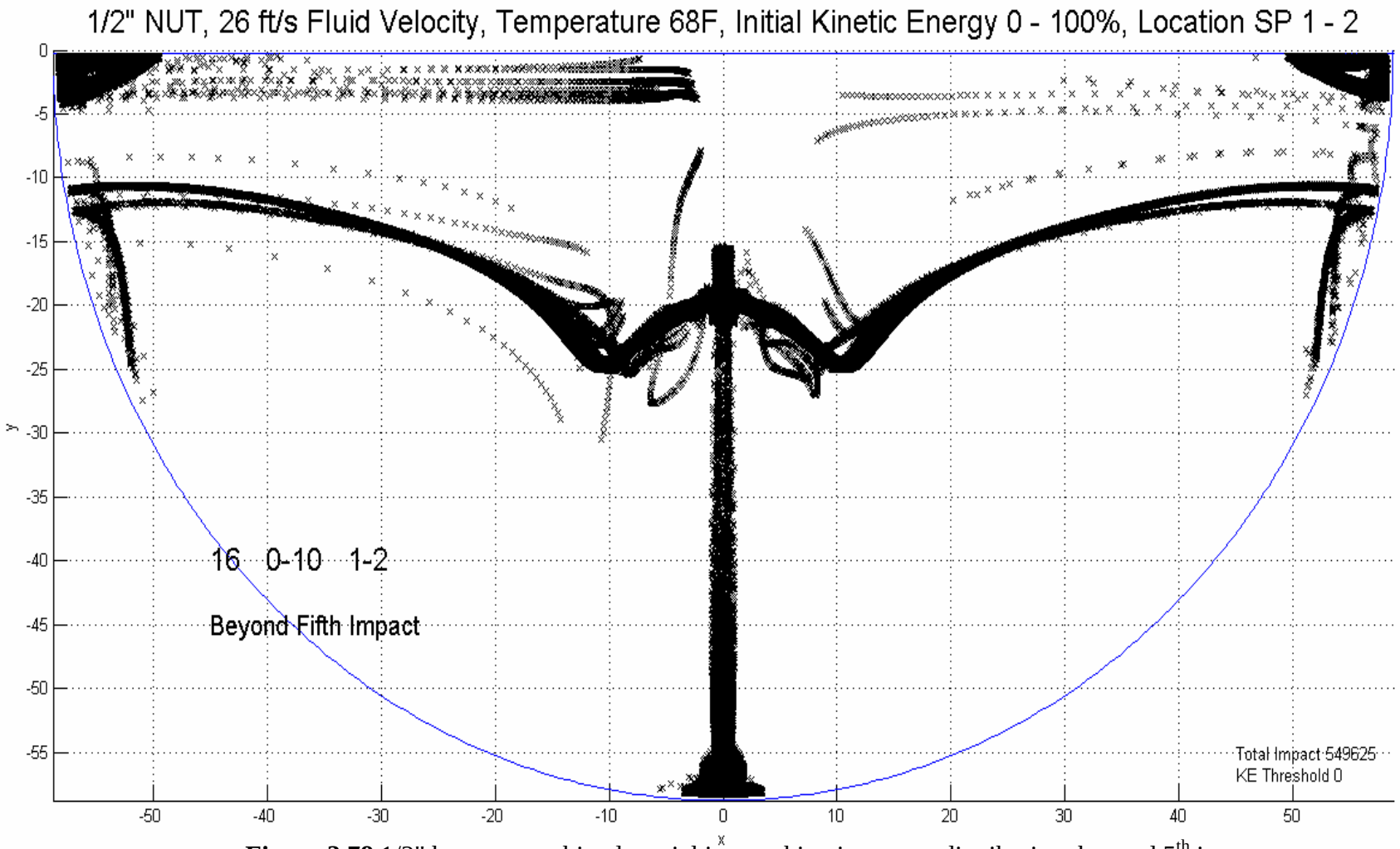

Figure 3.78 1/2" hex nut combined spatial impact kinetic energy distribution; beyond 5th impacts

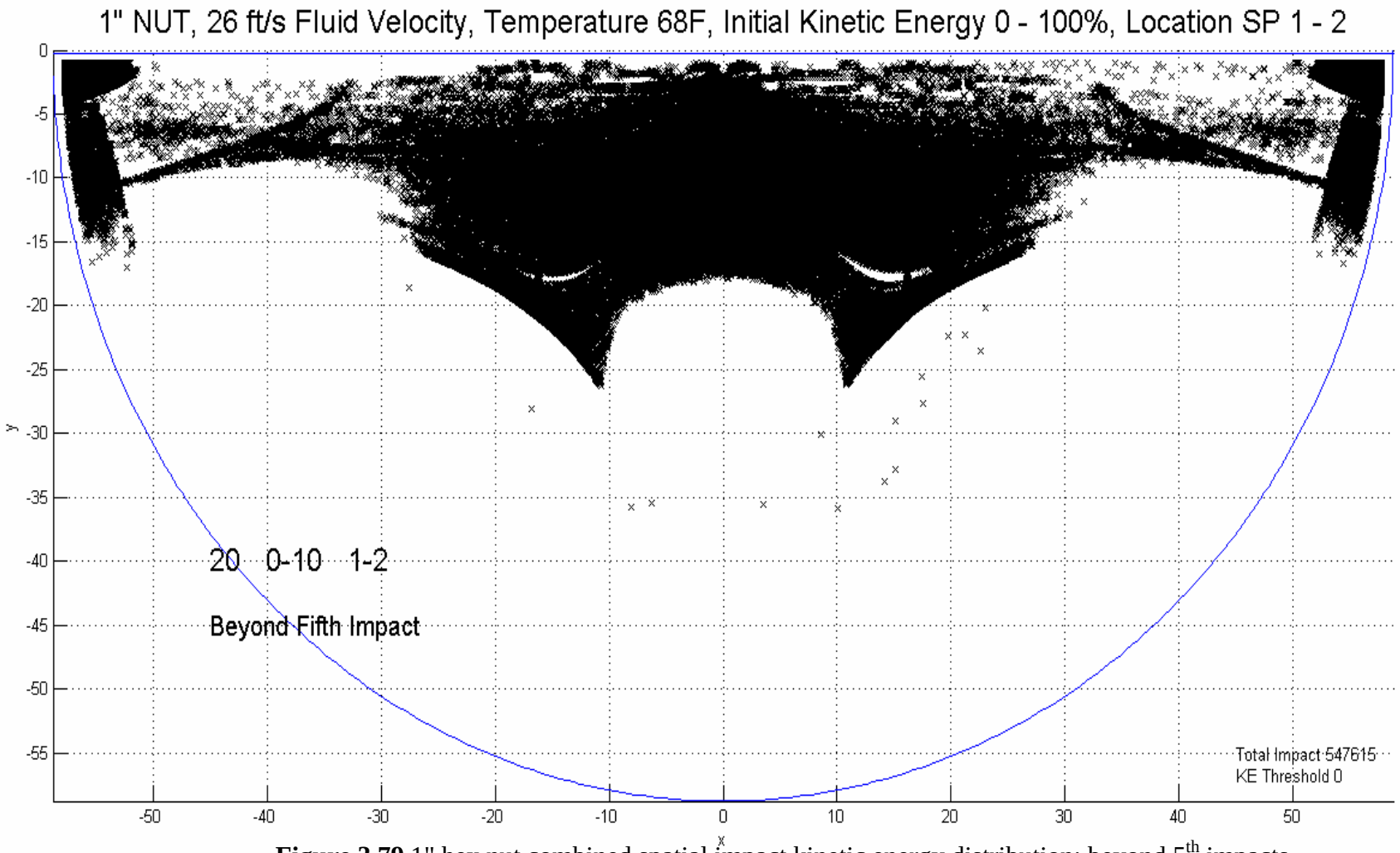

Figure 3.79 1" hex nut combined spatial impact kinetic energy distribution; beyond 5th impacts

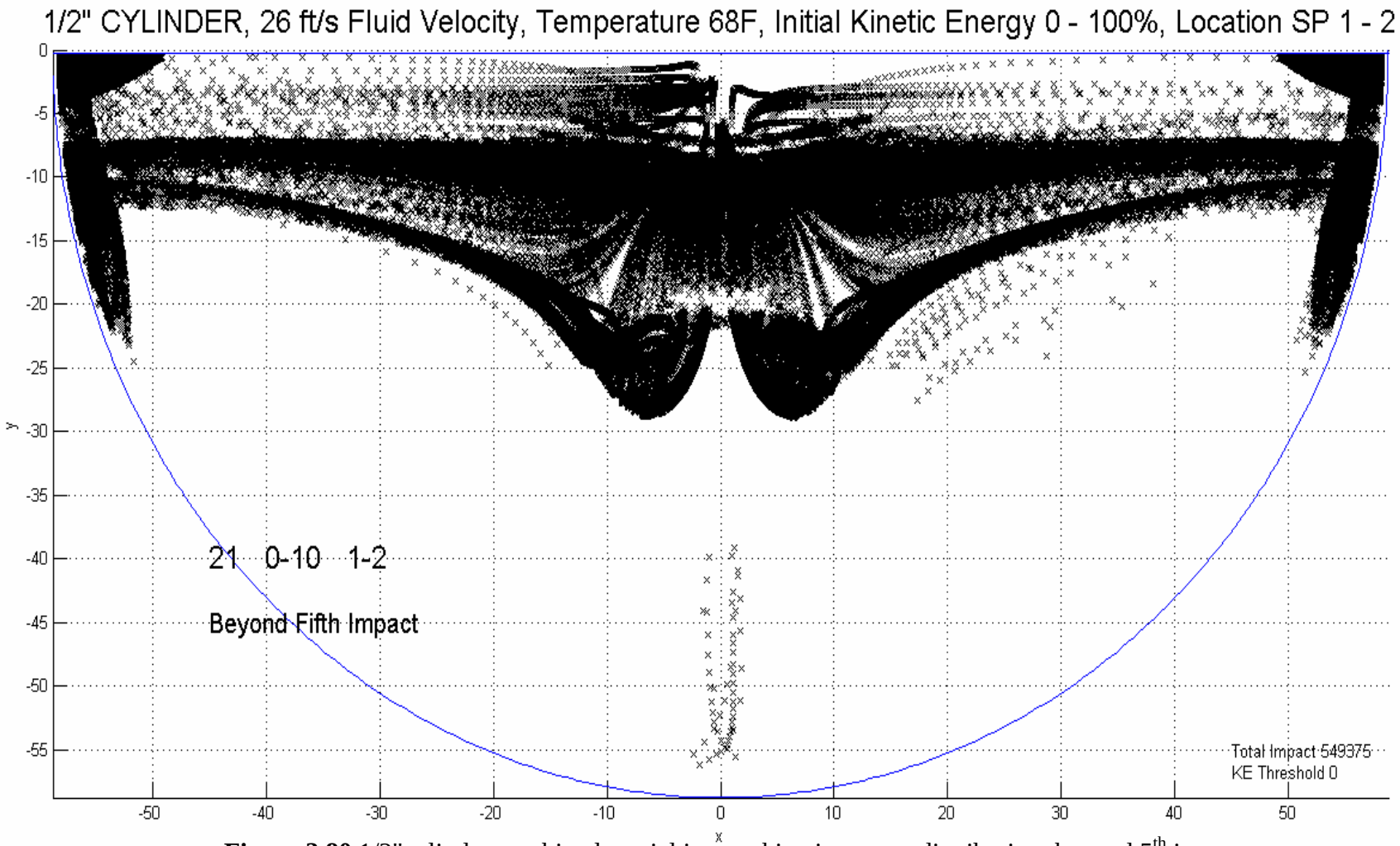

Figure 3.80 1/2"cylinder combined spatial impact kinetic energy distribution; beyond 5th impacts

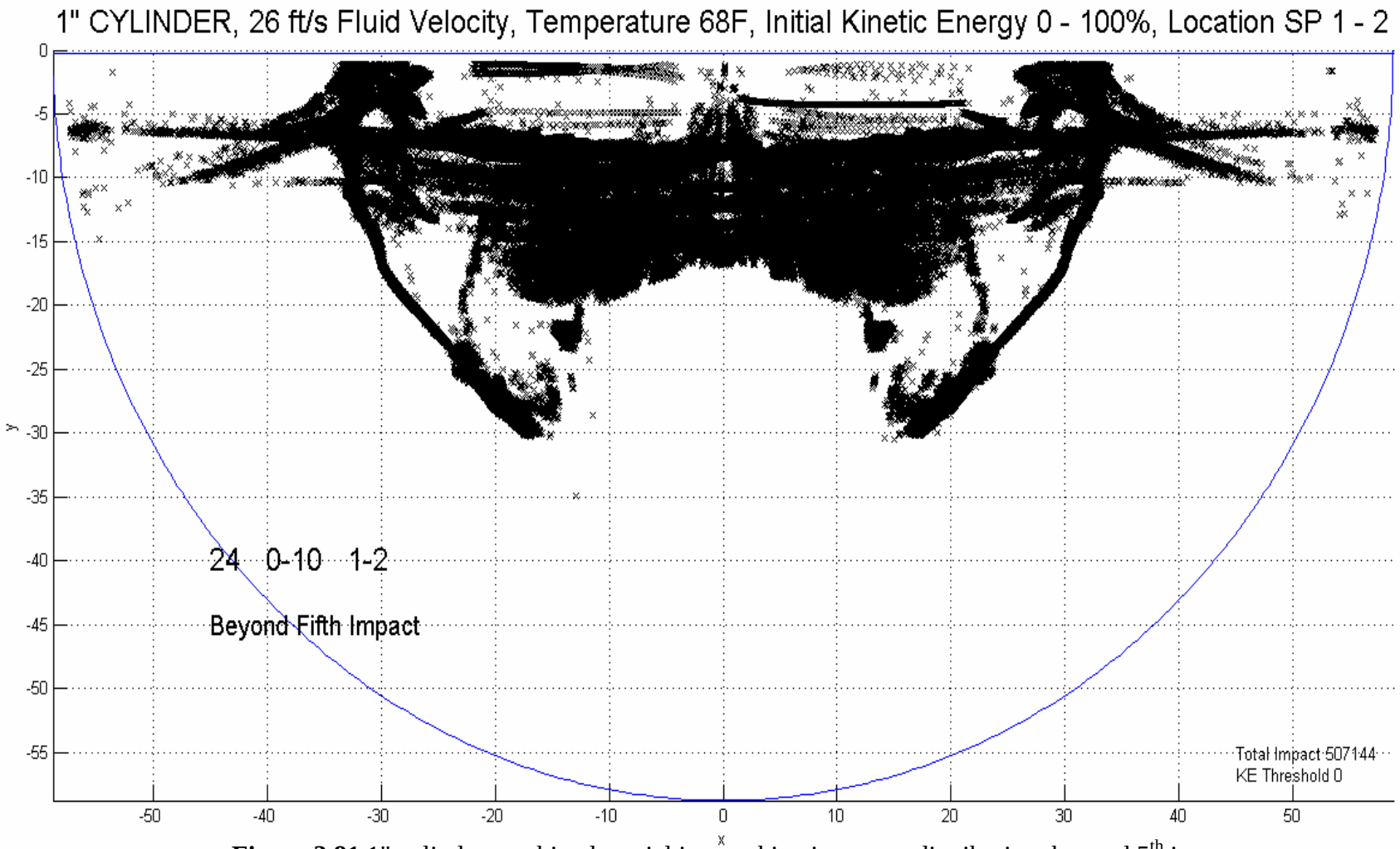

Figure 3.81 1" cylinder combined spatial impact kinetic energy distribution; beyond 5th impacts

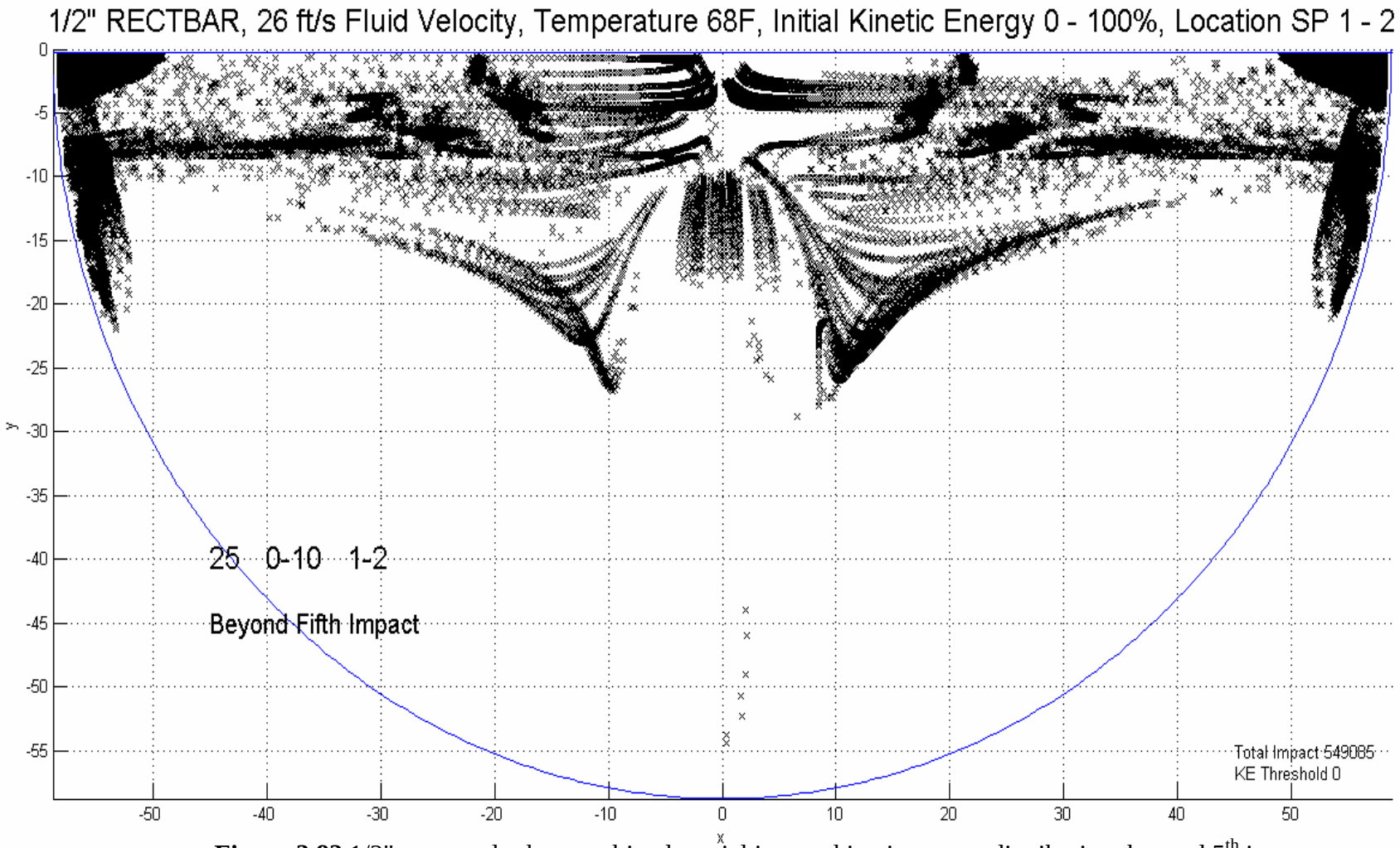

Figure 3.82 1/2" rectangular bar combined spatial impact kinetic energy distribution; beyond 5th impacts

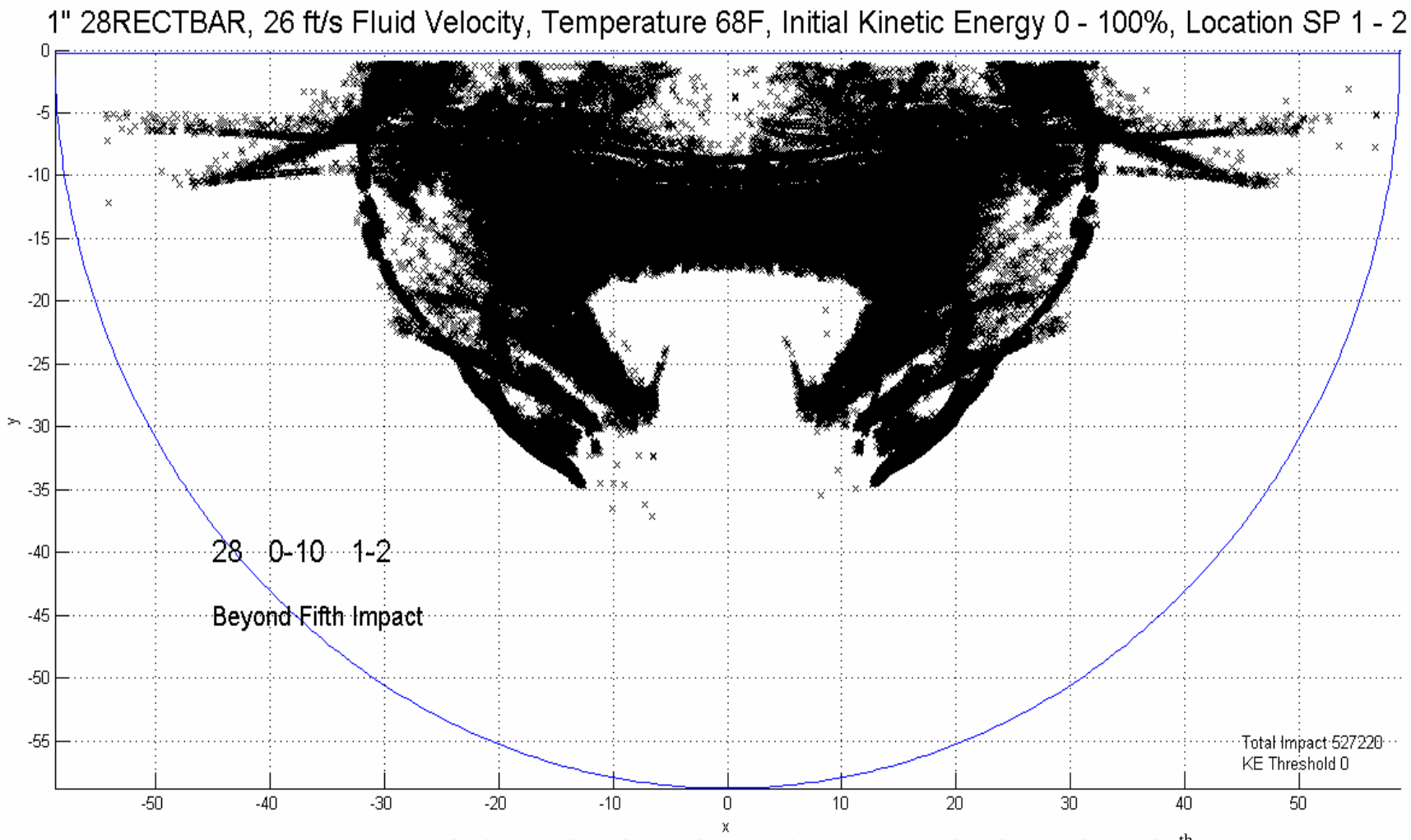

Figure 3.83 1" rectangular bar combined spatial impact kinetic energy distribution; beyond 5th impacts

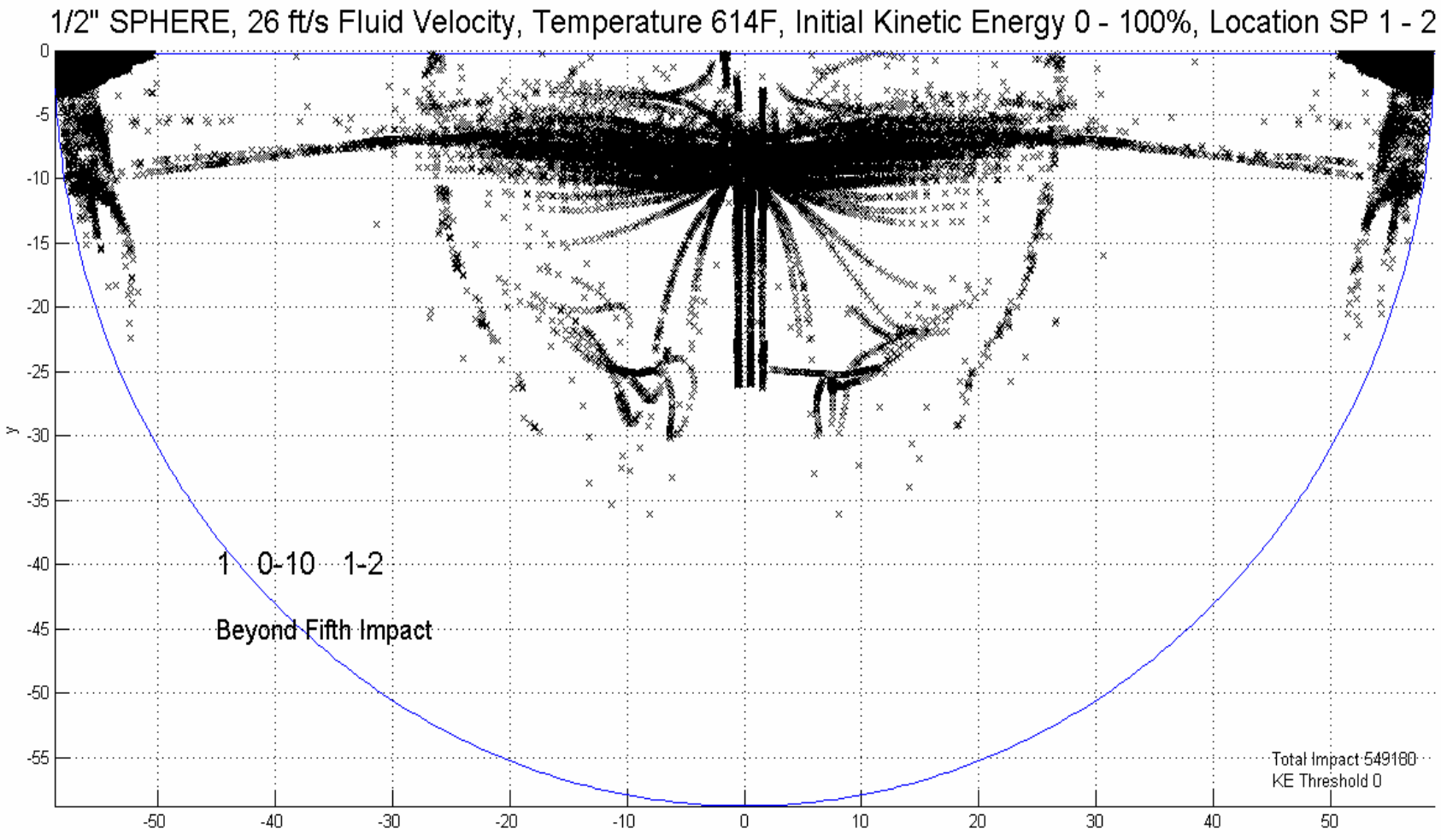

Figure 3.84 1/2" sphere combined spatial impact kinetic energy distribution 614^{0}F; beyond 5^{th} impacts

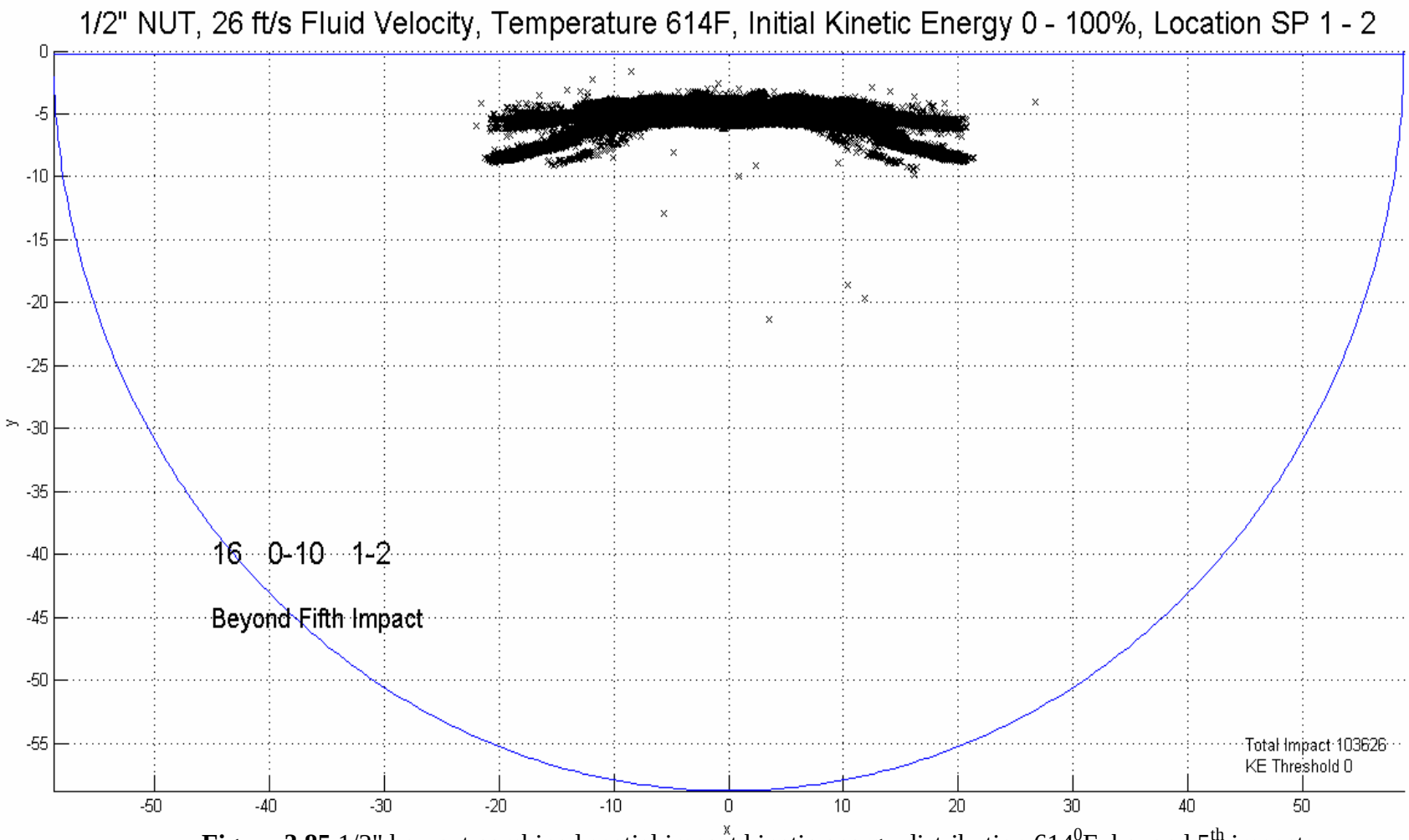

Figure 3.85 1/2" hex nut combined spatial impact kinetic energy distribution 614^{0}F; beyond 5^{th} impacts

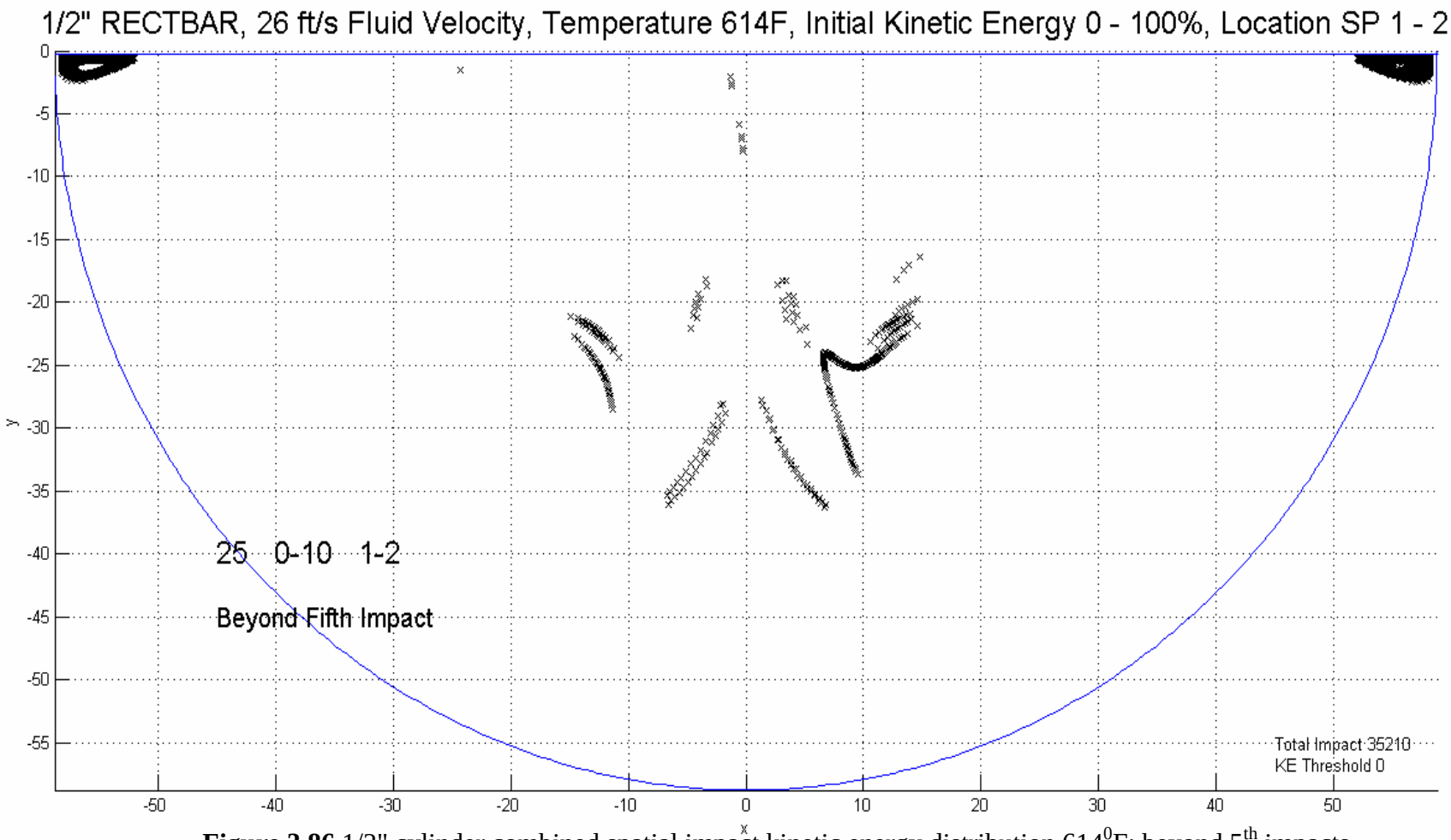

Figure 3.86 1/2" cylinder combined spatial impact kinetic energy distribution 614^{0}F; beyond 5^{th} impacts

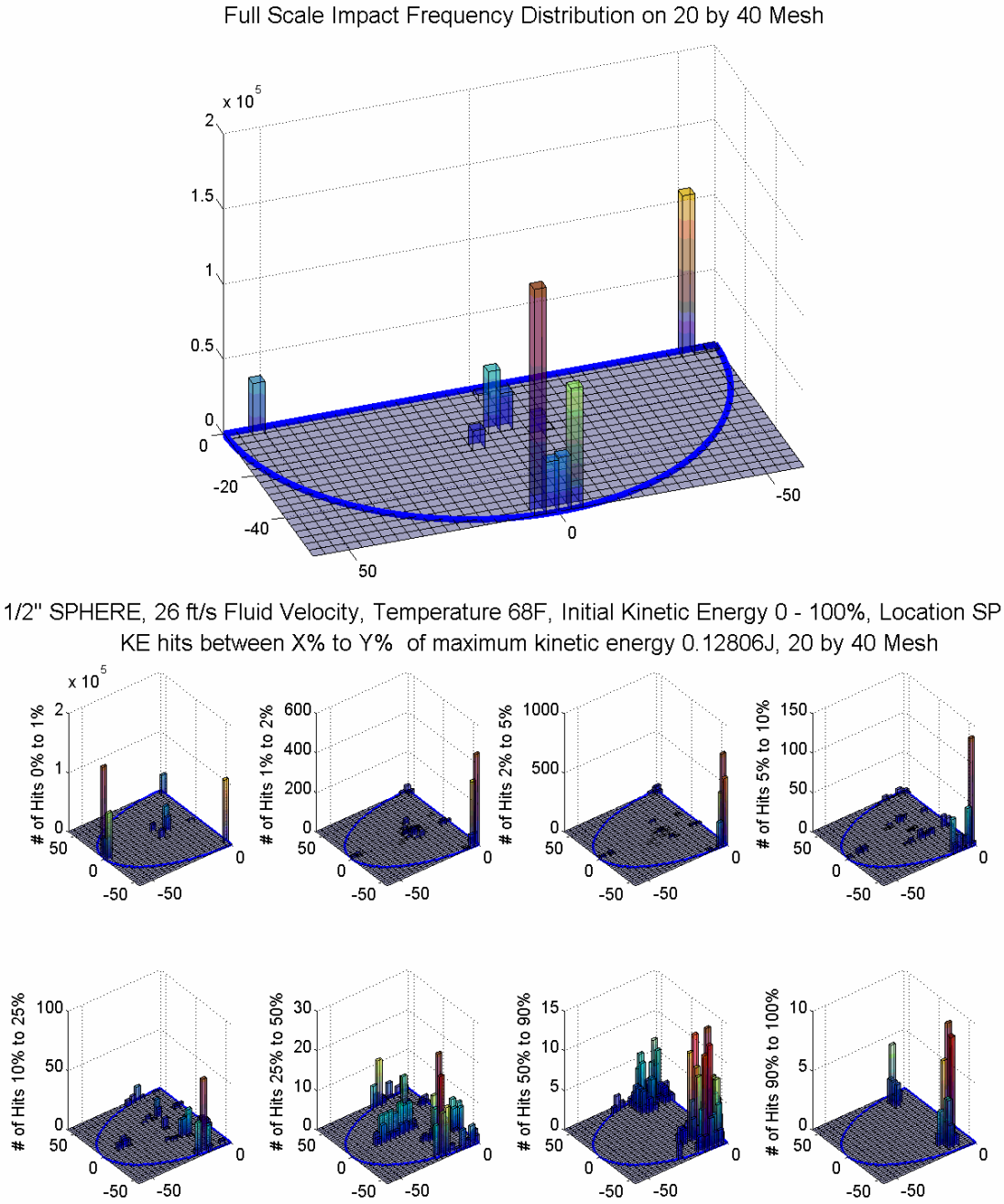

Figure 3.87 1/2" sphere combined spatial impact kinetic energy distribution as a function of impact energy; beyond 5th impacts

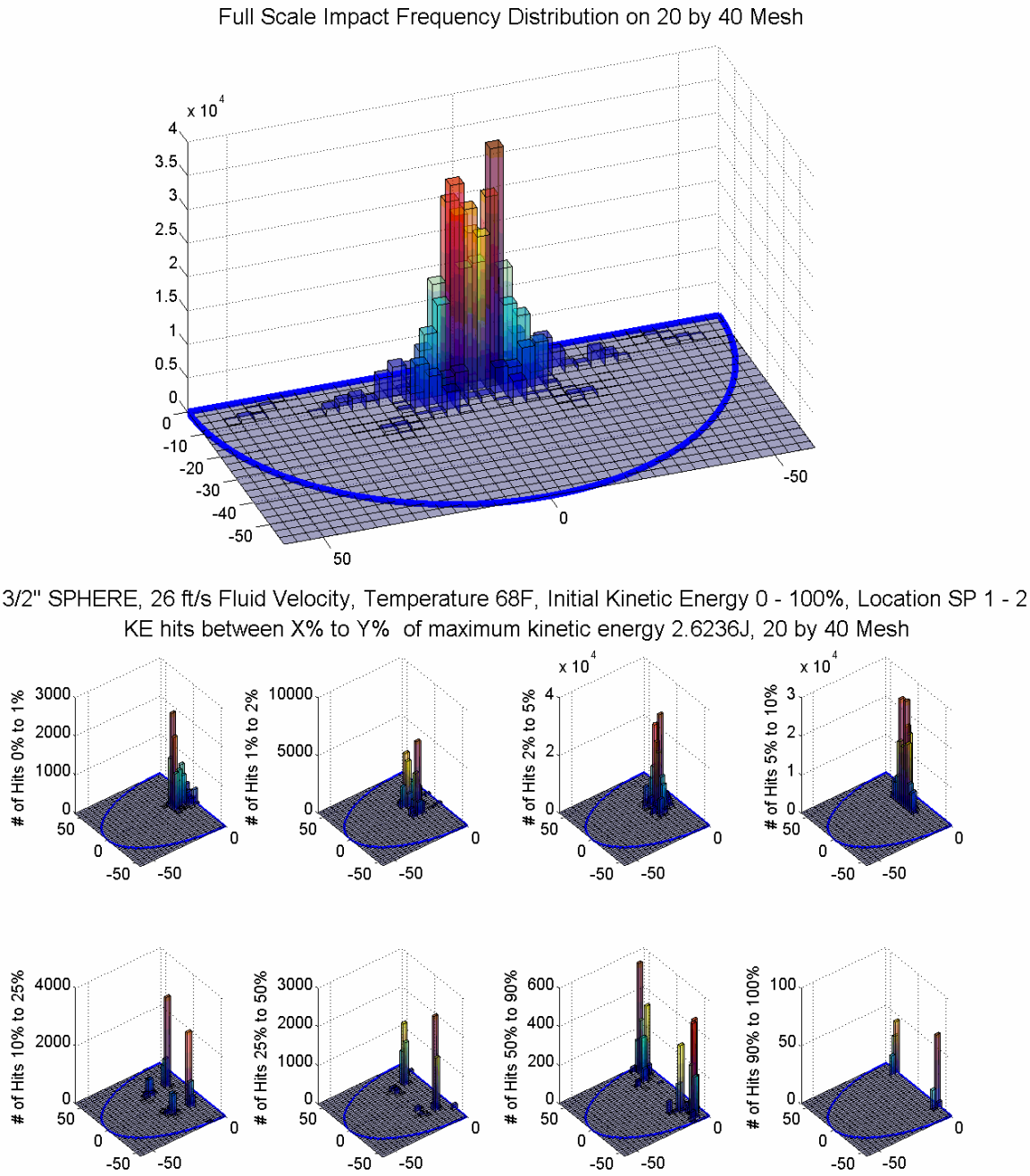

Figure 3.88 3/2" sphere combined spatial impact kinetic energy distribution as a function of impact energy; beyond 5th impacts

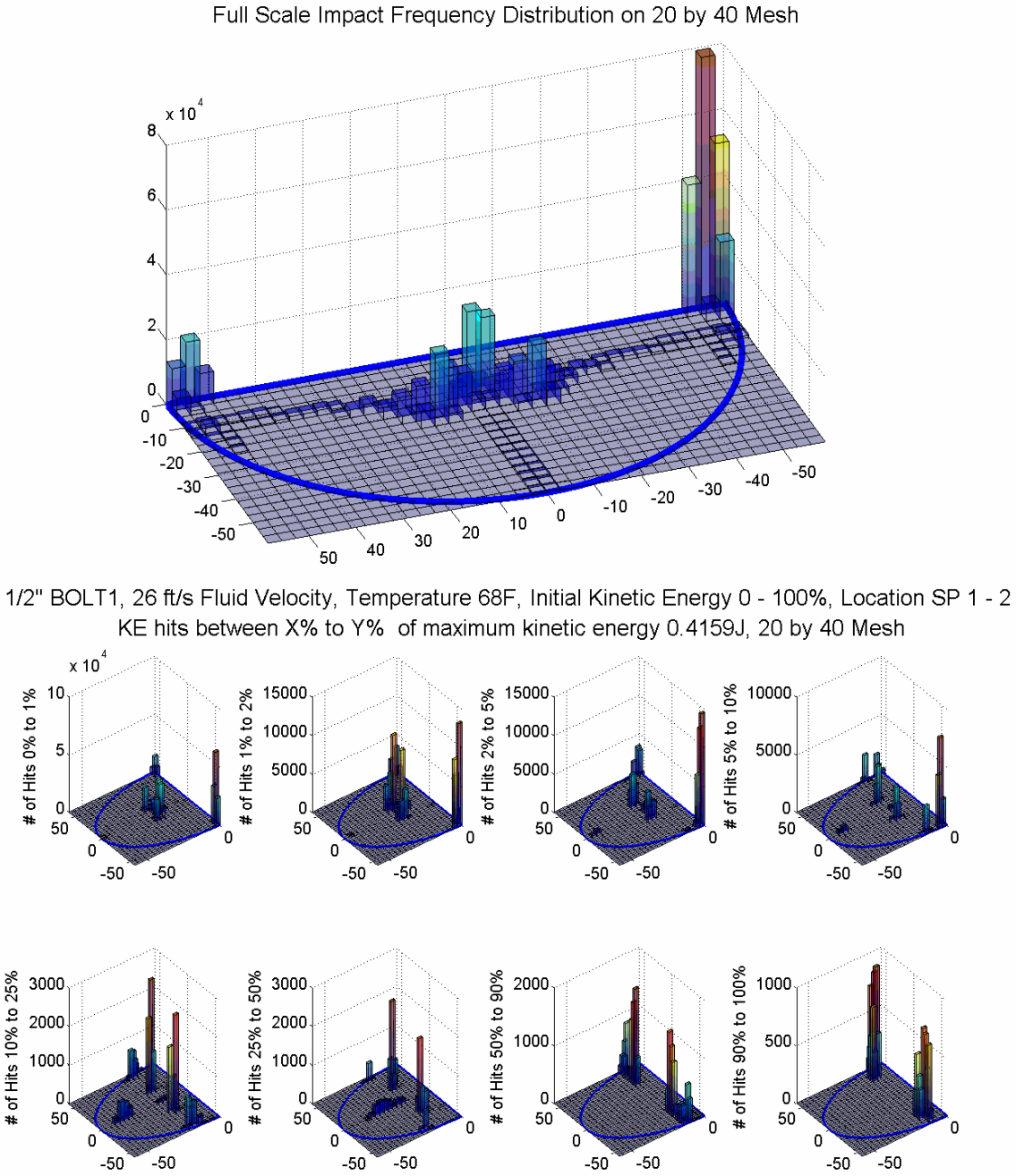

Figure 3.89 1/2" hex bolt type #1 combined spatial impact kinetic energy distribution as a function of impact energy; beyond 5th impacts

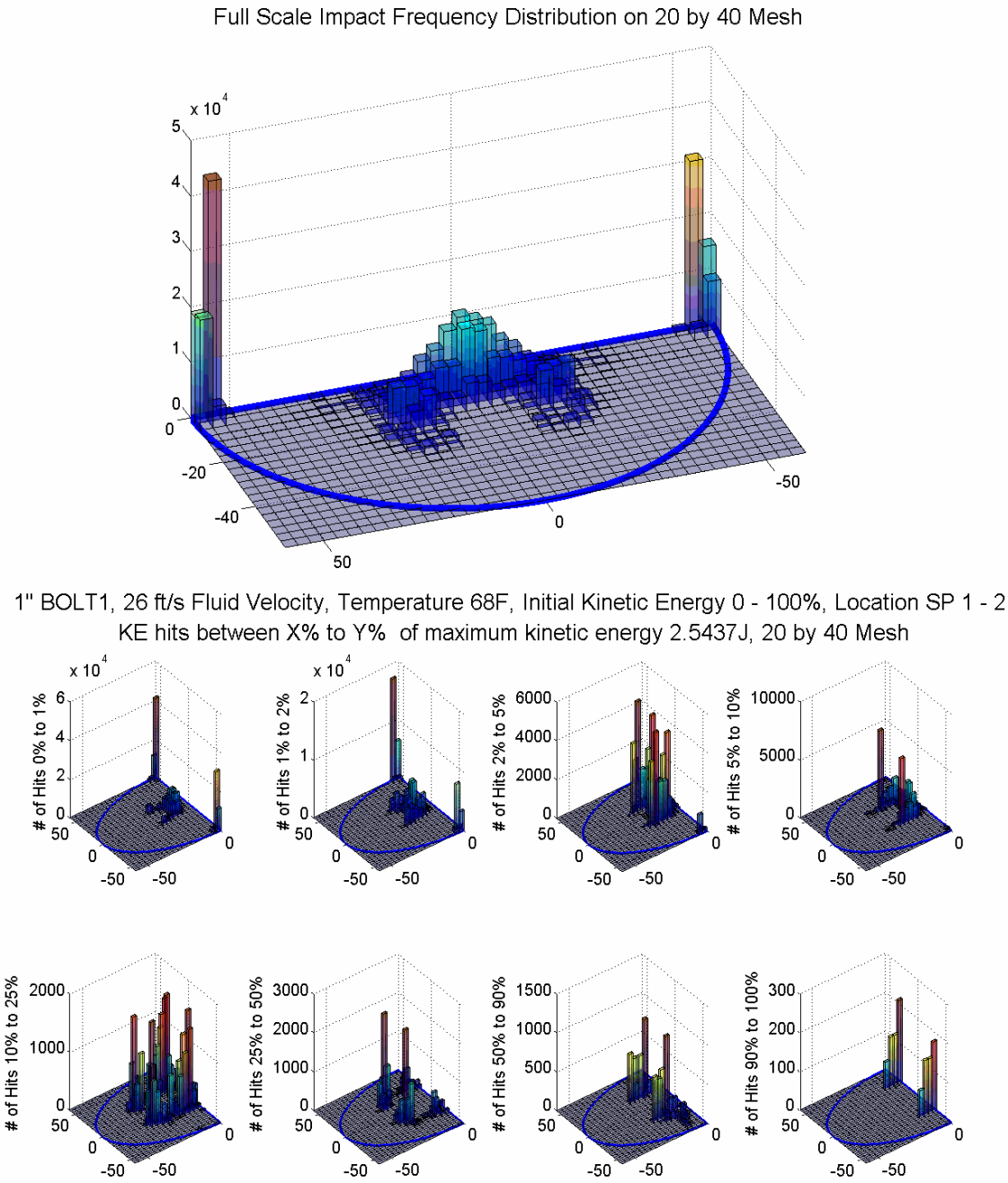

Figure 3.90 1" hex bolt type #1 combined spatial impact kinetic energy distribution as a function of impact energy; beyond 5th impacts

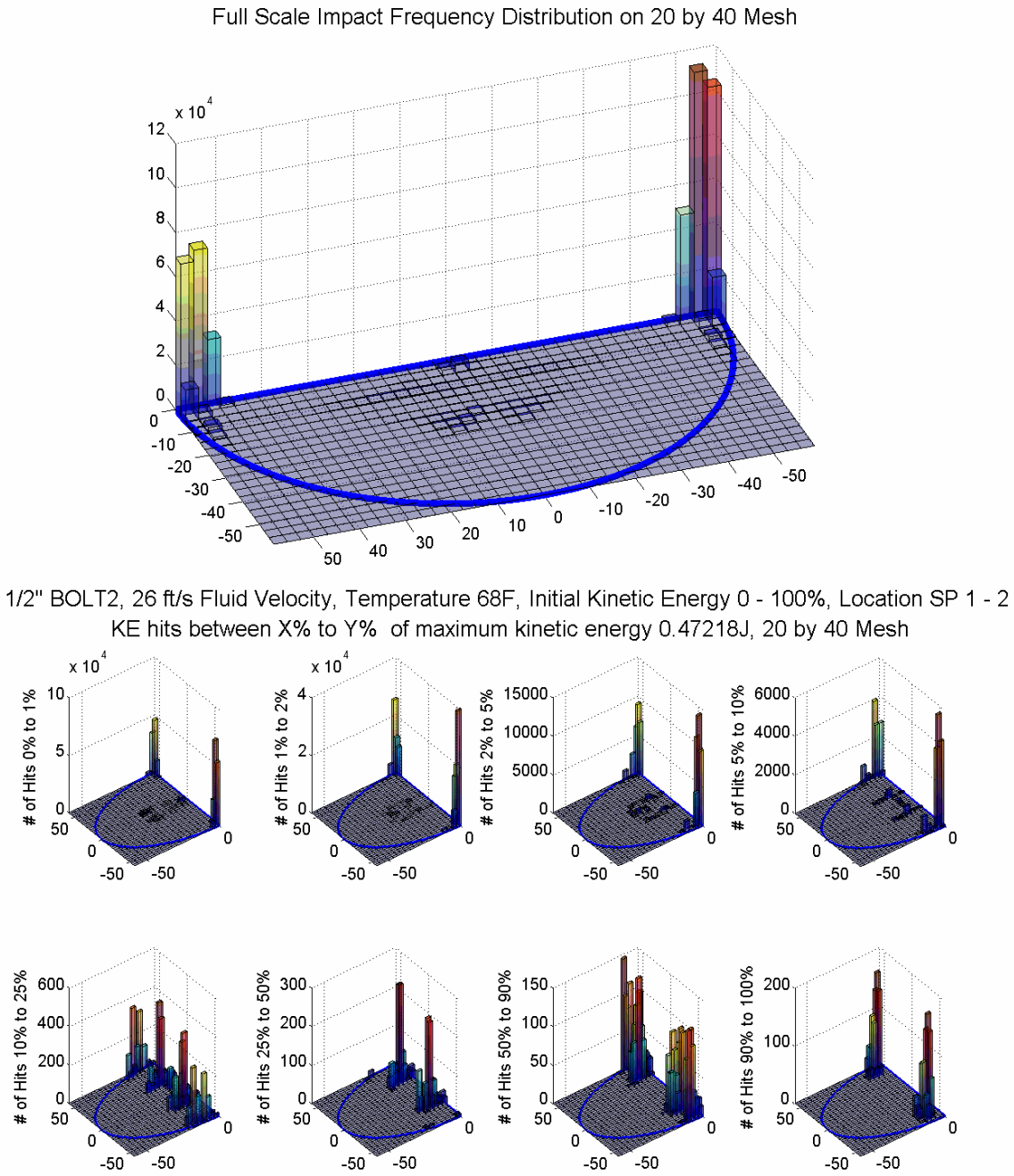

Figure 3.91 1/2" hex bolt #2 combined spatial impact kinetic energy distribution as a function of impact energy; beyond 5th impacts

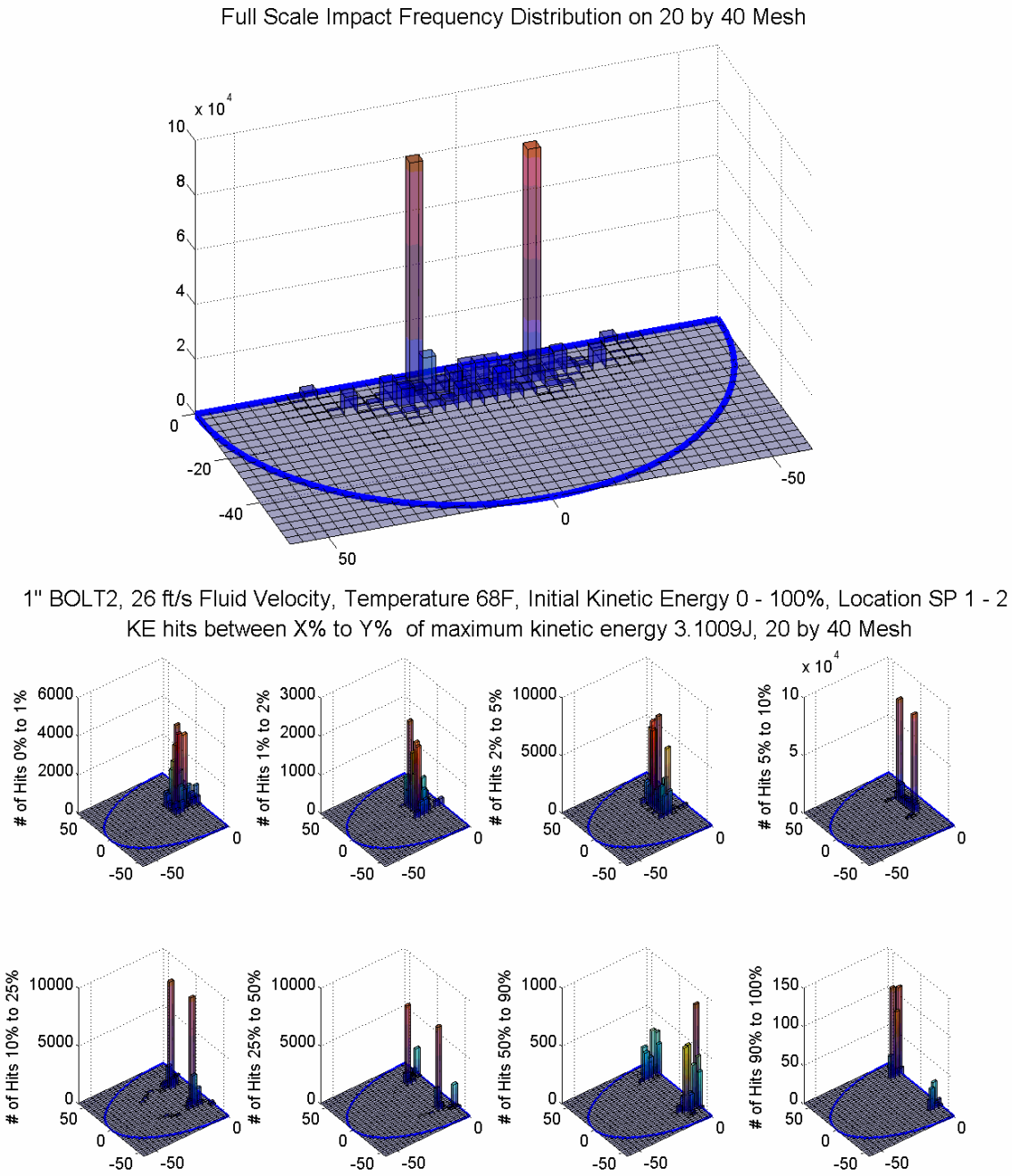

Figure 3.92 1" hex bolt type #2 combined spatial impact kinetic energy distribution as a function of impact energy; beyond 5th impacts

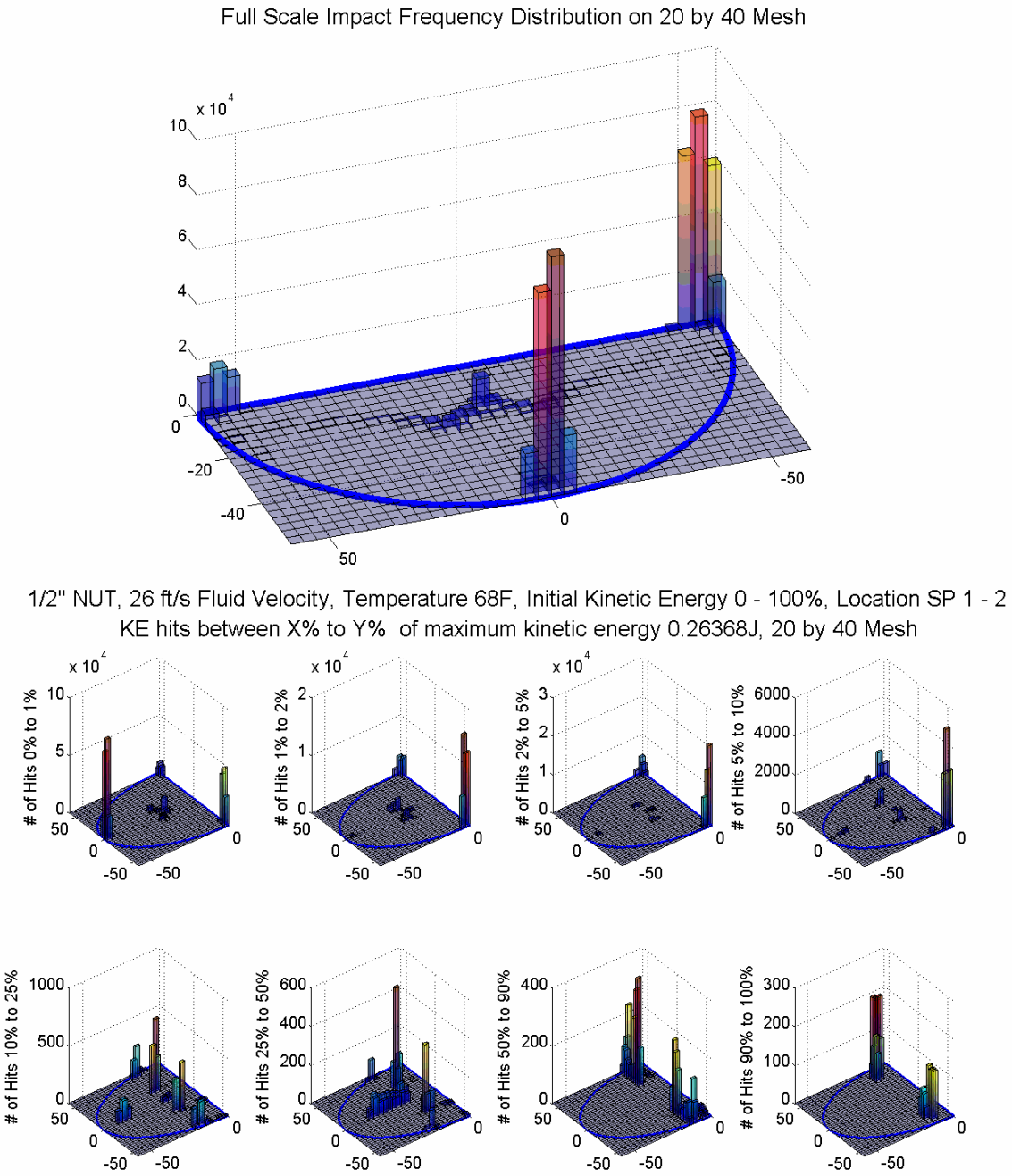

Figure 3.93 1/2" hex nut combined spatial impact kinetic energy distribution as a function of impact energy; beyond 5th impacts

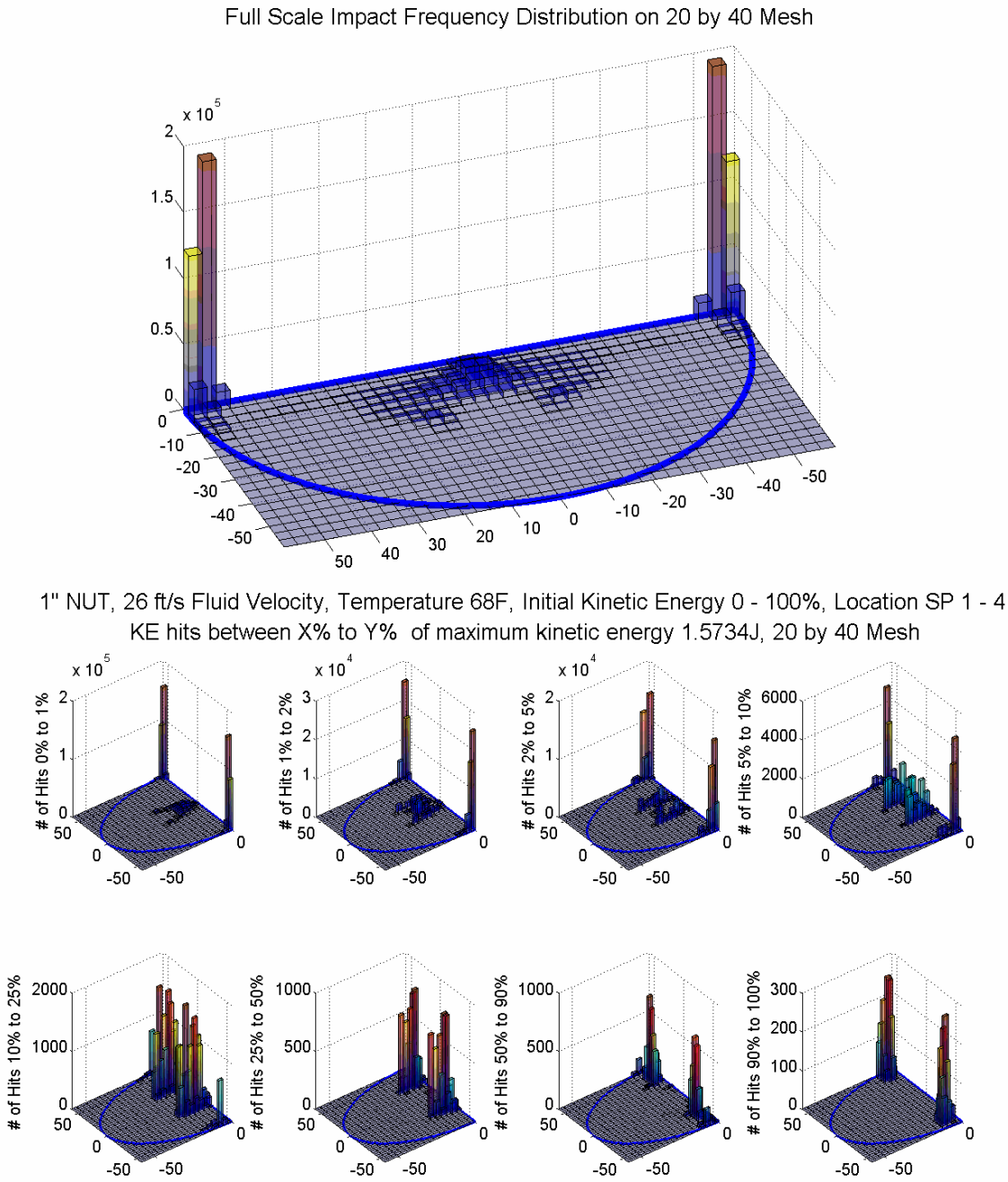

Figure 3.94 1" hex nut combined spatial impact kinetic energy distribution as a function of impact energy; beyond 5th impacts

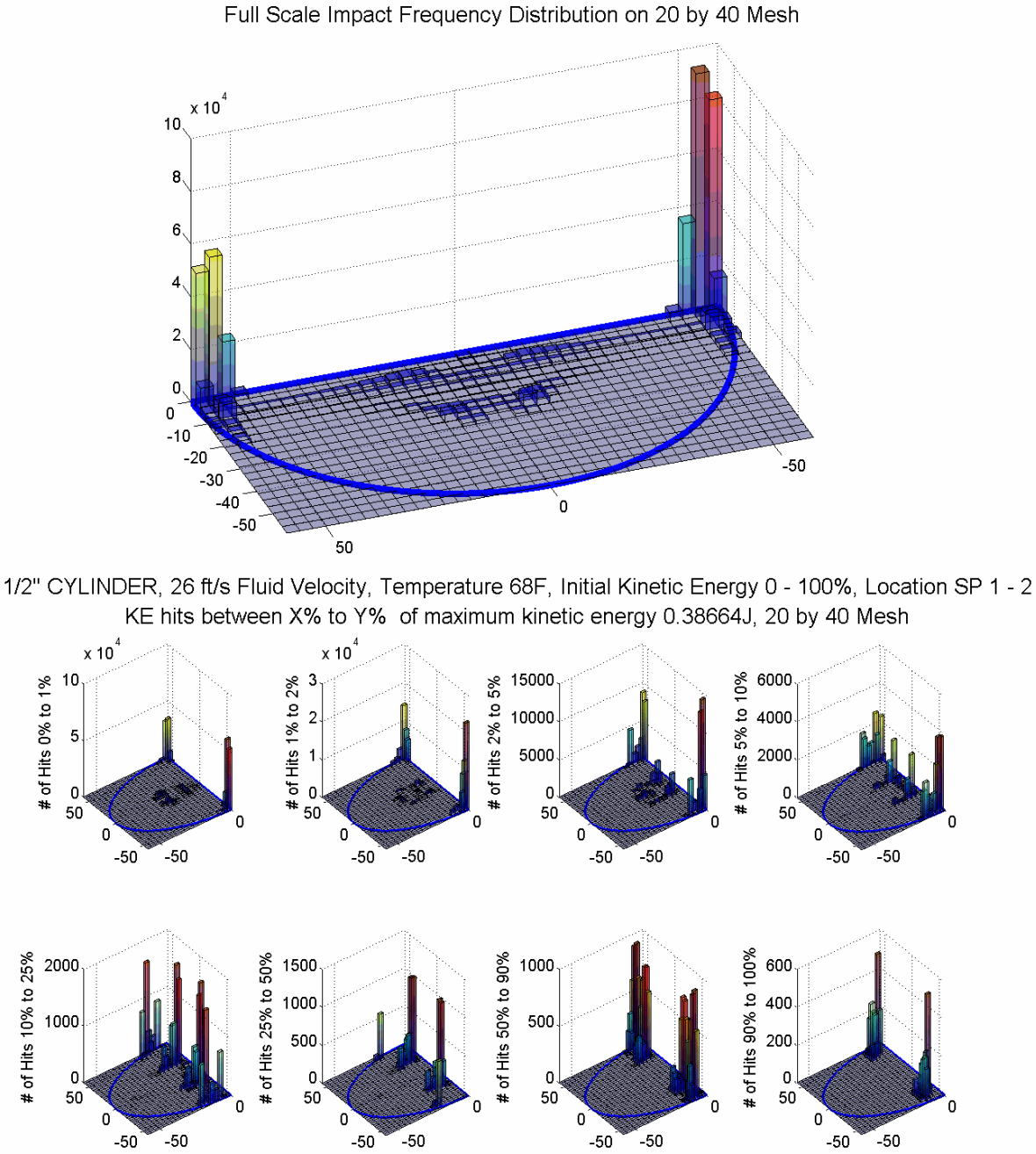

Figure 3.95 1/2" cylinder combined spatial impact kinetic energy distribution as a function of impact energy; beyond 5th impacts

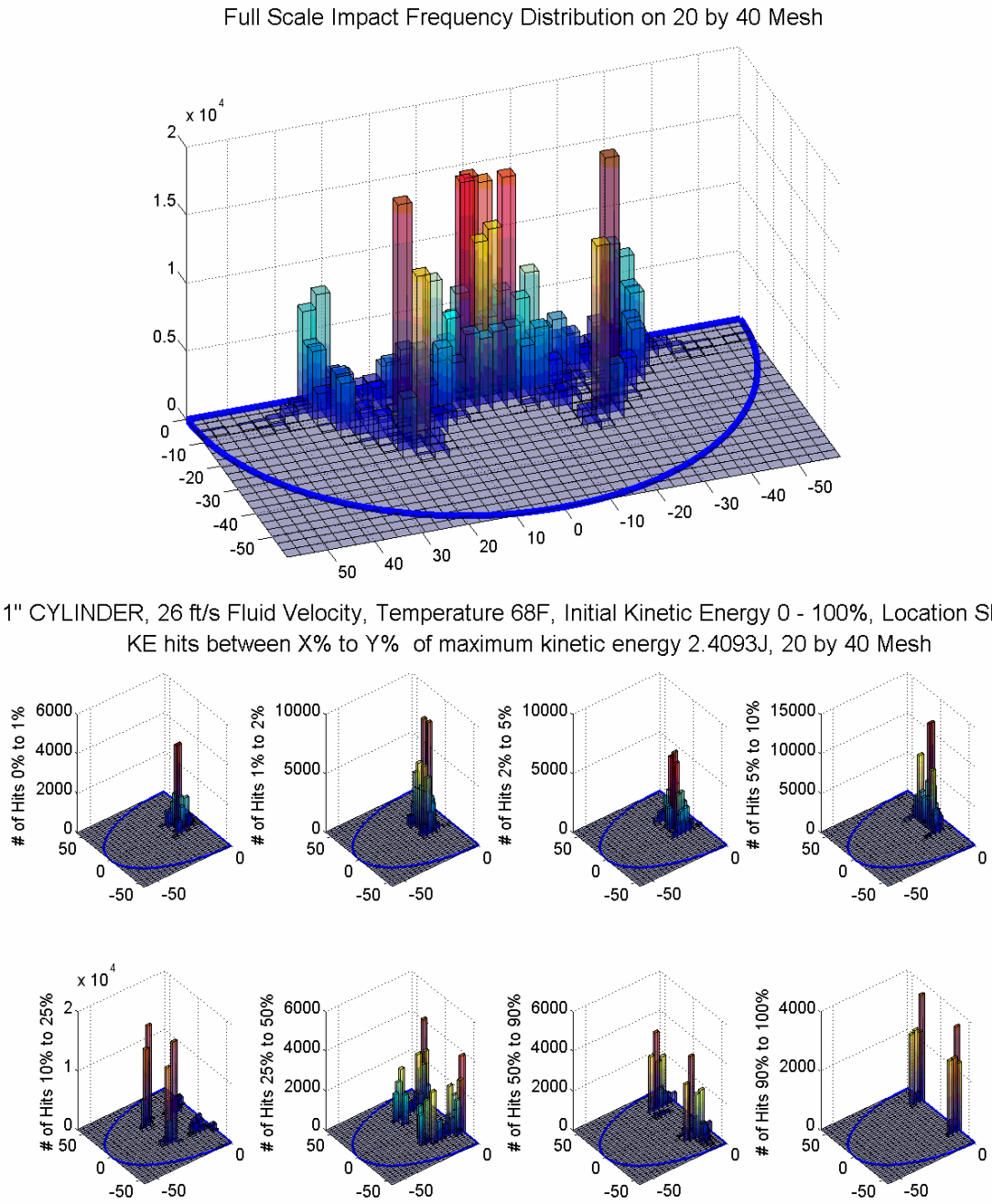

Figure 3.96 1" cylinder combined spatial impact kinetic energy distribution as a function of impact energy; beyond 5th impacts

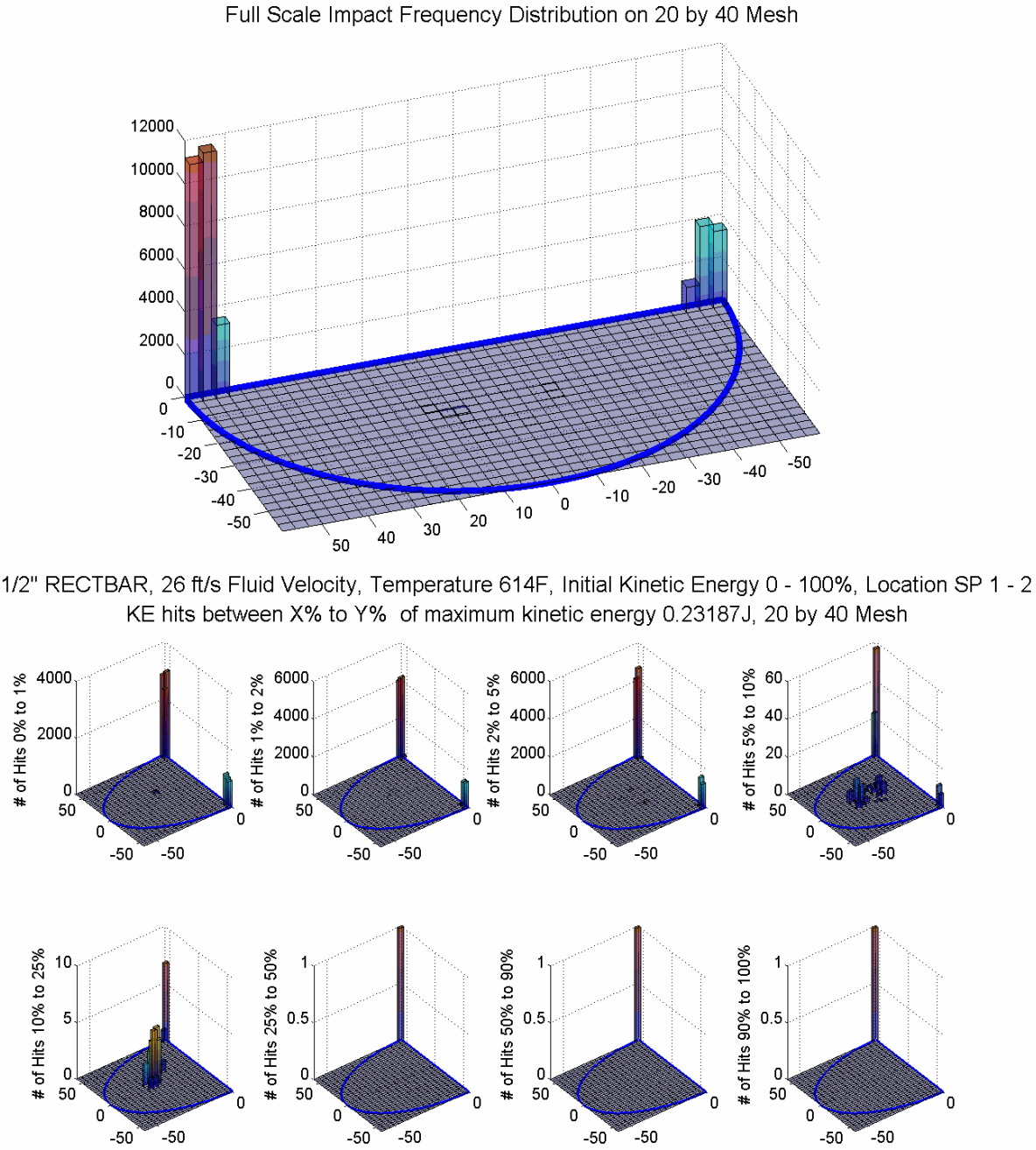

Figure 3.97 1/2" rectangular bar combined spatial impact kinetic energy distribution as a function of impact energy; beyond 5th impacts

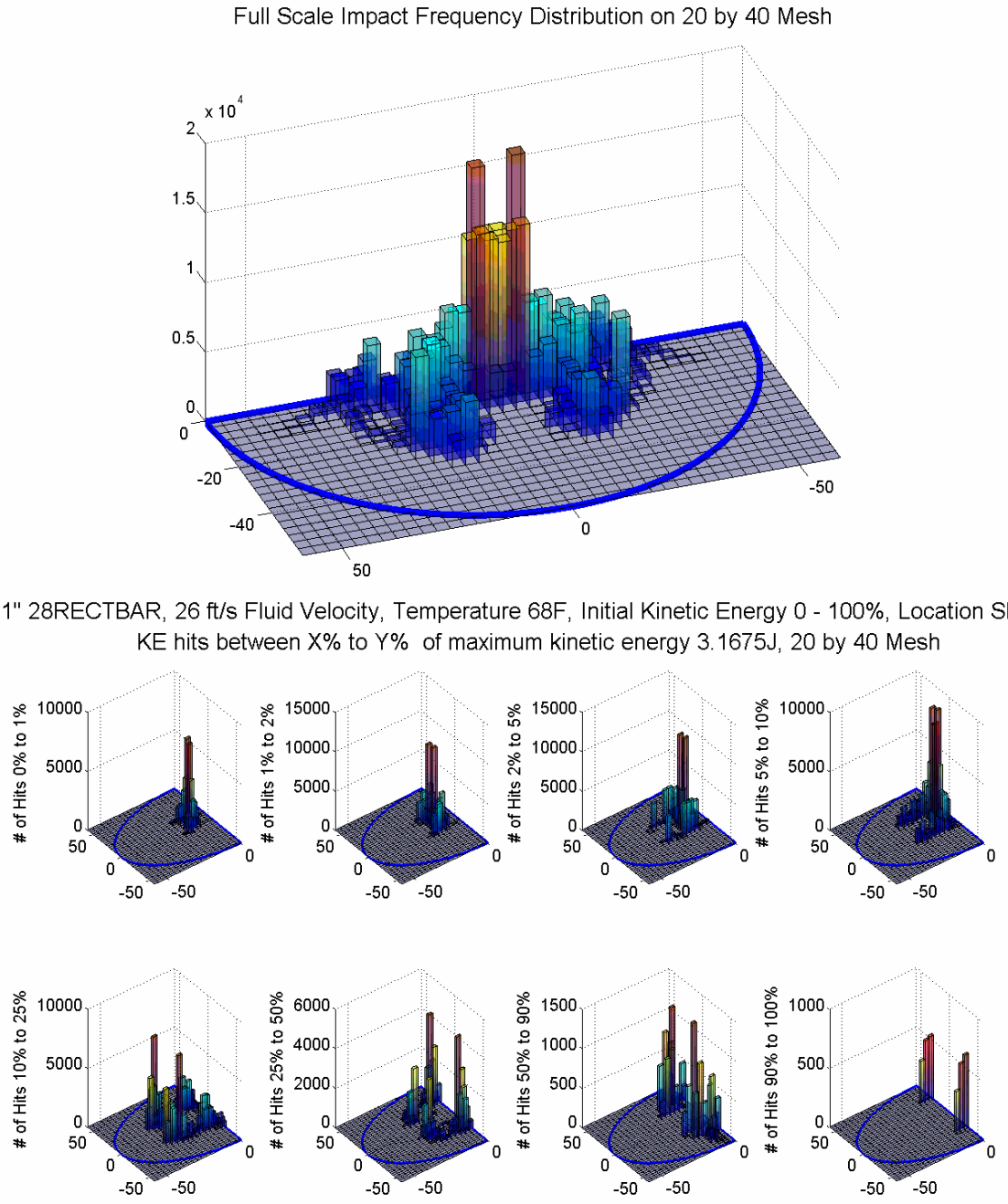

Figure 3.98 1" rectangular bar combined spatial impact kinetic energy distribution as a function of impact energy; beyond 5th impacts

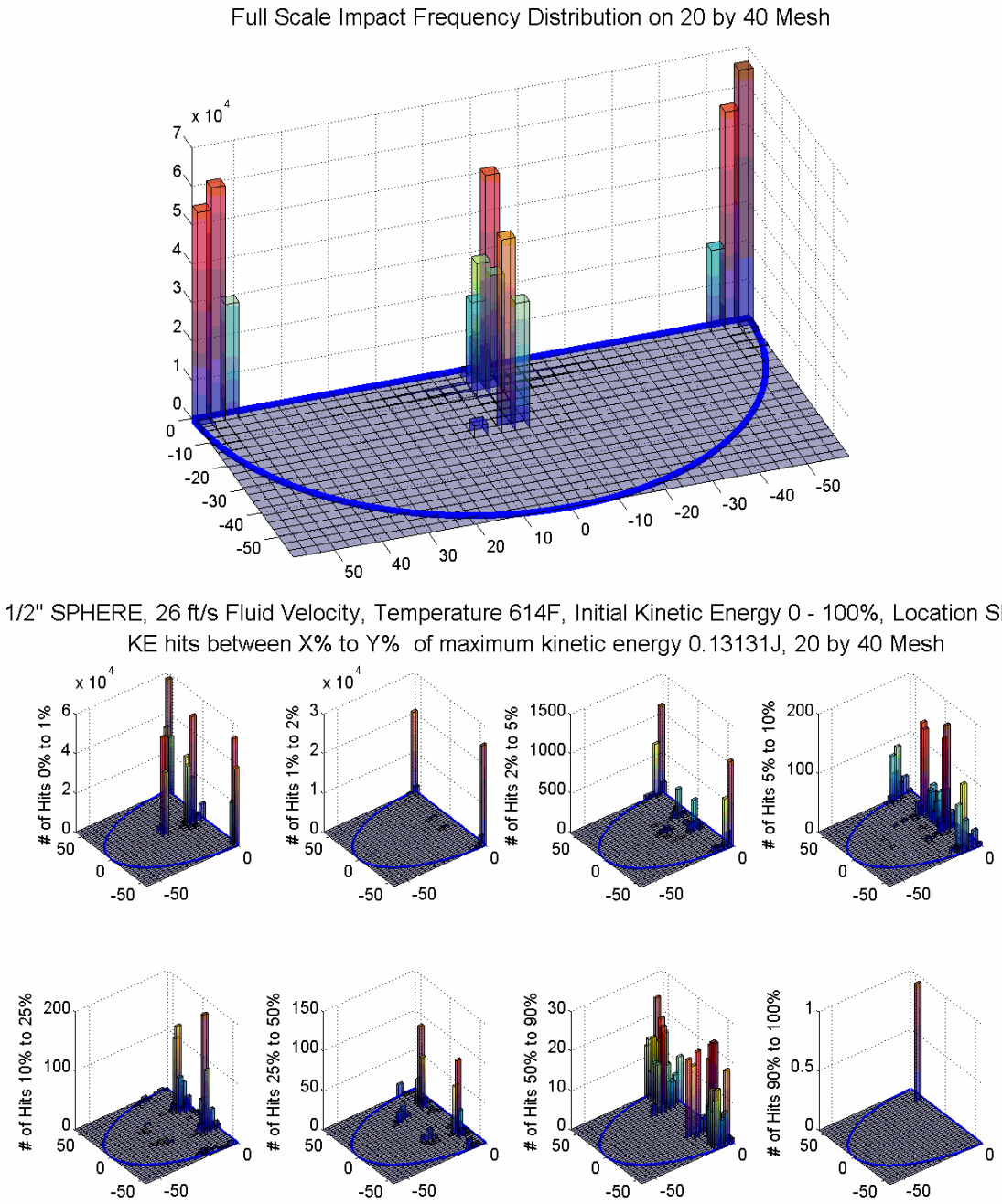

Figure 3.99 1/2" sphere combined spatial impact kinetic energy distribution as a function of impact energy 614^{0}F; beyond 5^{th} impacts

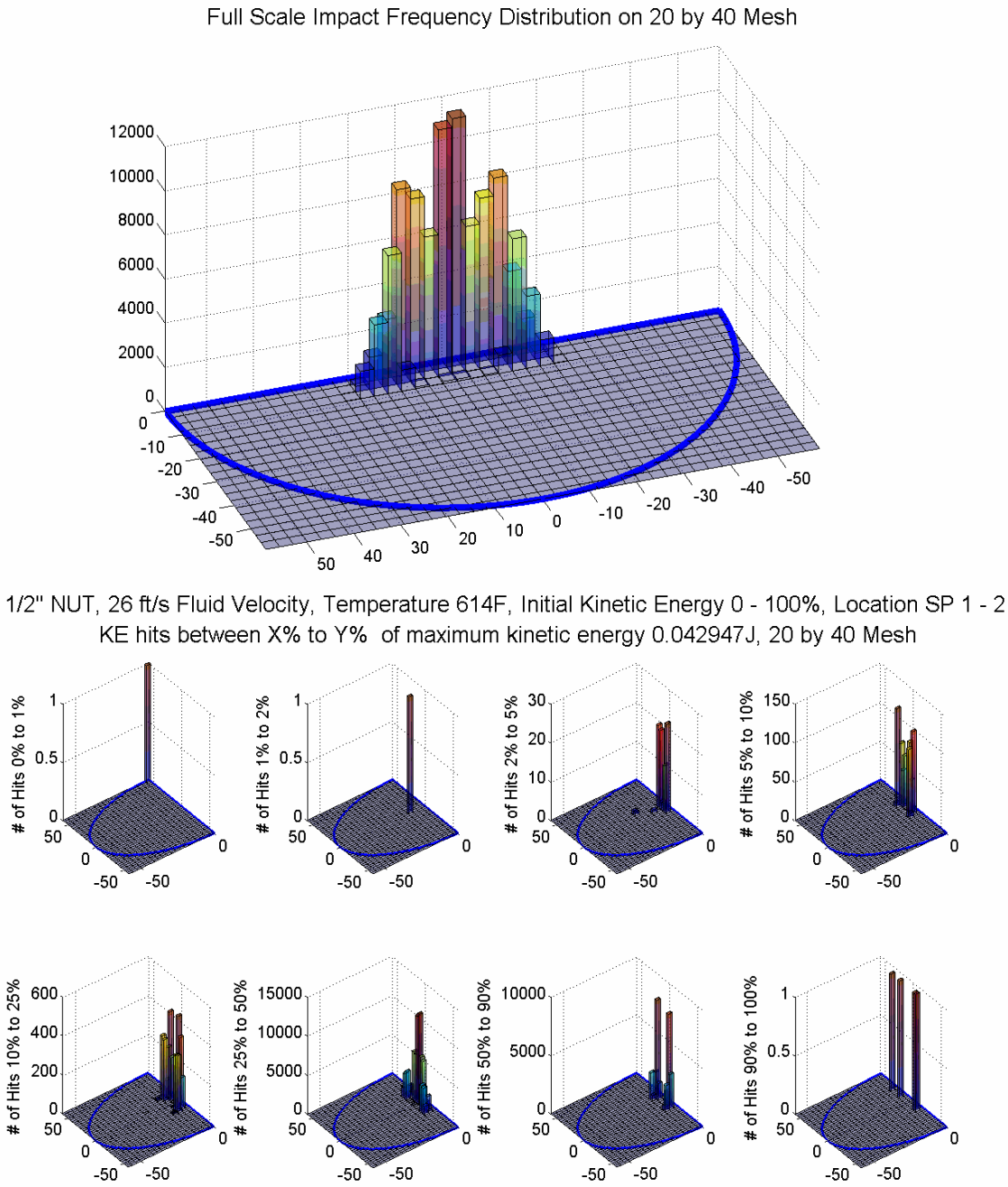

Figure 3.100 1/2" hex nut combined spatial impact kinetic energy distribution as a function of impact energy 614^{0}F; beyond 5^{th} impacts

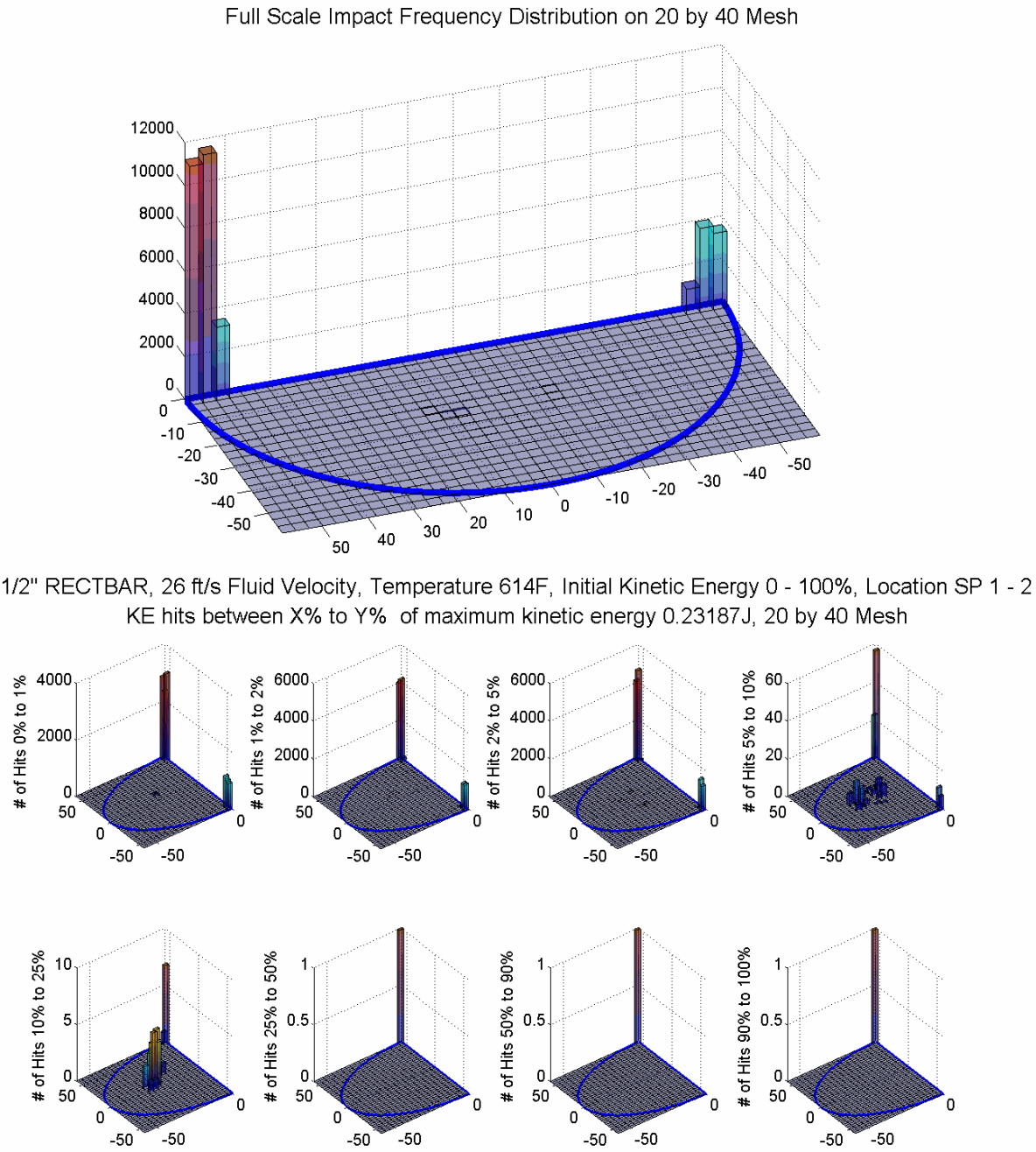

Figure 3.101 1/2" rectangular bar combined spatial impact kinetic energy distribution as a function of impact energy 614^{0}F; beyond 5^{th} impacts

Lastly, for Case2, these six figures represent histograms of impact kinetic energy as a function of part type. Each figure represents a different part class but all the axes have been scaled the same such that each figure is directly comparable. Figures for the sphere, hex nut and rectangular bar classes have all included their 614^0F impact kinetic energies as well. In all, there are a total of thirty-one histograms to compare. The Z-axis is scaled logarithmically and reflects the maximum cutoff for each run of 10,000 tube sheet impacts.

The heaviest part in each class was responsible for the largest number of high energy impacts. Overall, the 1” hex bolt type #2 impacts with the maximum force at 3.090 Joules which matches with the data shown in **Table 3.4**. The 1/2" cylinder is responsible for the highest mean impact kinetic energy for the first five impacts at 0.451 Joules.

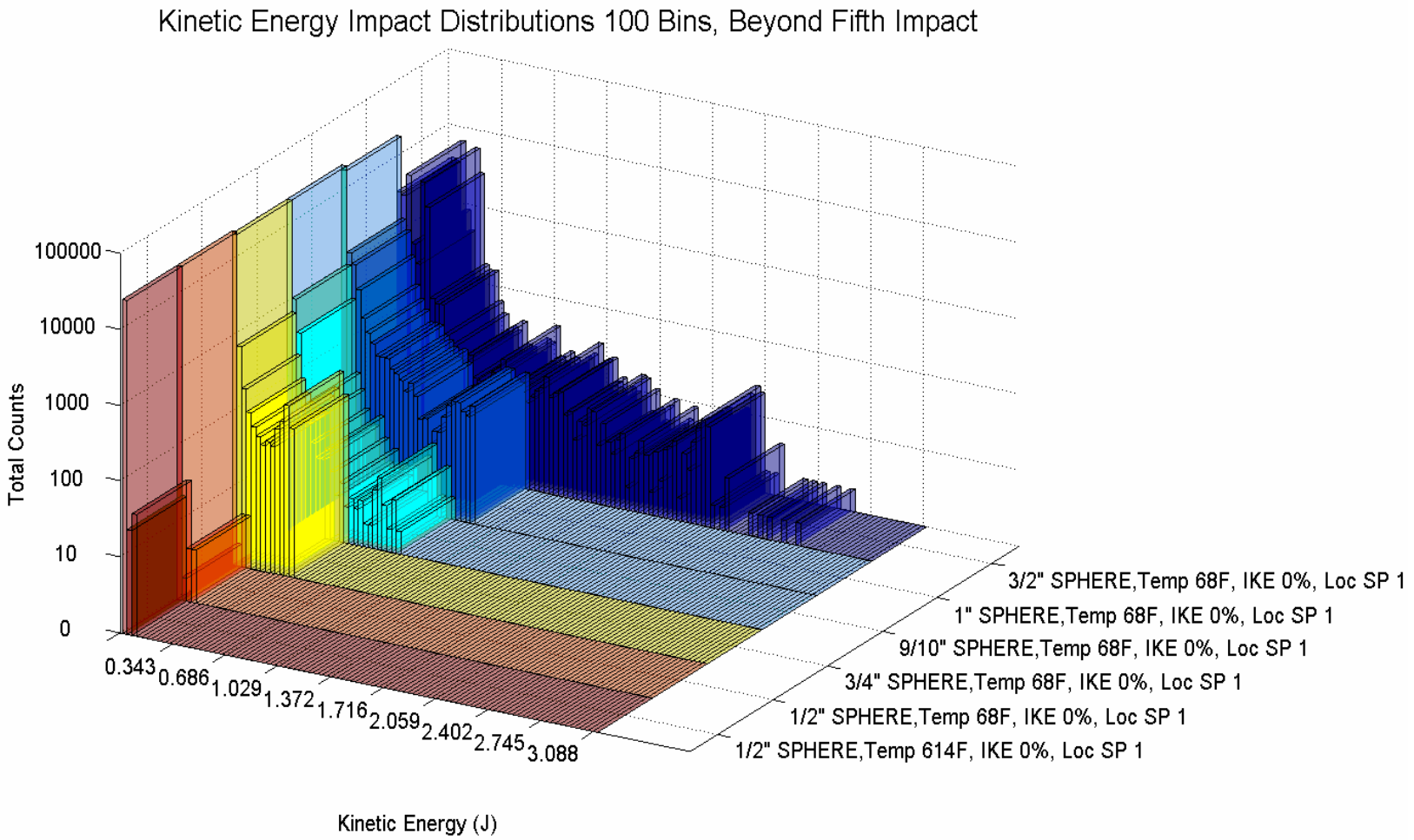

Figure 3.102 Sphere class kinetic energy distribution; beyond 5th impacts

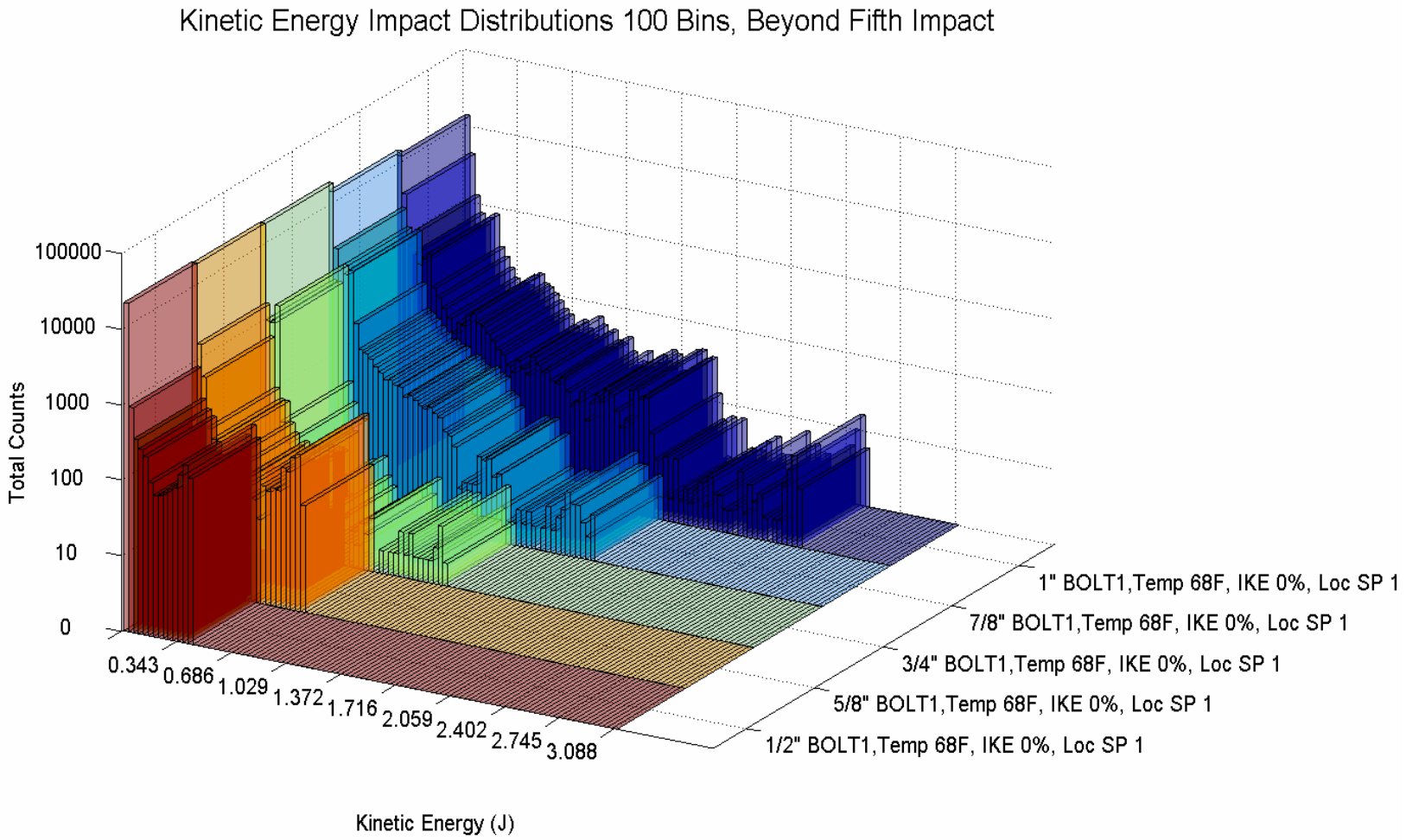

Figure 3.103 Hex bolt type #1 class kinetic energy distribution; beyond 5th impacts

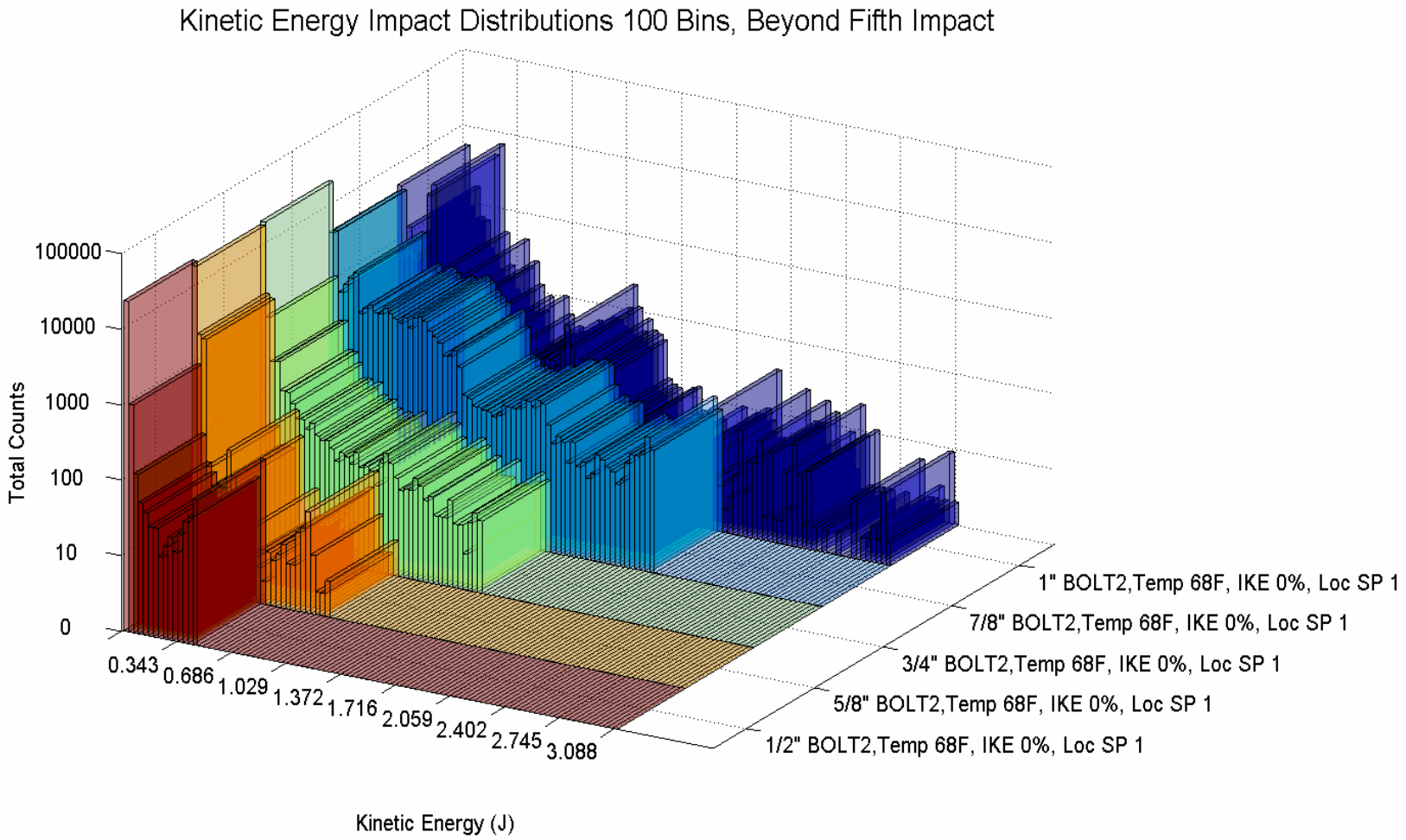

Figure 3.104 Hex bolt type #2 class kinetic energy distribution; beyond 5th impacts

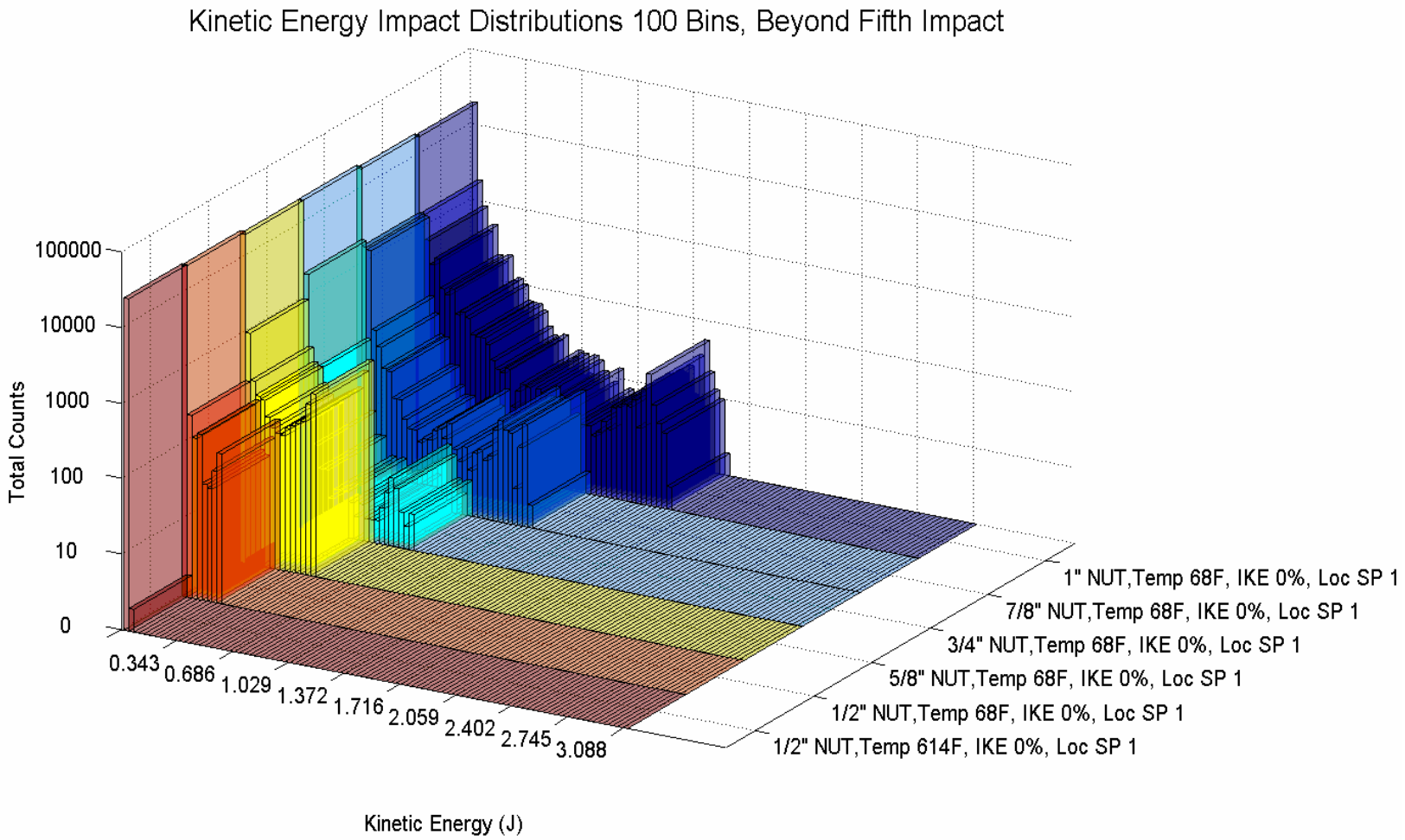

Figure 3.105 Hex nut class kinetic energy distribution; beyond 5th impacts

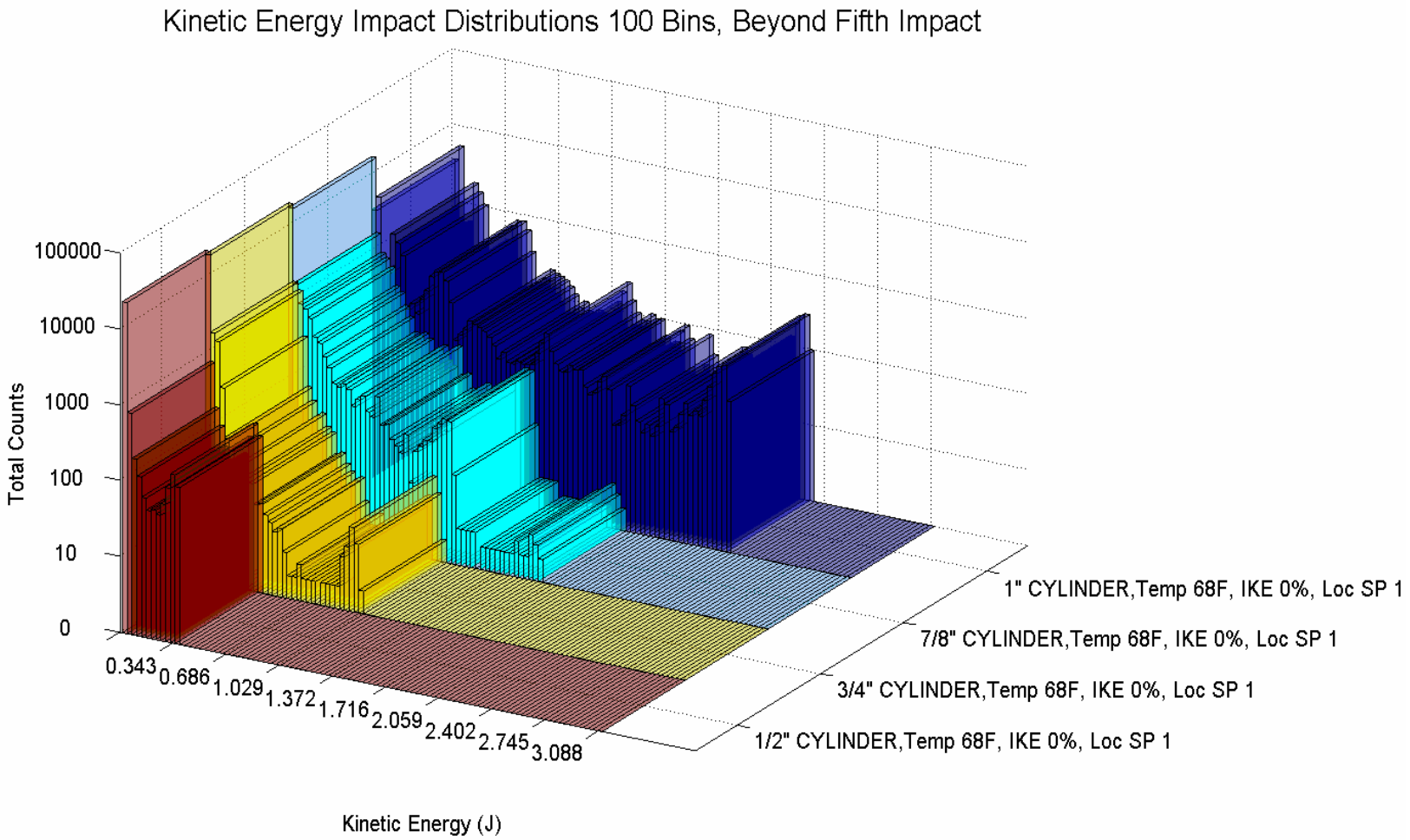

Figure 3.106 Cylinder class kinetic energy distribution; beyond 5th impacts

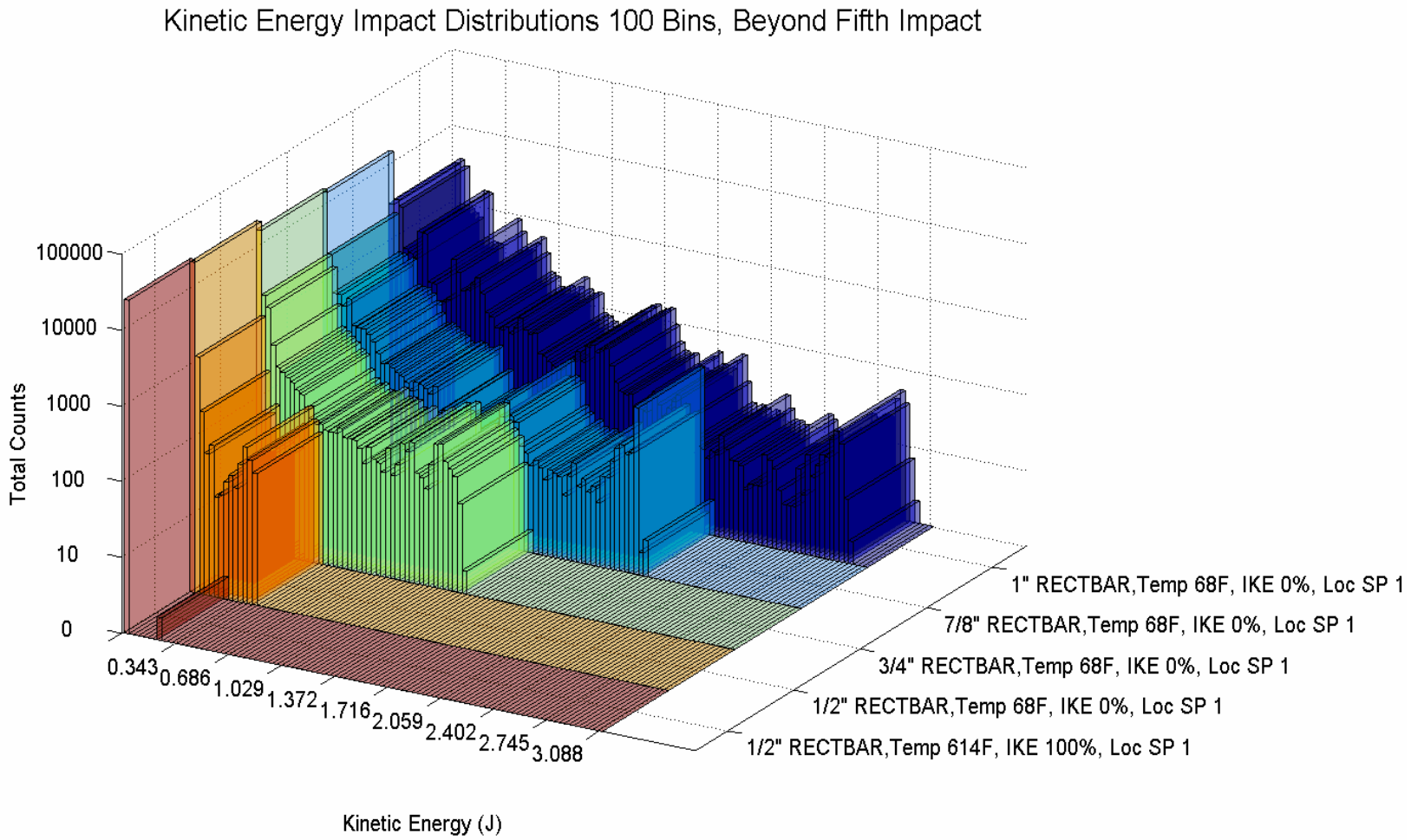

Figure 3.107 Rectangular bar class kinetic energy distribution; beyond 5th impacts

Chapter 4 Conclusions and Future Work

4.1 Conclusions

Analysis was carried out using 3-D CFD techniques to generate a flow velocity map inside a representative steam generator. Monte Carlo simulation results were benchmarked using prior scaled experiment results. Full scale simulations of various loose parts were completed and catalogued.

This process has yielded information on the types of parts that may be considered the most damaging under the conditions run. It has also yielded spatial and energetic impact distributions for all twenty eight parts outlined by Shi.

Overall, of the loose parts simulated at hot full power conditions, only the lightest were even able to come into contact with the tube sheet. It is not until lower fluid temperatures, where the water viscosity is higher is there significant impacts occurring on the tube sheet.

Mean and maximum impact kinetic energies have been outlined in **Chapter 3** for each loose part. Generally, the heaviest parts impacted with the most force but lighter parts may have impacted more consistently at high kinetic energies. Spatially, heavier parts concentrate in the center of the flow plume while lighter parts tend to spread out to the extremes of the tube sheet. Impacts as a function of energy are also given above for each class of part.

4.2 Future Work

Ultimately, a detailed sensitivity analysis should be performed to better outline which of the many parameters are most important in causing impact damage on the tube sheet. This analysis coupled with the uncertainties of the loose part monitoring systems could be used to predict possible distributions of damage rates to the tube sheets given a multitude of operating conditions.

Also, coupling of the three dimensional CFD analysis, the Monte Carlo Code written for this work and the codes previously written in Shi's work should be linked together to gain a more informed picture of the mechanisms occurring inside the steam generator inlet plenum.

REFERENCES

BARAFF, D.: An Introduction to Physically Based Modeling: Rigid Body Simulation II – Nonpenetration Constraints (1997). Unpublished Lecture Notes.

DONLEY, H.E., "The Drag Force on a Sphere," *UMAP Journal*, 12, 45 – 80 (1991).

(2009). *ESPI High Purity Metal Specialists.* Retrieved Jan. 7, 2010, from ESPICorp Inc., Ashland, OR. Web site: http://www.espimetals.com/.

LEE, A., MASIELLO, P.: ATHOS3 computer code verification: Volume 1, 2/3-scale test: Final report.Tech. rep., EPRI-NP-5557-Vol. 1, Westinghouse Electric Corp., Forest Hills, PA (USA). Steam Generator Technology Div. (1988).

LI, L.Y., WU, CY, THORNTON, C., "A Theoretical Model for the Contact of Elastoplastic Bodies," *Proceedings of the Institution of Mechanical Engineers, Part C: Journal of Mechanical Engineering Science*, 216, no. 4, 421-431 (2001).

"McGuire Nuclear Station Final Safety Analysis Report," Duke Power Company (1983).

MICHEL, B., PUYAL, C., "Operational and Economical Experience with Vibration and Loose Parts Monitoring Systems on Primary Circuits of PWRs," *Progress in Nuclear Energy*, 21, 469 (1988).

SHI, LIANG, *Nuclear Reactor Loose Part Impact Activity and Damage Mechanisms*, PhD Dissertation, North Carolina State University, Raleigh (1995).

THORNTON, C., "Coefficient of Restitution for Collinear Collisions of Elastic-Perfectly Plastic Spheres," *Journal of Applied Mechanics*, 64, 383 (1997).

WU, CHUAN-YU, LI, LONG-YUAN, THORNTON, COLIN, "Rebound Behaviour of Spheres for Plastic Impacts," *International Journal of Impact Engineering*, 28, 929 (2003).

YOUNG, M., TAKEUCHI, K., MENDLER, O., HOPKINS, G.: Prototypical steam generator (MB-2) transient testing program. Task plan/scaling analysis report.[PWR]. Tech. rep., NUREG/CR-3661, Westinghouse Electric Corp., East Pittsburgh, PA (USA) (1984).